Wintertime characteristic atmospheric circulation in the Grenoble basin and impact on air pollution

Enzo Le Bouëdec

To cite this version:

Enzo Le Bouëdec. Wintertime characteristic atmospheric circulation in the Grenoble basin and impact on air pollution. Meteorology. Université Grenoble Alpes [2020-..], 2021. English. NNT : 2021GRALU031 . tel-04148049

HAL Id: tel-04148049

https://theses.hal.science/tel-04148049

Submitted on 2 Jul 2023

UGA
Université
Grenoble Alpes

THÈSE

Pour obtenir le grade de

DOCTEUR DE L'UNIVERSITÉ GRENOBLE ALPES

Spécialité : **Océan, Atmosphère, Hydrologie**

Arrêtée ministériel : 25 mai 2016

Présentée par

Enzo LE BOUËDEC

Thèse dirigée par **Chantal STAQUET (directrice)**
et codirigéee par **Charles CHEMEL (co-encadrant)**

préparée au sein du **Laboratoire des Écoulements Géophysiques et Industriels (LEGI)**
dans **l'École Doctorale Sciences de la Terre, de l'Environnement et des Planètes (STEP)**

Circulation atmosphérique hivernale dans le bassin Grenoblois : caractérisation et impact sur la qualité de l'air

Wintertime characteristic atmospheric circulation in the Grenoble basin and impact on air pollution

Thèse soutenue publiquement le **3 Décembre 2021**,
devant le jury composé de :

Prof. Dino ZARDI
Université de Trente, Rapporteur

Prof. Joan CUXART RODAMILANS
Université des îles Baléares, Rapporteur

Dr. Alexander GOHM
Université d'Innsbruck, Examinateur

Dr. Thierry HEDDE
CEA Cadarache, Examinateur

Prof. Alain CLAPPIER
Université de Strasbourg, Examinateur

Dr. Jean-Luc JAFFREZO
Université de Grenoble Alpes, Président

Prof. Chantal STAQUET
Université de Grenoble Alpes, Directrice de thèse

Dr. Charles CHEMEL
NCAS, Co-Encadrant de thèse

Contents

Acknowledgments

General introduction **1**

1 Scientific background & research objectives **3**
- 1.1 Atmospheric dynamics . . . 3
  - 1.1.1 Global atmospheric dynamics . . . 3
  - 1.1.2 Focus on North hemisphere mid-latitude large-scale atmospheric dynamics . . . 5
  - 1.1.3 The atmospheric boundary layer . . . 6
  - 1.1.4 Atmospheric dynamics over complex terrain . . . 7
    - 1.1.4.1 Orographic channeling . . . 8
    - 1.1.4.2 Mountain thermally-driven wind system . . . 9
    - 1.1.4.3 Cold air pool . . . 11
- 1.2 Particulate matter air pollution . . . 12
  - 1.2.1 Emission sources . . . 12
  - 1.2.2 Health impact . . . 14
  - 1.2.3 Particulate matter evolution in the atmosphere . . . 14
- 1.3 Air pollution and tracer dispersion in complex terrain . . . 16
- 1.4 Specificities of the Grenoble Y . . . 18
- 1.5 Outline and research objectives . . . 19

2 Towards a Weather Type Decomposition tailored for the Grenoble Y **21**
- 2.1 Introduction . . . 21
- 2.2 Approaches to Weather Type Decomposition . . . 21
- 2.3 Desired characteristics of the Weather Type Decomposition . . . 23
- 2.4 Application to the Grenoble Y . . . 23
  - 2.4.1 A brief introduction of available databases . . . 24
    - 2.4.1.1 Large-scale data . . . 24
    - 2.4.1.2 Local scale data . . . 24
  - 2.4.2 A classical approach ($\mathcal{W}_1$) . . . 26
  - 2.4.3 A tailored classical approach ($\mathcal{W}_2$) . . . 29
  - 2.4.4 An attempt using neural networks . . . 32
    - 2.4.4.1 Introduction to convolutional and long short term memory neural networks . . . 32
    - 2.4.4.2 Non Linear dimension reduction . . . 34
    - 2.4.4.3 Resulting weather type decomposition ($\mathcal{W}_3$) . . . 37
  - 2.4.5 Classification based on physical grounds ($\mathcal{W}_4$) . . . 40
- 2.5 Concluding remarks . . . 43

3 Numerical simulations: set-up and evaluation 47
3.1 Selection and description of the episodes 47
3.1.1 Selection of the episodes 47
3.1.2 Description of the episodes 47
3.1.2.1 $\mathcal{E}_1$: Episode from 7th December 2013 to 18th December 2013 48
3.1.2.2 $\mathcal{E}_2$: Episode from 1st December 2016 to 5th December 2016 49
3.1.2.3 $\mathcal{E}_3$: Episode from 6th December 2016 to 11th December 2016 49
3.1.2.4 $\mathcal{E}_4$: Episode from 28th December 2016 to 2nd January 2017 1st 49
3.1.3 Summary 51
3.2 Numerical set-up 51
3.2.1 Domain description 52
3.2.2 Land use description 53
3.2.3 Snowpack initialization 55
3.2.4 particulate matter (PM) emission processing 57
3.2.5 Dynamical core 58
3.2.6 Physics parametrization 59
3.3 Smoothing of the topography 60
3.3.1 Description of the optimization problem 60
3.3.2 Application to the Grenoble valley 61
3.3.3 Trade-off between vertical resolution and steepness of the topography 63
3.4 Model evaluation 66
3.4.1 Meteorological variables 68
3.4.1.1 Winds at 10 m AGL 68
3.4.1.2 Vertical wind profile at ILL 68
3.4.1.3 2-meter air temperature 68
3.4.1.4 Vertical temperature profile at ILL 72
3.4.2 Possible causes for meteorological discrepancies 75
3.4.2.1 Underestimation of the Grésivaudan valley-flow speed . . . 75
3.4.2.2 Ill-channeling 75
3.5 Concluding remarks 77

4 Local atmospheric dynamics during Winter Anticyclonic Blocking episodes 79
4.1 Observed local circulation in the Grenoble Y 79
4.2 Similarities and differences between the episodes 84
4.2.1 Near-surface flows 84
4.2.1.1 Night time 84
4.2.1.2 Day time 85
4.2.1.3 Characterization of the valley exit jet 86
4.2.1.4 Near-ground interactions among the different valleys of the Grenoble Y 87
4.2.2 Vertical structure of the winds 89
4.2.3 Atmospheric stability 89
4.3 About low level stratus formation 94
4.4 Concluding remarks 95

5 Valley-scale dispersion during Winter Anticyclonic Blocking episodes 99
- 5.1 Identification of stagnation and ventilation zones 99
  - 5.1.1 Definition of stagnation and ventilation zones 99
  - 5.1.2 Definition of thresholds and statistical significance 100
  - 5.1.3 Discussion about the advection velocity 102
  - 5.1.4 Application to the simulated winter anticyclonic blocking episodes . 103
- 5.2 Evaluation of simulated pollution levels 104
  - 5.2.1 Comparison to measured pollution levels 104
  - 5.2.2 Possible reasons for the discrepancies 107
    - 5.2.2.1 Underestimation of subgrid scale eddy diffusivity 108
    - 5.2.2.2 Further hypotheses on the origin of the discrepancies . . . 114
- 5.3 Spatial variations of simulated particulate matter (PM) concentrations . . 114
  - 5.3.1 Ground-level variations 114
  - 5.3.2 Vertical profiles 116
  - 5.3.3 Impact of slope winds 119
  - 5.3.4 Interplay between atmospheric dynamics and emissions 121
- 5.4 Concluding remarks 123

Conclusions & Perspectives 125

A Supplementary figures 151

Acknowledgments

First of all, I would like to thank my thesis supervisors, Chantal and Charles, for allowing me to complete this PhD thesis. You provided me with a regular follow-up allowing a good balance between guiding me towards relevant axes of investigation while still granting me the freedom to develop the axes of interest to me. You also found the words that allowed me to carry on with this adventure at a time when the energy had left me, for which I am very grateful. I also wish to thank all the team of Mobil'Air for allowing me to take part in this adventure. The interdisciplinary aspect of this team allowed me to have a more comprehensive vision on my work while widening my spectrum of knowledge on topics such as social sciences and economics. Moreover, the conviviality within this team made the moments of meetings very pleasant, with a special mention for the few days of the Scientific Advisory Board of 2021.

Among the best memories I will keep of this adventure, the LEGI and its atmosphere clearly have a key position. Thanks to all the colleagues and friends I met there, especially for all the great moments and discussions/debates we were able to share in the cafeteria. A special mention for Miguel who was a golden office colleague! You took me on some great adventures in ski mountaineering and trail running! These adventures have given rise to a beautiful friendship that I hope will last a long time.

The completion of this PhD was only possible because I have the best friends, flatmates and family. Seeing you has always kept my spirits up, given me perspective, and most of all, kept me moving forward! With of course a very special mention for my sweetheart Léa who supported me on a daily basis, in both senses of the word, during the whole thesis writing process!

General introduction

Poor air quality, particularly in urban areas, has a demonstrable effect on human health. According to Cohen et al. (2017), exposure to particulate matter with diameter of less than 2.5 µm ($PM_{2.5}$) was responsible for the death of 4.2 million people worldwide in 2015, accounting for 7.6 % of annual global deaths. Furthermore it resulted in an additional 103 million disability adjusted life years (DALY; years lived with disability plus years of life lost). Overall it was found to be the 5th greatest risk factor for human beings.

Currently air pollution is of greatest concern in low- and middle-income countries. 59 % of the deaths and DALY reported for 2015 in the study by Cohen et al. (2017) are concentrated in South and East Asia. Several factors can account for these geographical disparities. For example, coal is still used extensively as an energy source in Asia, generating very significant particulate matter (PM) emissions. Europe has largely turned away from coal since the middle of the 20th century, the latter having been largely supplanted by oil. However recall that Europe at the pinnacle of the industrial revolution when coal was the primary source of energy, has also experienced very severe pollution episodes in the past such as the sadly famous “Great London smog” in 1952 (Esposito and Abramson, 2021). This energetic transition is the result of public policies introduced to improve air quality. This led, for example, to a 30 % decrease in particulate matter with diameter of less than 10 µm (PM_{10}) emissions in Europe between 2000 and 2020 according to the European Environment Agency (2020). Despite these efforts, air pollution remains a major concern in Europe with 417 000 premature deaths attributed to $PM_{2.5}$ exposure in 2018, according to the same study. Hence air pollution continues to be a topical issue, be it in the media, the scientific community or in politics.

Figure 1: Polluted episodes in the French Alps: in the Arve valley (left) and at Chambéry (right).

Alpine valleys are often associated with an idyllic setting and a feeling of a healthy environment linked to proximity to nature. However, urbanized valleys can suffer from very severe pollution episodes that can persist for several days or even weeks, as illustrated in Figure 1. More than 14 million people live in the Alps, which makes it one of the most densely populated mountain ranges in the world (Alpine convention, 2015). The latter report shows that the density of inhabitants in the Alps is very heterogeneous with very sparsely populated areas (in the interior of the massif; in remote valleys or in altitude) and very densely populated areas, mainly in the peri-Alpine area and at valley floors. Moreover, some territories continue to see their population density increase substantially, such as the French department of Haute Savoie, whose population has increased by 100 000 inhabitants (14 %) in ten years. This is why air pollution in complex terrain was and remains a major societal issue.

This study focuses on the Y-shaped valley system of Grenoble, hereafter referred to as the Grenoble Y for brevity (see Figure 2). Like other urbanized Alpine valleys the Grenoble Y experiences high pollution episodes, mainly from ozone in summer (Couach et al., 2003, 2004; Chemel et al., 2005) and PM in winter (Largeron and Staquet, 2016b). For illustration, Figure 3 shows that air quality is less than good in Grenoble for 38 and 47 % of the days in the calendar year 2013 and 2015, respectively.

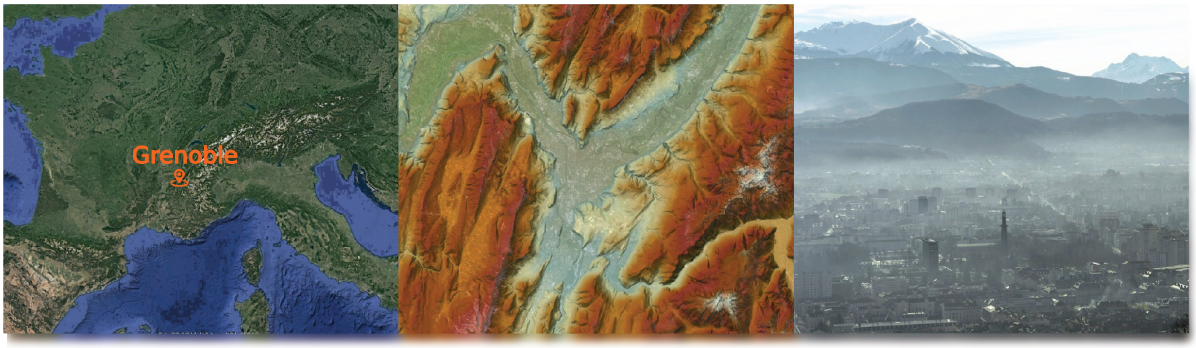

Figure 2: From left to right: **a)** geographical location of Grenoble **b)** Topography of the Grenoble Y **c)** Air pollution episode in Grenoble.

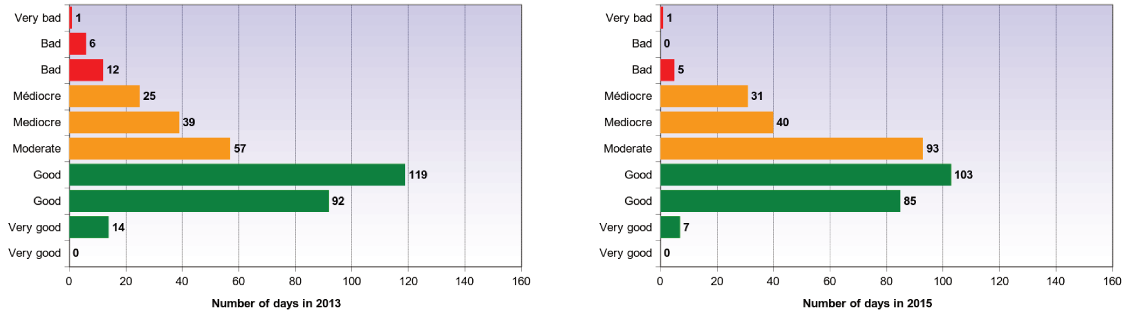

Figure 3: Air quality index as computed by the local air quality agency Atmo Aura for the calendar years 2013 (left) and 2015 (right). Data for the years 1994 to 2020 can be found at `https://www.atmo-auvergnerhonealpes.fr/publications/statistiques-des-indices-atmo-sur-grenoble`.

The inhabitants of Grenoble often describe their city as a “basin” (with a certain negative connotation) when it comes to explaining why it experiences heat waves and ozone pollution in summer, and very cold periods and high PM pollution in winter. The scientific concepts necessary to understand why complex terrain, ad more specifically that of the Grenoble Y, is prone to PM pollution episodes in winter are introduced in the next chapter. Limitations and gaps in our understanding will be discussed to motivate and position the present work.

Chapter 1

Scientific background & research objectives

1.1 Atmospheric dynamics

In general, the atmosphere is the layer (or layers) of gases maintained around a planet mostly by gravitational attraction. The Earth's atmosphere is organized in several successive layers containing mainly nitrogen (78.09 %), oxygen (20.95 %), argon (0.93 %) and carbon dioxide (0.04 %). The troposphere is the layer closest to the Earth's surface, which concentrates about three quarters of the mass of the atmosphere ($\approx 10^{18}$ kg). It extends on average twelve kilometers from the surface even if this altitude depends on the latitude: around 9 kilometers at the poles and 17 at the equator. Within this layer spatial heterogeneities of physical parameters such as pressure, humidity or temperature are responsible for the various weather situations that are observed on Earth as a function of space and time.

In section 1.1.1, some of the main processes responsible for the perpetual instability of the large-scale weather conditions are discussed. In section 1.1.2, particular attention is given to the major large-scale trends in the mid-latitudes of the northern hemisphere as they are key to determining the variability of weather observed in France. After a very brief description of the processes governing the atmosphere at large scales, the focus shifts to the part of the atmosphere where most part of life takes place: the atmospheric boundary layer. The typical diurnal evolution of the ABL for an idealized case – flat and homogeneous terrain subject to weak synoptic winds – is then discussed in section 1.1.3. Finally section 1.1.4 makes an inventory of the main mechanisms by which mountains influence local atmospheric dynamics.

1.1.1 Global atmospheric dynamics

The atmospheric dynamics observed on Earth results mainly from the radiative exchanges with the outer space (Geiger et al., 1995) which are distributed unevenly.

Figure 1.1 displays the mean horizontal insolation received at the Earth's surface. Overall, most energy is received between the equator and the mid-latitudes. The figure also provides a geometrical explanation for that differential heating of the Earth according to the latitude. Given the distance from the Earth to the Sun, the radiation can be assumed to be perfectly parallel and the energy received proportional to the surface perpendicular to the direction of propagation. The figure illustrates that, projected onto the Earth's surface, the same amount of energy will be distributed over a much larger area near the poles than near the equator. In addition, radiation will be absorbed more by the atmosphere at high latitudes because, again geometrically, it will cross the atmosphere over a greater distance. This are the main reasons why, generally speaking, the further away one gets from the equator the cooler is the region. The system Earth tends to smooth out these differences in temperature or pressure according to the second fundamental principle of thermodynamics.

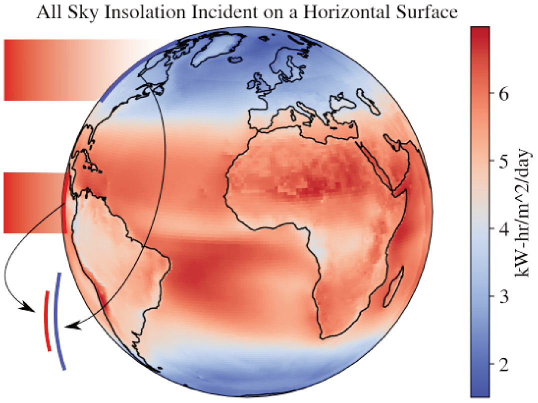

Figure 1.1: Climatological data of horizontal insulation provided by `https://power.larc.nasa.gov/data-access-viewer/`.

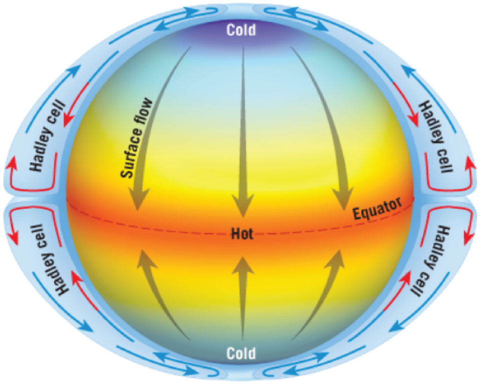

Figure 1.2: Schematic atmospheric circulation proposed by Hadley and valid on a non rotating Earth (extracted from Lutgens et al., 2018).

In 1735, Hadley proposed a global atmospheric circulation model to redistribute the unevenly received energy. This model, represented schematically in Figure 1.2, is idealized and is only valid on a non-rotating Earth. The maximum energy received by the surface at the equator would heat the air by convection. This air, warmer than its surroundings, would rise by buoyancy to the top of the troposphere (which is capped by a layer of warmer air). It would then move along the troposphere top boundary that is the tropopause towards the poles, cooling as it goes, causing the air mass to sink. The accumulation of air at the poles increases atmospheric pressure and helps to create a gradient between the pole (cold, high pressure air) and the equator (warm, low pressure air). This generates a wind that transports cold air from the poles to the equator, thus closing the so called Hadley circulation cell.

However the Earth rotates around its axis connecting the two poles. Since the Earth is wider at the equator than at the poles, by conservation of angular momentum, the Earth's surface rotates faster at the equator. This results in an apparent displacement for latitudinal moving air masses, commonly known as the Coriolis effect. This results in a modification of Hadley's global atmospheric circulation pattern, which is shown in Figure 1.3.

The reasoning is the same to start with: the excess heat at the equator causes the air masses there to rise. When they reach the tropopause, these air masses flow towards the poles. Due to the Coriolis effect, these air masses are then deflected eastwards until they are completely aligned with the latitudes around 30°. The lower branch of the cell undergoes the opposite Coriolis effect and is deflected towards the West. These prevailing winds from the east are called "trade winds". This circulation cell is referred to as the Hadley cell in reference to his first global circulation model. At the poles, the heat deficit creates an area of high pressure. The further away from the pole, the smaller is the heat deficit and the higher is the pressure relative to the poles. A circulation is therefore created from the poles towards the lower latitudes, which is deflected eastwards by the Coriolis effect. As the air moves away from the poles, it warms up and rises until it

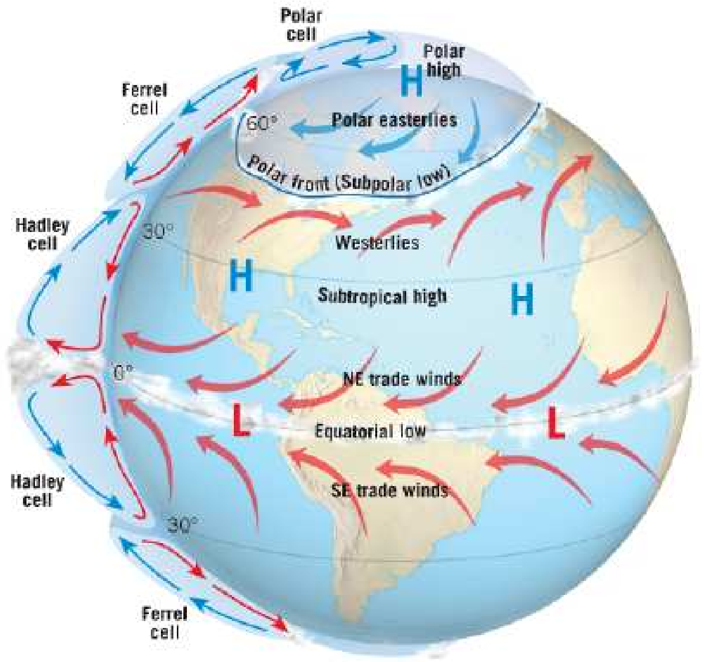

Figure 1.3: Schematic representation of the idealized 3-cell circulation model for the Earth (extracted from Lutgens et al., 2018).

reaches the tropopause. It then spreads towards the poles, cooling and sinking on its way. This circulation cell is called the "polar cell". Finally, the Ferrel cell is slightly different in that its origin is not directly thermal. It acts as a gear between the polar cell and the Hadley cell. As the surface winds of the Ferrel cell are oriented from the equator towards the poles, they are deflected towards the east. This is what gives rise to the predominant westerlies (or south-westerlies) in mid-latitudes (such as France).

1.1.2 Focus on North hemisphere mid-latitude large-scale atmospheric dynamics

The atmospheric circulation model presented above indicates a convergence zone around 30° between the Ferrel and Hadley cells involving a zone of high pressure (called subtropical high). In the same way the divergence zone between the Ferrel and Polar cells result in a zone of low pressure (called subpolar low). In general, geostrophic balance imposes that the intensity of the prevailing westerly winds between 30 and 60° depends on the intensity of this pressure difference. This is what the north atlantic oscillation (NAO) index, which can be estimated from the pressure difference between the Azores and Iceland, represents. Different weather patterns are expected in Europe depending on the positive and negative phases of this index (Hurrell et al., 2003), as shown in Figure 1.4. During the positive phases, the strong pressure gradient increases the intensity of the westerly winds, bringing more warm and humid air from the Atlantic Ocean to Europe. During the negative phases, as the westerly winds are inhibited, the Polar High brings cold and dry air over Europe. The low-pressure system can progress further south, generating higher precipitations over the Mediterranean area.

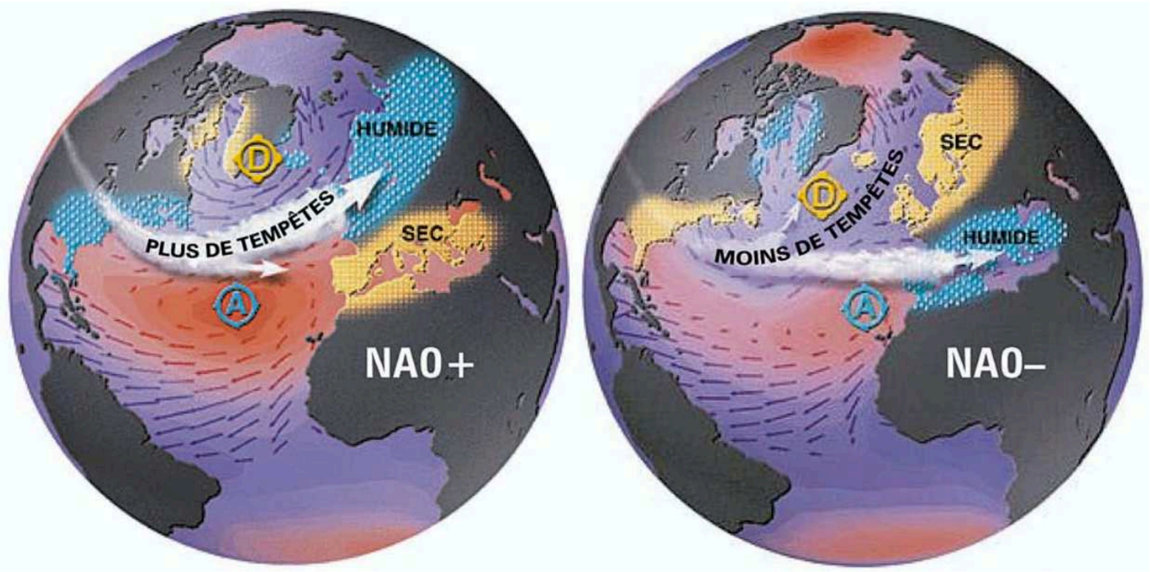

Figure 1.4: Schematic representation of the impact of the positive and negative phases of the NAO (extracted from Cassou, 2004).

1.1.3 The atmospheric boundary layer

It is traditional in meteorology to divide the troposphere – the first of the layers making up the atmosphere, comprising the greater part of its mass – into two parts: the atmospheric boundary layer (ABL) and the free troposphere. The ABL comprises the part of the troposphere that is directly influenced by the Earth's surface. For example, its temperature increases during the day and decreases at night under the influence of the daytime heating and nighttime cooling of the Earth's surface. On the other hand, the free troposphere, by its definition, does not undergo any diurnal variation of its temperature. Other physical phenomena that generate interactions between the ABL and the surface include frictional drag, evaporation, pollutant emissions or simply flow modifications induced by the topography (Stull, 2003).

Over flat and homogeneous terrain, the ABL has a characteristic diurnal evolution, as described briefly below based on Figure 1.5. A more exhaustive description can be found in Stull (2003) or Whiteman (2000).

Halfway through the day, a fully mixed layer extends across most of the ABL. This mixed layer is generated by the natural convection of warm air that has been heated by the Earth's surface. This convective mixed layer is surmounted by an entrainment zone in which air from the free troposphere is progressively mixed with that of the ABL, allowing it to develop upwards. Around sunset, the Earth's surface begins to cool as it radiates more energy than what it receives from the sun. The heat flux that is transferred from the Earth's surface to the atmosphere by thermal conduction (sensible heat flux) changes sign and the air near the ground is now cooled.

A layer of cold air develops close to the surface and grows progressively in height. This layer of air is said to be stable because colder (and therefore denser) air is topped by warmer (less dense) air. A vertical displacement of an air parcel in this stable layer implies that it would be warmer than its environment if it descends or colder if it rises. In both cases, a restoring force would bring it back to its initial position after some oscillations. The Brunt Vaisala frequency (N) corresponds to the frequency of these oscillations and characterizes the stability of an air layer. It is computed from Eq.1.1 where θ is the potential temperarure, g is the acceleration due to gravity on Earth and dz is the vertical displacement of the air parcel.

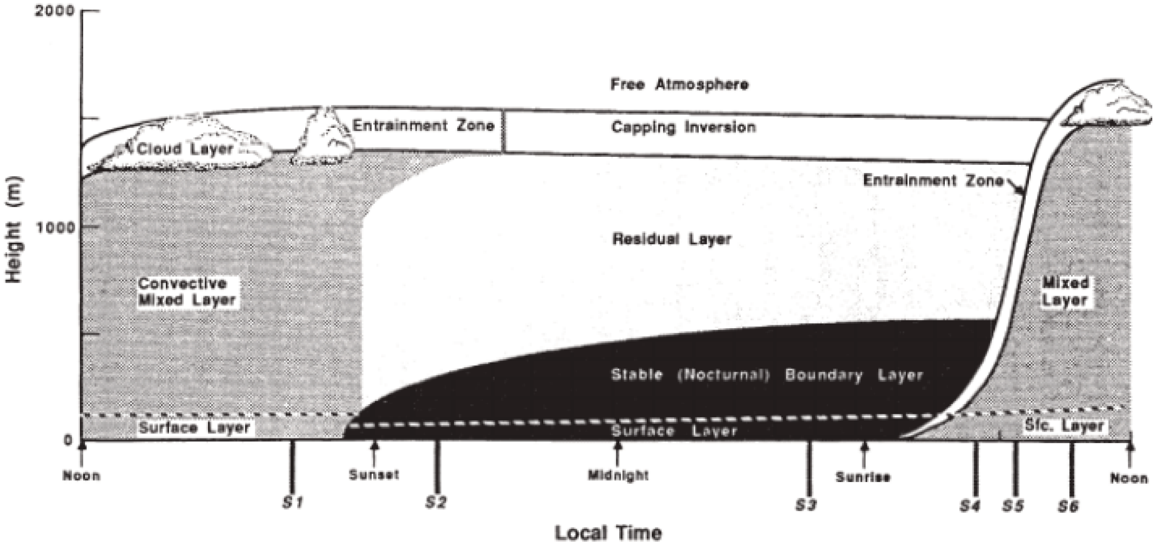

Figure 1.5: Schematic representation of the diurnal evolution of the ABL over a flat and homogeneous terrain and exposed to a quiescent synoptic wind (extracted from Stull, 2003).

$$\mathrm{N} = \sqrt{\frac{g}{\theta}\frac{d\theta}{dz}} \tag{1.1}$$

As a consequence, vertical movements are inhibited in a stable air layer. With convection inhibited, mixing ceases in what was the convective mixed layer, which is now called the residual layer. The residual layer is capped by a thermal inversion, which is a remnant of the entrainment zone and acts as an interface between the free troposphere and the ABL. Shortly after the sun rises, the sensible heat flux changes sign and natural convection gradually erodes the stable layer. Once the stable layer is completely mixed, the convective layer vertically grows very fast through the residual layer until it reaches the free troposphere.

This section describes the general behavior of the ABL over flat and homogeneous terrain under light synoptic winds. The next section describes the main processes by which this overall behavior of the ABL is modified over complex terrain.

1.1.4 Atmospheric dynamics over complex terrain

Mountains affect dynamics of the atmosphere from its largest to its smallest scales (Serafin et al., 2018). For example, an air mass can be forced to rise against a topographic feature like a mountain, if it has enough kinetic energy to do so. This imposed vertical motion cools the air, hereby facilitating condensation and allowing clouds to form. This is why heavier rainfalls are observed on the windward side of mountains that stand perpendicular to the prevailing winds.

This section aims to introduce the main mechanisms through which complex terrain does impact ABL dynamics within a valley as they are the fundamentals of this research work. These mechanisms can be divided into two major categories: *terrain-induced* effects where the topography imposes mechanical constraints resulting in the occurrence of specific wind modes in the valley (1.1.4.1), and *thermodynamical* effects for which winds are formed due to the interaction between radiative effects and topography (1.1.4.2). Geiger et al. (1995) proposed another naming convention for these two categories: the former are materializing “passive effect” of the topography on the atmospheric dynamics and the latter “active effects”.

1.1.4.1 Orographic channeling

The atmospheric circulation within a valley (or a system of valleys) results from an interaction between the large scale meteorology (which can be seen as the forcing of the system) and the topography. This section focuses on the mechanical part of these interactions (omitting the diurnal cycle and thermal considerations, which are discussed in the next section). For example, when a flow meets an obstacle, it either i) gets blocked or redirected, ii) gets channeled through a valley or a pass, or iii) rises and overcomes the obstacle. The outcome depends mainly upon the shape of the topography and the inertia of the flows.

When considering valleys, topographical constraints impose that the prevailing winds within the valley follow the valley orientation. This is known as wind channeling and it has been widely studied in the literature for single straight valleys. According to Whiteman and Doran (1993), there are two main processes that can result in such a wind channeling.

The first one, known as *forced channeling*, occurs when the synoptic winds above the valley are strong. These winds bring momentum from aloft down into the valley and generate an up- or down-valley wind within the valley. According to Weber and Kaufmann (1998) this channeling mode dominates in short and narrow valleys. The orientation depends upon the component of the synoptic wind velocity along the valley axis. Hence, the closer the synoptic wind direction and the valley axis are aligned, the more likely there is effectively a channeling. Another consequence is that a very slight change in the direction of the synoptic wind can lead to a complete reversal of the direction of the channeled wind within the valley. This is illustrated in Figure 1.6. Forced channeling in valley systems has received little attention to date. Drobinski et al. (2006) focused on determining the flow splitting in a 3-branch valley system with a constant input flow direction. However, at least to the best of the author’s knowledge, no studies explore forced channeling in truly complex valley systems (as is the Grenoble Y) for varying synoptic wind direction.

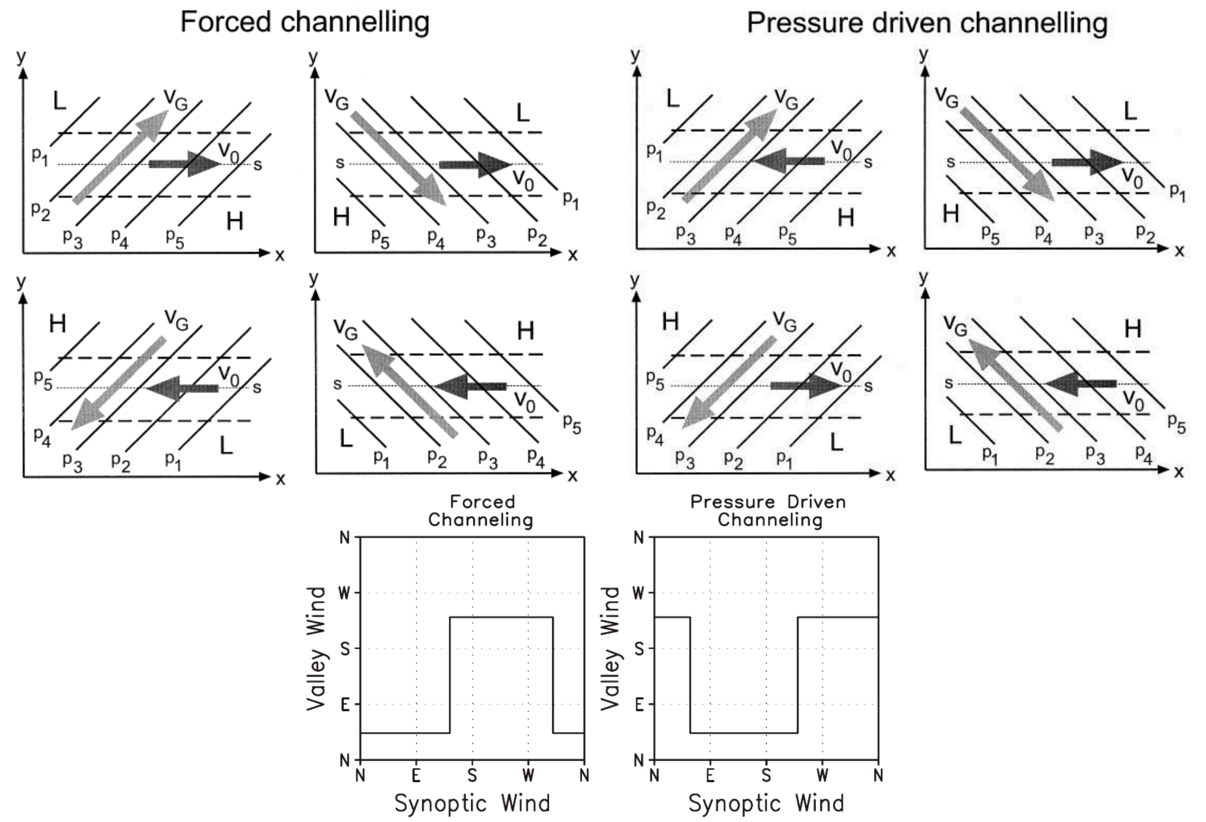

Figure 1.6: **Top**: Plan view of forced channeling (left) and pressure-driven channeling (right) in a long, straight, eastwest-oriented valley in the Northern Hemisphere for ridge-level geostrophic wind directions from southwest, northwest, northeast, and southeast: (dashed lines) valley sidewalls and (solid lines) isobars at ridge level with $p_{i+1} > p_i$; V_g is the geostrophic wind vector and V_0 is the surface wind vector in the valley, and s indicates the along-valley direction (extracted from Kossmann and Sturman, 2003). **Bottom**: Schematic illustration of the resulting wind direction in a valley as a function of the synoptic wind direction for forced channeling and pressure driven channeling (extracted from Carrera et al. (2009) and adapted from Whiteman and Doran (1993)).

The other channeling mode developed in Whiteman and Doran (1993) results from a pressure difference across the valley directly imposed by the large-scale pressure gradient of the air masses aloft. This process is referred to as *pressure driven channeling.* The winds generated are directed from the high-pressure end towards the low-pressure end, and increase in speed as the along-valley pressure gradient increases. For the same reason, this channeling is mostly observed in large scale and well defined valleys such as the upper Rhine valley (Vogel et al., 1986) or the Tennessee valley (Whiteman and Doran, 1993; Eckman, 1998)). This channeling mode is schematically illustrated in Figure 1.6.

1.1.4.2 Mountain thermally-driven wind system

The thermal processes leading to the build-up of a valley wind system associated to a topography – Geiger's so called active effects – have been first studied in the middle of the 20th century by Wagner (1938); Ekhart (1948); Defant (1949). These studies were translated and made available to english readers in Whiteman and Dreiseitl (1984). Since then, these processes have been widely studied and the core mechanisms are relatively well understood. This section aims to outline these mechanisms concisely. A more comprehensive, yet very clear, description can be found in Zardi and Whiteman (2013).

Thermally-driven winds are prevalent during anticyclonic episodes, which are associated with weak to moderate synoptic winds and more importantly where radiative processes are not suppressed by clouds. They result from the conjunction of 3 mechanisms established at different scales: slope flows, valley flows and plain-mountain circulations. These three flows undergo a change of direction twice a day associated with the diurnal cycle. They move up the relief during daytime (up-slope, up-valley and plain to mountain flows) and down at night (down-slope, down-valley and mountain to plain flows). Slope winds and valley winds are described hereafter as they are the dominant processes at the Grenoble Y scale.

Slope flows develop over the first two hundred meters above the slopes along the valley sidewalls. They flow up the slopes during the day (called anabatic winds or up-slope flows) and down the slopes at night (called katabatic winds or down-slope flows). The up-slope – down-slope – winds are created by heating – cooling – of the ground by radiative processes, which in turn transmit it excess – deficit – of heat by conduction to the neighboring air layer. This volume of air is therefore warmer – colder – than the rest of the air mass lying at the same altitude in the valley and therefore rises – or sinks – under the effect of buoyancy forces. Temperature gradients are strongest at the interface between the ground and the air layer. However, due to the friction forces at the ground, the velocity profile of these thermal winds reaches its maximum a few meters above the ground. They form the lower branch of closed circulation with a return flow moving vertically about the center of the valley to compensate the up or down slope flows. This cross-valley circulation is depicted schematically in Figure 1.7.

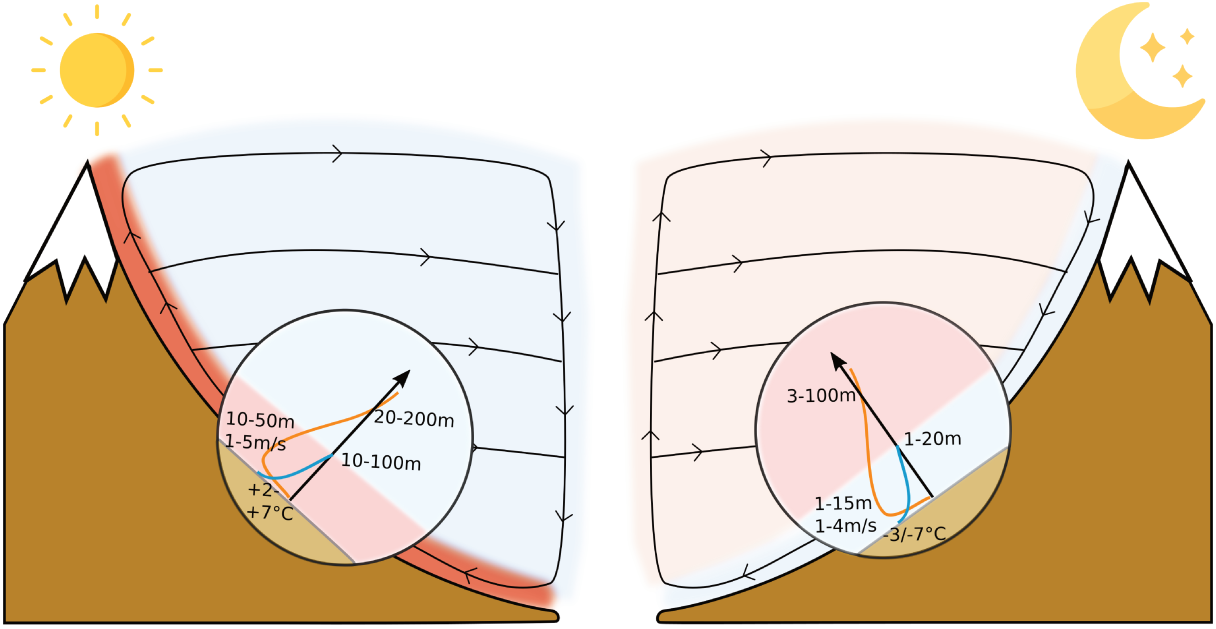

Figure 1.7: Schematic representation of up-slope (anabatic) winds to the left and down-slope (katabatic) winds to the right. *Inspired from Wagner (1938) for the closed circulation representation and Zardi and Whiteman (2013) for the slope wind profiles and characteristic orders of magnitude*

.

Valley wind system Valley winds share many characteristics with slope winds. They are thermally-driven winds that undergo a change of direction twice a day associated with the diurnal cycle. They move up the valley during the day and down the valley at night.

They too form the lower branch of a closed circulation. The main factor accounting for the build up of this wind is discussed below.

A valley has a larger ratio between its ground surface and the volume of air below a certain altitude (e.g. the height of the valley sidewalls) than a plain. For the same volume of air radiative effects are therefore amplified because of the increased surface area. This phenomenon was first studied by Wagner in 1932 and referred to as the topographic amplification factor (TAF). It is since then commonly used and discussed in details in, for example, Chow et al. (2013) and Whiteman (2000). This leads to a temperature gradient, and hence a pressure gradient, between the valley and the plain at the same altitude, which drives the along-valley wind. It is important to note that a valley wind can also develop, for exactly the same reasons, along a valley that is, for example, widening along its axis or opening into another valley. McKee and O'Neal (1989) linked variations in valley wind speeds to changes in the cross-sectional area in a plane perpendicular to the valley axis.

Most valleys in the world are the result of soil erosion by the prolonged passage of a fluid (glacier or river) over geological time scales. They therefore generally exhibit a gentle slope, which generates a slope wind (as explained in the previous paragraph) and therefore contribute to the development of along valley winds. However, although very often present, this mechanism is not essential and a valley wind can be set up in a valley with a flat bottom (Rampanelli et al., 2004).

The development of these valley winds necessarily generate compensating flows. In particular, a counter-flow is formed higher up, often above the valley ridges. Being further away from the ground and unconfined by the topography (therefore unprotected from large-scale winds) it is more rarely observed but always present in the idealized simulations (Rampanelli et al., 2004).

Valley winds develop with a certain time lag after slope winds. Indeed, they are generated by temperature differences between volumes of air that are much larger than the slope winds, and therefore with much more inertia. Moreover, slope winds can be viewed as a manifestation of the TAF. Indeed, the nocturnal heat deficit of a valley compared to a plain is first materialized by a heat deficit along the slopes that the slope winds progressively gather on the valley floor. In doing so, they contribute to the creation of a cold air pool (CAP) at the valley floor, which creates a pressure gradient with respect to the plain.

1.1.4.3 Cold air pool

A situation where a topographic depression (e.g. a valley or basin) is filled with air colder than the air aloft is called a CAP. CAPs can therefore form by the cooling of the air mass in the topographic depression, the heating of the air mass above, or a combination of both processes (Whiteman et al., 1999).

As for an ABL in flat and homogeneous terrain (see section 1.1.3), the sensible heat flux generates a layer of cold air (the stable layer; see Figure 1.5) close to the surface above the valley floor at night. However, unlike a plain, the air cooled by the same mechanism along the slopes collects at the valley floor as it is advected by the down-slope winds (see section 1.1.4.2). This phenomenon is all the more present as the interior of the topographic depression is protected, to some extent, from synoptic disturbances by its surrounding topographic features. This is the so-called "shielding effect", described for example in Vosper and Brown (2008) and Vosper et al. (2014). Hence, without channeling of the synoptic winds, it is common that CAPs develop at night at valleys' floor. For example, Conangla et al. (2018) report that over the course of a study from 2010 to 2014 in the Pyrenees, CAPs form 60 % of the nights, mostly in winter.

As mentioned earlier the development of CAPs is, despite the shielding effect, sensitive to the large-scale conditions. Indeed, Whiteman et al. (1999) showed that CAPs can strengthen or quickly erode if warm air (e.g. when a high pressure ridge is approaching) or cold air (e.g. when troughs are passing) is advected aloft, respectively.

The literature distinguishes two forms of CAPs: intraday CAPs and persistent CAPs (PCAPs) that last at least one complete diurnal cycle. Intraday CAPs result mainly from radiative effects and are generally associated with surface-based temperature inversion (since the CAP does not occupy the whole volume of the topographic depression). Whiteman (1982) concludes from experimental data that intraday CAPs break-up under two combined effects: the growth of the convective boundary layer and the fact that the remaining cold air, then sitting above warmer air, sinks.

The mechanisms behind PCAP formation are complex and multiple. First of all, PCAPs mostly occur in the middle of winter since this is the period of the year when the surface receives the least short-wave radiation, de facto limiting natural convection. For example, Whiteman et al. (2001) showed from a 10-winter database (from 1989 to 1999) for the Columbia basin that PCAPs are on average twice as frequent in December and January than in November and February. However, the presence of a low level stratus can inhibit natural convection and promote the persistence of CAPs, even in autumn or spring (Zhong et al., 2001). In general, the intensity and longevity of PCAPs appear to be dominated by the large-scale conditions. They usually form after a warming of the air at mid-altitude that accompanies the arrival of a high pressure system and are generally destroyed by the passage of a marked trough (Whiteman et al., 1999; Zhong et al., 2001; Reeves and Stensrud, 2009; Lareau and Horel, 2015).

Among the reasons why PCAPs are studied is the fact that they are associated with severe air pollution episodes. Indeed, the resulting stratification suppresses vertical transport. In addition, the shielding effect reduces horizontal transport. Therefore, when PCAPs form in an urbanized area, the emitted pollutants are trapped and the air quality deteriorates significantly. For example, Whiteman et al. (2014) and Silcox et al. (2011) show that pollutants accumulate linearly over the first 4 days of PCAPs in the Salt Lake valley. Numerous valleys and basins (Salt Lake valley, Inn valley, Columbia basin, Arve valley, etc...) are concerned by air pollution episodes triggered by PCAPs.

1.2 Particulate matter air pollution

Several compounds are referred to as air pollution. Among the main atmospheric pollutants one can find carbon monoxide, lead, sulfur dioxide, nitrogen dioxide, ozone and PM. In Europe, according to a report by the EEA (European Environment Agency, 2020), the most harmful pollutants are $PM_{2.5}$, nitrogen dioxide, and ozone causing respectively 417 000, 55 000 and 20 600 premature deaths in 2018. In this study we focus on those with the greatest health impact, namely PM.

Particulate matter (PM) is the general term used to describe solid particles and liquid droplets found in the air. The composition and size of these airborne particles and droplets vary greatly.

1.2.1 Emission sources

Air quality is closely linked to the substances emitted into the atmosphere by human activities and some natural sources. Anthropogenic pollution is mainly concentrated in urbanized areas, near industrial zones or major traffic routes. The largest emissions are those resulting from the transport, industry, heating and agriculture sectors, which are examined below.

Transport Transport accounts for 12 % of PM_{10} emissions at the European level (European Environment Agency, 2020) and 14 % for the Auvergne Rhône Alpes region[1], which includes Grenoble. All major types of transport emit PM. For example, shipping emits primary pollutants in gaseous form (nitrogen dioxide and sulfur dioxide) which can be converted by chemical interactions into PM (mainly sulfates and nitrates). Matthias et al. (2010) showed that shipping in the Baltic Sea can be the source of long-range transport of PM over the European continent. However, PM emissions from road transport largely dominate over other modes of transport in urban areas (Pant and Harrison, 2013). Vehicular emissions have three main sources: i) particles ejected by the exhaust pipe mainly from combustion, ii) particles emitted from wearing parts such as brakes, tires, clutch, road surface...etc and iii) re-suspension of particles on the ground. It is interesting to note that following regulatory efforts on particles emitted by the exhaust system, the share of emissions from wear and tear and re-suspension is increasingly significant (Pant and Harrison, 2013).

Industry Industry accounts for 22 % of PM_{10} emissions at the European level but only 14 % for the Auvergne Rhônes Alpes region. These are mainly industries such as cement plants, chemical plants, metallurgical plants, waste incineration plants, etc. These emission sources are peculiar in that they are very intense and localized: they are called point sources. As a result of increasingly strict regulations, the contribution of the industrial sector to PM_{10} emissions is decreasing significantly over time: a 40 % reduction over Europe between 2000 and 2018 according to the EEA. However, they remain the major source of heavy metal emissions, which are harmful to health and the environment.

Heating Heating is the main source of PM_{10} emissions, both in Europe (accounting for 41 % of total emissions) and in the Auvergne Rhône Alpes region (accounting for 54 % of total emissions). The local air quality agency estimates that, for the region, 97 % of these emissions come from heating by biomass combustion. The Grenoble region is particularly sensitive to pollution from wood burning, even though in the urban area this type of domestic heating is used very little. This is mainly due to the fact that historically the inhabitants of the tributaries of the Grenoble basin heat their houses mainly through wood burning. The awareness of the problems linked to wood burning is actually fairly recent (Jaffrezo et al., 2005), but is now considered as one of the main levers to limit pollution in the Grenoble basin.

Agriculture The contribution of agricultural activities to PM_{10} emissions is estimated to be 18 % for both Europe and the Auvergne Rhône Alpes region. These emissions are very difficult to characterize because they are surface based and extremely dependent on the time of year (tillage, harvesting) or meteorological factors (dry or wet soil). However, the health impacts of air pollution from agriculture are mostly attributed to ammonia, which is not addressed in this study.

The emissions mentioned so far are exclusively of anthropogenic origin. However, some of the airborne particles are obviously of natural origin. The most striking example is the case of a sandstorm, for which the concentrations of fine particles can rise to several thousand micrograms per cubic meter. Moreover, Vautard et al. (2005) showed

---

[1] `https://www.atmo-auvergnerhonealpes.fr/article/sources-de-pollution`

that Saharan sands could explain significant PM concentrations in Europe for specific episodes. For illustrative purposes, Weijers et al. (2011) found that natural emissions accounted for 19 to 24 % of the PM_{10} concentration at a rural measuring station.

1.2.2 Health impact

The World Health Organization estimates that 4.2 million people die every year due to outdoor pollution. Even if PM is not the only air pollutant involved, it accounts for the majority of these losses.

Characterizing the health impacts of PM is complex for many reasons. The main factor is probably the diversity of particles that are hidden behind the term “PM”. Indeed, the diversity of sources (see previous section) implies that PM are in fact a complex mixture. Health impacts vary according to the composition of this mixture. For example, Novack et al. (2020) shows a statistical correlation between the occurrence of asthma and PM of anthropogenic origin but not of natural origin.

In this context, the very way of characterizing PM air pollution has been questioned. Indeed, the focus is on the mass of these fine particles per unit volume, without any discrimination as to the toxicity of these particles. This is why the scientific community is interested in other indicators, such as the Oxidative Potential, which is still under debate but could overcome the problem of taking into account non- or less harmful particles in pollution mitigation policies (Weber et al., 2018; Daellenbach et al., 2020).

The review conducted by Anderson et al. (2012) on the health impacts of PM indicated that populations with long-term exposure to PM have a significantly higher risk of suffering a cardiovascular event and have a higher mortality rate. Respiratory diseases are also exacerbated by exposure to PM, particularly through the creation of oxidative stress in the lungs. Short but very intense exposures to PM result in a small increase in cardiovascular events within a few days of the pollution peak. Finally, the various studies in the literature showed a proportional response between exposure and adverse effects on human health. In general, there is a scientific consensus that finer particles such as $\text{PM}_{2.5}$ are more directly harmful – in the sense that statistical correlations are stronger – than coarser particles such as PM_{10}.

1.2.3 Particulate matter evolution in the atmosphere

After a brief review of the PM origin and its health impacts, let us consider its dispersion in the air. The mechanisms involved can be divided into three categories, which are discussed in turn below.

Advection and diffusion In physics, a scalar is a quantity whose value depends only on the point at which it is evaluated and is independent of the coordinate system. In particular, this implies that a scalar has no direction, as opposed to a vector quantity. In a meteorological system, the temperature, pressure or concentration of a chemical species are scalars.

Any scalar within a fluid flow is dispersed by the flow. This is reflected by the advection-diffusion equation, also known as the scalar transport equation.

$$\frac{\partial c}{\partial t} = \underbrace{\nabla \cdot (\kappa \nabla c)}_{\text{diffusion}} - \underbrace{\nabla \cdot (\boldsymbol{v} c)}_{\text{advection}} + \underbrace{R}_{\text{sources and sinks}} \tag{1.2}$$

where:

- c is the scalar of interest, such as PM concentration
- κ is the diffusion coefficient
- $\boldsymbol{v}$ is a vector quantity that describes the motion of the flow
- R describes the whole sources and sinks for the considered scalar
- ∇ stands for the gradient and $\nabla\cdot$ for the divergence

Advection (sometimes also called convection) refers to the transport experienced by a quantity when it is placed in a fluid in motion. In the same way as dye in a river, airborne PM are transported by the fluid in which they are in suspension.

Diffusion reflects how molecular agitation tends to homogenize the initially heterogeneous concentration of a scalar in a medium, whether or not it is in motion. It takes place in solids (heat diffusion for example) as well as in fluids. It can be seen as a consequence of the second principle of thermodynamics. Generally speaking, in a fluid in motion, advection dominates over diffusion.

Gravitational settling and re-suspension Fine particles are often classified according to their size, in particular according to their diameter. However, there is no reason why these particles should be spherical, and by extension why the diameter would be a definite quantity. This is a misuse of language and actually refers to their equivalent aerodynamic diameter. It corresponds to the diameter that a sphere of water suspended in the air with the same deposition velocity as the particle in question would have. This analogy is the basis for some of the instruments used to measure the mass of PM in the air.

PM therefore by definition tend to fall down as a result of gravity, and eventually to be deposited on the surface. The larger is their equivalent dynamic diameter, the higher is their deposition rate. Consequently, $PM_{2.5}$ remain suspended in the air longer and be transported over greater distances than PM_{10}. For the same reason, the concentrations of $PM_{2.5}$ decrease less rapidly with altitude than that of PM_{10}. Once deposited on the ground, PM can be re-suspended by road traffic or wind gusts close to the ground. Apart from general considerations and orders of magnitude it is difficult to summarize these effects because of the number of factors on which they depend (see for instance Fowler et al., 2009).

Particulate matter chemistry In a previous section, the different emissions sources of PM emitted directly into the atmosphere have been introduced. However, several chemical processes lead to the production of additional PM from precursors (referred to as secondary PM). The main PM precursors are sulfur dioxide (SO_2), nitrogen oxides (NO_x), ammonia (NH_3) and Volatile Organic Compounds (VOCs) (Fuzzi et al., 2015). PM between 2.5 and 10 micrometers in equivalent aerodynamic diameter are essentially primary particles, whereas $PM_{2.5}$ incorporates primary and secondary particles in comparable proportions[2].

---

[2] `https://document.environnement.brussels/opac_css/elecfile/Air%2023`

1.3 Air pollution and tracer dispersion in complex terrain

The dispersion of air pollution (or of tracers) is strongly constrained by specificities of atmospheric dynamics in complex terrain (see section 1.1.4). It is typically investigated through two complementary axes: numerical simulations and measurement campaigns. A recent and thorough review by Giovannini et al. (2020) summarized major achievements and progress as well as open questions and current challenges in relation to our understanding of air pollution dispersion in complex terrain. This review covers the topic both from a measurement perspective and a numerical perspective.

This section focuses on numerical modeling for real cases studies. The emphasis is put on required grid resolutions and the duration of the episodes considered. Table 1.1 summarizes information for different studies, which are discussed below.

There are essentially two main approaches for numerical simulations of pollutant transport: the Eulerian approach and the Lagrangian approach. The Eulerian approach treats the pollutant (particle or gas) as a continuous phase using conservation equations applied on a control volume. The Eulerian approach is therefore constrained by the discretization of the domain considered as it considers average concentration within a grid cell. The Lagrangian approach treats each particle or plume individually by tracking its exact position. Unlike the Eulerian approach, this approach does not suffer from constraints on the discretization of the domain, potentially at the price of a very high computational cost if the number of particles considered is large. One can refer to Giovannini et al. (2020) for a more detailed comparison of these two approaches. Among the studies cited, both approaches are similarly favored.

Article	Model	Chem	dx, dy	dz	Duration	Domain size [km]	Location
Grell et al. (2000)	MCCM (MM5 + RADM2)	Yes	1 km	15 m	5 days	≈ 50 × 50	Swiss italian border
Tong et al. (2005)		Yes					Hong-Kong
de Foy et al. (2009)	WRF → Flexpart	No	3 km		20 days	≈ 94 × 94	Mexico city
Szintai et al. (2010)	COSMO	No	1.11 km	20	2 days	220 × 220	Leventina (Switzerland)
Saide et al. (2011)	**WRF-Chem**	Yes	667 m		6 days	≈ 60 × 50	Santiago (Chile)
Castelli et al. (2011)	RAMS → MINERVE → SPRAY	No	1 km → 100 m	24 m	10 days (x3)	101 × 81	Fréjus (FR-IT)
Balanzino et al. (2012)	RAMS → **CAMx**	Yes	5 km		3 months	250 × 250	Northern Italy
Ritter et al. (2013)	**WRF-Chem**	Yes	2 km		1 year (x2)	420 × 170	Switzerland
Neemann et al. (2015)	WRF → **CMAQ**	Yes	4 km		7 days	235 × 235	Uintah basin (US)
Toro A et al. (2019)	WRF	No	1.11 km	50 m	12 days	84.3 × 84.3	Santiago (Chile)
Tomasi et al. (2019)	WRF → [CALPUFF, SPRAY-WEB]	No	333 m	30 m	36 hours	58.8 × 58.8	Bolzano (Italy)
Ferrero et al. (2019)	WRF-Fire	No	111 m		145 hours	13 × 13	Idaho (US)
Diémoz et al. (2019)	COSMOi2 + [LAGRANTO, **FARM**]		2.8 km → **1 km**		1 month (x3)	Italy	Italy
Quimbayo-Duarte et al. (2021)	WRF-Chem	No	111 m	9.2 m	6 days	42.4 × 42.4	Passy (France)

Table 1.1: Real case numerical simulations of pollutants (tracers or with chemistry) performed in complex terrain. Model names are in blue when a Lagrangian approach is used and in **bold** when chemical reactions are included.

Some of these studies focus on specific and well defined in time episodes. Toro A et al. (2019) investigated the physical processes involved in the occurrence of a severe PM_{10} pollution episode, with peak values of more than $600\,\mu g\,m^{-3}$, in 2014 in Santiago (Chili). Tomasi et al. (2019) evaluated the numerical simulations produced by different modeling systems – Weather and Research Forecasting (WRF) coupled with either the standard Gaussian model CALPUFF or with the SPRAY-WEB Lagrangian model – for two tracer releases performed in Bolzano (Italy) during the BTEX campaign. Ferrero et al. (2019) used WRF-Fire to simulate a measurement campaign on smoke plumes originating from fires conducted in 2013 in the USA. Quimbayo-Duarte et al. (2021) simulated a pollution episode documented in a measurement campaign in the Passy valley (France) in 2015. The terrain associated with some of these sites can be highly complex. For example, for both Passy and Bolzano, the main valleys and tributaries may be only a few kilometers wide. This set requirements for a minimum horizontal resolution in order to capture the main topographic features. The city of Santiago is also clearly located in complex terrain, but at the bottom of a larger basin (of the order of a dozen kilometers wide). This is why the studies dedicated to Santiago (Saide et al., 2011; Toro A et al., 2019) can use a coarser horizontal resolution but must consider a larger domain.

Other studies focus on air quality over longer timescales and larger spatial scales. Balanzino et al. (2012) focused on PM (primary and secondary) over northeastern Italy for the months of December to February. Ritter et al. (2013) used WRF-Chem to simulate NO_2, O_3 and PM_{10} concentrations over the whole of Switzerland for two calendar years. Unlike the case studies mentioned above, these simulations use coarser grid resolutions despite the very complex terrain considered. It is likely that this choice is due to the technical inaccessibility (computational cost, emission detail) associated with finer resolutions.

1.4 Specificities of the Grenoble Y

The purpose of this section is to summarize the various studies that have already been conducted on the Grenoble Y. A first series of studies focused on ozone pollution episodes for summer periods (Couach et al., 2003, 2004; Chemel et al., 2005). Couach et al. (2003) showed from measurements (LIDAR) and numerical simulations (METPHOMOD) over 3 days in July 1999 that the maximum height of the convective boundary layer was about 2700 m AGL. Moreover, the atmospheric circulation in the southern branch of the Grenoble Y (where the LIDAR was located) was dominated by thermal winds. A strong wind (7 to $10\,m\,s^{-1}$) developing up to 1800 m ASL and moving up the valley was observed during the day (between 9 am and 8 pm local time), while a weak (1 to $2\,m\,s^{-1}$) down-valley wind was observed at night. It was also noted that the ozone production cycle is dominated by the thermal wind cycle. Chemel et al. (2005) showed using numerical simulations that a shear layer overlies the boundary layer and traps ozone-rich air masses over the valley floor causing persistent ozone pollution episodes.

Other works, in particular Largeron's doctoral thesis (Largeron, 2010; Largeron and Staquet, 2016a,b), focused on the Grenoble Y and more particularly on the ABL's dynamics during fully developed PCAP for the winter 2006-2007. It was observed in Largeron and Staquet (2016a) that i) the inversion height is of the order of 1200 m ASL, ii) the temperature gradient across the inversion is of the order of 20 K and iii) the atmospheric circulation in the valley is decoupled from the quiescent anticyclonic large-scale circulation. In Largeron and Staquet (2016b) it was shown that out of the 10 pollution episodes occurring during the winter 2006-2007, 9 coincided with the formation of a PCAP and 1 resulted from long-range transport. It was also shown that the formation of a PCAP results from large scale advection of warm air masses at mid-altitude. In this work, the decoupling of the atmospheric circulation in the valley is simulated only over a two-day period in the heart of the strongest thermal inversion of the winter 2006-2007 and for quiescent large-scale conditions. More specifically, it is not characterized how this decoupling reacts for the whole diversity of PCAP, i.e. for i) less pronounced temperature inversions or ii) less stable large-scale conditions.

1.5 Outline and research objectives

The overall aim of the present work is to better characterize the exposure of the inhabitants of the Grenoble Y (see Figure 2) to PM in wintertime using numerical simulations with an emphasis on the PM transport resulting from the atmospheric dynamics. Grenoble is of particular interest because it is one of the cities in France with the worst air quality. According to the air quality agency, 35 days in 2016 exceeded the regulatory thresholds for daily-averaged PM_{10} ($50\,\mu g\,m^{-3}$). These PM pollution episodes occur almost exclusively in winter when a CAP develops (Largeron and Staquet, 2016b). Since the transport of pollutants is constrained by the topography, as long as the CAP persists, the emitted pollutants accumulate from day to day, producing severe pollution episodes.

The measured concentration of PM in the air results from two major processes, transport by atmospheric dynamics and chemical reactions, which apply to the emitted PM and their precursors. To reproduce numerically these concentration levels, three aspects must be represented as well as possible (see 1.2.3):

- **Emissions**: What quantities of PM and precursors are being emitted? When and where exactly are they emitted ?
- **Atmospheric dynamics**: Once emitted, PM is transported by atmospheric dynamics.
- **Chemical reactions**: PM is composed of a wide variety of constituents. In order to model how PM interacts chemically with their environment it is necessary to know the chemical composition of i) the environment and ii) the chemical species that are emitted.

This study focuses on the impact of atmospheric dynamics on pollutant dispersion. Chemical considerations are not addressed, so that PM is considered de facto as chemically inert particles. Primary PM emissions are approximated using the most detailed emission inventory available for the area, kindly provided by the local air quality agency and secondary PM production is neglected.

The complex topography around Grenoble affects not only air quality but also atmospheric dynamics. Mountains are known to impact the atmospheric dynamics from synoptic scale through the excitation of planetary-scale waves (Hoskins and Karoly, 1981; Held, 2002) to the smallest scales as they alter turbulent mixing (de Franceschi et al., 2009). Therefore, the higher the resolution of numerical weather prediction (NWP) models, the more of these scales of interactions can be resolved in these models. For some relatively narrow valleys resolving correctly the topography involves using sub-kilometer resolutions and sometimes well below. As an illustration, a discussion presented in section 3.2.1 concludes that for the Grenoble Y the topography is only reasonably captured for a horizontal resolution of about 100 m. Moreover, atmospheric dynamics in stably stratified conditions are characterized by smaller vertical scales than in unstable conditions (Cuxart, 2015). These considerations set requirements in terms of model horizontal and vertical grid resolution. The numerical burden of such simulations, despite the increasing computing capacity, prohibits simulations over long time scales. Previous studies therefore considered episodes lasting a couple of days, whether they are interested in dynamic processes (Umek et al., 2021; Golzio et al., 2021; Connolly et al., 2021) or pollutant transport (see section 1.3). However, epidemiologists currently rely on long term exposure (time scales of one year) to assess the health impacts of PM air pollution on the population.

Hence, the present work aims to identify a framework providing scope for an extrapolation of characteristic elements obtained from high resolution numerical simulations of one or several shorter episodes over longer time scales. In particular, it address the question of whether or not the concept of weather type (WT) – which groups together meteorological situations sharing common attributes – is a suitable tool for this purpose. In an attempt to meet this aim, the following scientific questions are investigated:

(I) Can a limited number of WTs characterize most of the atmospheric circulations observed within the Grenoble Y ?

(II) What are the requirements to capture the main atmospheric processes of the Grenoble Y in the numerical simulations? Are these simulations reasonably representative of what happened?

(III) For each identified WT, is it possible to identify from numerical simulations a representative atmospheric circulation in the Grenoble Y?

(IV) For each identified WT, what are the stagnation and ventilation zones based on an analysis of the dynamics? Taking into account the variability of PM emissions, is it possible to infer the heterogeneity in terms of spatial distribution of PM concentration?

Question (I) is addressed in Chapter 2. Chapter 3 presents in detail the numerical setup, the meteorological conditions of the simulated episodes as well as a systematic evaluation of the simulations against the available measurements. Chapters 4 and 5 focus on the inter-comparison of the different episodes in terms of atmospheric dynamics and resulting spatial variations in pollutant concentration, respectively.

Chapter 2

Towards a Weather Type Decomposition tailored for the Grenoble Y

2.1 Introduction

As mentioned in the general introduction, the objective of this chapter is to determine a limited number of WTs at large-scale and for wintertime that result in characteristic atmospheric dynamics within the Grenoble Y.

A non-exhaustive review of the different Weather Type Decomposition (WTD) proposed in the literature along with their applications is presented in section 2.2. The characteristics that the WTD must meet in order to fulfill our requirements are derived from technical and physical considerations in section 2.3. The different approaches used to achieve this decomposition are presented in section 2.4. Finally, based on the results presented in this chapter, to choice to focus only on winter anticyclonic blocking episodes is motivated in section 2.5.

2.2 Approaches to Weather Type Decomposition

WTD is a well established concept in synoptic meteorology and climatology. It was first introduced in the middle of the previous century by Rex (1950), who identified manually (i.e. using a subjective method) common points among several blocking episodes at large-scale. The GrossWetterLagen WTD by Hess and Brezowski (1952) was the first detailed WTD performed manually and comprised 29 WTs over Europe. Another well-known example of manual classification is the one made by Lamb (1972) for the British Isles, based on the direction and vorticity of the geostrophic flow. Although very practical, it has the limitation of being applicable only to limited portion of the globe. Subjective methods suffer from being hardly applicable to large datasets and not reproducible. This explains why WTD only really emerged at the end of the 20th century with the simultaneous development of large databases, automatic identification methods, and computing power.

Two approaches prevail among the wide range of objective WTD methods being documented in the literature. One is based on optimization algorithms that identify common features between different objects based on a certain metric, which are then clustered into classes. Typically, it was applied to large domains and therefore the meteorological variables selected were preprocessed using a principal component analysis (PCA). Such an approach rely on key-choices: what variables to consider and over which extent, what algorithm to perform the clustering ? Michelangeli et al. (1995) proposed a WTD resulting in 4 WTs for wintertime for Europe by applying a PCA and a K-Means algorithm (K-MEANS) to 40 years of reanalyses of geopotential heights at 700 hPa covering the north Atlantic area. Similar results are reported by Cassou (2008) following an analogous procedure but using geopotential heights anomalies at 500 hPa. Plaut and Simonnet (2001) used a combination of PCA and K-MEANS on a SLP database lasting 120 years and found that 5 clusters were more relevant to study the relation between the WTs and the local climate in France. Carefully choosing the variables may allow to produce WTs that are more relevant for some applications: Plaut and Simonnet (2001) and Boé and Terray (2008) focused on precipitations and therefore included precipitation-related variables in the inputs. Note that the recent development of machine learning has allowed the emergence of various other clustering algorithms that were also used to perform WTDs. For example, Hewitson and Crane (2002) used Self Organizing Maps and Vrac et al. (2007) used hierarchical ascendant clustering (HAC).

The other prevailing approach was proposed by Jenkinson and Collinson (1977), and relies on the characterization of the direction and vorticity of the geostrophic flow from 16 SLP values spatially distributed at large-scale (forming a “+”-like pattern). This allows to classify the geostrophic flow into 26 WTs: 8 directional regimes (N, NW, W, SW, S, SE, E, NE), 2 geostrophic regimes (Anticyclonic or Cyclonic) and 16 hybrid regimes (AN, ANW,..., CE, CNE). Jones et al. (1993) showed that this approach could be considered as an objectivization of Lamb’s WTD (Lamb, 1972). For this approach, the extent of the domain considered is restricted and the variable considered and the number of classes are constrained. However, variants exist, for example Trigo and DaCamara (2000) merged the hybrid regimes in their corresponding directional regime (but with a lower weight), hence retaining 10 WTs, to study precipitations over Portugal.

Examples of WTD applications WTDs have a wide range of applications in meteorology. For example, Trigo and DaCamara (2000); Ramos et al. (2014); Boé and Terray (2008), observed clear statistical correlation between WTs and precipitation for Portugal, the Iberian Peninsula and France, respectively. For precipitation, Garavaglia et al. (2010) proposed a bottom-up approach with the derivation of synoptic WTs based on a classification of the precipitation observation network over France. For winds, Jiménez et al. (2009) exhibited connection between 6 regional wind patterns in the Spanish Pyrenees and WTs based on pressure patterns on a national scale. WTs are also used to extract trends from very long time series (such as climate simulations): Hoffmann and Schlünzen (2013) and Santos et al. (2016) used WTs to evaluate the impact of climate change on urban heat islands in Germany and precipitations over Western Europe, respectively.

WTs are also often used to relate atmospheric dynamics to observed pollution levels. For example, Hsu and Cheng (2019) focused on the relationship between WTs and observed pollution in Taiwan. Russo et al. (2016) made the same connection between WTs and high pollution levels through recirculation and stagnation indexes (which are also used in this work; see section 5.1.1). Finally, several studies used WTs as input values to forecast or downscale PM concentrations (Demuzere et al., 2009; Demuzere and van Lipzig, 2010; Beck et al., 2014).

2.3 Desired characteristics of the Weather Type Decomposition

The multiplicity of approaches to achieve WTDs, and the resulting diversity of decompositions, has been discussed in the previous section. It follows that, for the time being, there is not one and only one universally accepted WTD in the community. Rather, WTDs are to be seen as a toolkit. Hence, for the present work, it is necessary to define the expected characteristics of the WTD so as to identify the most relevant approach.

The objective is to determine WTs for the wintertime that produce a characteristic atmospheric circulation in the Grenoble Y, and so have the following properties:

$\mathbf{H_{loc}}$ **Characteristic atmospheric flow in the Grenoble valley**: Since pollutants are dispersed by the atmospheric circulation in the Grenoble Y, the observed local atmospheric circulations must be similar within each WT.

$\mathbf{H_{few}}$ **A limited number of WTs**: Expensive simulations would have to be performed for each WT in order to evaluate if the distribution of pollutants is predictable for each WT. For this study to be feasible, a limited number of WTs is required.

$\mathbf{H_{long}}$ **Time-persistent episodes**: Episodes for a given WT must – on average – persist over a couple of days so as to filter the effects of the diurnal cycle.

$\mathbf{H_{syn}}$ **Synoptic homogeneity within a WT**: This condition follows naturally from the previous items. So as to observe similar local weather conditions in the Grenoble Y (pressure, temperature, horizontal wind components and stratification) between different episodes within a given WT, the variability of synoptic conditions from one episode to another within a WT must be small.

The approach proposed by Jenkinson and Collinson (1977) seems promising in terms of homogeneity in the local atmospheric circulations H_{loc} as each episode within a WT would experience similar large-scale forcing by construction. However, episodes are unlikely to be persistent (not fulfilling H_{long}) as it is very rare that large-scale wind and geostrophic vorticity remain the same for several days in a row. Moreover, the number of WTs (26) implies that H_{few} is not fulfilled either. Hence this approach appears to be not appropriate.

2.4 Application to the Grenoble Y

This section describes the different attempts to achieve a WTD that meets the objectives introduced in the previous section. The datasets that are used are discussed in section 2.4.1. In section 2.4.2, the most promising WTD approach is first identified from the literature, and then reproduced so as to identify possible shortcomings with respect the requirements defined in section 2.3. This WTD is then customized so as to consider the resulting meteorological conditions in the Grenoble Y in section 2.4.3. This is followed by a description of an innovative approach trying to take advantage of recent developments in artificial intelligence in section 2.4.4. Finally, some interesting perspectives arising from a simple classification are discussed in section 2.4.5. For the sake of brevity, each of the WTDs derived in this work will be referred to as $\mathcal{W}_i$ where $1 < i < 4$.

2.4.1 A brief introduction of available databases

2.4.1.1 Large-scale data

Any WTD is based on existing input datasets. WTDs often rely on long time records as the inter-annual variability of climate is at least 30 years (Woollings et al., 2015). At large scales, reanalysis data from the European Centre for Medium-Range Weather Forecasts (ERA5) is appropriate as this dataset contains the main meteorological variables with a 30 kilometers horizontal resolution on a global scale from 1979 to present with hourly outputs. Besides, this dataset is commonly used in scientific applications, such as for WTD and forcing of limited area NWP models. Unfortunately, the ERA5 dataset is too coarse to capture local variability in complex terrain, and especially for the Grenoble Y, which is 6 km wide at most. Having a more accurate description of the meteorological conditions and atmospheric circulations observed locally in the Grenoble Y over the same would be desirable.

2.4.1.2 Local scale data

In-situ measurements In this section, all in-situ measurements existing in the Grenoble valley and available to the author are presented. Despite being one of the 15 largest cities in France, Grenoble has relatively few in-situ meteorological measurements. The measurements presented here span over the period 2011-2017 and have been collected from different actors and organizations, which the author would like to thank.

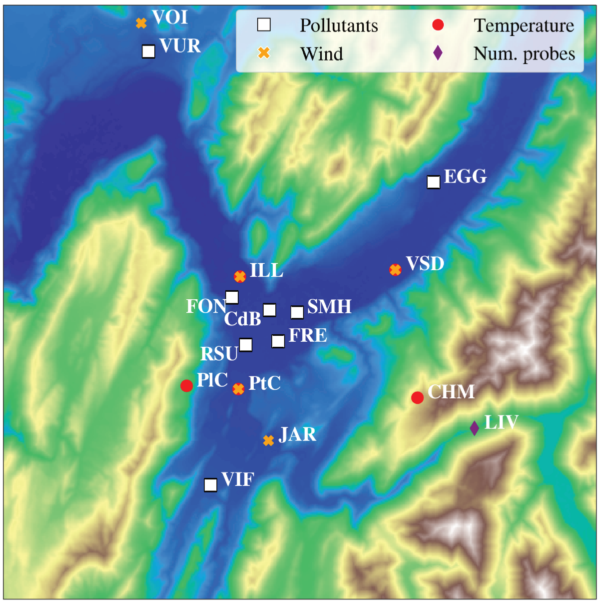

Figure 2.1: Stations locations and type of measured data.

The meteorological variable(s) recorded and the location within the Grenoble valley are summarized in Table 2.1 and Figure 2.1. As an additional indication, satellite images of the surroundings of the various stations are presented in Figure A.1.

Each of the three branches of the Grenoble valley has a wind measurement station. However one can notice that JAR is very prone to feel localized wind effects due to the proximity and complexity of the neighboring terrain. Hence this station can not really be envisioned as representative of the dynamics in the southern branch. Moreover, the ideally placed VSD station has a minimum detection threshold of $0.5\,\mathrm{m\,s^{-1}}$ and an accuracy of $0.1\,\mathrm{m\,s^{-1}}$ and 10°. These characteristics make the data from this station somewhat difficult to use in practice when the near-surface winds are weak.

Station ID	Lat.	Lon.	Alt. [m ASL]	Variables	Pollution type
CdB	45.183	5.725	212	PM_{10}	Urban *Background*
CHM	45.128	5.878	1727	T_{2m}	
EGG	45.279	5.882	260	PM_{10} $PM_{2.5}$	Suburban *Background*
FON	45.190	5.686	210	PM_{10}	Urban *Background*
FRE	45.162	5.735	214	PM_{10} $PM_{2.5}$	Urban *Background*
GGB	45.180	5.720	214	PM_{10}	Urban *Traffic*
ILL	45.206	5.694	213	$T_{2,60,100m}$ $U_{10,20,60,100m}$ $V_{10,20,60,100m}$ P	
JAR	45.092	5.732		U at 10 m AGL V at 10 m AGL	
PlC	45.127	5.647	948	T_{2m}	
PtC	45.127	5.699	247	T_{2m} U at 10 m AGL V at 10 m AGL	
RSU	45.158	5.704	241	PM_{10} $PM_{2.5}$	Suburban *Traffic*
SMH	45.183	5.753	219	PM_{10} $PM_{2.5}$	Urban *Background*
VIF	45.058	5.676	310	PM_{10}	Suburban *Background*
VSD	45.217	5.849	219	T_{2m} U at 10 m AGL V at 10 m AGL	
VUR	45.127	5.589	280	PM_{10}	Urban *Background*

Table 2.1: Main characteristics of *in-situ* measurement stations available for the Grenoble valley. T_{xm}, U_{xm} and V_{xm} stands for measurements at x m AGL of temperature, west to east wind speed and south to north wind speed, respectively.

Reanalysis Unfortunately in-situ measurements available to the authors result in a too short a dataset to perform a WTD (though useful to evaluate a WTD). Durand et al. (2009) produced a reanalysis dataset, using the SAFRAN meteorological model, designed for snow-related analysis over the Alps. Several meteorological parameters (such as temperature, humidity, etc...) are available over the period 1960-2017 for the Chartreuse massif. This reanalysis dataset is not focused on the Grenoble Y, but it has the advantages of i) being in reasonable agreement with a nearby in-situ measurement station (Durand et al., 2009) and ii) covering a long-period of time. It can therefore be used as a proxy for local conditions observed in the Grenoble Y when deriving WTDs.

2.4.2 A classical approach ($\mathcal{W}_1$)

A sensible first step is to reproduce the classical PCA+K-MEANS approach (Michelangeli et al., 1995; Cassou, 2008) so as to identify if it meets the requirements (see section 2.3). Indeed, it has only very few WTs over the winter, fulfilling $\mathrm{H}_{\mathrm{few}}$, and yields persistent episodes (fulfilling $\mathrm{H}_{\mathrm{long}}$).

Deriving the WTD The WTD proposed by Michelangeli et al. (1995) consisted in applying a PCA on time series of geopotential heights at 700 hPa time series (covering the whole North Atlantic Ocean), and applying a K-MEANS with 4 clusters on the resulting reduced dataset. Here, the hourly geopotential at 500 hPa (Z_{500}) from ERA5 ranging from 1979 to 2017 is used, covering from 30° N to 80° N latitudes and from 80° W to 30° E longitudes (160 per 440 points). Following Cassou (2008), the clustering is performed on anomalies rather than on raw data. Anomalies are obtained by taking the difference between the instantaneous Z_{500} field and the daily mean. Daily means are computed for every julian day (extra days for leap years being removed) and then smoothed temporally using a 15-day moving average (± 7 days). Since the K-MEANS are very sensitive to the dimensionality (Hinneburg and Keim, 1999), anomalies are first projected into a lower dimensional space using a PCA. So as to retain 95 % of the original dataset's variance, the first 22 principal components are kept. The optimal number of cluster is set to be 4 following what was done by Michelangeli et al. (1995) and Cassou (2008). In the present work the clustering is performed on hourly Z_{500} fields, possibly resulting in episodes lasting a couple of hours. So as to retain persistent episodes only ($\mathrm{H}_{\mathrm{long}}$), episodes lasting less than 48 consecutive hours are discarded from the following analysis. Discarded episodes accounts for about 9 % of the original dataset, thereby confirming that this WTD yields persistent episodes.

Evaluation at large-scale Results obtained for winter are presented in Figure 2.2 and are consistent with the results obtained for wintertime by Michelangeli et al. (1995) and Cassou (2008). Indeed one can recognize the following synoptic situations from top to bottom and left to right: winter anticyclonic blocking (WAB) (C0), Atlantic Ridge (C1), NAO- (C2) and NAO+ (C3). The ratios among the different WTs are consistent with those reported by Cassou (2008). The WAB and the NAO+ regimes dominate the other two regimes. This is all the more remarkable as different datasets were used: 700 hPa geopotential heights provided by NOAA from 1949 to 1992 were used by Michelangeli et al. (1995) and 500 hPa geopotential heights anomalies provided by NCAR from 1974 to 2007 were used by Cassou (2008).

Figure 2.3 shows that, among large scale circulations within the winter anticyclonic blocking regime (WAB), Grenoble can experience low to high Z_{500} anomalies, thereby providing misleading information for the Grenoble Y. Furthermore Figure 2.2 indicates

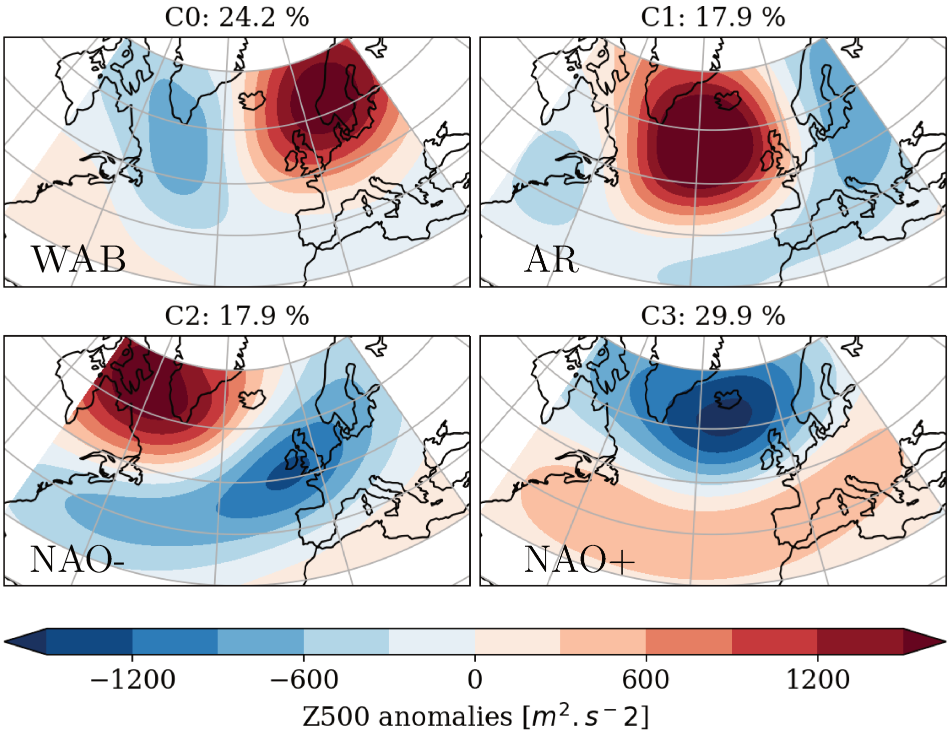

Figure 2.2: Centroids for $\mathcal{W}_1$ in winter. From top to bottom and left to right : winter anticyclonic blocking (WAB), Atlantic Ridge AR, NAO- an NAO+. *As a reminder, the centroid of a WT represent the average of all elements belonging to that WT.*

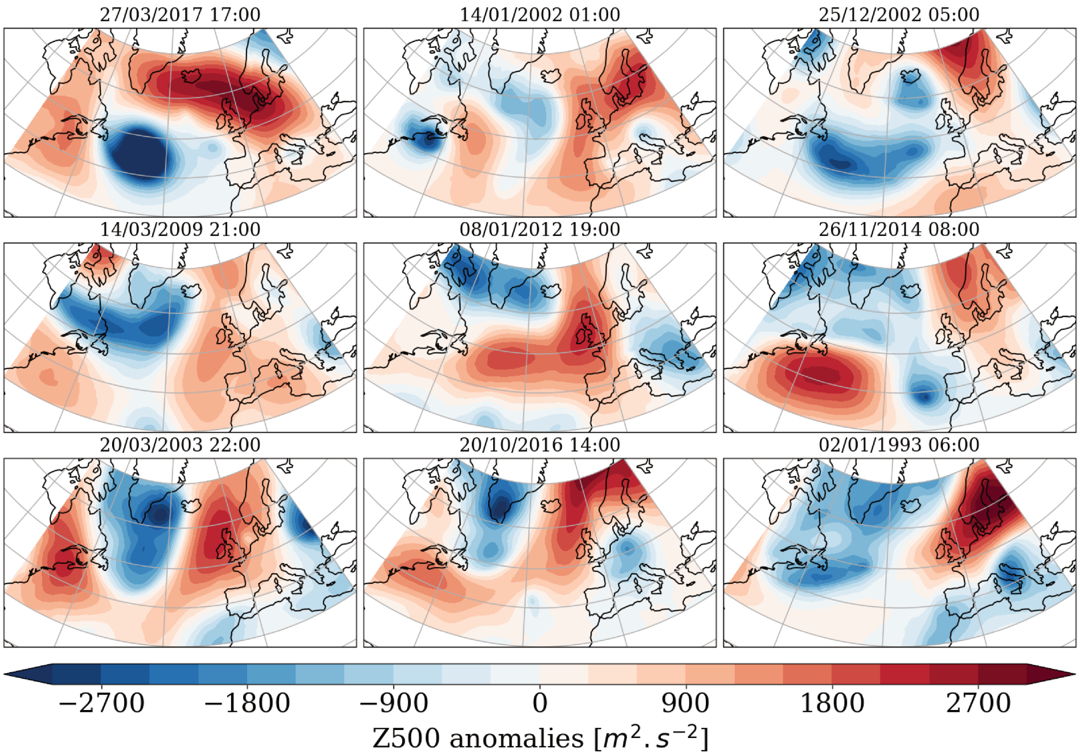

Figure 2.3: 9 random elements corresponding to WAB from $\mathcal{W}_1$ (C0)

that Grenoble lies near the edge of positive/negative anomalies areas for some regimes (such as WAB and NAO+). As no local information is given to the clustering model, it has no ways of making a discrimination between these large-scale situations based on specificities of atmospheric dynamics in the Grenoble Y. This is because this WTD has been originally designed for western Europe and not to target one specific location. Moreover random samples shown in Figure 2.3 exhibit a high large-scale variability, probably testifying that H_{syn} is not fulfilled.

Evaluation at local scale In order to investigate atmospheric circulations within the Grenoble Y for each regime H_{loc}, it is possible to introduce another classification that focuses solely on the atmospheric circulation patterns observed in the Grenoble valley. In the following, this approach is performed with local observations over the winters from 2011 to 2017. It is assumed here that the Grenoble Y is composed of three branches that channel the wind perfectly and whose measurement stations are therefore representative of the branch behavior. Each branch is either in a state of outflow from the Grenoble basin (noted `+`), inflow towards the Grenoble basin (noted `-`) or neutral (corresponding to wind speeds less than $0.5\,\mathrm{m\,s^{-1}}$). Thus, each triplet of observations (one in each branch) necessarily belongs to one of the 27 atmospheric circulation modes resulting from the combinations of these different states. For illustration purposes, two local circulation modes are shown in Figure 2.4a.

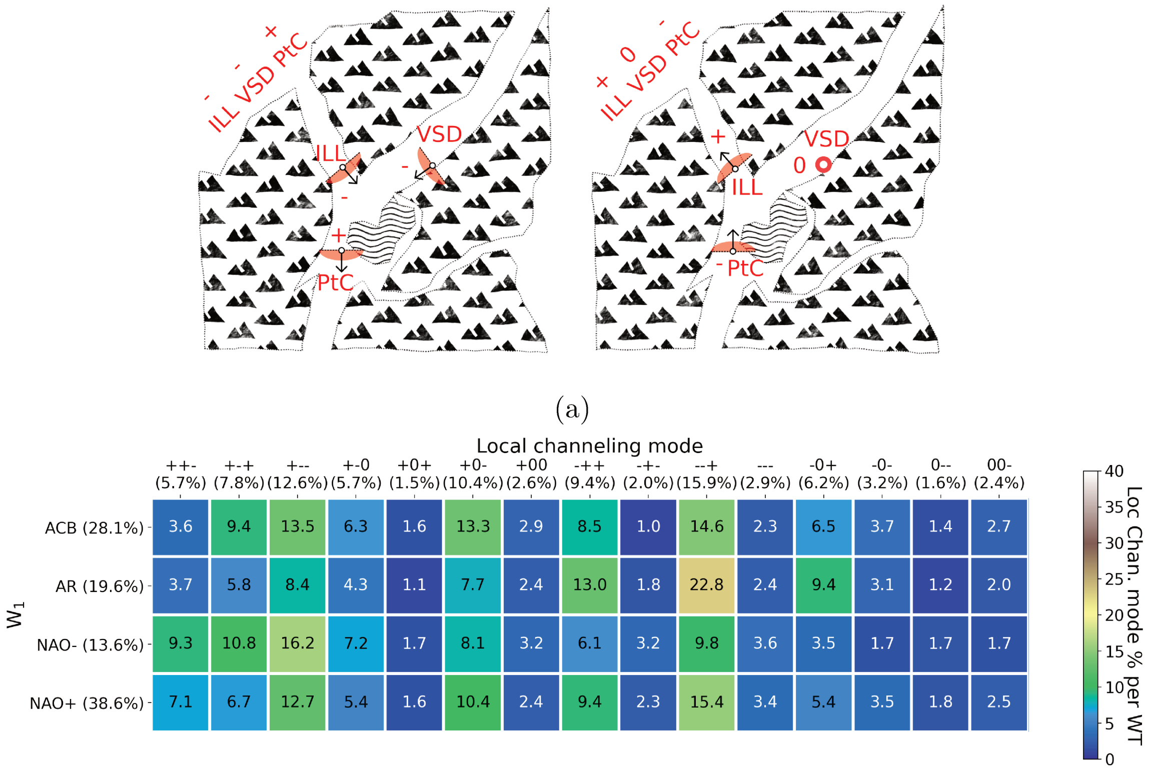

(a)

W_1 \ Local channeling mode	++- (5.7%)	+-+ (7.8%)	+-- (12.6%)	+-0 (5.7%)	+0+ (1.5%)	+0- (10.4%)	+00 (2.6%)	-++ (9.4%)	-+- (2.0%)	--+ (15.9%)	--- (2.9%)	-0+ (6.2%)	-0- (3.2%)	0-- (1.6%)	00- (2.4%)
ACB (28.1%)	3.6	9.4	13.5	6.3	1.6	13.3	2.9	8.5	1.0	14.6	2.3	6.5	3.7	1.4	2.7
AR (19.6%)	3.7	5.8	8.4	4.3	1.1	7.7	2.4	13.0	1.8	22.8	2.4	9.4	3.1	1.2	2.0
NAO- (13.6%)	9.3	10.8	16.2	7.2	1.7	8.1	3.2	6.1	3.2	9.8	3.6	3.5	1.7	1.7	1.7
NAO+ (38.6%)	7.1	6.7	12.7	5.4	1.6	10.4	2.4	9.4	2.3	15.4	3.4	5.4	3.5	1.8	2.5

(b)

Figure 2.4: (a): Schematic illustration of two local atmospheric circulation modes `--+` and `+0-`. (b): Distribution of local atmospheric circulation modes according to each of the $\mathcal{W}_1$ regimes for winters from 2011 to 2017.

Figure 2.4b shows the frequency of occurrence of the main local atmospheric circulation modes for the winters from 2011 to 2017 for each of the WTs in $\mathcal{W}_1$. Modes not presented are those that appear less than 1.5 % of the time during the winters considered, meaning that they are less than half as frequent as modes that would be equally distributed over winter (3.7 %). The proportions of the four WTs for the period 2011-2017 are significantly different from those observed over the period 1979-2017. For example, NAO+ increases from 29.9 to 36 %. The differences observed can be explained by two factors: i) episodes of less than 48 hours are not removed here, which accounted for 9 % of the time from 1979 to 2017 and ii) the length of the time series used at local scale is much shorter than that at large-scale, so that inter-annual variability is more pronounced. According to Figure 2.4b, the similarity condition in the local atmospheric circulations H_{loc} is clearly not met as frequencies in winter and frequencies within each of the WTs are similar. The following section modifies this classification so as to try to overcome the problems encountered with respect to H_{syn} and H_{loc}.

2.4.3 A tailored classical approach ($\mathcal{W}_2$)

Tailoring the WTD to the Grenoble Y In the previous section it was identified that $\mathcal{W}_1$ was not specific enough for the Grenoble Y, neither at large-scale or at local scale. As an attempt to address these limitations local data are added to the inputs of the K-MEANS. Such an approach is common in the literature, for example Plaut and Simonnet (2001) and Boé and Terray (2008) added precipitation data to the inputs of the K-MEANS so as to derive WTs that were more relevant for their objectives.

No dataset covering a large part of the 1979-2017 period is available for Grenoble to the author, and so we use the reanalysis dataset provided by Durand et al. (2009) and briefly presented in 2.4.1. Both temperature and wind speed are used as they affect air pollution in the Grenoble Y. Winds are responsible for pollutant transport and temperatures impact emissions through domestic heating and control atmospheric stability.

Considering inputs of different nature for the K-MEANS involves subjectivity as this algorithm is based on euclidean distances. Since the relative magnitude of different inputs scales with their relative importance in the WTD, it is common to scale each input with, for example, a standard scaler (transformed data have a zero-mean and unit variance) or a min-max scaler (transformed data are comprised between two values; e.g. -1 and 1). This ensures that the different inputs contribute with similar weights to the obtained WTD, but subjectivity remains and, according to the author, no perfect solution exists.

The adopted solution here is semi-empirical. The idea is to keep the main features of $\mathcal{W}_1$ since this approach has already been applied successfully for a couple of different tasks (see section 2.2), emphasizing its representativity of real underlying physical processes. Hence, the author has been looking for the maximal weight that could be given to the local data allowing to keep almost identical Z_{500} anomalies patterns for the centroid of each cluster.

To do so, the PCA results are first scaled between $[-1, 1]$ by dividing the reduced dataset by its absolute maximum value. This approach is motivated by two elements, both to preserve the characteristics of $\mathcal{W}_1$. First of all, to preserve the reduced dataset distribution one does not want to use a standard scaler but would prefer, for example, a min-max scaler. Moreover the reduced dataset also encompasses information regarding the relative importance of the principal components (these principal components being ordered by their magnitudes, with the first one being the largest). For that reason one does not want to use a scaler on individual principal components, but rather to use the same scaling on all the components. The temperature and wind speed from the reanalysis dataset (scaled individually by a minmax scaler), are concatenated to the scaled reduced Z_{500} anomalies, and together are used as input to the K-MEANS.

Sensitivity tests are then performed by multiplying local data (wind speed and temper-

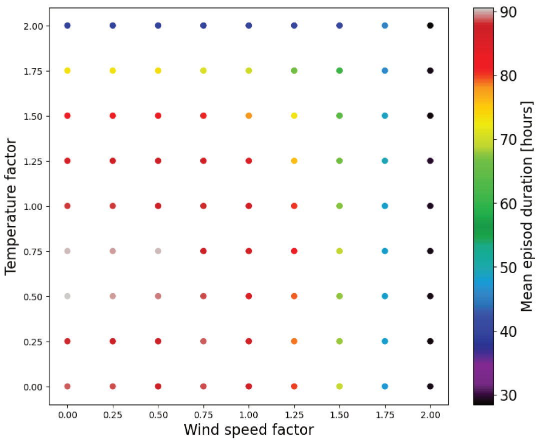

(a) Mean duration

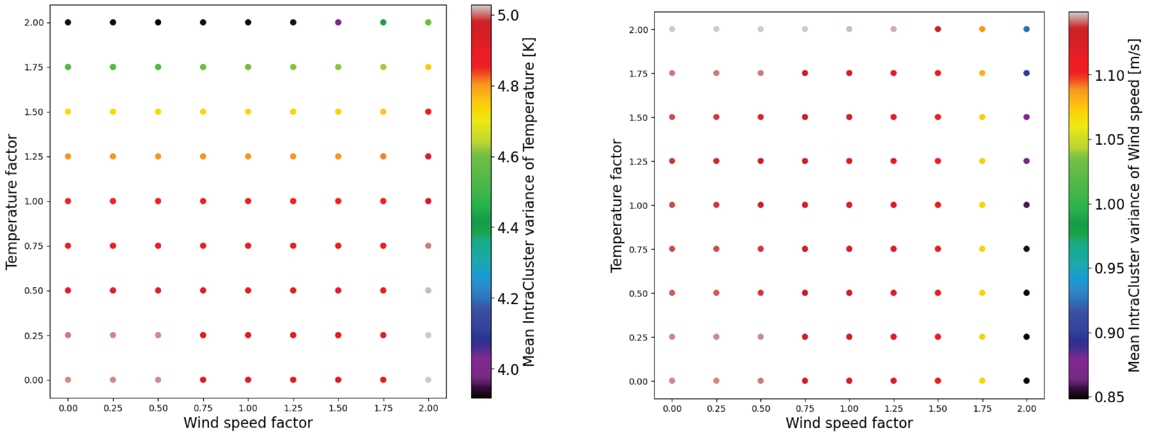

(b) Mean Air Temperature intracluster variance (c) Mean Wind speed intracluster variance

Figure 2.5: Sensitivity of the WTD to a multiplicating factor applied to wind speed and temperature (obtained from reanalysis) before applying the K-means. "Mean" refers to the operators used to combine the results of the four clusters.

ature from reanalysis data at Col de Porte; see section 2.4.1) by factors ranging from 0 to 2 with 0.25 increments, and keeping the large-scale data constant. Results are interpreted using three metrics (average over the four clusters) presented in Figure 2.5: mean episode duration (see Figure 2.5a), and mean intracluster variance of air temperature (see Figure 2.5b) and wind speed (see Figure 2.5c). The lower is the variance, the more homogeneous is the variable considered in each WTs.

As expected, Figures 2.5b and 2.5c shows that the higher are the multiplicative factors, the lower are the mean intracluster variances. Figure 2.5a illustrates that WTDs based on local data (or following a local to large-scale approach) are likely to be non-compatible with $\mathrm{H}_{\mathrm{long}}$ since the more importance is given to local data the shorter are the episodes obtained. Based on these results, taking as multiplicative factors for winter of 1.25 for temperature and 1.0 for wind speeds allows i) to keep a reasonable temporal duration of episodes ($\approx 80\,\mathrm{h}$) and ii) to be more discriminating as regards the local response when compared to $\mathcal{W}_1$ (temperature and wind speed intracluster variance are reduced by about 20 and 25 %, respectively). Figure 2.6 presents the centroids of the WTD using these multiplicative factors, hereafter referred to as $\mathcal{W}_2$.

Evaluation of $\mathcal{W}_2$ No visible difference can be observed in the clusters' centroids between Figure 2.2 and 2.6, showing that the chosen weights did not perturbed the centroids,

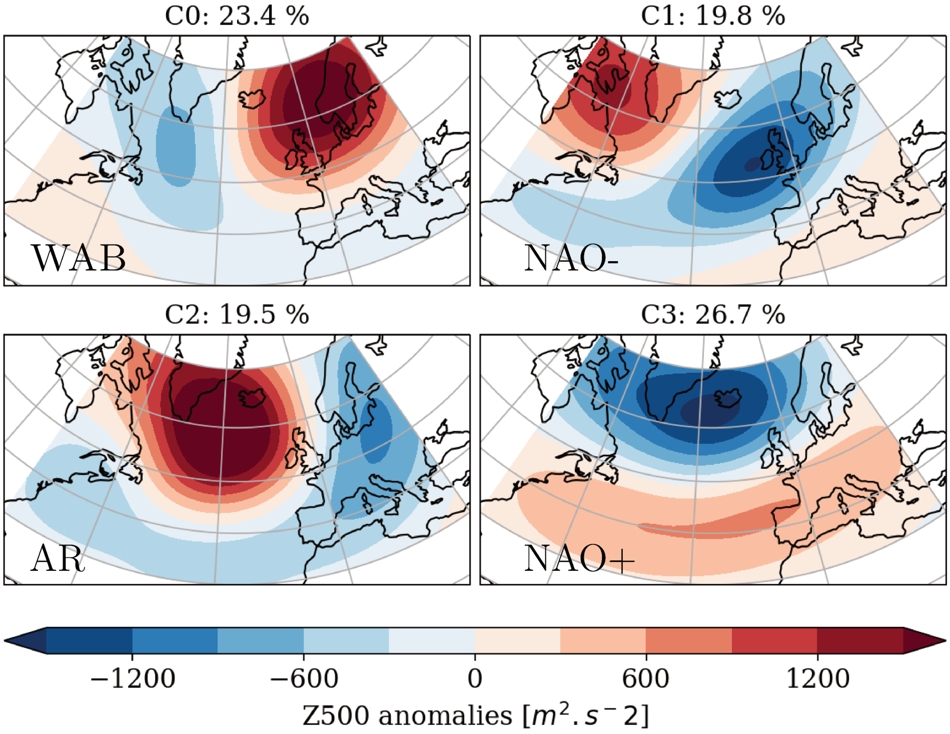

Figure 2.6: Centroids for $\mathcal{W}_2$ in winter. Beware the order of the regimes is different to that of Figure 2.2.

as desired. The frequencies of each WT are also very close to the results of $\mathcal{W}_1$ with a slight over-representation of NAO- and atlantic ridge (AR), which is reflected in an under-representation of NAO+ and WAB.

$\mathcal{W}_2$ meets the limited number of WTs $\mathrm{H}_{\mathrm{few}}$ and the episodes duration $\mathrm{H}_{\mathrm{long}}$ requirements. However Figure 2.7 shows that large-scale conditions may again differ significantly from their corresponding WT centroid, even close to Grenoble, implying that $\mathrm{H}_{\mathrm{syn}}$ is not satisfied. As an illustration, on the 18 February 1985 at 9 am, Grenoble experiences strong negative anomalies within the WAB cluster. This could imply that insufficient weight was given to local data, as emphasized by the fact that $\mathcal{W}_2$ is not more discriminating with respect to local circulations than $\mathcal{W}_1$ (and hence that $\mathrm{H}_{\mathrm{loc}}$ is not fulfilled; see Figure A.2). However it has been shown that, by giving a more important weight to local data, the average duration of the episodes obtained are markedly reduced (see Figure 2.5a). Hence, taking into account local data does not allow the K-MEANS to find another optimum where Grenoble would be more central with respect to the centroids' positive or negative anomalies areas. In sum, $\mathcal{W}_2$ does not meet the $\mathrm{H}_{\mathrm{syn}}$ and $\mathrm{H}_{\mathrm{loc}}$ requirements either.

Would another approach achieve the stated objectives? The vast majority of methods developed to perform WTD (including $\mathcal{W}_1$ and $\mathcal{W}_2$) do not take explicitly into account the temporal dimension of the problem, which is crucial here. For example, when dealing with the WAB regime, one essential aspect is that it corresponds to a blocking, which is by a definition, a pattern persistent in time. For $\mathcal{W}_1$ and $\mathcal{W}_2$, the solution was to use a post-processing technique to remove every episode lasting less than 48 hours from the WTD. However, not considering temporal information in the approach makes it difficult to properly detect time varying synoptic patterns. The next section evaluates if performing a WTD taking into account the temporal component, using artificial neural network (ANN) specialized in processing temporal fields, would help to achieve our objectives.

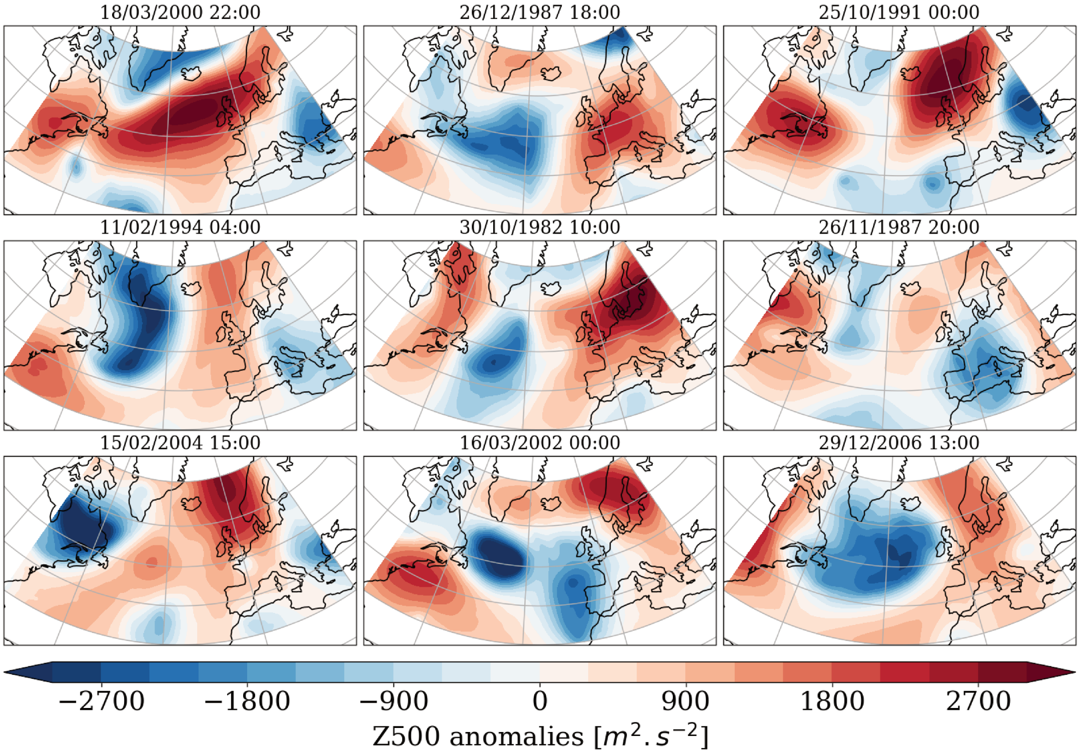

Figure 2.7: Random elements of C0 for $\mathcal{W}_2$.

2.4.4 An attempt using neural networks

As explained in the previous section, ANNs are expected to be ideal candidates to deal with time-varying fields. Indeed, specialized methods were developed to deal not only with spatial fields (such as convolutional layers) but also with timeseries (such as long short term memory (LSTM) layers). After a brief introduction to neural networks in section 2.4.4.1, we detail the methodology used in section 2.4.4.2 and the results obtained in section 2.4.4.3.

2.4.4.1 Introduction to convolutional and long short term memory neural networks

Neurons and multi-layer perceptrons The theoretical grounds for ANN go back to 1943 when McCulloch and Pitts first modeled a neuron as a logical switch that could be activated (or inhibited) depending on the weighted sum of its inputs (which can in turn originate from other neurons). Figure 2.8 is a schematic representation of such a neuron. One can note that the logic (in other words the non-linearity) is generated through the help of the activation function, which is typically some sort of step function acting as a threshold.

These neurons can be used to perform complex tasks once properly trained and organized together. To introduce neural networks, these two aspects must be presented, at least in a simplified manner. As regards their collective organization, the most simple form is a succession of layers of neurons forming a so called multi-layer perceptron which is illustrated in Figure 2.9. ANNs are typically trained using the back-propagation algorithm, which relies on a loss function (typically MAE, RMSE,... etc). The first step in the training is to initialize the parameters of the ANN (randomly, or not) and to evaluate the output via the loss function selected. Using a gradient descent (or related method) the ANN parameters are updated backwards (from the output towards the input) so

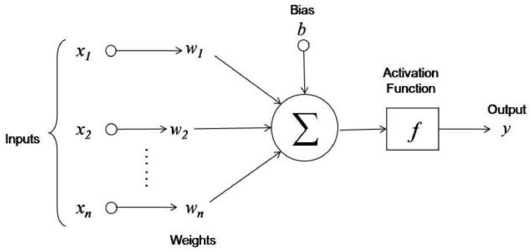

Figure 2.8: Schematic representation of a neuron. The output of this neuron is computed as $y = f\left(b + \sum_{i=1}^{n} x_i \times w_i\right)$. It has therefore $n + 1$ parameters (weights and bias) and one hyperparameter : the activation function.

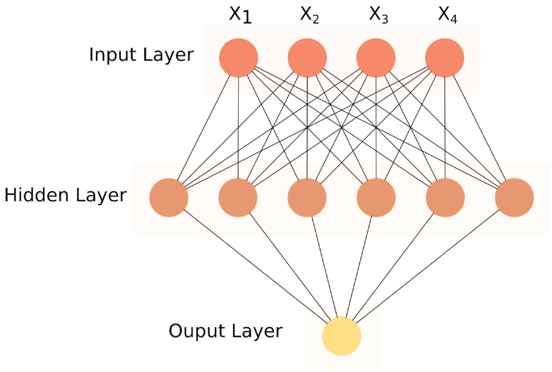

Figure 2.9: Schematic representation of an hypothetical multi-layer perceptron. Circles represent neurons, and shading the so called layers.

that the current input results in a more satisfying answer (minimizing or maximizing the loss). This procedure is repeated over inputs until convergence is reached. This approach, combined with the fact that ANN tends to have a large number of parameters, makes it necessary to evaluate the model ability on data which were not used for training. This is referred to as the generalization ability of the model, which can be seen as its resilience to perturbations in the inputs.

Let us return to the hypothetical network in Figure 2.9 which takes four inputs and generate an output using a single hidden layer. Such layers are sometimes denominated “fully connected” or “dense” layers in reference to the exponential number of connections (and hence parameters) that are generated between successive layers. This characteristic makes them practically unusable for some applications without preprocessing. For example, using a perceptron with a single hidden layer of n neurons on our 160×440 spatially-resolved Z_{500} anomalies would immediately involve $160 \times 440 \times n + n \approx 70400 \times n$ parameters.

Convolutional and long short-term memory neural networks ANNs are known to outperform classical methods, especially in image processing, that may involve inputs of even much higher dimension. Such performances became possible with the development of convolutional layers. These layers convolve their input by a certain number of filters. Thus, irrespective of the size of the input field, a convolution layer consisting of a single filter of size (5×5) has only 25 parameters to train. Their limited number of parameters allows for deeper networks (i.e. with greater stacking of hidden layers). The first layers generally detect coarse and simple patterns. For example, among the first filters, it is very common to find patterns similar to Robinson compass masks acting as directional gradient detectors or Sobel operators acting as edge detectors. Figure 2.10 shows the outputs of two directional filters applied to a field of Z_{500} anomalies. Complex patterns can be captured by the successive application of numerous filters. Another great advantage is that these patterns, whether they are simple or complex, are captured irrespective of their position in the field. Among famous networks using stacking of convolutional layers for image recognition one can cite the ResNet network introduced by He et al. (2015) or the Visual Geometry Group (VGG) network introduced by Simonyan and Zisserman (2014).

However, convolutional layers as described above have no ability to take into account time or context, which is crucial for many applications. For that reason LSTM cells have been developed. They are designed in such a way that they loop over each time frame,

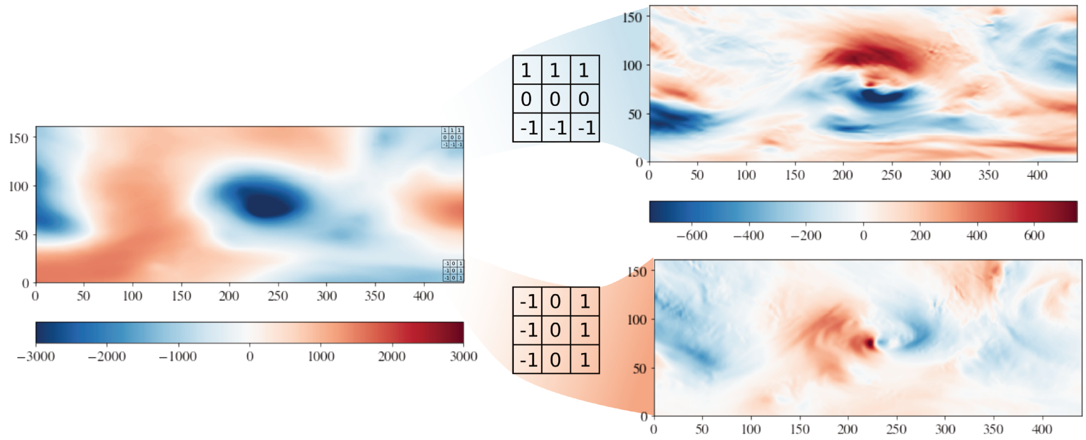

Figure 2.10: Illustration of outputs of an hypothetical convolutional layer using 2 (3×3) directional filters. If input size is of shape (n_x, n_y) then output shape is $(n_x, n_y, 2)$ and the number of parameters to train is $2 \times (3 \times 3)$.

propagating forward in time a so called “cell state” and a “hidden state”. The cell state is carefully updated at each step using trainable gates and can be thought of as being the long term memory. The hidden state represents the relevant information for the next iteration and stands for the short term memory. As a crude analogy with computer science, it can be compared with the cache memory. Trainable parameters in such units usually are fully connected layers but can be conveniently replaced by convolutional operations when dealing with images or multi-dimensional fields.

Recently, neural networks using these features have been used and brought satisfying results in meteorology. For instance Weyn et al. (2019) designed a network to forecast Z_{500} and Vlachas et al. (2018) designed a network to forecast the dynamics of a barotropic vorticity model. Neural networks are not limited to forecasting. For example, a convolutional neural network (CNN) was designed and trained to perform a binary classification of polar cyclones (Krinitskiy et al., 2018).

2.4.4.2 Non Linear dimension reduction

This section focuses on the methodology used to achieve a non-linear dimension reduction including the temporal component. This dimension reduction will be used to perform another WTD in section 2.4.4.3. As explained previously, the objective of this step is to achieve a more efficient dimension reduction than that of PCA since it would retain spatial auto-correlations (through convolutional layers) and would inherently account for the temporal dimension (through LSTM).

Before we can devise a strategy to reduce the dataset, it is first necessary to think about how to introduce the temporal component into the dataset. In light of our objectives, it seems interesting to gather Z_{500} anomalies into sequences of 4 consecutive days in order to perceive a clear large-scale evolution during each event. Besides, 4 days also corresponds to the expected timescale of the episodes. In order to keep a reasonable amount of dimensions in the reduced space, each sequence of 4 days is represented by 4 fields spaced out by 24 hours each. In summary, for a date d, the inputs (and therefore outputs) of the network will be sequence of Z_{500} anomalies corresponding to the dates $[d_{-3}, d_{-2}, d_{-1}, d]$.

Model architecture Here, fairly simple ANN architectures, inspired by VGG (Simonyan and Zisserman, 2014), are used. The `Keras` and `Tensorflow` python libraries for deep learning are utilized for the implementation.

Designing a ANN is a difficult task as one must set many parameters, thereby offering an infinite number of possible solutions. In particular, it is necessary to set the model general architecture by deciding how many layers to stack (the model's depth) and the nature of the layers (dense layers, convolutional layers, etc...). Once this is set-up, one needs to decide on the number of parameters of the model (also called the model complexity) by setting the hyperparameters for each of the layers. For example, for each dense layer, one needs at least to set the number of neurons and the activation functions.

Dimension reduction using ANN is commonly achieved through architectures using two mirroring networks (which together form an autoencoder): the encoder, which brings original data to the reduced dimension space (hereafter referred to as the bottleneck), and the decoder that reconstructs the data in the original dimension. Comparing the output with the input allows to assess how much information was retained in the reduced dimension space.

In this work we consider two similar autoencoders of relatively low depth considering that the patterns to be captured are essentially simple and geometrical. Indeed, Z_{500} anomaly fields have much smaller spatial variations than landscape photographs for example.

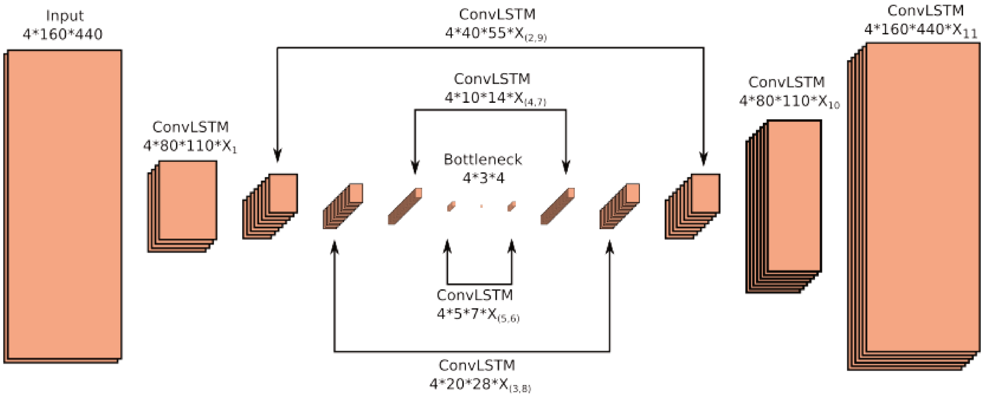

(a) M1 : Full convolutional long short term memory (ConvLSTM)

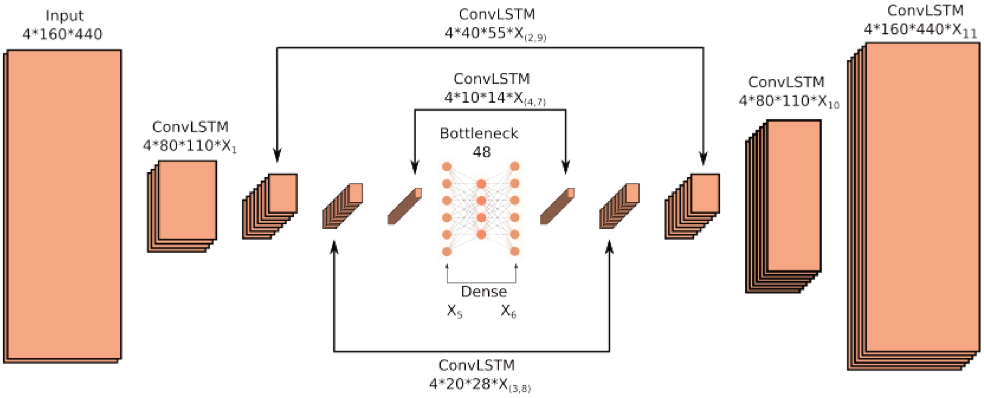

(b) M2 : convolutional long short term memory (ConvLSTM) + Dense

Figure 2.11: Schematic illustration of the convolutional long short term memory (ConvLSTM) autoencoders used to perform the dimension reduction. Each ConvLSTM layer is depicted as a simple Conv for readability as a fourth dimension would be required in the drawing otherwise. Dimension of fields however include time : (n_timesteps, latitude, longitude, n_filters).

These two architectures, represented schematically in Figure 2.11, consists mainly of a sequence of convolutional long short term memory (ConvLSTMs) layers in both the encoder (dimension reduction part; before the bottleneck) and the decoder (reconstruction part; after the bottleneck). Regularization layers (referred to as Batch Normalization) are sometimes inserted between two successive layers (as in VGG). The only difference between these two architectures is related to the bottleneck. In the first architecture, M1, the bottleneck and the adjacent layers are also ConvLSTM layers. In the second architecture M2, these 3 layers are replaced by dense layers. The two architectures therefore share the same depth. When dealing with ConvLSTM layers, the field dimensions reduction is done by using strides in the encoder part, and the augmentation through upsampling in the decoder part. These operations are illustrated schematically in Figure 2.12.

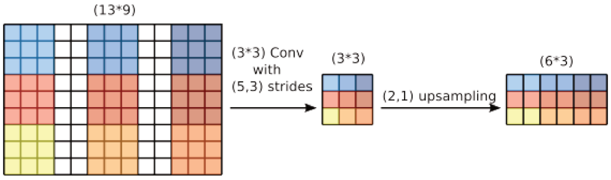

Figure 2.12: Schematic representation of a (3 × 3) convolutional (Conv) applied on an input field of dimension (13 × 9). For this operation, colors represent the area on which the filter is applied to the left and the resulting value to the right. For the subsequent upsampling operation, colors represent a value.

Different network complexities are however tested for these two configurations by varying the number of filters (or neurons) in each layer (noted X_i with $1 < i < 11$ in Figure 2.11). These different configurations are described further in the following paragraph.

Evaluation of the dimension reduction Neural networks being very sensitive to the normalization of input data, the Z_{500} anomalies are projected between 0 and 1 using a MinMax scaling which preserves the original distribution (as opposed to standard scaling for example). In order to check that the model does not fall into the trap of over-fitting, one year out of 9 is kept out of the training process for validation purposes.

To evaluate the model performance, it is natural to choose PCA as baseline comparison since i) it is a linear method that does not take into account spatial auto-correlations or time and ii) it is simple to implement and very frequently used. This architecture uses for its hidden representation $4 \times 12 = 48$ parameters for a sequence of 4 fields. To compare this architecture fairly with PCA, it is therefore necessary to establish the score of a PCA with 12 components only. We recall that PCA is linear, and therefore the average error on one field or 4 would be the same. One theoretical difference lies in the fact that for PCA each of the fields is considered independent, whereas in the network considered here a parameter may contain part of the information for one or more of the other fields. On average over the entire dataset, a 12-component PCA produces a reconstruction MAE of $322.7\,\mathrm{m^2\,s^{-2}}$ or $2.431\,\%$ when scaled between 0 and 1.

From Table 2.2 it is clear that M2 performs better than M1. M1 can hardly match the scores of the PCA while M2 outperforms it systematically. The impact of the architecture is most likely due to the fact that the pure LSTM network is constrained by its intrinsic awareness of time. Indeed, the internal sequences of the LSTM layers are set to be kept throughout the whole network. Consequently, the values of the reduced field in the LSTM layers are associated with one of the four days of the sequence considered. So a value associated with the first day of the sequence has an impact on that day and the three following days (thanks to the LSTM) but a value associated with the third day will only have an impact on itself and the 4th day (because the LSTM only goes forward in time). Inserting dense layers around the bottleneck allows the model to learn how best to combine the temporal features captured by the LSTM layers without being constrained

Arch	N. Params	N Red	Act. Func.	Filter numbers	epochs		MAE (Train.|Valid.)[%]
PCA	852k	12	linear	–	–	–	2.431|–
M1	354k	48	tanh	[8, 16, 32, 32, 16] [8, 16, 32, 32, 16, 8]	293		2.341 | 2.511
M1	268k	48		[4, 8, 16, 16, 8] [4, 8, 16, 32, 32, 32]	547		2.397 | 2.497
M1	152k	48	tanh	[4, 8, 16, 16, 8] [4, 8, 16, 32, 16, 8]	311		2.525 | 2.551
M1	89k	48	tanh	[4, 8, 16, 16, 8] [4, 8, 16, 16, 8, 4]	86		2.6656 | 2.676
M2	288k	48	tanh	[4, 8, 16, 16, 1, 96] [8, 8, 16, 32, 32, 32]	139		1.844 | 1.844
M2	139k	48	tanh	[4, 8, 16, 16, 1, 96] [8, 8, 16, 16, 16, 16]	140		1.899 | 1.899
M2	64k	48	tanh	[4, 8, 8, 8, 1, 96] [8, 8, 8, 8, 8, 8]	160		1.877 | 1.878
M2	64k	48	linear	[4, 8, 8, 8, 1, 96] [8, 8, 8, 8, 8, 8]	116		1.982 | 1.989

Table 2.2: Main results of the dimension reduction obtained with different configurations. Numbers displayed in blue emphasize configurations that outperforms the PCA.

by the arrow of time.

M1 displays clear bias in performance between the training set and the test set (referred to as over-fitting), when M2 does not show a bias. By perturbing each of the 48 values resulting from the dimension reduction of a physical field by M1 and M2, the M1 model seems to be more prone to generate non-physically plausible fields. This implies that M1 is worse at generalizing than M2 and might explain why M1 is biased.

The relatively low spatial variability of the fields of Z_{500} anomalies is probably responsible for the fact that the results do not seem to improve significantly with model complexity for neither M1 nor M2. This is probably also why M1 and M2 manage to do as well or better than PCA with up to more than 10 times less parameters.

M2 with 62k parameters and *tanh* as activation function was retained since, despite its low complexity, it provides good performance scores and it does not seem biased. For illustrative purposes, Figure 2.13 shows an example of a comparison between a reconstructed field and the original field using this configuration.

Note that the neural networks designed here yield reduced datasets with each of the 48 dimensions having the same relative importance, in contrast to what a PCA would produce. This feature does not impact the reconstruction task but complicates the classification task that follows.

2.4.4.3 Resulting weather type decomposition ($\mathcal{W}_3$)

For this WTD the approach is slightly different to that used for $\mathcal{W}_1$ and $\mathcal{W}_2$. Indeed, the originality of this approach lies in using a time-sequence instead of using snapshots. Although it makes sense from a physical point of view, taking into account the temporal component is unusual in the literature. One such example can be found in Philipp et al. (2016) where a WTD relying on a 4-day sequence is integrated in an inter-comparison of

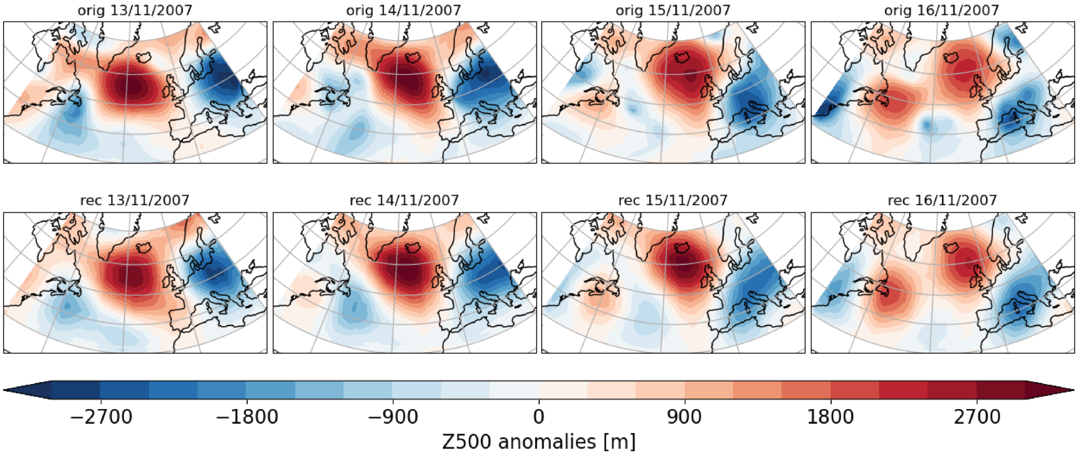

Figure 2.13: Example of reconstruction of an input from the test dataset using the auto-encoder. Top row: original field; Bottom row: reconstructed field.

WTDs. As the expected benefits of this approach concern large scales, local data are not included here, allowing to compare with the classical approach $\mathcal{W}_1$. This choice is made at the expense of satisfying $\mathrm{H}_{\mathrm{loc}}$.

Another classical clustering method is used here to determine WTs: the HAC. This method has the advantage of always providing the same results for the same input dataset, in contrast to K-MEANS, which is inherently stochastic. The principle of this method is to associate a cluster to each entry in the input dataset. Then the two most similar groups according to a chosen metric are merged. This process is repeated until all data are combined into a single cluster. One then chooses the desired number of clusters based on, for example, a dendrogram where the y-axis represents the distance between the two merged sub-clusters.

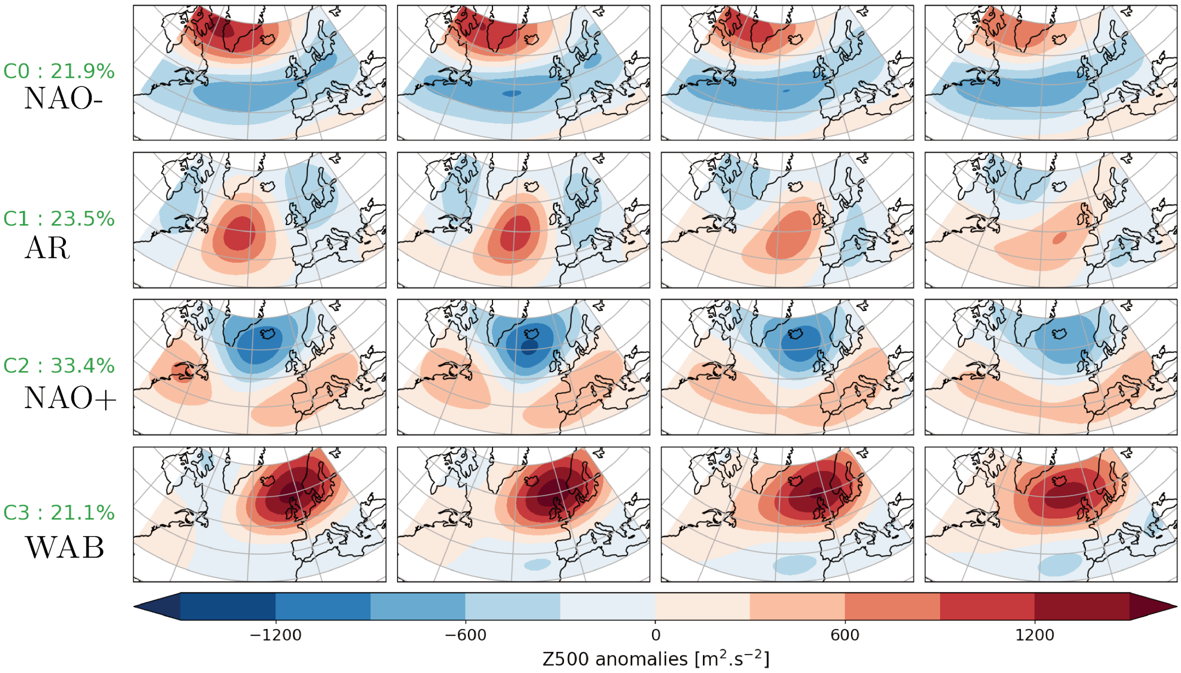

Figure 2.14: Centroids of HAC with 4 clusters for $\mathcal{W}_3$ in winter. Each row represents a cluster. A column represents, from left to right, $[d-3, d-2, d-1, d]$.

Figure 2.14 shows the resulting centroids using a 4 cluster HAC (${\mathcal{W}_3}^4$) on the reduced dataset obtained through the convolutional LSTM autoencoder described in the previous section. Unlike $\mathcal{W}_1$ and $\mathcal{W}_2$, the centroids now represent a sequence of 4 consecutive days. By focusing on one of the columns (i.e. one of the snapshots for each cluster), it is possible to recognize the centroids obtained for both $\mathcal{W}_1$ and $\mathcal{W}_2$. The frequencies of occurrence are also similar to those found in $\mathcal{W}_1$ and $\mathcal{W}_2$. Focusing now on the rows, and thereby on the day-to-day evolution within a centroid, one observes very little variation in the pattern (except for C1; the AR regime, for which there is a noticeable "weakening" in the pattern), as if accounting for the temporal component had not made any difference.

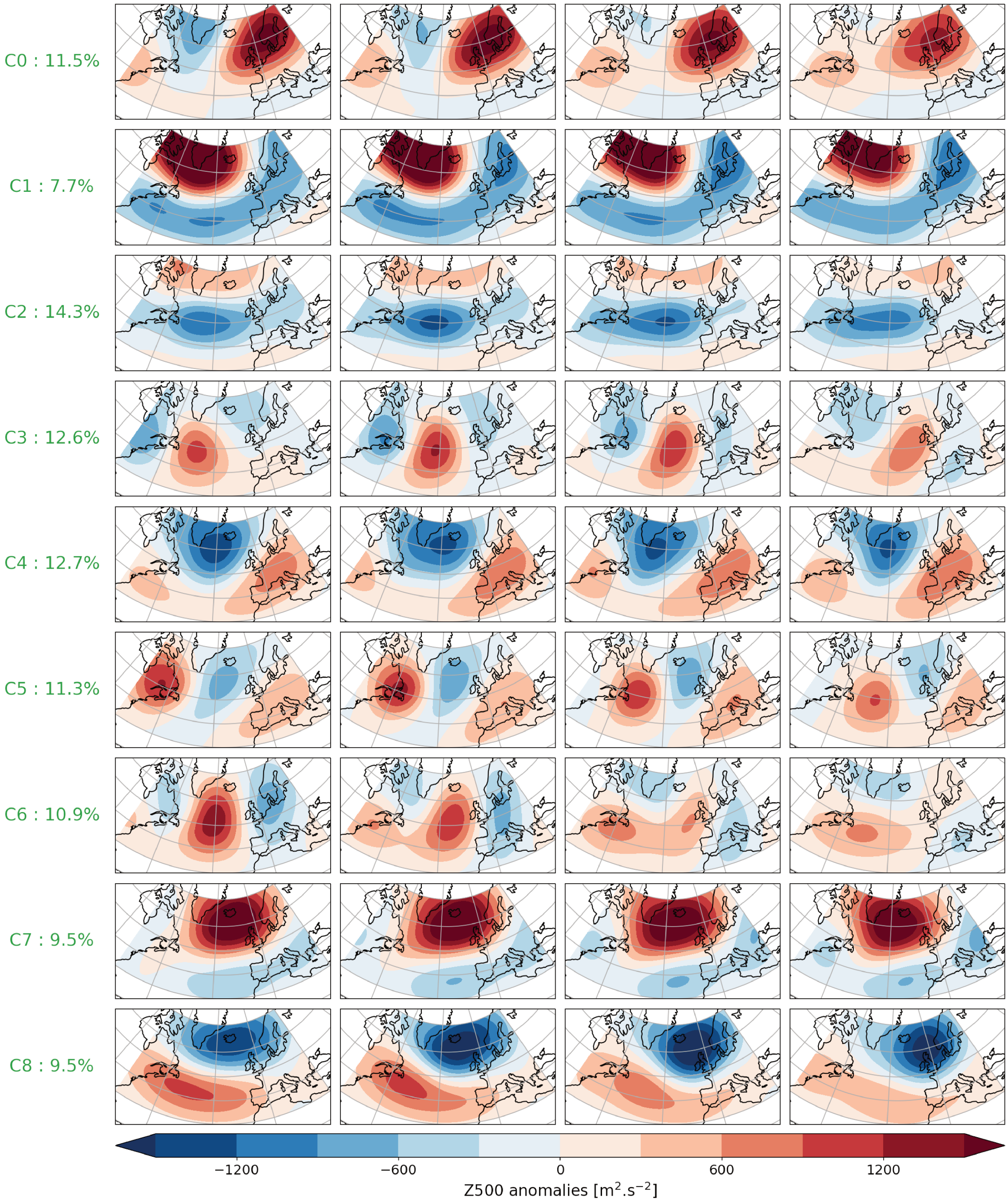

Figure 2.15: Same caption as Figure 2.15 but for 9 clusters.

If we now examine the centroids produced by keeping not 4 but 9 clusters for the winter (Figure 2.15; $\mathcal{W}_3{}^9$), the picture is different. Cluster C6, which accounts for about

10 % of the time, exhibits a large-scale picture where a high anomaly system over the Atlantic Ocean is joined by another high anomaly system arriving from the west. C3 shows the west to east progression of a positive anomaly system from eastern US coasts to western Europe coasts. C0 and C8 – corresponding to the WAB and NAO+ regime in ${\mathcal{W}_3}^4$ –, do not undergo a day-to-day evolution but the magnitude of the anomalies are higher in ${\mathcal{W}_3}^9$ than in ${\mathcal{W}_3}^4$, indicating less intracluster variability. Hence, using 9 clusters demonstrates the added-value of taking into account the temporal component, as opposed to using 4 clusters. This implies that, when 4 clusters are used, the temporal evolution is hidden by the intracluster variability inherent in using such a small cluster number.

The previous observations allow for further interpretation of the centroids obtained using 4 clusters (in either $\mathcal{W}_1$,$\mathcal{W}_2$ or ${\mathcal{W}_3}^4$). Two types of patterns can be distinguished. The first type of pattern exhibits a spatial structure where the anomalies are localized and relatively high, such as the positive anomalies of the WAB (C0 in $\mathcal{W}_1$ and C3 in $\mathcal{W}_3$). The second type of pattern shows a spatial structure with a broader extent but with weaker amplitude, such as the negative anomalies in NAO- (C2 in $\mathcal{W}_1$ and C0 in ${\mathcal{W}_3}^4$) or the positive anomalies in NAO+ (C3 in $\mathcal{W}_1$ and C2 in ${\mathcal{W}_3}^4$). The first type results from large-scale blocking situations, typically exhibiting high and standing anomalies, resulting in high localized average anomalies in the centroid. Weaker and wide-spread patterns (like NAO regimes) result from the west-to-east passage of numerous positive or negative anomalies, yielding lower averages. From this point of view, temporal variations were already implicitly taken into account in e.g. $\mathcal{W}_1$.

Based on Figure 2.15, it would be tempting to relax the constraint $\mathrm{H}_{\mathrm{few}}$ so as to benefit from taking the temporal evolution into account. However, even using 9 clusters, intracluster variability of large-scale atmospheric situations remains too high to meet the $\mathrm{H}_{\mathrm{syn}}$ requirement, implying that one would have to further relax the constraint on the number of WTs. Furthermore, due to the non-linear relationship (imposed by the topography) between large-scale atmospheric circulations and locally observed atmospheric circulations, one would probably need to consider a much larger set of WTs. These considerations show that the WTD requirements as initially envisioned are mutually exclusive.

The following section presents how WAB episodes that are relevant for the Grenoble Y are identified using local measurements; satisfying the $\mathrm{H}_{\mathrm{loc}}$, $\mathrm{H}_{\mathrm{long}}$ and $\mathrm{H}_{\mathrm{syn}}$ requirements.

2.4.5 Classification based on physical grounds ($\mathcal{W}_4$)

From a physical perspective, the atmospheric stability is expected to play a major role in PM dispersion. Temperature inversions are typical of winter anticyclonic conditions. It may therefore be interesting to examine the impact of pressure and temperature inversion on the PM concentrations observed at FRE (which is a background pollution station). This is shown in Figure 2.16a.

Four regimes can be distinguished in this figure. A highly polluted regime corresponds to high pressure and strong temperature inversions (Γ_{PT}). A weakly polluted regime is associated with low pressures and low temperature inversions ($\Gamma_{\emptyset}$). Two intermediate regimes with high values for one parameter and low values for the other are associated with moderate levels of pollution. Visually, it seems that a threshold value for the vertical gradient of temperature, around $-3\,\mathrm{K\,km^{-1}}$, separates clearly the regimes. For the pressure the picture is not so clear. Indeed, it appears that the value of the pressure threshold depends on whether the vertical gradient of temperature is above or below the threshold. Therefore, 3 thresholds are identified in order to classify this space into 4 categories: one for the vertical gradient of temperature and two for pressure.

The threshold for the vertical gradient of temperature ($-2.5\,\mathrm{K\,km^{-1}}$) and for pressure

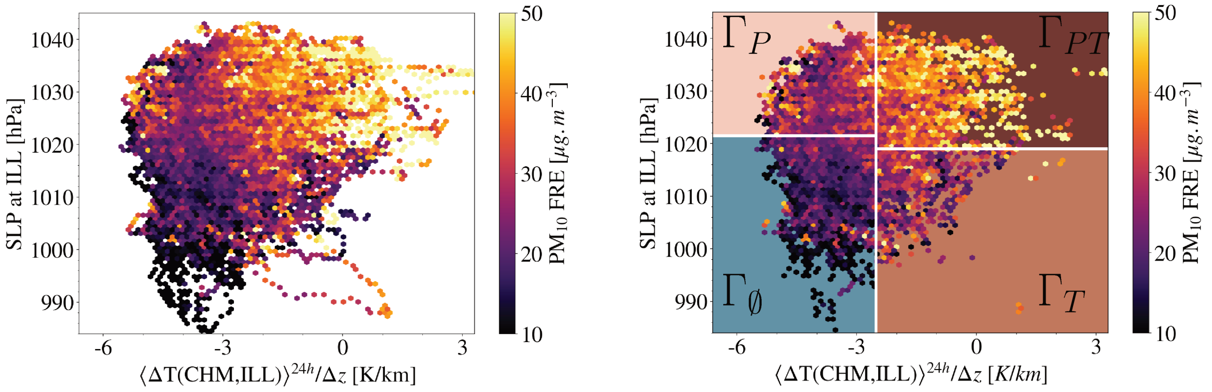

(a) Raw hexagonal plot

(b) Superimposed classification

Figure 2.16: Hexagonal plot of averaged hourly PM_{10} concentrations at FRE over winters from 2011 to 2017 as a function of the temperature difference between CHM and ILL and the SLP at ILL.

Regime	Avg. PM_{10} [$\mu g\,m^{-3}$]	% of PM_{10}	% of time
$\Gamma_\emptyset$	19.3	29.8	40.5
Γ_T	27.5	9.3	8.9
Γ_P	27.1	31.8	30.9
Γ_{PT}	38.8	29.1	19.7

Table 2.3: Frequencies of occurrence and corresponding average measured concentrations of PM_{10} for the winters from 2011 to 2017 for the $\mathcal{W}_4$ regimes. PM_{10} measurements are those from the FRE monitoring station (urban background).

(2021.5 and 1019 hPa) presented in Figure 2.16b are obtained by retaining the solution providing a minimal total intracluster variance after scanning the parameter space, following a decision-tree-like analysis. Interestingly, the threshold for the vertical gradient of temperature determined here is close to the $-3\,\mathrm{K\,km^{-1}}$ threshold chosen by Largeron and Staquet (2016b) to determine temperature inversion episodes during the winter 2006-2007. Table 2.3 presents the frequencies of occurence and the corresponding average measured PM_{10} concentrations for the four regimes. One notes that Γ_{PT} explains the same proportion of winter PM_{10} ($\approx 30\,\%$) than $\Gamma_\emptyset$ while it appears only half as often (20 % against 40 %).

Figure 2.17 shows the time series of meteorological variables of interest and the regimes for three consecutive winters. It is interesting to note that the regime Γ_{PT} captures the episodes of high pollution (with possibly short interludes of intermediate regimes).

From this classification it appears that local measurements related to large-scales features (atmospheric pressure and atmospheric stability) allow to derive coherent local responses in PM_{10} concentration. To assess if this WTD satisfies H_{loc}, Figure 2.18 shows the local atmospheric circulations within the valley for each regime. In $\Gamma_\emptyset$ all the main circulation modes occur but one notices that `-**` modes are all more frequent than their average proportion in winter. This is also the case for the Γ_P regime. Hence, these two regimes can not be associated with a characteristic atmospheric local circulation. Conversely the `+**` modes dominate in Γ_T and even more so in Γ_{PT}, for which their frequencies of occurrence increase by up to 100 % compared to their respective winter averages (e.g. `+0-` in Γ_{PT}). The favored modes are however not the same: `+--` is accompanied by `+-+` in Γ_T and by `+0-` in Γ_{PT}. The fact that, when the threshold for the vertical temperature gra-

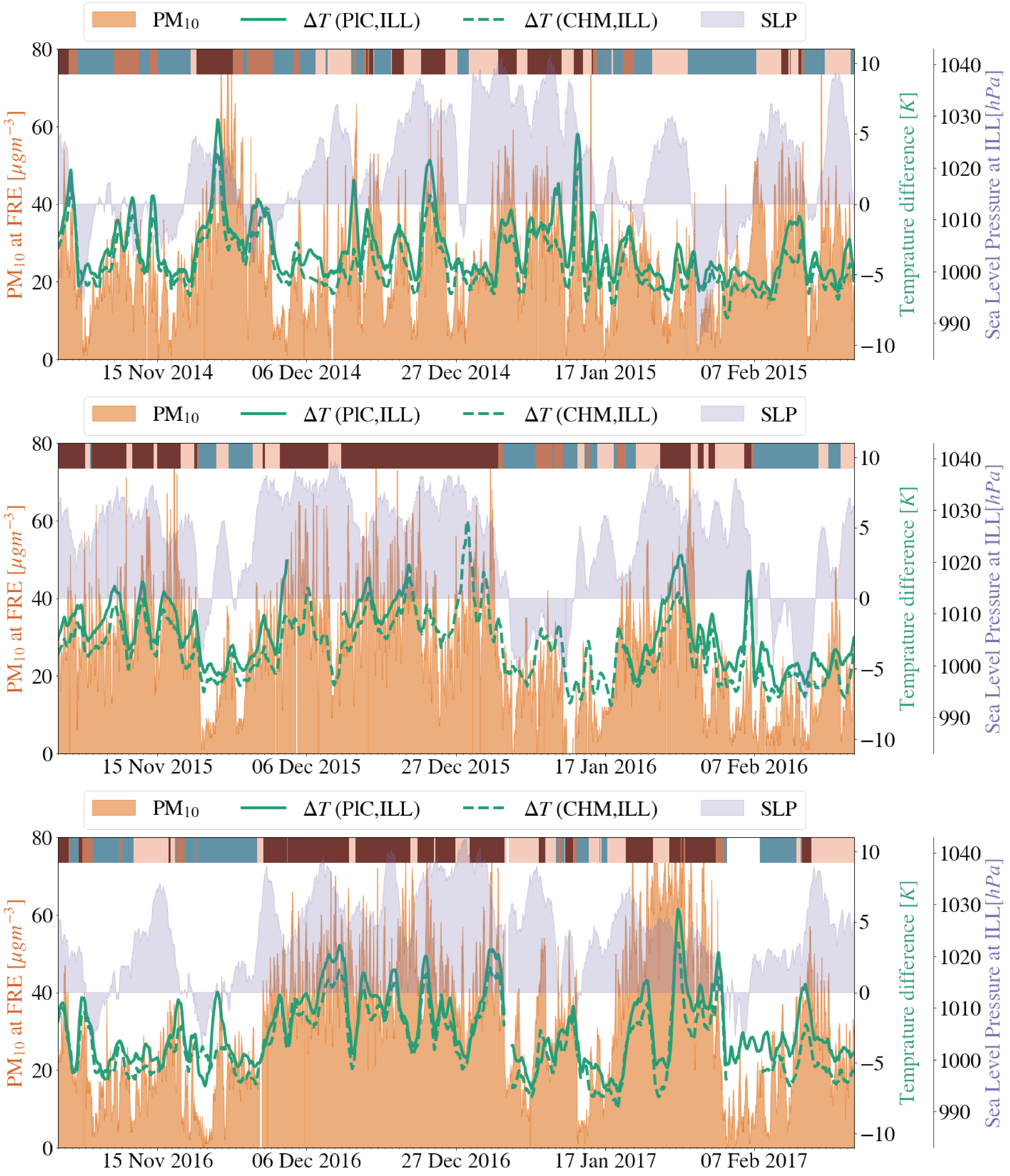

Figure 2.17: Time-series of meteorological variables and the regimes for the winters in 2014, 2015 and 2016, from top to bottom, respectively. Colors at the top of the figure corresponds to those used in Figure 2.16b and refer to $\mathcal{W}_4$ regimes. PM_{10} concentrations are those measured hourly at FRE, an urban background measurement station. Rolling averages over 24 hours are performed on temperature differences. The SLP is measured at ILL. See section 2.4.1.2 for a description of the measurement stations.

dient is exceeded (Γ_T and Γ_{PT}), the `-**` modes are essentially absent, suggests that there exists a characteristic circulation when temperature inversion occurs, as hypothesized in Largeron and Staquet (2016a) for the Grenoble Y. The Γ_{PT} regime, which account for 29 % of PM_{10} in winter, appears to fulfill H_{loc} and thereby stands as the ideal candidate to simulate numerically.

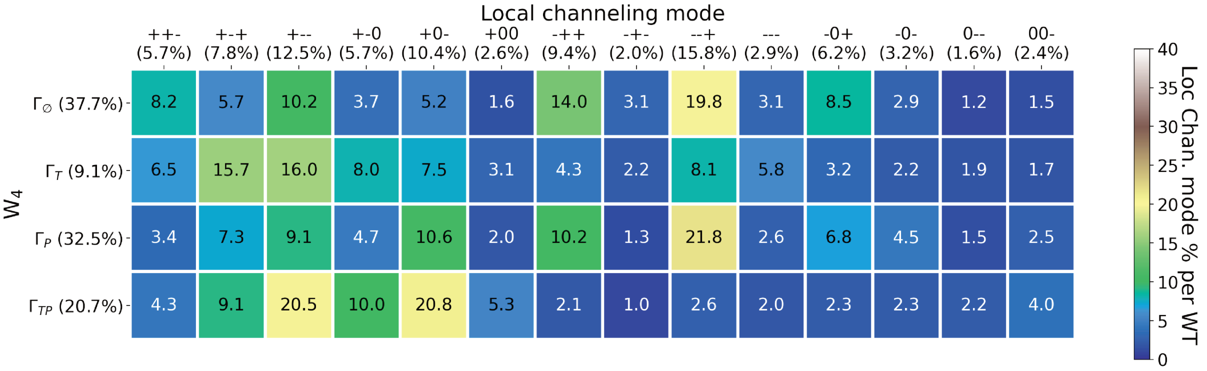

	++- (5.7%)	+-+ (7.8%)	+-- (12.5%)	+-0 (5.7%)	+0- (10.4%)	+00 (2.6%)	-++ (9.4%)	-+- (2.0%)	--+ (15.8%)	--- (2.9%)	-0+ (6.2%)	-0- (3.2%)	0-- (1.6%)	00- (2.4%)
$\Gamma_\varnothing$ (37.7%)	8.2	5.7	10.2	3.7	5.2	1.6	14.0	3.1	19.8	3.1	8.5	2.9	1.2	1.5
Γ_T (9.1%)	6.5	15.7	16.0	8.0	7.5	3.1	4.3	2.2	8.1	5.8	3.2	2.2	1.9	1.7
Γ_P (32.5%)	3.4	7.3	9.1	4.7	10.6	2.0	10.2	1.3	21.8	2.6	6.8	4.5	1.5	2.5
Γ_{TP} (20.7%)	4.3	9.1	20.5	10.0	20.8	5.3	2.1	1.0	2.6	2.0	2.3	2.3	2.2	4.0

Figure 2.18: Distribution for winters from 2011 to 2017 of the main local atmospheric circulation modes according to each of the $\mathcal{W}_4$ regimes. A given value represent the proportion of corresponding local circulation mode within the regime considered (implying that this table is to be read line by line). Percentages given along with labels correspond to the average proportion in winter. The atmospheric circulation modes are introduced graphically in Figure 2.4a.

2.5 Concluding remarks

The several attempts of WTD ($\mathcal{W}_1$, $\mathcal{W}_2$ and $\mathcal{W}_3$) did not achieve the desired characteristics listed in 2.3. The key outcomes that emerged from this chapter are listed below:

- From a general point of view, performing a WTD is not an easy task because the data lacks underlying internal structure. To understand this point, a caricatured comparison can be used. Let's take on the one hand a classification between images of dogs and cats and on the other hand a classification of synoptic meteorological fields. The former must distinguish between very distinct objects, which could be associated with a discrete process. Dimension reduction methods will easily capture the underlying structure and form two distinct, more or less compact distributions. Certainly, some cats will be closer to the dog space or lie somewhere in between. But, even so, it will be easy for a classification algorithm to make a good overall distinction between them. Conversely, meteorological fields are by nature the result of a continuous process with no real equilibrium position. The superposition of many time sequences generates a space with no apparent structure, i.e. very dense and homogeneous. The application of linear and non-linear dimension reduction techniques, as done here and elsewhere (PCA in sections 2.4.2-2.4.3, t-SNE, UMAP, ConvLSTM autoencoders in section 2.4.4), does not lead to a space less dense and less homogeneous. This conclusion is exactly the same as that drawn by Philipp et al. (2016) from an intercomparison on WTDs. It also explains why the WTDs are so different depending on the methods used to obtain them or the meteorological variables selected. Hence, WTDs are better considered as a toolbox to draw from depending on the purpose.

- Classical WTDs for western Europe (Michelangeli et al., 1995; Cassou, 2008) based on large-scale data, as derived in $\mathcal{W}_1$, have Grenoble sitting in between or at the edge of positive and negative Z_{500} anomalies in the centroids. For example, in the case of the WAB blocking, the centroid places the anticyclone over the British Isles and Grenoble is only slightly under its influence. Cyclonic episodes in Grenoble may therefore be part of this WT. As such this WTD is not suitable for a study focused on Grenoble.

- When taking into account local observations, as in section 2.4.3, the problem identified in the preceding item is not completely resolved (see Figure 2.7). Either these observations are given significant importance and then the ability to generalize the large-scale situation is lost, or they only enable to distinguish between the episodes at the boundaries of different large-scale regimes.

- Neural networks outperform significantly the classical and turnkey tools for dimension reduction (namely the PCA), reducing the reconstruction MAE by about 25 %. Such a performance is only possible by introducing dense layers in the network; otherwise the performance is only comparable to that of the PCA. Furthermore, although promising on paper, the introduction of the temporal component (see section 2.4.4) does not resolve the challenges encountered for the classification task. The reason for that is probably that the limit on the number of clusters prevents the WTD to make better use of the temporal component. Finally, the theoretical benefits achievable by neural networks may require a lot of effort and *a priori* knowledge to be effectively achieved. The author therefore advises to check that none of the off-the-shelf methods meet the requirements before embarking on neural networks.

- The highly non-linear relationship between the large scales and the local response in the Grenoble valley, through wind channeling in particular, makes it very difficult to reconcile these two scales. A small change in wind direction at large scale due to a small displacement of a cyclone could result in a complete wind reversal within the valley (see Whiteman and Doran, 1993). It is therefore impossible to obtain a unique local response for a representative large-scale situation as shown in Figure 2.4b. Yet, whatever the approach, a limited number of WTs necessarily leads to a high variability within each of these regimes. It is therefore likely that the characteristics as formulated in section 2.3 result in an over-constrained problem in light of the natural variability of the observed meteorological situations. The approach envisaged in this work could, according to the author, prove to be successful by significantly relaxing the constraint on the limited number of WTs. However, this, *de facto*, makes the initial objective (to study each the atmospheric dynamics characteristic of each WT through fine-scale numerical simulations) unattainable.

The initial objective appears compromised, but only partially. Indeed, it is clear that in light of the preceding conclusions, obtaining a set of n episodes (n being small) whose dynamics in the Grenoble valley are representative for most of the observed situations is generally illusory. However, this study focuses on air quality, which is the poorest when conditions in Grenoble are anticyclonic for a long period. Focusing on the WAB episodes has several advantages. First of all, the large-scale situation is generally steady over the area of interest. Moreover, under these conditions, the Grenoble Y is assumed to be dynamically decoupled from the synoptic conditions above(Largeron and Staquet, 2016b). This is consistent with Figure 2.18 which shows a very large over-representation of certain local circulation modes during these episodes. Thus, the attention will be restricted to the WAB regime in the following chapters.

Chapter 3

Numerical simulations: set-up and evaluation

In the previous chapter it was shown that, for a small number of WTs, only the WAB regime has the potential to be associated with a characteristic atmospheric circulation in the Grenoble Y. The aim of this chapter is to present and characterize the numerical simulations of WAB episodes, which are then analyzed in Chapters 4 and 5. For this purpose, the different measurement datasets available (see section 2.4.1.2) are used, in combination with synoptic data, to select and describe a relevant set of WAB episodes (see section 3.1). The numerical model is introduced in section 3.2. In section 3.3.3 the fidelity of the model topography and the vertical resolution of the model grid are discussed so as to define the numerical setup employed. Finally, the simulations are evaluated by a systematic comparison of simulated data with their counterpart observed in section 3.4.

3.1 Selection and description of the episodes

3.1.1 Selection of the episodes

As shown in the previous chapter, methods based on large-scale data do not allow to identify episodes that belong with certainty to the WAB regime for the Grenoble Y (see sections 2.4.2, 2.4.3 and 2.4.4). Since we are concerned here only about the WAB regime, it is possible that one or more of the blocking index(es) could have been informative in this task but this approach has not been explored in this work.

It has been shown in the previous chapter that high pollution episodes are mostly associated with the Γ_{PT} regime (see section 2.4.5), which develops during WAB episodes. Hence WAB episodes correspond to those episodes that are persistent in the Γ_{PT} regime (over several days). Four such episodes capturing a significant part of the intrinsic variability of the Γ_{PT} regime (see Figure 3.1) have been selected. These episodes are presented individually in the following section.

3.1.2 Description of the episodes

This section briefly describes each of the episodes in terms of some key meteorological variables observed locally in the Grenoble Y. In order to keep the description brief, the large-scale fields are shown in Appendix A, with the exception of the mid-level winds (700 hPa) immediately above the Grenoble Y which are presented to provide a local picture of the large-scale winds.

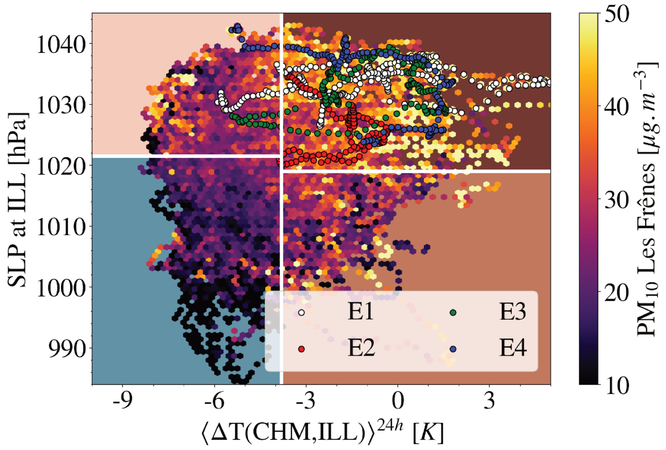

Figure 3.1: Position of the 4 episodes selected ($\mathcal{E}_1$, $\mathcal{E}_2$, $\mathcal{E}_3$ and $\mathcal{E}_4$) in the classification presented in section 2.4.5. Each colored circle represent an hour of the episode considered.

3.1.2.1 $\mathcal{E}_1$: Episode from 7th December 2013 to 18th December 2013

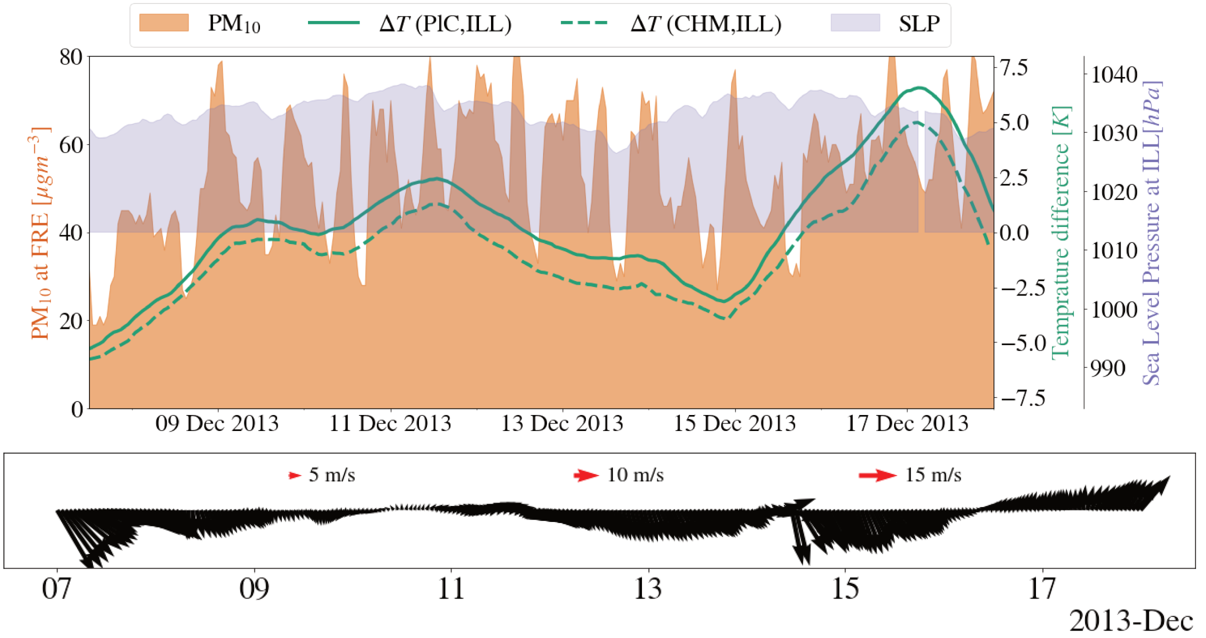

Figure 3.2: **Top:** Time-series of dynamical variables for $\mathcal{E}_1$. SLP is measured at ILL (see Figure 2.1). VSD, PlC and CHM temperature measurements lie respectively at 220, 900, and 1700 m ASL. PM$_{10}$ concentrations are extracted from the FRE monitoring station, representative for urban background concentrations. **Bottom:** Temporal evolution of the wind at 700 hPa from ERA5 near Grenoble (located at 45.25 latitude, 5.75 longitude).

Figure 3.2 display in-situ measurements for $\mathcal{E}_1$. One can notice that before the episode the pollution level was very low. When the inversion starts to build-up (materialized by the increasing temperature difference between higher altitude and valley floor stations) pollutants concentration attain a sort of threshold level from the second day. The strength of the temperature inversion varies continuously during the episode, with a minimum on 14 December 2013 as a cold front passes through (see the bottom panel of 3.2) and a substantial increase immediately afterwards. PM concentrations only respond very partially to these fluctuations.

3.1.2.2 $\mathcal{E}_2$: Episode from 1st December 2016 to 5th December 2016

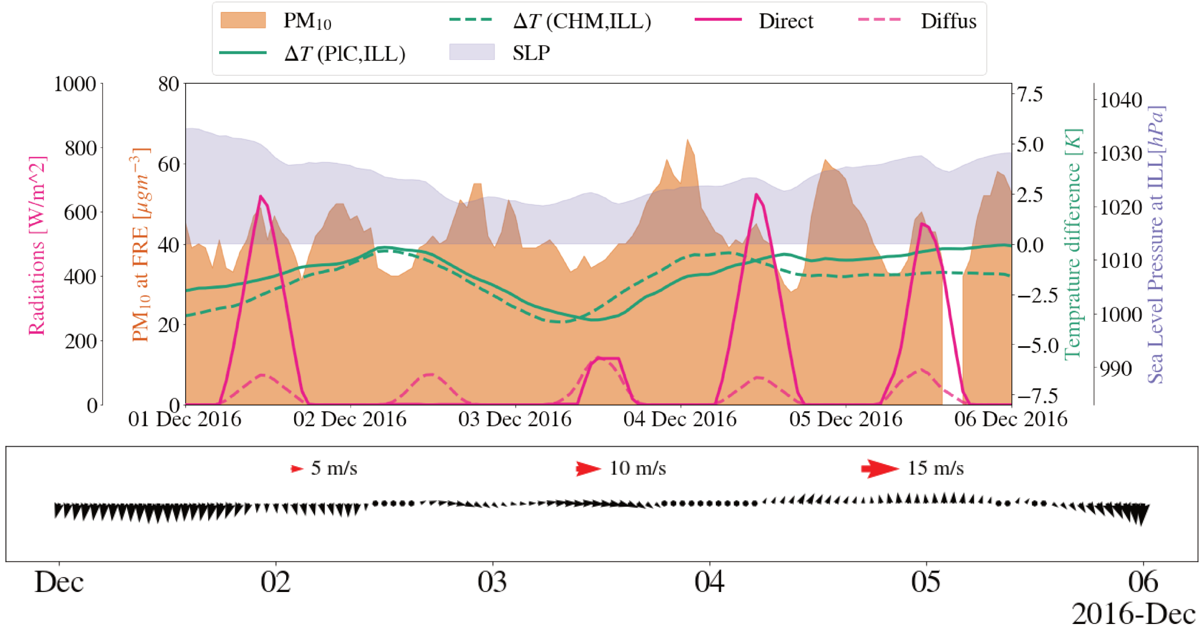

Figure 3.3: Same caption as Figure 3.2 for $\mathcal{E}_2$

This episode is much less anticyclonic than the others with an average SLP of 1025 hPa. The temperature inversion is on average less pronounced than for $\mathcal{E}_1$ and $\mathcal{E}_3$. However, PM concentration levels are high throughout the episode (but do not present very high concentration peaks). As for $\mathcal{E}_1$ the PM_{10} concentrations do not seem to be impacted by a cold front that is approaching, causing a drop in the strength of the temperature inversion and the presence of an elevated cloud cover on 2 and 3 December 2016.

3.1.2.3 $\mathcal{E}_3$: Episode from 6th December 2016 to 11th December 2016

During this episode the sky over Grenoble is clear and the atmospheric pressure, the strength of the temperature inversion and the PM_{10} concentrations are relatively large. When a cold front passes on 12 December 2016, clouds form and the inversion strength is significantly reduced but this does not affect the PM_{10} concentration much.

3.1.2.4 $\mathcal{E}_4$: Episode from 28th December 2016 to 2nd January 2017 1st

This episodes starts from a very high pressure state, with a weak temperature inversion an weak to moderate PM_{10} concentration. In contrast to what is observed for the other episodes, PM_{10} concentration appears to be directly influenced by the constantly increasing strength of the temperature inversion. On 1 January 2017, a low-level stratus develops in the valley (visible from satellite images[1]), explaining the decrease in incoming radiation. On 2 January 2017, the low level stratus disappeared and was replaced by large-scale clouds.

---

[1] `https://www.meteo60.fr/aller-plus-loin/archives-cartes/satellites/visible/01-01-2017`

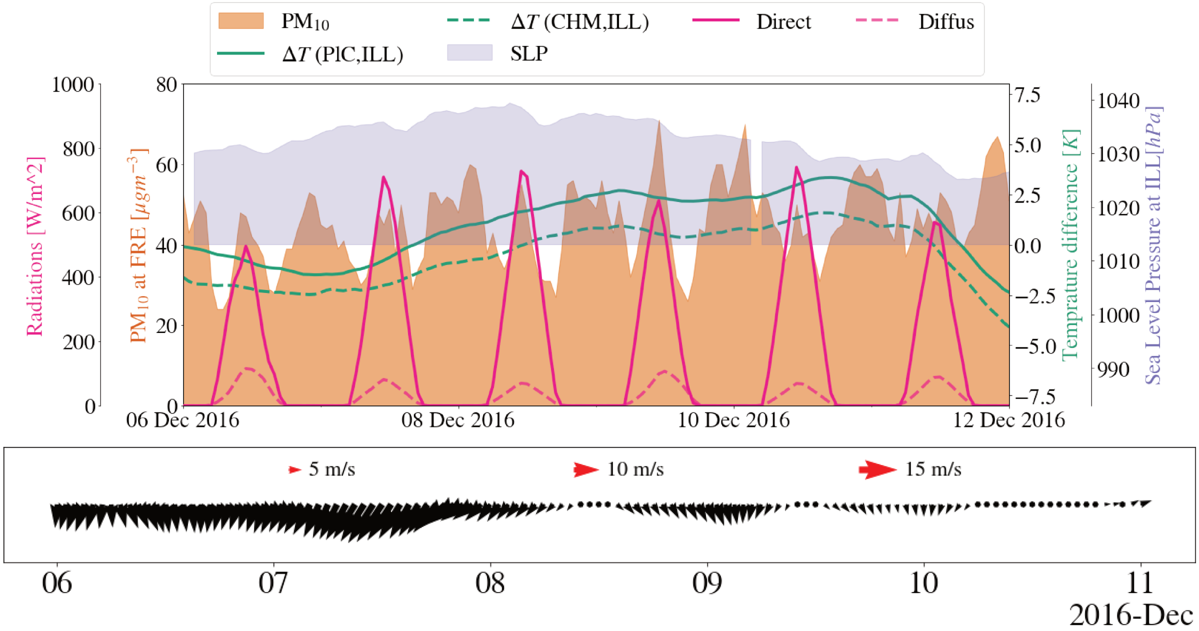

Figure 3.4: Same caption as Figure 3.2 for $\mathcal{E}_3$.

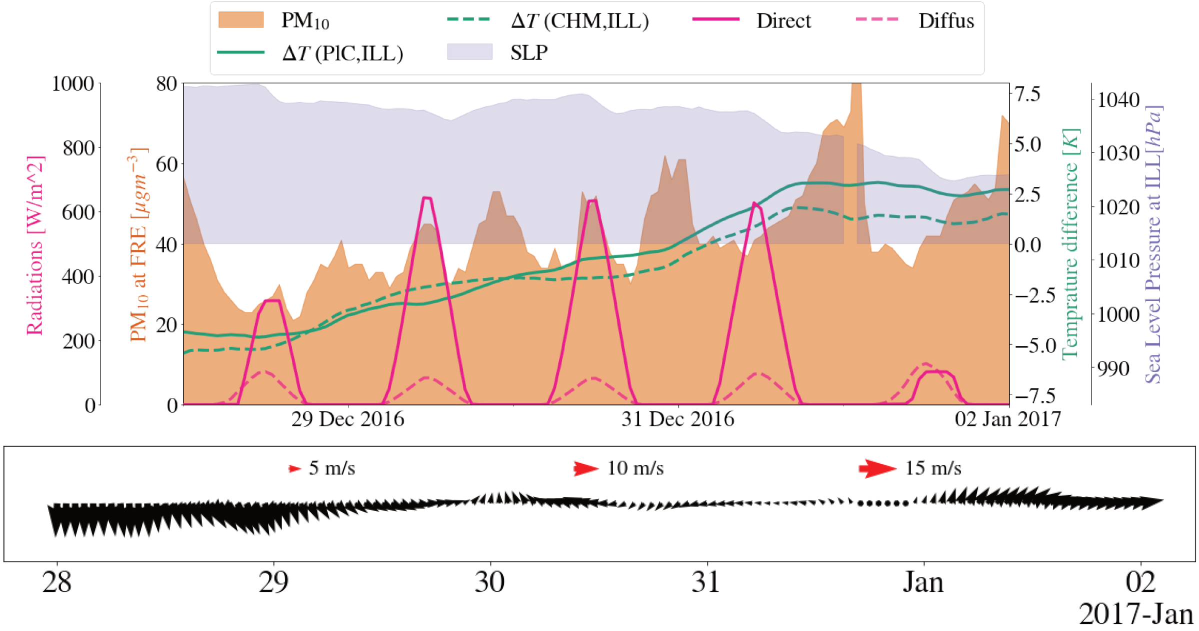

Figure 3.5: Same caption as Figure 3.2 for $\mathcal{E}_4$.

3.1.3 Summary

This section summarizes, together with Table 3.1, the different episodes simulated. Consistent with the results of Pelly and Hoskins (2003), all the episodes correspond, at large-scale, to the breaking – whether cyclonic or anticyclonic – of an upper-level Rossby wave.

Episode	$\mathcal{E}_1$	$\mathcal{E}_2$	$\mathcal{E}_3$	$\mathcal{E}_4$

Configs. (cf. section 3.3)	`t28c`	`t28f`
		`t42c`
			`t28c`
			`t28ced`
			`t42c`
				`t28c`
				`t28cd`

Simulated period	07/12/2013 18/12/2013 (12 days)	01/12/2016 06/12/2016 (5 days)	06/12/2016 12/12/2016 (6 days)	28/12/2016 01/01/2017 (4 days)
Synoptic situation	Anticyclonic Rossby wave-breaking	Cyclonic Rossby Wave Breaking	Anticyclonic Rossby wave-breaking	Anticyclonic Rossby wave-breaking
ΔT(CHM,ILL) [°C]	**-1.10** | 3.6 $[-7.8, 9.0]$	**-1.8** | 2.7 $[-5.8, 5.0]$	**-0.45** | 2.9 $[-7.8, 7.5]$	**-1.8** | 3.3 $[-7.2, 8.5]$
PM_{10} [$\mu g\,m^{-3}$]	**51.8** | 16.2 $[10, 89]$	**42.8** | 8.1 $[28, 66]$	**45.3** | 9.9 $[24, 71]$	**41.4** | 12.3 $[21, 109]$
SLP [hPa]	**1033** | 2.6 $[1026, 1038]$	**1025** | 3.8 $[1020, 1034]$	**1033** | 3.7 $[1025, 1039]$	**1037** | 4.7 $[1024, 1042]$
Key dynamical features	Varying ΔT, Strongly Anticyclonic	Variable skies, Weakly Anticyclonic	Constant ΔT, Strongly Anticyclonic	Low level stratus on January 1st 2017

Table 3.1: Overview of the different episodes simulated and their main characteristics. `tXX` refer to a topography with a maximum slope angle of XX ; `c` and `f` refer respectively to a coarse (≈ 16.5 m) or a fine near-surface vertical resolution (≈ 13 m). `e` stands for a slightly extended domain and `d` for an increased minimum turbulent diffusion for scalars. Scalar values correspond to **avg**|std [min,max].

3.2 Numerical set-up

The spatial extent and numerical characteristics of the domains considered are presented in section 3.2.1. The consideration of land use is discussed in section 3.2.2. Finally, the initialization of the snow cover and the inclusion of the PM emission inventory in the model are presented in sections 3.2.3 and 3.2.4, respectively. Attention is paid to the numerical aspects in relation to the resolution of the Navier Stokes equations. The WRF model and the main numerical methods on which it is based are briefly introduced in 3.2.5. Choices of physics parametrization are discussed in 3.2.6. Finally, numerical issues arising from the representation of the highly complex topography around the Grenoble basin are discussed in section 3.3.

3.2.1 Domain description

As a preamble to the presentation of the domains considered, it is necessary to discuss what resolution is required to capture the topography of the Grenoble Y. A mesoscale simulation with a horizontal resolution of 1 km cannot capture properly the channeling of atmospheric flow in the Grenoble Y, where valleys are 6 km wide at most. To illustrate this discussion, Figure 3.6 represents the topography of the domain of interest for different horizontal resolutions.

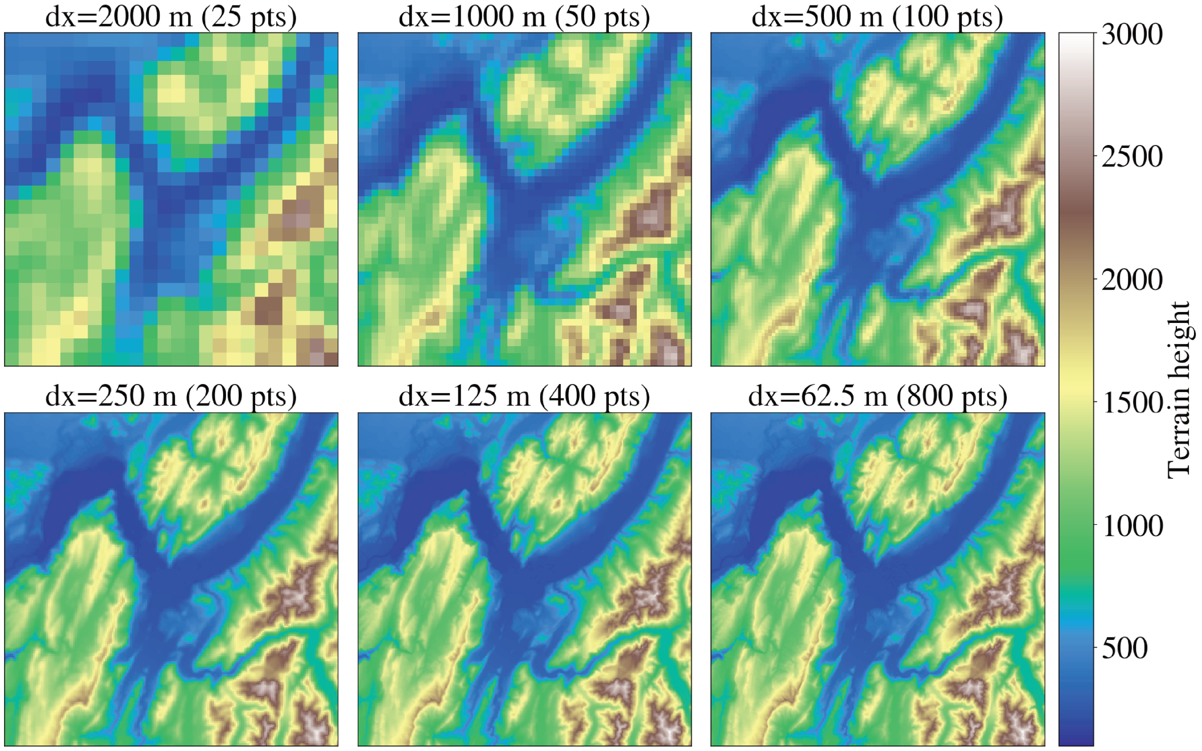

Figure 3.6: Representation of the topography of the Grenoble Y at varying resolutions. The characteristics given for the x-axis (horizontal resolution and number of points) apply also to the y-axis. These domains are realized from the interpolation of a dataset with 30 m horizontal resolution.

Visually, the detail of the topography appears with each doubling of the horizontal resolution down to a resolution of 125 m. The topography resolved at 62.5 m appears almost identical to that resolved at 125 m because of the pixel size. Assuming that at least ten points perpendicular to the axis of a valley are needed to start resolving the atmospheric circulation in a valley, Figure 3.6 shows that the main branches of the Grenoble Y impose a horizontal resolution of less that 500 m. Besides it is known that the effective resolution of a numerical model is much lower than its grid spacing (6 to 8 times according to Skamarock, 2004). Hence, a horizontal resolution of about 100 m is required to resolve the flow at the valley scale.

To achieve the desired horizontal resolution (Δx) four nested domains (using 1 way nesting) with respective Δx of 15 km, 3 km,1 km and 0.111 km are used to resolve the atmospheric dynamics in the Grenoble Y. Their geographical extent in depicted in Figure 3.7. The topography is interpolated onto WRF grids from the SRTM dataset at 30 m

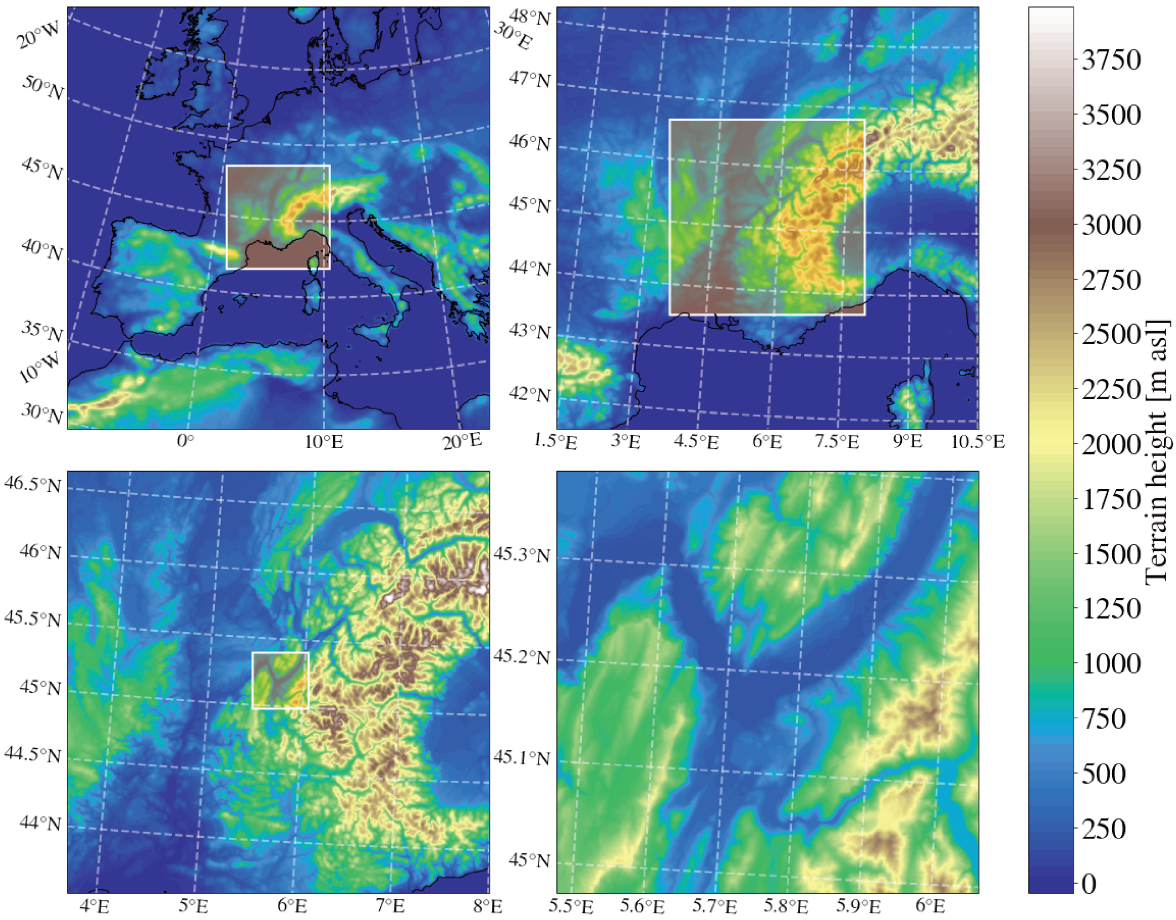

Figure 3.7: Geographical extent of the 4 nested domains and their corresponding topography. The orange square stands for the geographical extent of the subsequent nested domain.

horizontal resolution. When considering the 111 m horizontal resolution, most of the topographic features are captured and the maximum slope angle reaches 67 degrees. Naming conventions used throughout this work for the different areas of the innermost domain are illustrated in Figure 3.8. The colored areas correspond to masks used to carry out spatial studies, particularly in Chapters 4 and 5.

The distribution of mass points along the vertical is set to be denser close to the ground compared to the default WRF distribution. The height of the first mass points above the ground surface depends on the smoothing applied to the topography (see section 3.3) but is always between 11 and 18 m AGL for all the simulations performed in this work. 91 points are used along the vertical. These information are summarized in Table 3.2.

3.2.2 Land use description

The Earth's surface boundary for NWP models as it impacts physical processes in many aspects. For example radiative exchange are modified through a modification of its aldebo and the flow is directly impacted through friction. Numerous studies show the necessity of having an accurate and up-to-date high resolution land use description (Santos-Alamillos et al., 2015; Schmidli et al., 2018; Golzio et al., 2021). Specifically, Schmidli showed that an accurate land use description is particularly important to correctly resolve the valley winds in the Swiss Alps over an 18-day summer period.

For this work, the land cover is prescribed using the Corine Land Cover (CLC) dataset

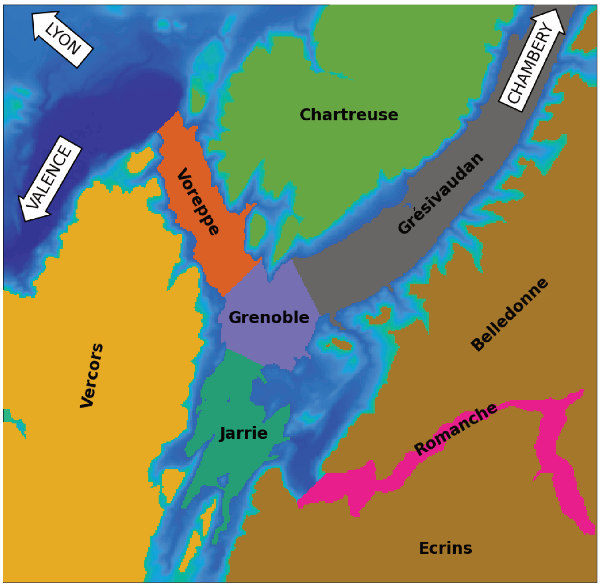

Figure 3.8: Naming convention used for the main valleys and massifs.

from 2018, which covers the whole Europe at 100 m horizontal resolution. This dataset is commonly used for numerical weather simulations (Santos-Alamillos et al., 2015; Umek et al., 2021). As it uses its own land-use categories, it has been mapped to the United States Geological Survey land use categories in a similar fashion to what was proposed in Pineda et al. (2004). The whole procedure to ingest this dataset in WRF is described in a git repository [2], which can be accessed upon demand.

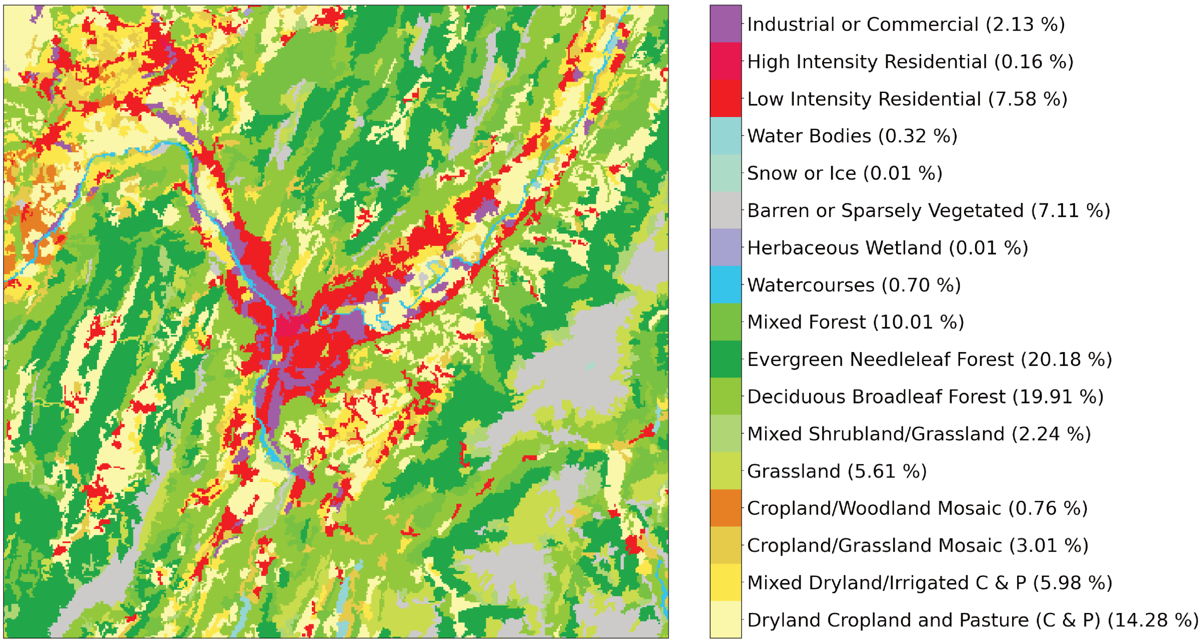

Figure 3.9: Land-use description from CLC for the innermost domain.

Figure 3.9 shows the resulting land-use for the innermost domain D4. This domain is mostly covered by forest ($\approx 50\,\%$). It is worth noting that residential and commercial areas occupy about $10\,\%$ of the domain. Figure 3.10 focuses on the land-cover used in the model around the available measurement station (introduced in section 2.4.1.2). It

---

[2] `https://gricad-gitlab.univ-grenoble-alpes.fr/lebouede/wps_dev`

		Domains			
	Set-up	**D1**	**D2**	**D3**	**D4**
δt [s]		60	12	4	1/5
$n_x = n_y$		202	246	340	406
n_z		91	91	91	91
Δx [m]		15000	3000	1000	111.111
Δz_0 [m]	`f`	[12.28, 14.04]	[12.03, 13.8]	[11.71, 13.62]	[12.39, 13.47]
	`c`	[15.8, 18.1]	[15.54, 17.88]	[15.13, 17.60]	[16.01, 17.39]
ϕ_m [°]	t_{28}	≈ 4	≈ 22	≈ 37	28
	t_{42}				42

Table 3.2: Domain related characteristics for the simulations considered in this study. δt is the model integration timestep; n_x and n_y the number of grid points in the west-east and south-north directions; n_z the number of vertical levels; Δx stands for the horizontal resolution; Δz_0 is the first mass point height and ϕ_m is the maximum slope angle. `f` and `c` stands for *finer* and *coarser* vertical distributions of mass points. t_{28} and t_{42} refer to two configurations allowing different thresholds for maximum slope angles, as discussed in more detail in 3.3.

can also be noted that the air quality station FRE, which is supposed to be a background station located in a park (see Figure A.1), is in fact perceived as being located in a low residential area for the model. This information can be important when interpreting the results.

Figure 3.10: Landuse for each stations within the WRF model based on CLC18. Corresponding aerial view are presented in Figure A.1.

3.2.3 Snowpack initialization

By default the snowpack would be initialized from the outputs of the global model that is used to initialize the model (ERA5). The relatively coarse resolution of ERA5 ($\Delta x = \Delta y \approx 25$ km) is not "adapted". The left side of Figure 3.11 shows the snowpack initialized using ERA5 data for December 1, 2016 for the two innermost domains. For domain 3 in particular, the discrepancy between the granularity of the topography and that of the

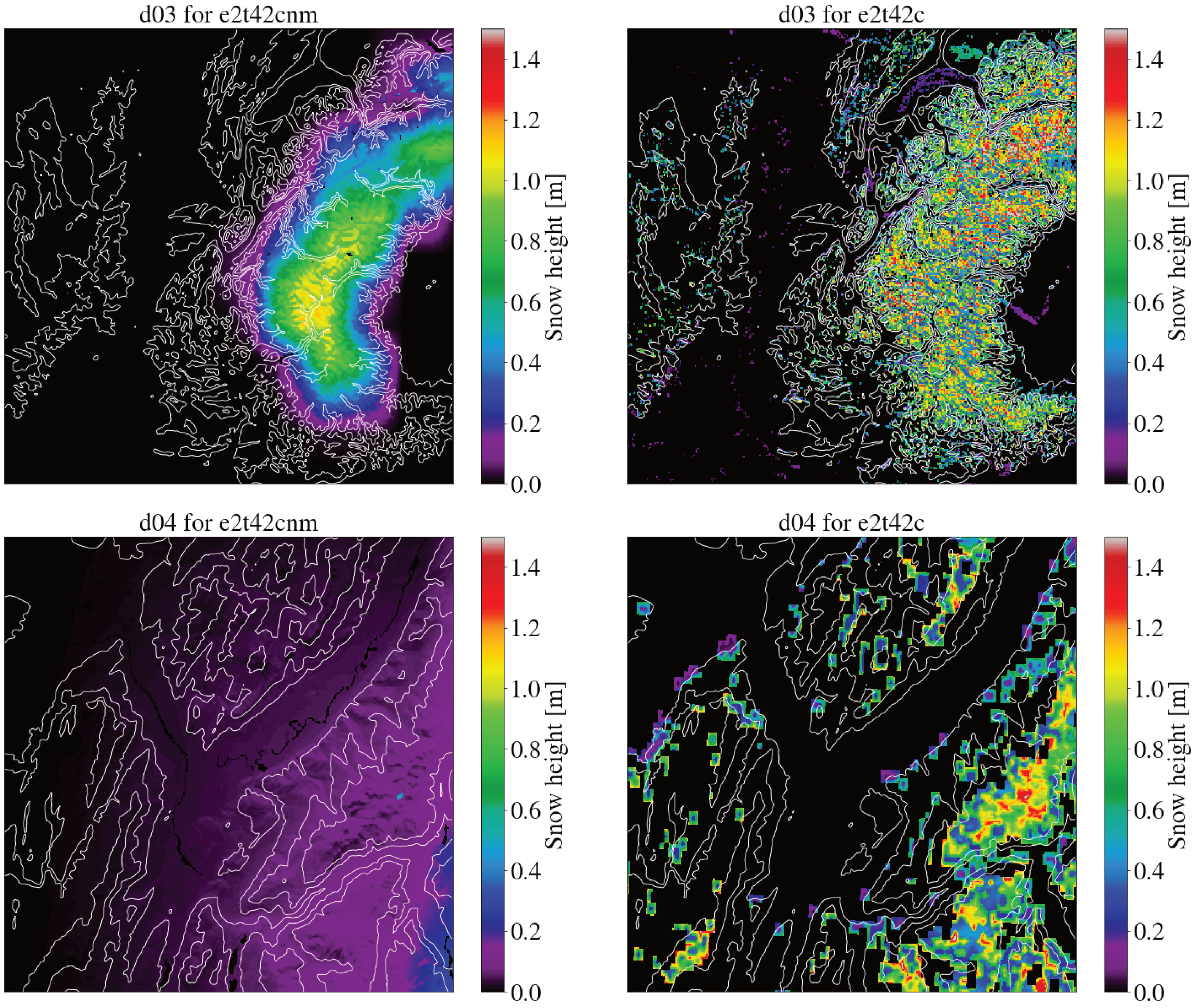

Figure 3.11: Snowpack initialization for December 1st, 2016 with ERA5 data (left) and with the postprocessing of MODIS albedo (right) for domains 3 (top) and 4 (bottom).

snow cover initialized by ERA5 is evident. In addition, the peri-Alpine areas (such as the western part of the Alpine arc) are not covered by any snow. Even more problematic is the fact that, in the innermost domain, the Grésivaudan valley (north-western branch; see Figure 3.7) and part of the Grenoble basin are covered with snow, in disagreement with satellite observations. This snow cover, despite its thinness, would have a considerable impact on the radiative and thermal exchanges between the ground and the atmosphere.

Moreover it has been shown by several studies in the literature that errors in the snowpack initialization could lead to non-negligible discrepancies between simulations and measurements. Indeed Tomasi et al. (2017) showed that using WRF with a coarsely initialized albedo led to a substantial underestimation of T_{2m}. Furthermore, Whiteman et al. (2014) showed statistically that snow-related variables correlate well with pollution peak occurrences in the Salt Lake Valley.

Following a similar procedure as in Arduini (2017), albedo initialization is performed using the MODIS data ($\Delta x = \Delta y \approx 500\,\mathrm{m}$). As they are satellite data, cloud cover can prevent daily observations from being complete. To deal with this, the previous 5 days' observations are also integrated providing that they allow to complete missing information. The satellite albedo is then used to initialize the snowpack prognostic variables. The snow cover is updated to match the non-zero values of the satellite albedo. The snowpack age is determined by inverting an empirical function fitted in Livneh et al. (2010). Snowpack height is computed with an empirical function based on altitude. Snow density can not be

SNAP	Sector
01	Combustion in energy and transformation industries
02	Non-industrial combustion plants
03	Combustion in manufacturing industry
04	Production processes
05	Extraction and distribution of fossil fuels and geothermal energy
06	Solvent use and other product use
07	Road transport
08	Other mobile sources and machinery
09	Waste treatment and disposal
10	Agriculture

Table 3.3: Description of the Selected Nomenclature for Air Pollution (SNAP) sectors

retrieved directly as a function of snow albedo as shown by Bohren and Beschta (1979). However, snow density can be roughly estimated through the snow's age via another empirical function (Meløysund et al., 2007). The initialization procedure is described in a git repository [3] and the resulting snow heights are also presented in Figure 3.11.

3.2.4 PM emission processing

The emission inventory is provided by the local air quality agency AtmoAURA. It gives the total annual emissions in tons per 100 m grid cell and per Selected Nomenclature for Air Pollution (SNAP) (see Table 3.3) for the entire innermost domain. Emissions are given for the calendar year 2016 and are here considered as representative for the period 2011-2018. It is necessary to apply a deconvolution on these data to generate time-dependent emissions. For example, it is obvious that the emissions caused by domestic heating depend on the considered period of the year. To do this, temporal emission profiles provided in the report by Schaap et al. (2005) are used.

A set of modulations for each SNAP is proposed by month of the year, day of the week and hour of the day (displayed in Figure 3.12). The emissions for a given date and time are obtained by multiplying the corresponding inventory value by the three appropriate modulation factors. These emissions must be converted from gridded to surface based because WRF does not operate on the same mesh as the emission inventory. The field is then rewritten according to the classic procedure for ingesting data via WRF Preprocessing System (WPS). The procedure and the scripts used are presented in detail in a git repository[4].

The surface emissions averaged over an episode are presented in Figure 3.13 for illustrative purposes. Emissions are clearly concentrated in urban areas, where both domestic heating and road traffic are heavily present. For the area of interest, SNAP 2, 7, 4 and 10 are responsible for 66 %, 18 %, 5 % and 5 % of local PM_{10} emissions, respectively.

For the results presented in Chapter 5, surface emissions (expressed in $\mu g\, m^{-2}\, s^{-1}$) are converted into $\mu g\, m^{-3}$ to be added to the tracer field at each time step. Strictly speaking, the advection module of the WRF model expects the tracers to be expressed as a mixing ratio (e.g. $\mu g\, kg^{-1}$). Taking into account this correction (by further dividing surface emissions by the density) yields only minor differences on a 4-day simulation. The mean

---

[3] `https://gricad-gitlab.univ-grenoble-alpes.fr/lebouede/wps_dev`

[4] `https://gricad-gitlab.univ-grenoble-alpes.fr/lebouede/wps_dev`

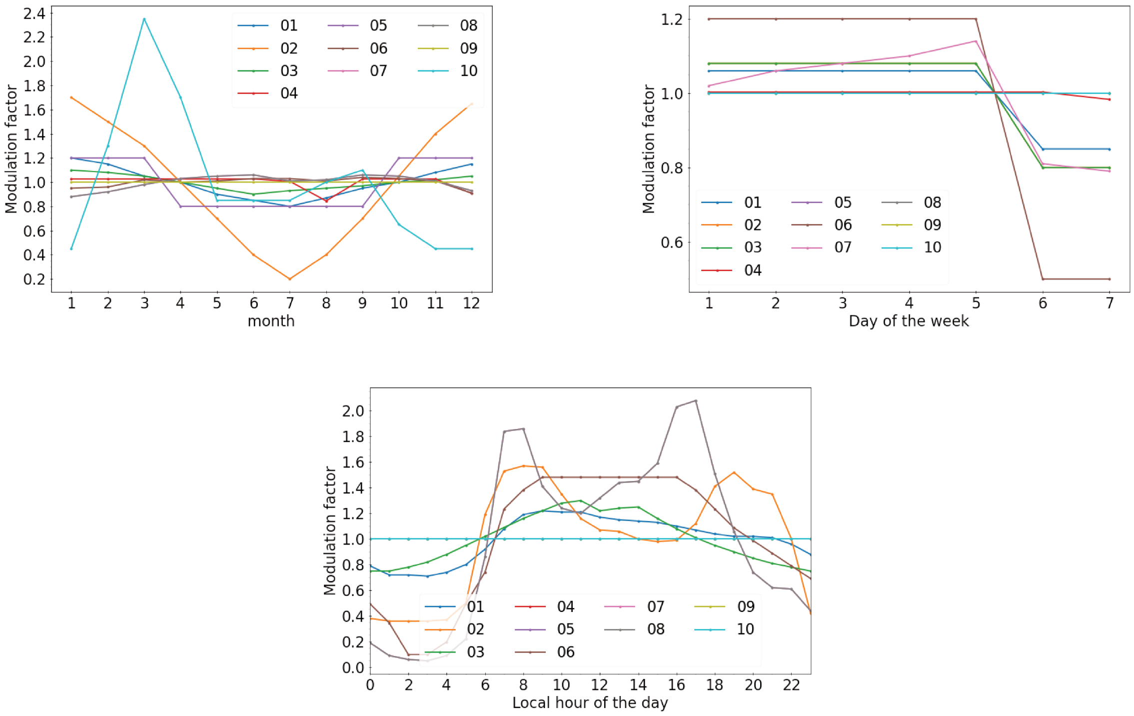

Figure 3.12: Temporal deconvolution factors from Schaap et al. (2005) for each month of the year (top-left panel), day of the week (top-right panel) and hour of the day (bottom panel). Numbers given in legend correspond to the SNAP sectors described in Table 3.3.

absolute difference is, on average over the Grenoble Y, 0.07 µg m^{-3} with a maximum of 0.34 µg m^{-3}.

3.2.5 Dynamical core

The WRF model is mainly designed for simulations at mesoscale where the horizontal resolution is typically ranging from a couple of hundred meters to a couple of tenth of kilometers. As used in this work, WRF resolves an Eulerian, fully-compressible and non-hydrostatic version of the Navier-Stokes equation using a terrain-following coordinate system. The WRF model uses a third-order Runge-Kutta scheme for the time integration with timesteps being specified in Table 3.4. WRF introduces a sub-time step (which subdivides the main integration time step) for which only the acoustic modes – which propagate much faster than the rest of the flow – are resolved. This time step is called the sound timestep δt_s and in the simulations presented here $\delta t_s = \frac{\delta t}{10}$. Fifth order advection schemes are used for both vertical and horizontal advection of both momentum and scalar variables. Turbulence closure is handled through a first-order horizontal Smagorinsky closure down to Δx =1 km and 1.5-order prognostic TKE closure for higher horizontal resolution.

The WRF model proposes two different approaches to solve the vertical mixing in the planetary boundary layer (PBL). The first approach considers that the domain discretization does not allow to correctly solve the atmospheric dynamics within the PBL, that is where the resolution is not fine enough compared to the height of the boundary layer (ideally, at least ten grid points in each direction are located within the PBL). Here, that is the case of the three outermost domains. It is therefore necessary for these domains to parameterize the impact of the PBL on the vertical mixing using a PBL model (see

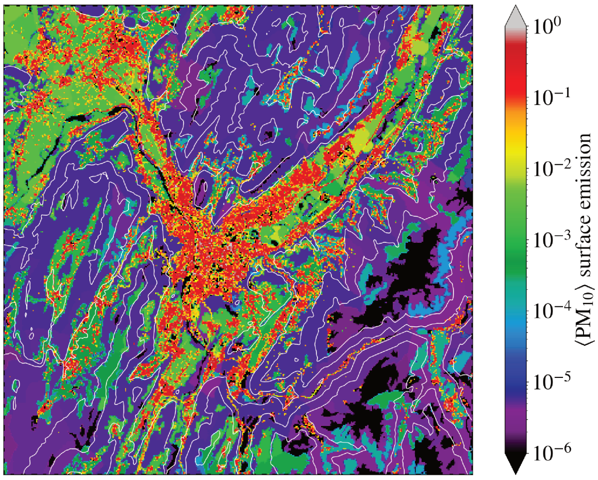

Figure 3.13: Averaged surface emission of PM_{10} for one complete episode. *Units are not shown purposely as this Figure is for illustrative purposes only.*

section 3.2.6). The second approach is to explicitly calculate the vertical mixing in the PBL from a 3D turbulence scheme. This is appropriate where the discretization effectively captures the most energetic vortices (the upper bound of the Inertial Subrange). Such simulations can then reasonably be qualified as large eddy simulation (LES). It is possible however to consider that, in view of the discretization, an LES-type approach – without respecting all the assumptions – remains a better approximation than the available PBL parametrizations. Considering that (very) stably stratified situation are investigated here, the LES-type approach is perhaps better referred to as High Resolution Mesoscale Simulation Read (see Cuxart, 2015, for a comprehensive discussion on the subject).

3.2.6 Physics parametrization

The physics parametrization schemes used for the numerical simulations are summarized in Table 3.4. As mentioned previously, PBL schemes approximate the vertical mixing in the PBL. Several studies have compared the performance of PBL schemes (Marjanovic et al., 2014). For example Xie et al. (2012) and Deppe et al. (2013) showed that the differences between the schemes are generally modest, but YSU ranks among the best performing. Based on this information, this scheme was chosen.

Models	Parametrization	WRF option
Micro-physics	Morrison 2-moment (Morrison et al., 2009)	10
PBL	YSU (Hong et al., 2006)	1
land surface	Noah Land-Surface Model (Chen and Dudhia, 2001)	2
Longwave radiation	RRTMG (Iacono et al., 2008)	4
Shortwave radiation	RRTMG (Iacono et al., 2008)	4
Surface layer	Monin Obukhov similarity scheme	1
Urban physics	Urban canopy model	0

Table 3.4: Main physics parametrization chosen for all the simulations described in this study.

All simulations presented in this work use Morrison's double moment micro-physics parametrization, the RRTMG short- and long-wave radiation parametrizations and the NOAH land surface model. Besides, slopes effect on radiation and topographic shading parametrizations are also activated. Regarding urban physics, the vertical resolution used is too coarse to use a multi-layer urban model. Indeed rooftops in Grenoble and its surroundings lie in great majority below the first mass point height. For this reason urban areas have been treated as a impervious surface with increased roughness.

3.3 Smoothing of the topography

The higher is the vertical resolution near the surface, the better the simulations will be able to capture certain physical phenomena such as down-slope winds, which are established within a few meters above the surface. Ideally, there should be several mass points within the first 10 meters above the ground along the vertical (Chow et al., 2013).

However, increasing the vertical resolution often leads to a highly distorted grid as the horizontal resolution remains much coarser. When terrain following or sigma coordinates system are used, distorted grids over steep slopes can generate numerical errors when evaluating horizontal gradients (Mahrer, 1984; Klemp et al., 2003; Zängl et al., 2004; Bao et al., 2018). These errors can in turn generate numerical instabilities in the simulations. To prevent this, modelers often smooth the topography and/or use special dynamics options such as time-offsetting (Marjanovic et al., 2014). Time-offsetting is intended to dampen the propagation of vertical acoustic modes. In the present case the two approaches are used: the topography is smoothed via the algorithm presented in the following subsection and the vertical acoustic modes are almost suppressed using a strong time off-centering (`epssm`$= 0.9$).

The objective of this section is to describe an optimal topography smoothing procedure – newly introduced in the course of this work – based on a maximum slope steepness criterion. It will therefore first be presented from a mathematical point of view in section 3.3.1. The results of its application onto the innermost domain are then discussed in section 3.3.2, focusing on the actual changes in orography. The impact of choosing one topography over another in terms of dynamics is discussed later in this chapter (section 3.3.3).

3.3.1 Description of the optimization problem

Let us define $\mathbf{h_0}$ as the original terrain height once interpolated on the WRF model grid of size (n_x, n_y). Let us also denote by $\bar{\mathbf{h}}$ (of same shape as $\mathbf{h_0}$) the target terrain height respecting some constraints. The constraints are defined here as a maximum angle ϕ_m allowed for the slopes of the target topography. Δx and Δy being given, one can compute the maximum vertical difference between two adjacent points Δz_{max} as:

$$\Delta z_{max} = \tan\left(\frac{\pi\phi_m}{180}\right) \times \Delta x \tag{3.1}$$

Considering each point of the topography as a variable, then the problem has $n_x \times n_y$ degrees of freedom. Let us denote by $\vec{b}$ the vector of length $n_x \times n_y$ populated with all the values in $\mathbf{h_0}$. Finally let us introduce the factor $\vec{x}$, a vector of size $n_x \times n_y$, by which $\vec{b}$ must be multiplied in order to obtain the smoothed topography ($\bar{\mathbf{h}}$).

Then one can reconstruct the target topography[5]

---

[5] $\vec{b} \odot \vec{x} = b_i x_i$

$$\bar{\mathbf{h}} = \text{reshape}\left[\vec{b} \odot \vec{x}, (n_x, n_y)\right] \tag{3.2}$$

by solving the following optimization problem[6]

$$\begin{cases} \text{Minimize} & \|\vec{b} \odot (\min(\vec{x}-1,0)) \times n\|^2 + \|\vec{b} \odot (\max(\vec{x}-1,0)) \times p\|^2 \\ \text{Subject to} & \max(|\nabla_x(\bar{\mathbf{h}})|) \leq \Delta z_{max} \\ & \max(|\nabla_y(\bar{\mathbf{h}})|) \leq \Delta z_{max} \\ & \max(|\nabla_{xy}(\bar{\mathbf{h}})|) \leq \Delta z_{max} \times \sqrt{2} \end{cases} \tag{3.3}$$

where $\nabla_{x|y|xy}$ is the difference operator along the x-axis | the y-axis | the diagonal. If no constraints are saturated in the initial topography, then $\vec{x}$ is none other than the identity vector, giving a null cost function and resulting in no modification of the topography.

In order to have a finer control over the resulting topography, penalization factors p and n have been inserted in the cost function. For example, $p > n$ implies a higher penalization for points that sit higher in the smoothed topography than in the original one ($x > 1$). This will result in a topography where the altitudes at which valley floors lie are better preserved at the cost of lowering more the surrounding heights. Conversely, if $p < n$, the optimum better preserves the peaks even if it requires a significant increase in height for certain parts of the topography (such as valley floors).

It has been decided to focus the constraints on the slope steepness and the cost function on the terrain height. Other mathematical formulations could be envisaged. For example, let us consider a mountain range that largely does not respect the slope constraints. In the current configuration, this will result in a very spatially homogeneous slope whose steepness is equal to the constraint. In particular, the spatial variations initially present along this slope will have been suppressed. It is possible that some applications may be sensitive to these small-scale variations, and thus to their disappearance. In this case, it would be necessary to think about adding information to the cost function that is less local than the terrain height difference at the point considered.

3.3.2 Application to the Grenoble valley

To assess the robustness of the method, the algorithm to smooth the topography, introduced in the previous section, is applied here to the innermost domain.

The algorithm is tested for two different regimes: one regime with $\phi_m = 42°$, corresponding to the maximum slope set by Quimbayo-Duarte (2019), which used the WRF model in the Passy valley, and another regime with $\phi_m = 28°$, appearing as close to the lower bound of acceptable values for ϕ_m (see Figure 3.14). For the 42° (28°) configuration 3.1 % (19.5 %) of the grid cells do not respect the maximum slope threshold, yielding 1.6 m (15.3 m) mean absolute difference between the smoothed and the original topography. To further show the value of this method, the 28 degree scenario will be illustrated for $n = p$ (no penalty is introduced) and for $n < p$ (it is more cost-effective to lower the topography than to raise it). For brevity, the configurations have the following naming convention: `tXXnIpJ` with XX the maximum angle, and I and J the penalization factors. The resulting topographies are compared in terms of terrain height differences and slope steepness.

---

[6] An exemple of python scripts to solve this problem using `cvxpy` is also provided at `https://gricad-gitlab.univ-grenoble-alpes.fr/lebouede/wps_dev`.

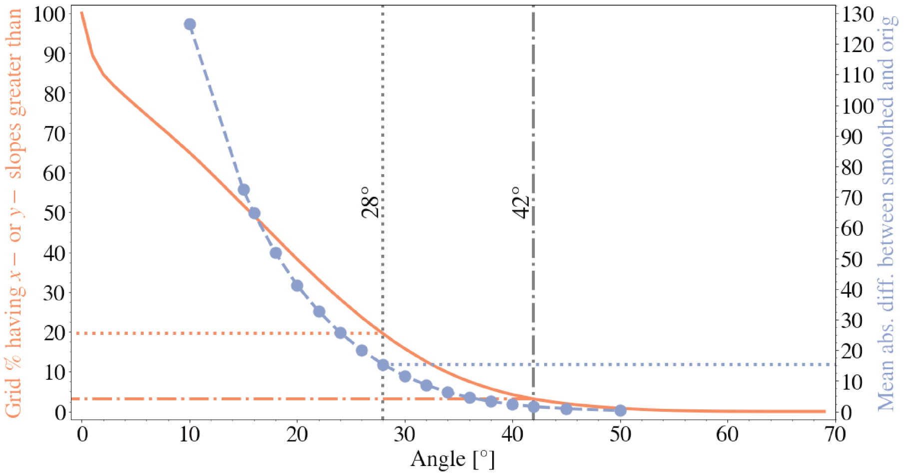

Figure 3.14: Left axis: percentage of grid cells with slopes above a certain threshold (indicated on the x-axis). Right axis: Mean absolute difference in meters between the original topography and one that is smoothed so that no slopes exceed a certain threshold (indicated on the x-axis) using the algorithm defined in section 3.3.1 with no penalization ($n = p$).

Terrain height differences Figure 3.15 shows the differences between the original topography – i.e. the SRTM data directly interpolated on the WRF grid without any smoothing – and three configurations: `t28n1p1`, `t28n1p5` and `t42n1p1`. For both the 28 and 42 degree configurations, only areas of complex terrain are impacted by the smoothing of the topography. In particular, the Grenoble valley floor remains intact in all configurations. As expected, `t42n1p1` is substantially less affected than `t28n1p1` by the smoothing procedure. The Vercors and the Chartreuse remain almost unaffected except locally for the vertical cliffs that border them. The Romanche valley, which is very deep and narrow, must nevertheless be subject to a significant smoothing despite the possibility of representing it with slopes of up to 42 degrees. The maximum height differences range from -185 to 287 m.

By setting $\phi_m = 28°$, the cliffs of the Vercors and Chartreuse are smoothed over several grid-cells. The Romanche valley is most affected. In the `t28n1p1` configuration the valley floor is raised by up to 393 m and the surrounding peaks are lowered by up to 515 m. The introduction of a penalization allows the algorithm to be oriented so that the heights at which the valley floors sit are better preserved. In the present case it may help, for example, to better preserve the temperature differentials between the Romanche valley and the Grenoble basin. In the `t28n1p5` configuration the valley floor is raised by a maximum of 138 m, but the surrounding peaks must be lowered by up to 731 m.

Figure 3.16 illustrates the differences between the resulting topographies from a statistical point of view. One clearly notices that the original height distribution and the one for $\phi_m = 42°$ are very similar. This statistical representation is especially useful to illustrate the penalization introduced. Without penalization, the smoothed quantiles are either below or above the original quantiles so as to preserve the average height of the relief. Penalization disturbs this equilibrium by introducing a positive or negative bias. The optimization algorithm then finds another equilibrium position set by the introduced penalization. This figure also illustrates that, through the optimization process, the response to the introduced penalization is non-linear.

Slopes probability density function (PDF) Figure 3.17 compares the PDF of slopes for the resulting topographies. The smoothing algorithm appears to compress

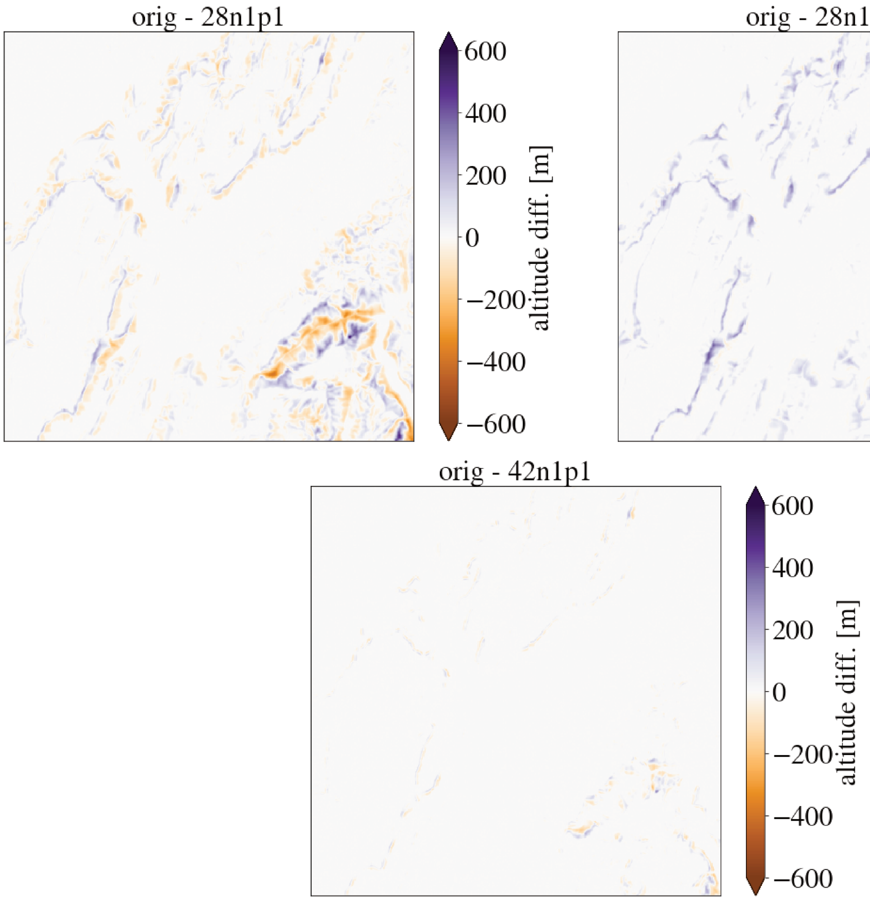

Figure 3.15: Difference between the original topography interpolated on the model grid and the smoothed topographies for 3 configurations: `t28n1p1`, `t28n1p5` and `t42n1p1`.

the PDF tails within the allowed slope range, generating peaks close to the threshold values (dotted lines). These peaks are more clearly marked for $\phi_m = 28°$ than for $\phi_m = 42°$. An additional peak, materialized by the dashed lines, may be noticed (especially for $\phi_m = 28°$). It is generated when constraints on both the diagonal and either the x- or y-axis are saturated. Indeed, if two of the sides of a triangle are constrained, the third side is geometrically imposed. These peaks match exactly with the slope angle corresponding by the non-saturated constraint of that configuration computed with Eq. (3.4).

$$\phi_2\ [°] = \arctan\left(\tan\left(\frac{\pi\theta_m}{180}\right)\times\left(\sqrt{2}-1\right)\right) * \frac{180}{\pi} \tag{3.4}$$

This secondary peak emphasizes the effect of taking into account diagonal constraints when smoothing the topography. Otherwise both vertical and horizontal constraints can be saturated simultaneously and can lead to unexpected steep slopes (e.g. diagonal slopes of 46.7° with a threshold fixed to 28°).

3.3.3 Trade-off between vertical resolution and steepness of the topography

So as to better resolve the flow within the Grenoble Y, the finest vertical resolution would be desirable. However, this would be at the expense of reducing the steepness of the topography. Indeed, using a steeper topography sets constraints on the finest vertical resolution that allows the WRF model simulations to be numerically stable (Connolly

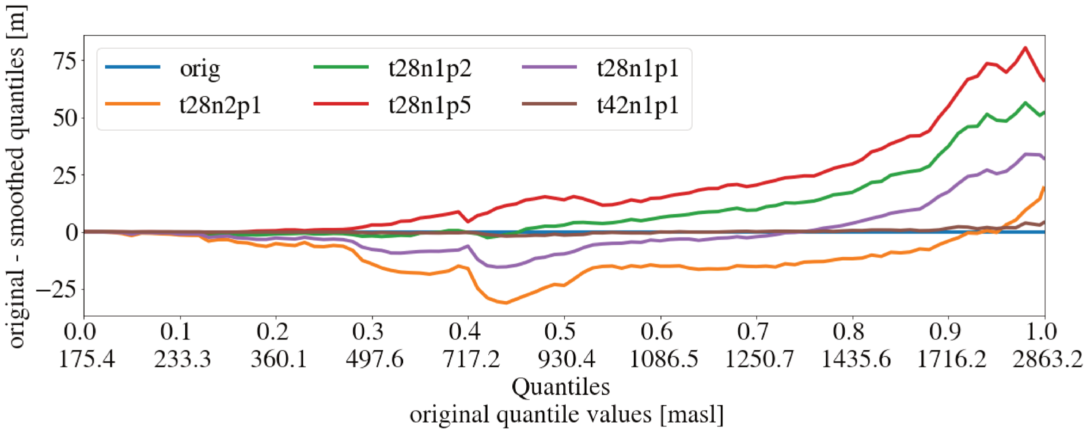

Figure 3.16: Intercomparison of height quantiles for different topography configurations. On the x-axis one can read the quantiles (valid for all curves) as well as the values associated with the quantile for the original configuration only.

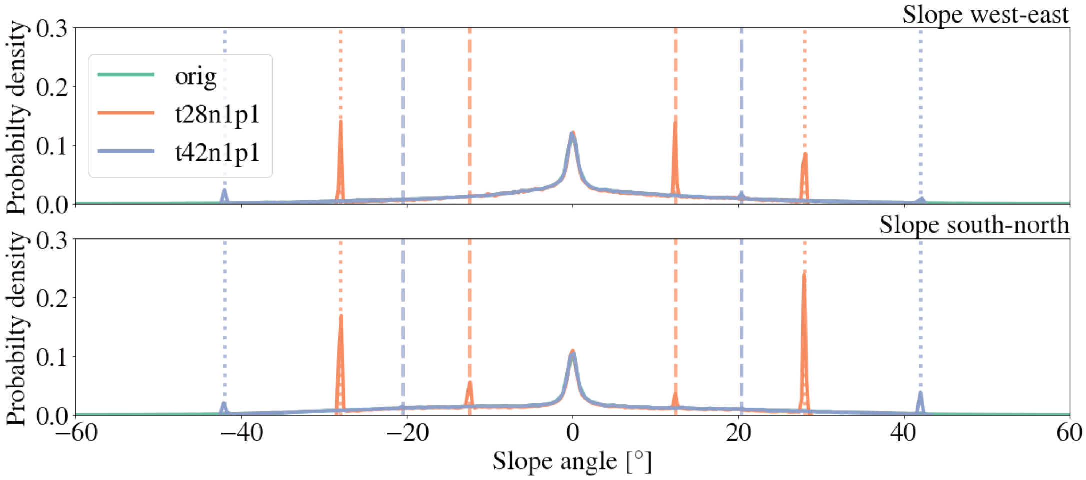

Figure 3.17: probability density function (PDF) of slopes in the x and y directions in the innermost domain for the original topography and the topographies smoothed at 28 and 42 degrees with penalization. Dotted vertical line represent the along-grid maximum slope angle allowed. Dashed lines correspond to secondary peaks computed from 3.4.

et al., 2021). To guide the selection of ϕ_m for the simulations performed in this work, simulations using $\phi_m = 42°$ and $28°$ are compared in the following. With $\phi_m = 42°$, it has been found that the vertical resolution immediately above the ground had to be coarser than 16 m while for $\phi_m = 28°$, it had to be coarser than 12.5 m.

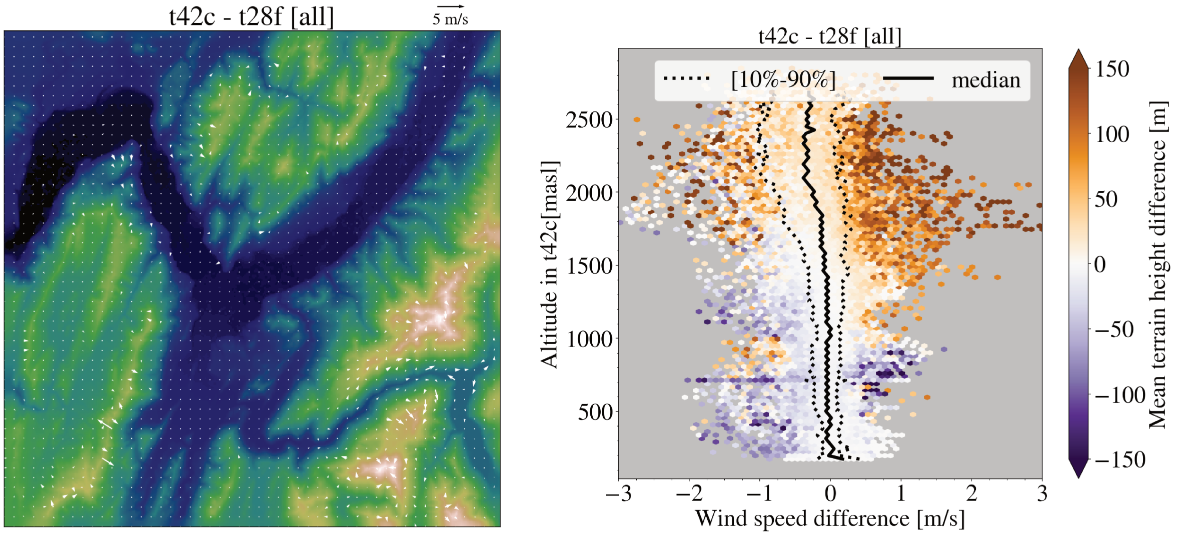

(a)

(b)

Figure 3.18: **(a)**: Difference in average horizontal wind speeds at 10 m AGL between `t42c` and `t28f` for $\mathcal{E}_2$. **(b)**: Hexagonal plots of wind speed difference between `t42c` and `t28f` for $\mathcal{E}_2$ with respect to the altitude in `t42c`. Points are colored by the mean terrain height difference between the two topographies. Black continuous and dotted lines indicate the median and 10 and 90th percentiles, respectively.

Figure 3.18 presents the differences in mean horizontal wind speeds at 10 m AGL between `t28f` and `t42c`. Figure 3.18a shows that the wind velocity differences are on average zero near the surface in the Grenoble Y and are significant only where the height differences between the topographies are large (see Figure 3.15). Figure 3.18b indicates that the differences are greater when the variations in terrain heights are large. Up to 1500 m ASL 80 % of the wind speeds do not show significant differences between `t42c` and `t28f`. Above 1500 m ASL, grid cells whose altitude are significantly higher in `t42c` are mostly associated with stronger winds. Neither the change in vertical resolution nor the change in steepness of the topography between `t28f` and `t42c` appear to have an integrated effect on the near surface atmospheric circulation in the Grenoble Y.

Figure 3.19 presents differences between `t42c` and `t28f` in terms of T_{2m}. Figure 3.19a shows that the reliefs are globally colder and the valley floor consistently but very slightly warmer for `t42c` than for `t28f`. The temperature differences are therefore not confined to the areas where the land-forms have been modified. As for wind speeds, T_{2m} differences between the two configurations are smaller at lower elevations but they increase steadily with altitude. The significant variations in terrain height are also associated with larger temperature differences between the two configurations. However, the picture is slightly different than for the winds in that valley atmosphere is overall colder for `t42c` than that for `t28f`. It seems therefore that for the near-surface temperature there is an integrated effect of the change of the steepness of the topography (or in the vertical resolution).

The two previous figures characterize differences that are confined close to the ground (2 and 10 m AGL). Since we are interested in pollutants transport, it is essential to characterize differences in terms of atmospheric stability. Figure 3.20 shows, for both configura-

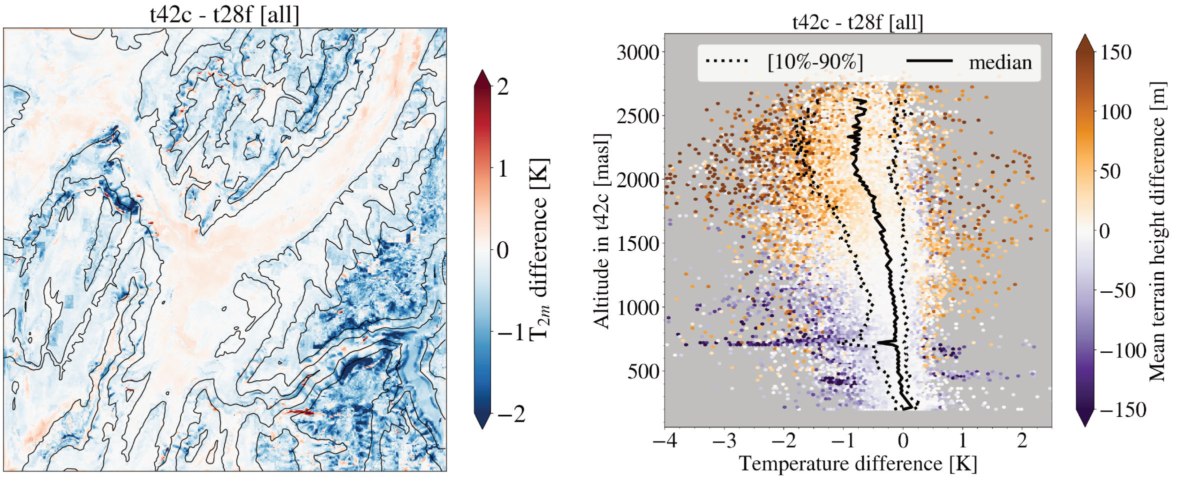

(a) (b)

Figure 3.19: **(a)**: Difference in average T_{2m} between `t42c` and `t28f` for $\mathcal{E}_2$. **(b)**: Hexagonal plots of wind speed difference between `t42c` and `t28f` for $\mathcal{E}_2$ with respect to the altitude in the original topography. Points are colored by the mean terrain height difference between the two topographies. Black continuous and dotted lines indicate the median and 10 and 90th percentiles, respectively.

tions, the temporal and vertical evolution of $\frac{\partial \theta}{\partial z}$ spatially averaged over the Grenoble basin (cf. Figure 3.8). Visually one can observe that, although slight variations are noticeable, the general structure of the vertical potential temperature gradient is almost identical in both configurations. Figure 3.20 also shows a comparison of the inversion heights and valley heat deficits for the two configurations. Mean absolute differences between `t42c` and `t28f` for H and inversion heights are $1.66 \times 10^5\,\mathrm{MJ\,m^{-2}}$ and 66.5 m, respectively. The relative differences are small (3 and 6 %, respectively).

In sum, significant wind or temperature differences are observed only locally where the topography is strongly modified (see Figures 3.18 and 3.19). Hence, atmospheric dynamics at the valley floor of the Grenoble Y – which matter the most for pollutant transport – are not significantly different. For temperature, an integrated but tenuous effect is observed. When considering the atmospheric stability over the entire vertical column of air in the Grenoble basin, the differences remain small (see Figure 3.20). It thus seems that it is the large scales of the topography that dominate the overall atmospheric dynamics in the Grenoble Y. It also appears that the gain in vertical resolution from one configuration to the other is not enough to substantially change the simulated dynamics. Hence, it has been decided to simulate the episodes with the `t28c` configuration so as to be conservative for a wider range of large-scale forcing.

3.4 Model evaluation

Before any interpretation of the simulation outputs it is necessary to assess the quality of the results. To this end, simulated data are compared to their counterpart observed data in section 3.4.1, introduced in section 2.4.1.2. This comparison is followed in section 3.4.2 by a physical interpretation of the observed differences.

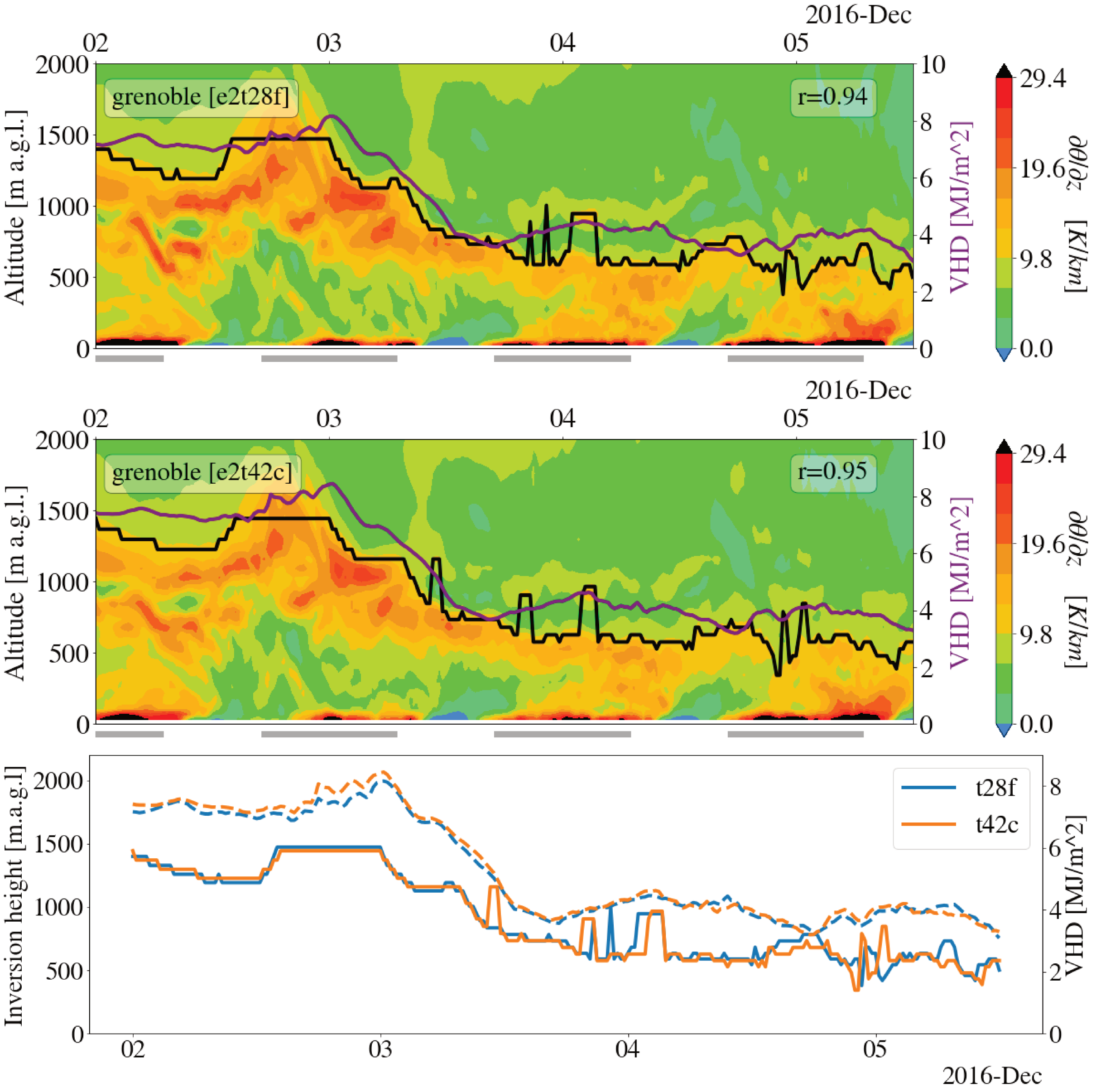

Figure 3.20: Simulated vertical gradient of θ, averaged over Grenoble (cf. Figure 3.8), for $\mathcal{E}_2$ for `t28f` (top) and `t42c` (middle). The inversion height (solid black line) corresponds to the highest value in altitude from the ground up to 1500 m AGL where $\frac{\partial \theta}{\partial z} > 9.8\,\mathrm{K\,km^{-1}}$. The heat deficit H (purple curve, right-hand axis) is calculated for Grenoble from the ground up to 1500 m AGL. The coefficient Pearson correlation coefficient (r) (indicated in the top-right corner of each figure) is the Pearson correlation coefficient between the inversion height and H. The lower figure compares on the same graph the temperature inversion heights (solid lines) and valley heat deficit (dashed) obtained for `t28f` and `t42c`.

3.4.1 Meteorological variables

3.4.1.1 Winds at 10 m agl

Given that the purpose of the simulations is to study the dispersion of PM in the Grenoble Y, it is crucial that these simulations reproduce correctly the winds in the valley, and particularly near the surface. Weak wind regimes – as is the case in most of the selected episodes – are known to be more difficult to simulate. For example, Jimenez and Dudhia (2013) show that the error in the simulated wind direction in complex terrain using WRF is inversely proportional to the wind speed. Finally, it is also known for wind resource assessment that WRF scores increases as stability decreases (Fern et al., 2018). In particular wind speed errors and correlations are the worse when considering thermal inversions. Figures 3.21 and 3.22 show timeseries of U and V for the 4 episodes at ILL and PtC, respectively.

For $\mathcal{E}_1$, there is a good agreement between simulated and measured wind until 14 December 2013, when the simulated wind diverges from the observed wind. Another such discrepancy occurs at the end of the simulated time period for $\mathcal{E}_2$. These two periods are not included in any of the subsequent analyses in this manuscript except in section 3.4.2 to investigate their origin. Apart during these periods, the simulated wind is generally in very good agreement with observations despite low wind speeds. For instance the increase in the V component during $\mathcal{E}_2$ is very well captured at ILL.

3.4.1.2 Vertical wind profile at ILL

This subsection focuses on the comparison of the simulated winds with the vertical measurements available at ILL. This comparison is presented graphically in Figure 3.23. Several interesting remarks can be drawn from this figure. First of all, there is a good general agreement between simulations and observations. For example, periods of weak winds (beginning of $\mathcal{E}_2$, end of $\mathcal{E}_4$) and strong winds (end of $\mathcal{E}_2$) are well captured by the simulations. Furthermore observations display a clear daily pattern with winds weakest around noon and generally stronger at night times, marking the footprint of thermally driven winds. This pattern is more apparent at 60 and 100 m AGL than in measurements below. The simulations correctly capture this daily pattern except during the second half of $\mathcal{E}_3$ when the simulated winds are very weak. It is also possible to note that overall the wind speed seems to be slightly but systematically underestimated in the simulations above 20 m AGL.

One can also notice some discrepancies. Consistent with the ground-level wind comparisons, simulations in the last days of $\mathcal{E}_1$ and at the very end of $\mathcal{E}_3$ are significantly different from observations. Indeed, a strong north-westerly wind dominates within the first 100 meters of the atmosphere in the simulations whereas the measurements indicates weak south-easterly winds. The origin of these discrepancies is discussed in section 3.4.2.

3.4.1.3 2-meter air temperature

This section presents a comparison between measured and simulated T_{2m} for the different episodes. For this purpose 3 stations, staggered on different altitudes, are considered: ILL at the valley floor (213 m ASL), PlC at mid-altitude (948 m ASL) and CHM considered at high altitude (1727 m ASL). The results are presented in two different ways: statistically in Table 3.5 and graphically in Figure 3.24 as a comparison of the observed and measured time series for $\mathcal{E}_3$.

The first observation is that a good correlation is obtained between measurements and simulations. Table 3.5 shows that Pearson correlation coefficients are about 0.7, except

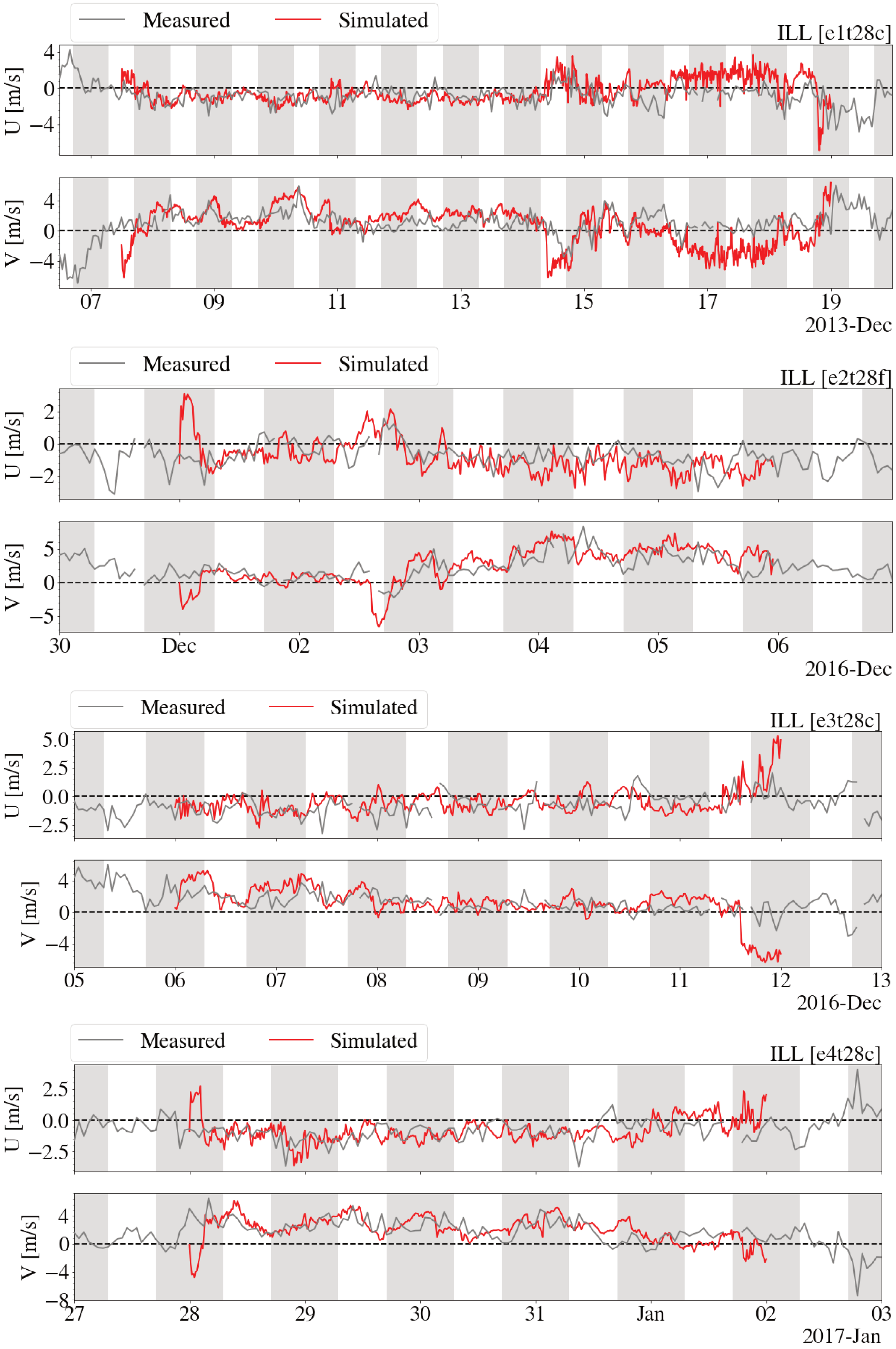

Figure 3.21: Comparison of measured and simulated winds at 10 m AGL at ILL for $\mathcal{E}_1$, $\mathcal{E}_2$, $\mathcal{E}_3$ and $\mathcal{E}_4$. Gray shading corresponds to nighttime.

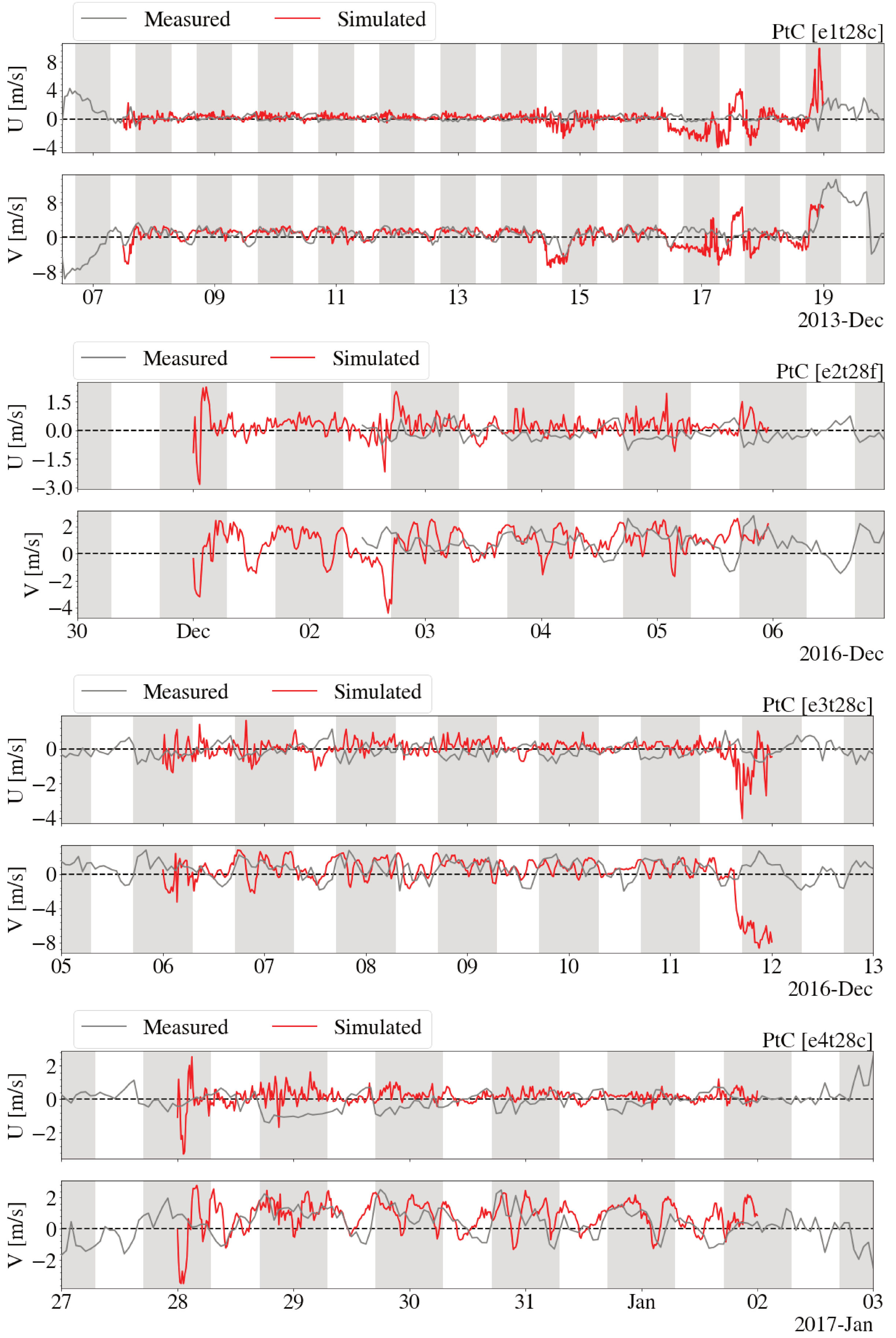

Figure 3.22: Comparison of measured and simulated winds at 10 m AGL at PtC for $\mathcal{E}_1$, $\mathcal{E}_2$, $\mathcal{E}_3$ and $\mathcal{E}_4$. Gray shading corresponds to nighttime.

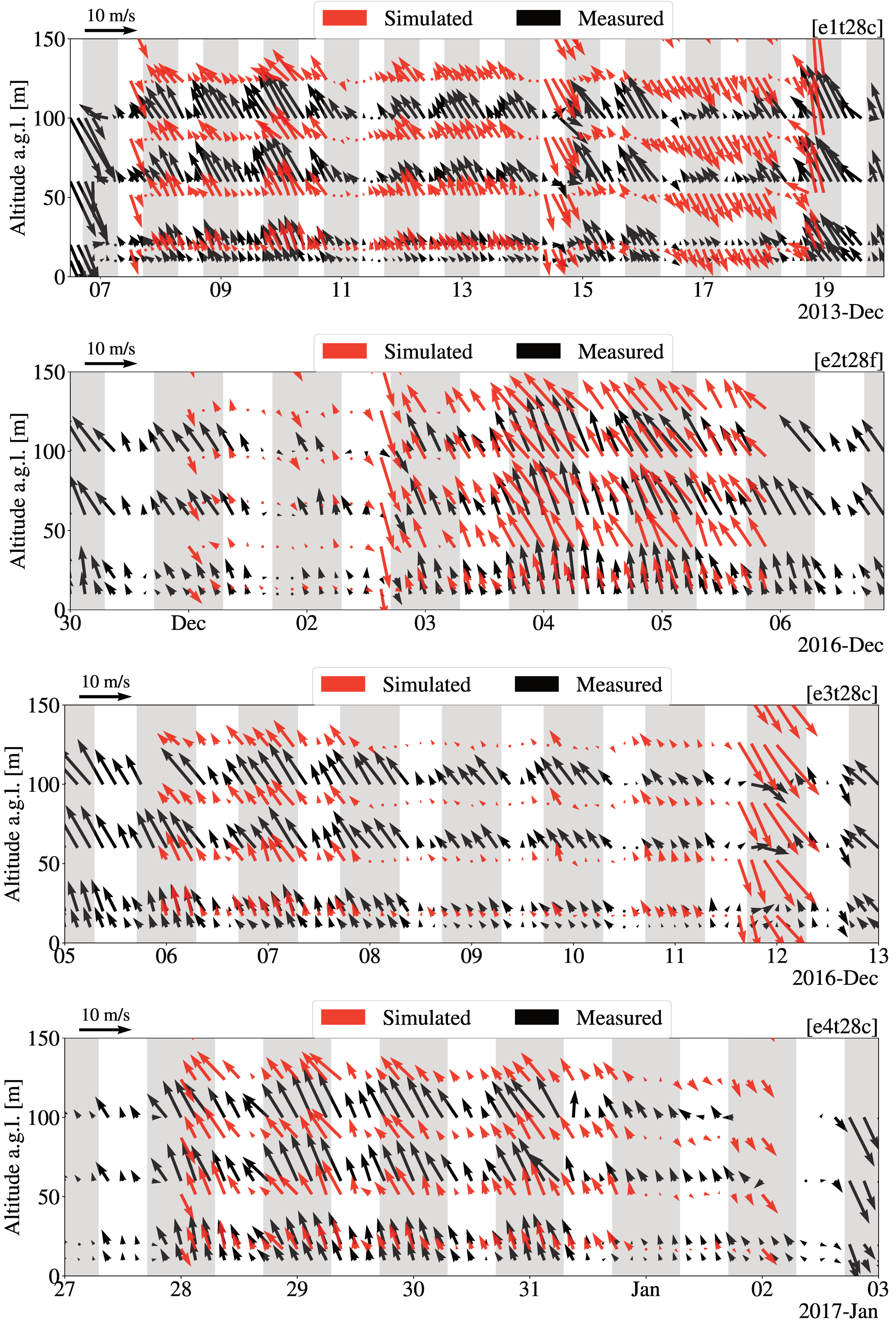

Figure 3.23: Comparison of vertical profile of winds at ILL for $\mathcal{E}_1$,$\mathcal{E}_2$,$\mathcal{E}_3$ and $\mathcal{E}_4$. Gray shading corresponds to nighttime.

			R	RMSE	BIAS	MAE
e1	t28c	ILL	0.71	2.17	1.02	1.68
		PlC	0.76	3.33	-2.51	2.87
		CHM	0.81	3.4	-2.64	3.01
e2	t28f	ILL	0.78	1.99	1.1	1.48
		PlC	0.79	1.96	1.01	1.57
		CHM	0.54	2.98	0.41	2.36
e3	t28c	ILL	0.85	2.21	1.47	1.79
		PlC	0.71	1.7	0.22	1.25
		CHM	0.78	3.9	-3.23	3.51
e4	t28c	ILL	0.56	3.37	2.33	2.72
		PlC	0.47	3.12	2.31	2.48
		CHM	0.62	4.07	-2.52	3.34

Table 3.5: statistics for T_{2m}, computed from hourly averaged output for the periods considered as valid (see section 3.1). Stations whose names appear in blue are covered by snow in the simulations.

for $\mathcal{E}_4$. Figure 3.24 shows that for $\mathcal{E}_3$ the minima and maxima are captured accurately at both ILL and PlC. For ILL this good agreement with measurements extends to $\mathcal{E}_1$ and $\mathcal{E}_2$, which share similar MAEs ($\approx [1.5\,\mathrm{K}, 2\,\mathrm{K}]$). In terms of MAEs, PlC is as well captured as ILL except for $\mathcal{E}_1$ (where it happens to be covered with snow). This range of MAEs is consistent with scores obtained in other studies such as Suárez-Molina (2021) over the Canary islands. For CHM the situation is slightly different as the temperature is systematically underestimated and the afternoon peak exhibits a cut-off. This behavior also extends to the other episodes (as evidenced by similar MAEs for $\mathcal{E}_1$ and $\mathcal{E}_4$). The fact that CHM is not covered by snow for $\mathcal{E}_2$ might explain why the metrics are not comparable with the other episodes.

Stations that are covered by snow are systematically associated with strong negative biases when compared to the measurements (see Table 3.5). This negative bias may suggest that these stations are erroneously considered to have a snow cover, causing a significant heat deficit near the ground. It is possible that the horizontal resolution of the dataset used to initialize the snowpack, namely 500 m, is too coarse. Unfortunately, the authors do not have a way of verifying this information directly from measurements or photographs. An overestimation of the albedo or snow water equivalent for the snow cover could also induce underestimations of T_{2m}, as noted by Tomasi et al. (2017). Given the altitude of CHM and the time of year, it seems more likely that the problem is related to the handling of the snow (snowpack characteristics, interactions with micro-physics) rather than a simple problem of snow cover.

Still according to Table 3.5, MAEs are higher for $\mathcal{E}_4$ than for the other three episodes. Figure 3.25 provides a clue as to the origin of these discrepancies. It can be seen that the cooling of the valley floor is less marked in the simulations than in the measurements. The temperature inversion therefore seems to be less well captured for this episode than for the others.

3.4.1.4 Vertical temperature profile at ILL

Vertical profiles of simulated and measured temperatures at the ILL mast at 60 and 100 m AGL are compared for $\mathcal{E}_3$ in Figure 3.26. The comparisons between simulations and

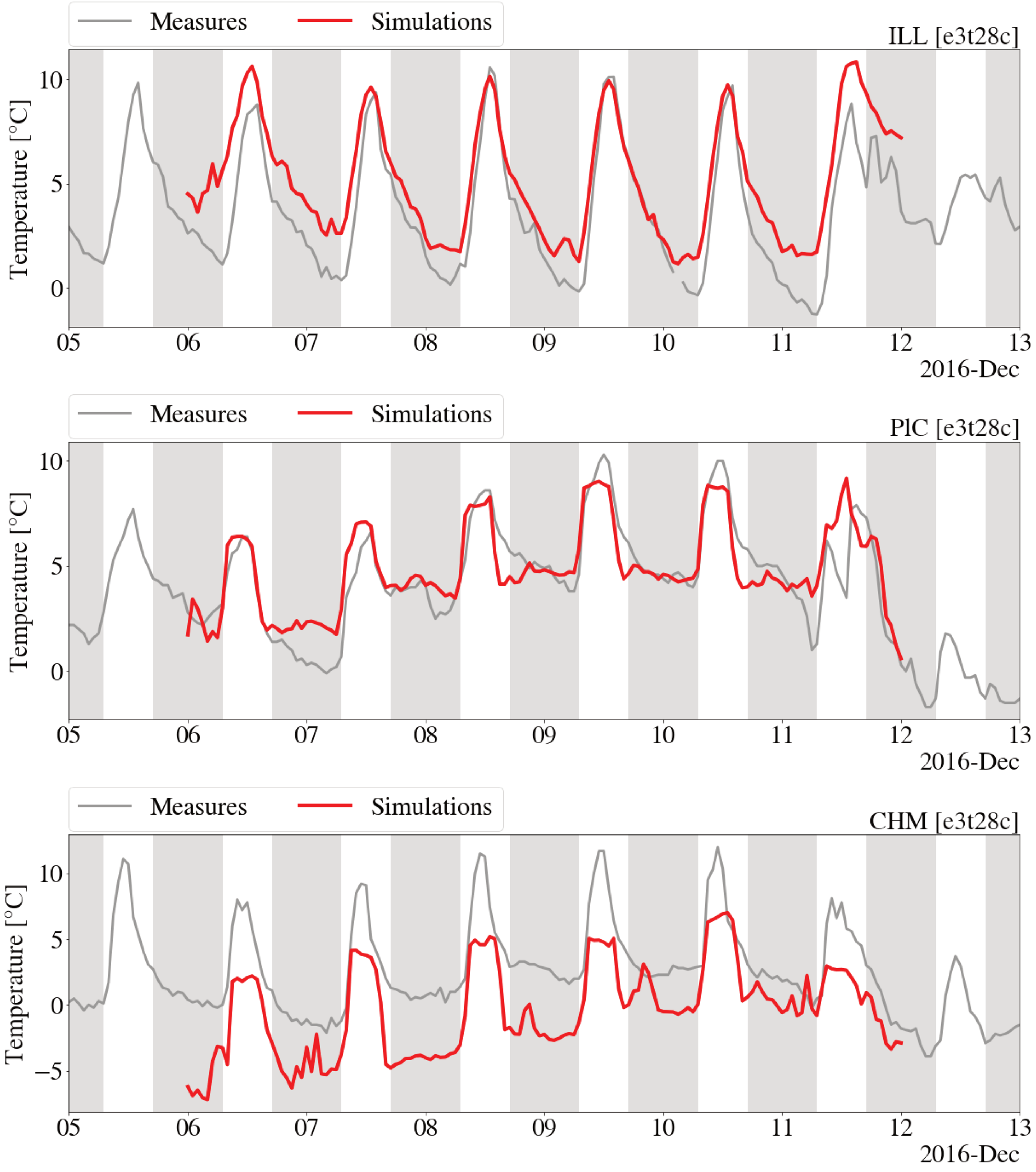

Figure 3.24: Time-series of T_{2m} at three measurement stations lying at different altitudes for $\mathcal{E}_3$. Gray shading corresponds to nighttime.

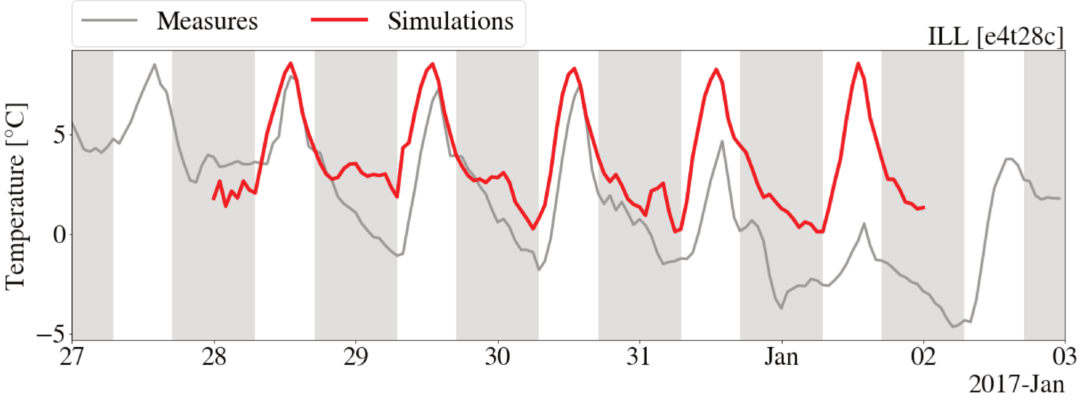

Figure 3.25: Time-series of T_{2m} at ILL for $\mathcal{E}_4$.

measurements are not as good as for the near-surface temperature. Indeed, simulated temperatures are systematically overestimated (at 60 and 100 m AGL) except around the solar zenith. In other words, it seems that the temperature variability associated with the diurnal cycle is underestimated in the simulations. As a matter of fact, night-time cooling is systematically underestimated, as is daytime warming. A similar behavior is found in all the simulated episodes, which suggests that his error lies in a physical phenomenon that is not or poorly captured.

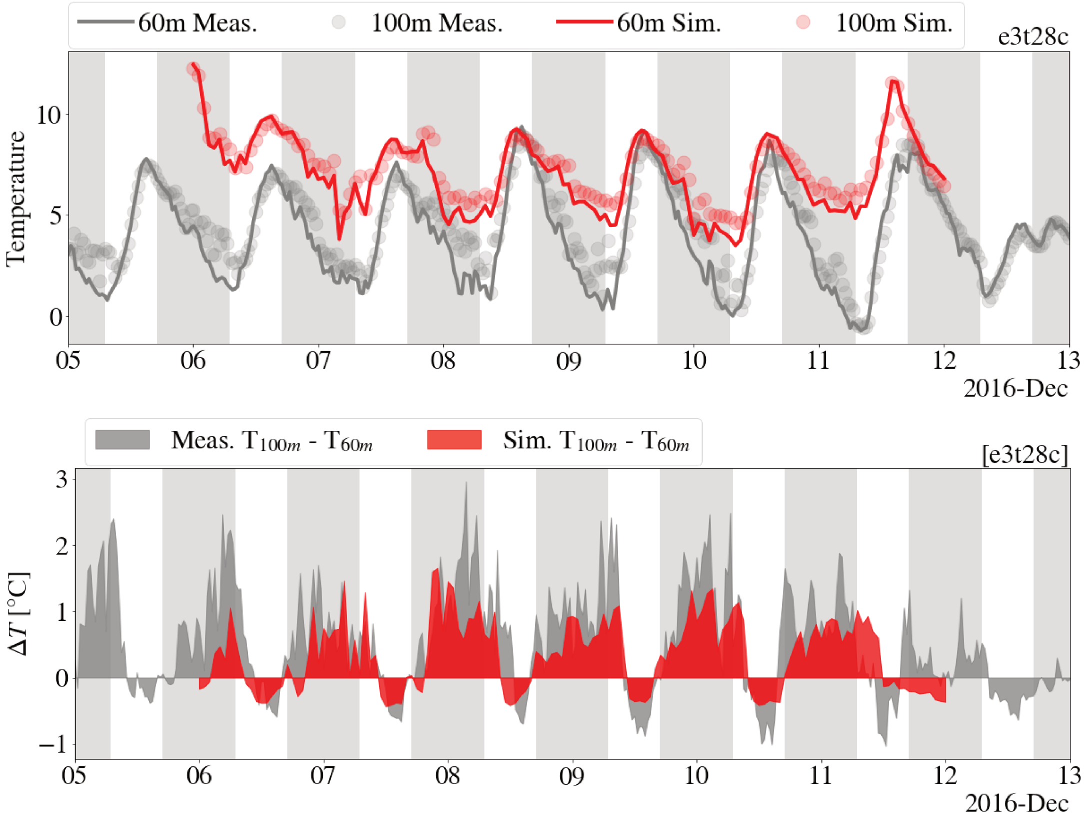

Figure 3.26: Comparisons with available measurements for the vertical temperature structure near the ground at ILL for $\mathcal{E}_3$. The top figure shows the measured and simulated absolute temperature at 60 (solid line) and 100 m AGL (transparent points). The bottom figure represents the simulated and measured temperature difference between 100 and 60 m AGL.

However, it is interesting to note that the temperature gradients between 100 and 60 m AGL (and thus the atmospheric stability of the air layer in-between these two altitudes) are well captured. It can be seen from Figure 3.26 that the daily dynamics and the amplitude of the vertical temperature gradients are reproduced fairly accurately.

Vertical profiles of simulated and measured absolute temperature for two specific days, are presented in Figure 3.27. As stated above, a good agreement between simulations and measures is found in the afternoon, especially between 3 and 6 pm. This indicates that weak natural convection or neutral atmosphere due to radiative heating of the ground is fairly well captured. However, the low level inversion is clearly overestimated in the simulations. If we consider the valley heat deficit (which is visually interpreted as the integral between the vertical temperature profile and a dry adiabatic lapse rate), it is greater in the simulations. The most noticeable difference is at the core of the night and below the first measurement point on the ILL mast (60 m AGL). In light of these profiles, this error might be concentrated within the first 20-30 m AGL, but a lack of measurements at this altitude does not allow for a clearer conclusion.

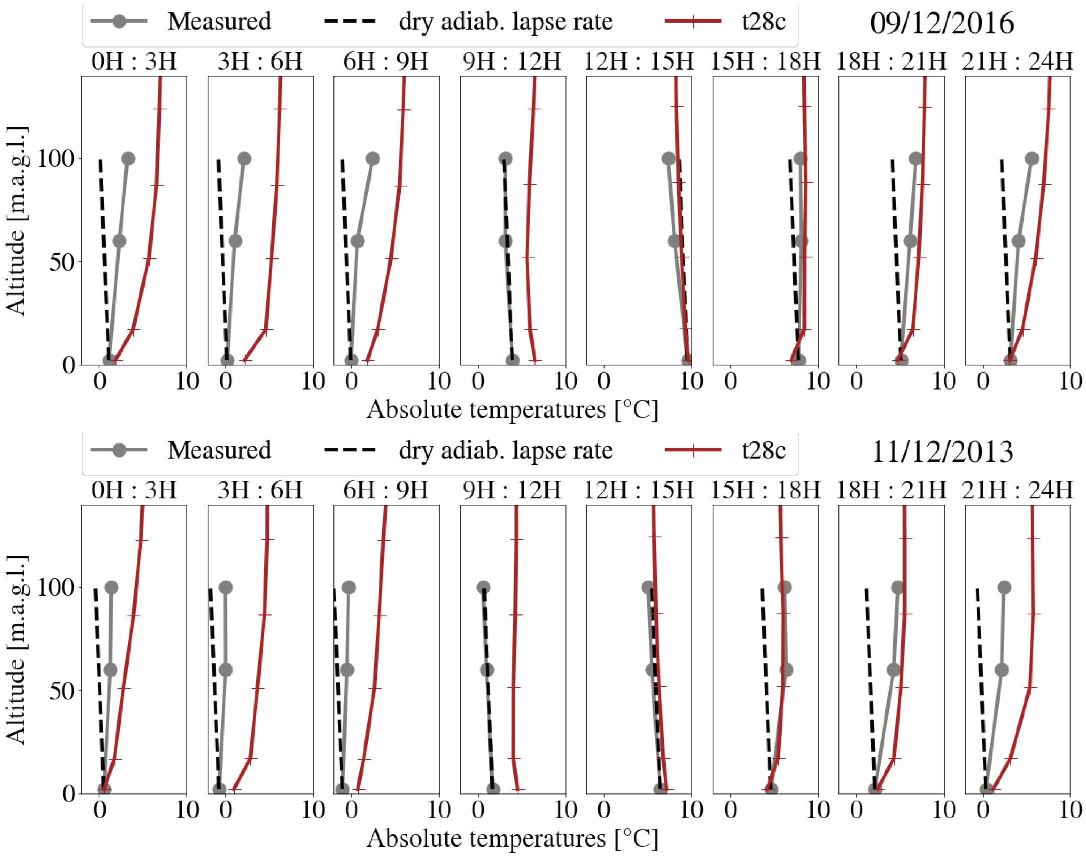

Figure 3.27: Comparisons with available measurements of vertical temperature profiles averaged over 3 hours at ILL for two distinct days.

3.4.2 Possible causes for meteorological discrepancies

3.4.2.1 Underestimation of the Grésivaudan valley-flow speed

In the previous section, it has been pointed out that the down-valley wind blowing from the Grésivaudan valley towards the Voreppe valley is underestimated, especially away from the ground (e.g. see Figure 3.23). This section focuses on the analysis of several factors that could explain this underestimation.

Absence of down-slope winds ? The vertical resolution of the model does not allow down-slope winds to be resolved properly or at all. This would result in a deficit of cold air being conveyed from the massifs flanks to the valleys floor. This could explain the slight temperature overestimation in the late night at ILL (see Figure 3.24). This heat deficit would in turn reduce the temperature difference between the Grenoble basin and the Rhone plain and thus the speed of the Grésivaudan valley-flow. Unfortunately, even if this hypothesis seems likely, it is difficult to verify it due to the lack of measurements.

3.4.2.2 Ill-channeling

As shown in sections 3.4.1.1 and 3.4.1.2 simulations sometimes exhibit a wind in the Voreppe valley that is reversed compared to the observations (see for instance the last few days of $\mathcal{E}_1$ and the end of $\mathcal{E}_3$). Possible reasons are explored here.

Large-scale flow First and foremost, it is natural to explore a possible discrepancy between the synoptic situation in the simulations and the one that actually occurred.

However the synoptic winds at 500 hPa over the Grenoble valley only exhibit minor differences with respect to those provided by ERA5. It is still possible that the reanalyses themselves are inaccurate. However, this reanalysis dataset is more than widely used and its quality is very rarely questioned. Therefore, this hypothesis cannot be completely ruled out but it is unlikely to provide the main reason for the discrepancy.

Size and resolution of the innermost domain Another cause could be the size of the innermost domain that was chosen for numerical stability reasons. Indeed, when using nesting in WRF, it is recommended to use grid size reduction factors of 3, 5 or 7 at most. The fact that this study uses a factor 9 could therefore be problematic, since the topography of the parent domain of the innermost domain is at a relatively coarse resolution.

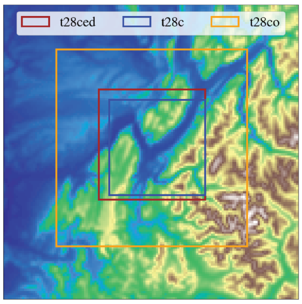

Figure 3.28: Spatial extents of the innermost domains in different configurations

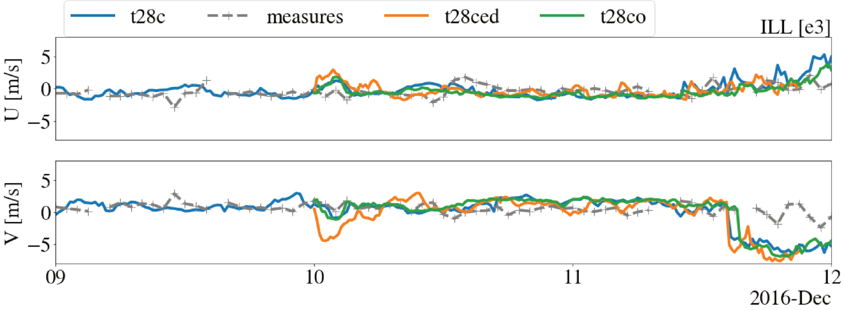

Figure 3.29: Comparison of observed wind at ILL with simulated winds for different configurations.

Two tests were carried out to explore this possibility. The first test uses the same numerical configuration but with the innermost domain increased by about 25 % (`t28ced`), allowing the inclusion of a topographical barrier to the north west of the domain. The second test uses an innermost domain with a horizontal resolution of 200 m meters but significantly larger (`t28co`). These domains are depicted in Figure 3.28. Only minor differences appear between these three configurations when evaluating winds at ILL (see Figure 3.29). Hence the origin of the significant differences is probably not related to the innermost domain size nor to its horizontal resolution.

Representation of the terrain within the innermost domain Whether with maximum slopes of 28 or 42 degrees, the simulations yield very similar results. It is unlikely that a much more accurate topography would resolve the inappropriate wind channeling.

Sensitivity to initial conditions Atmospheric dynamics is known to be sensitive to initial and boundary conditions. However, initializing the model at a later time does not appear to lead to major differences in the flow in the Grenoble Y.

Underestimation of valley flows The possibility for this reverse channeling to be linked with the systematic underestimation of the Grésivaudan valley flow remains the most plausible hypothesis in the author's opinion. A stronger valley wind would imply that the valley is better sheltered from external disturbances. One can think of this sheltering as thermal shielding given that external warmer air masses would encounter more difficulties to mix with a colder valley or dynamical shielding where a stronger valley wind would prevent more external air masses from penetrating into the valley. Figure 3.23 for $\mathcal{E}_3$ seems consistent with this hypothesis. Indeed, around December 11, 2016, a weakening of the Grésivaudan valley flow is observed in the measurements, which could be interpreted as a competition between the valley wind and a synoptic channeling in the opposite direction. It is possible that, as the measured valley wind is stronger, it prevents a reversal of the valley wind.

3.5 Concluding remarks

- The numerical set-up is described in terms of domains characteristics (in section 3.2.1) and choices of physics parametrizations (in section 3.2.6). Particular attention is paid to the initialization of certain variables such as snow cover (see section 3.2.3), land use (see section 3.2.2) and the PM emission inventory (see section 3.2.4).

- A new method to smooth the topography in an optimal way with constraints applied to the slope steepness is introduced. It is first presented from a mathematical point of view in section 3.3.1. Results in terms of slope distribution and terrain heights for the Grenoble Y are discussed in section 3.3.2. In addition to proposing an optimal solution, a fine control of the results can be obtained by adding penalization factors to the cost function. Two different configurations are then compared in terms of simulated dynamics: one with a topography with maximum slopes of 28 degrees and with a first mass point around 13 m AGL and one with maximum slopes of 42 degrees and a first mass point around 17 m AGL. For both configurations, the height of the first mass point is the lowest allowing for numerically stable results. The differences in terrain height between these two topographies can be rather significant, hundreds of meters apart in places. Significant winds or temperature differences are observed locally when the topography is strongly modified. However, it appears that the dynamics at the bottom of the Grenoble Y – which matter for pollutant transport – are not significantly affected. As for temperature, an integrated but tenuous effect is observed. It thus seems that it is the large scales of the topography that dominate the overall dynamics of the Grenoble Y. It also appears that the gain in vertical resolution from one configuration to the other is not enough to improve – or at least to impact– the simulated dynamics. In light of this information, it was decided that the other episodes should be simulated in a `t28c` configuration so as to maximize the vertical resolution.

- The model is evaluated in terms of its ability to reproduce the available measurements (see section 3.4) for the episodes considered (see section 3.1). The simulations demonstrate a good overall agreement with the measurements. For example, the diurnal cycle associated with a persistent down-valley wind, which is stronger at night than during the day, is well captured (see Figures 3.21 and 3.23). It is noted, however, that the intensity of this valley wind is slightly underestimated, especially at 60 and 100 m AGL. Such behavior was observed with a similar set-up for Perdigao (Portugal) in Wagner et al. (2019) without a clear explanation being provided. The most likely hypothesis would be the low or non-resolution of down-slope winds due to the relatively poor vertical resolution. Temperatures are also well represented in the model for $\mathcal{E}_1$, $\mathcal{E}_2$ and $\mathcal{E}_3$, especially at the valley floor and at mid-valley's height (see Figure 3.24). Nonetheless, some systematic differences with the measurements are to be noted. The night-time cooling is underestimated at the valley floor at the end of the night. This could be explained by insufficient down-slope winds. Also, with increasing altitude the simulated diurnal temperature peak is capped and takes the appearance of a step function. Finally, the presence of snow at the valley floor seems to be at the origin of a negative bias between simulated and measured temperatures. It is likely that, despite the efforts made to initialize the snow (see section 3.2.3), errors are still present in the extent or characteristics (height, albedo, water content) of the snowpack.

- For the last days of $\mathcal{E}_1$ and the last half-day of $\mathcal{E}_3$, the simulations show an atmospheric circulation in the Voreppe valley that is opposite to that measured. Several hypotheses are explored to try to understand the origin of this discrepancy in section 3.4.2.2: e.g. the fidelity of the topography; the large-scale flow; the sensitivity to the size and horizontal resolution of the domain and the sensitivity to the initialization date. None of these factors, at least in the ranges explored, can explain the origin of this erroneous wind channeling. The most likely hypothesis remains the underestimation of the valley wind (perhaps linked to the misrepresentation of down-slope winds), which could shelter less the Grenoble Y from an external synoptic disruption.

Chapter 4

Local atmospheric dynamics during Winter Anticyclonic Blocking episodes

In the previous chapter, the methods used for the numerical simulation and the WAB episodes selected for this work were described. The aim of this chapter is to study the local atmospheric dynamics that develop in the Grenoble Y during WAB episodes.

If a CAP develops, it is most often dynamically decoupled from the flow above. For instance Vrhovec (1991) observed a complete decoupling between the CAP dynamics and the synoptic wind aloft in numerical simulations of the Slovenj Gradec valley (Slovenia). The same observation was made for the Grenoble valley at the core of a WAB episode with a marked thermal inversion (Largeron and Staquet, 2016a). In chapter 2, it was shown statistically that, when a temperature inversion sets in, one circulation pattern prevails in the Grenoble Y irrespective of the large-scale wind direction. This also indicates a decoupling of the Grenoble valley atmospheric dynamics in the presence of a CAP. The atmospheric dynamics would then be essentially driven by thermal winds. However Arduini et al. (2020) compared a realistic simulation and a semi idealized simulation of a WAB episode in the Arve valley (French Alps) with a vanishing large-scale wind. They conclude that thermal winds alone do not account for the variability of the CAP due to a coupling between the large-scale wind and a tributary along-valley flow.

The aim of this chapter is to characterize the variations of the within-valley atmospheric circulations observed for the different episodes. Can they be explained by the large-scale conditions? More to the point, can one identify an atmospheric circulation that is characteristic of WAB episodes in terms of pollutant transport in the Grenoble valley?

As a preamble, an analysis of the atmospheric circulation in the Grenoble Y, based on measurements for the entirety of the 2011-2018 winters (WAB and non-WAB episodes), is presented in section 4.1). Then, the episodes selected for this study are compared in terms of atmospheric circulation (see section 4.2.2) and thermal structure (see section 4.2.3). Finally, the impact of fog or low-level stratus on the dynamics of the atmosphere (see section 4.3) is discussed.

4.1 Observed local circulation in the Grenoble Y

This section reports on the atmospheric dynamics observed via the classification of local atmospheric circulations introduced in section 2.4.2. As a reminder, it is assumed here that the Grenoble Y is composed of three branches that channel the wind perfectly and whose measurement stations are therefore representative of the branch behavior. Each branch is either in a state of outflow from the Grenoble basin (noted `+`), inflow towards the Grenoble basin (noted `-`) or neutral (corresponding to wind speeds less than $0.5\,\mathrm{m\,s^{-1}}$). Thus, each triplet of observations (one in each branch) necessarily belongs to one of the 27 atmospheric circulation modes resulting from the combinations of these different states. Moreover a star symbol at a certain position denotes that the corresponding station can experience any of the modes. An illustrative example is included in Figure 4.1. In the following the origin of these local wind circulation patterns is examined: thermal effects, forced channeling or both. The transitions between the different modes are then examined. Finally, the results are synthesized with the view to obtain a typical evolution of the local wind circulations for a winter day.

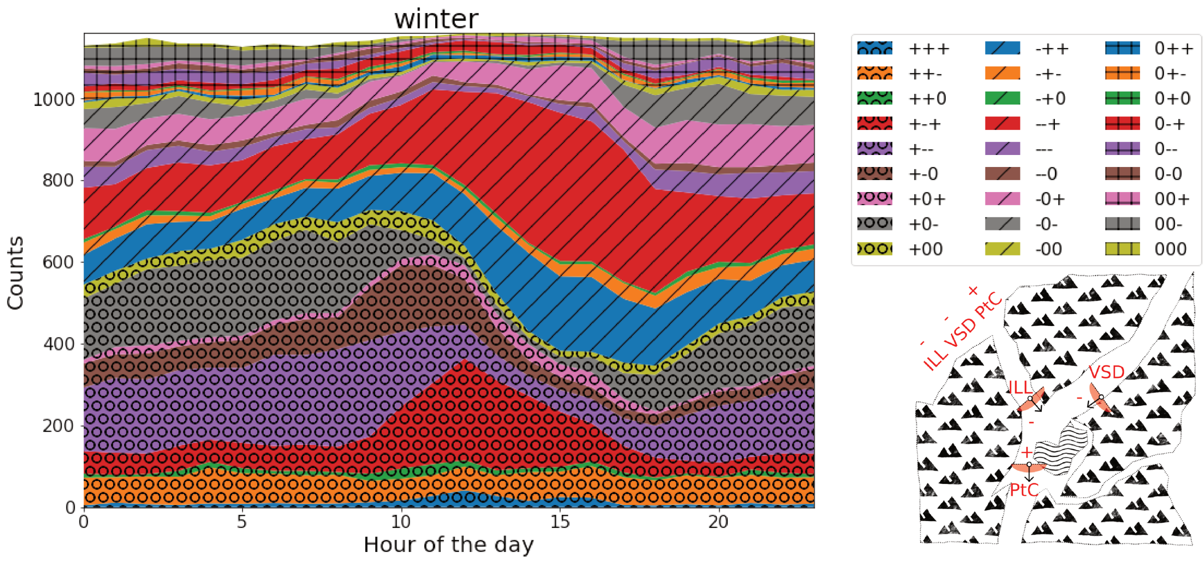

Figure 4.1: Frequency of occurrence of each of the 27 local circulation modes as a function of the hour of day for winters from 2011 to 2018. The bottom right figure recalls the naming conventions for local within-valley atmospheric circulation modes introduced in section 2.4.2.

Diurnal variations It is worth noting that these modes are essentially intraday (indeed, 12 % of the episodes last more than 6 hours; 5 % more than 12 hours and 1 % more than 24 hours). The number of occurrences of each of these modes according to the time of the day (see Figure 4.1) show that there is a very marked daily seasonality. For example, the `+**` modes (flowing away from Grenoble through Voreppe, *marked with circles*) are more frequent at night and in the morning, while the `-**` modes, marked with hatches, are more frequent in the afternoon (as discussed below). Conversely, other modes do not have a daily profile, such as `++-`. Finally, some modes like `--+` or `+-+` seem to have both a diurnal component and a constant (independent of the time of day) component.

Since the large-scale forcing does not exhibit daily seasonality, the constant components ought to result from the passive effects of the topography on the large-scale flow (forced or pressure-driven channeling). Figure 4.2 supports the hypothesis that these modes are (large-scale-)forced modes. As a matter of fact, the modes `++-`,`-0+` and `-++` (which have a marked constant component) are very dependent on the orientation of the large-scale wind.

It seems natural to see the daily seasonality as the signature of the thermal winds (introduced in section 1.1.4.2). For example, one expects to have a prevailing down valley

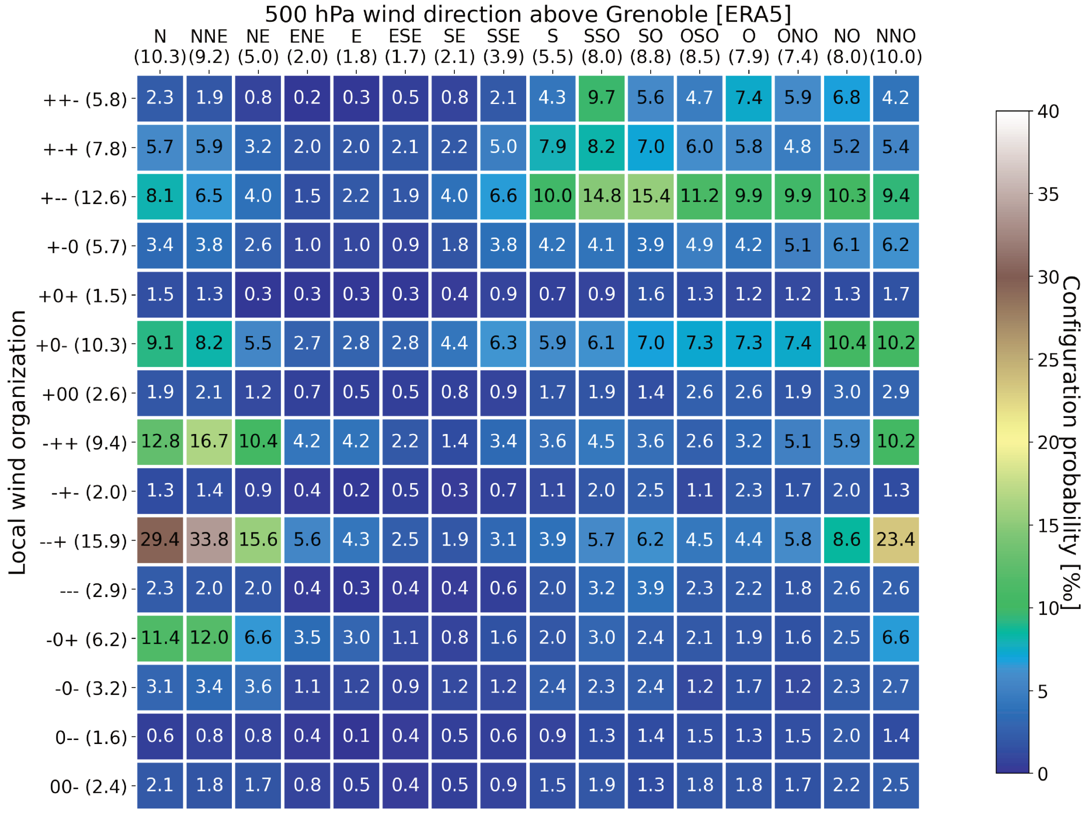

	N (10.3)	NNE (9.2)	NE (5.0)	ENE (2.0)	E (1.8)	ESE (1.7)	SE (2.1)	SSE (3.9)	S (5.5)	SSO (8.0)	SO (8.8)	OSO (8.5)	O (7.9)	ONO (7.4)	NO (8.0)	NNO (10.0)
++- (5.8)	2.3	1.9	0.8	0.2	0.3	0.5	0.8	2.1	4.3	9.7	5.6	4.7	7.4	5.9	6.8	4.2
+-+ (7.8)	5.7	5.9	3.2	2.0	2.0	2.1	2.2	5.0	7.9	8.2	7.0	6.0	5.8	4.8	5.2	5.4
+-- (12.6)	8.1	6.5	4.0	1.5	2.2	1.9	4.0	6.6	10.0	14.8	15.4	11.2	9.9	9.9	10.3	9.4
+-0 (5.7)	3.4	3.8	2.6	1.0	1.0	0.9	1.8	3.8	4.2	4.1	3.9	4.9	4.2	5.1	6.1	6.2
+0+ (1.5)	1.5	1.3	0.3	0.3	0.3	0.3	0.4	0.9	0.7	0.9	1.6	1.3	1.2	1.2	1.3	1.7
+0- (10.3)	9.1	8.2	5.5	2.7	2.8	2.8	4.4	6.3	5.9	6.1	7.0	7.3	7.3	7.4	10.4	10.2
+00 (2.6)	1.9	2.1	1.2	0.7	0.5	0.5	0.8	0.9	1.7	1.9	1.4	2.6	2.6	1.9	3.0	2.9
-++ (9.4)	12.8	16.7	10.4	4.2	4.2	2.2	1.4	3.4	3.6	4.5	3.6	2.6	3.2	5.1	5.9	10.2
-+- (2.0)	1.3	1.4	0.9	0.4	0.2	0.5	0.3	0.7	1.1	2.0	2.5	1.1	2.3	1.7	2.0	1.3
--+ (15.9)	29.4	33.8	15.6	5.6	4.3	2.5	1.9	3.1	3.9	5.7	6.2	4.5	4.4	5.8	8.6	23.4
--- (2.9)	2.3	2.0	2.0	0.4	0.3	0.4	0.4	0.6	2.0	3.2	3.9	2.3	2.2	1.8	2.6	2.6
-0+ (6.2)	11.4	12.0	6.6	3.5	3.0	1.1	0.8	1.6	2.0	3.0	2.4	2.1	1.9	1.6	2.5	6.6
-0- (3.2)	3.1	3.4	3.6	1.1	1.2	0.9	1.2	1.2	2.4	2.3	2.4	1.2	1.7	1.2	2.3	2.7
0-- (1.6)	0.6	0.8	0.8	0.4	0.1	0.4	0.5	0.6	0.9	1.3	1.4	1.5	1.3	1.5	2.0	1.4
00- (2.4)	2.1	1.8	1.7	0.8	0.5	0.4	0.5	0.9	1.5	1.9	1.3	1.8	1.8	1.7	2.2	2.5

Figure 4.2: Probability of occurrence (in ‰) of each combination of of the main local circulation modes (that occur more than 1.5 % of the winter) as a function of the large-scale wind orientation above Grenoble for winters from 2011 to 2018. The numbers in parentheses represent the proportion of occurrence (in %) of a local atmospheric circulation pattern or large-scale wind direction during the winters considered.

wind at night. This configuration corresponds to the `+--`, mode which indeed presents a strong seasonality with a frequency of occurrence greater at night (from 8 pm to 8 am). On the other hand, in the afternoon, winds moving up the valleys are expected, which corresponds to the `-++` mode. This mode has indeed an higher frequency of occurrence in the afternoon. However the preferred mode is `--+`.

Transitions between the different modes Since many modes exhibit daily seasonality that does not appear to be perfectly in phase, it is interesting to understand how the modes interoperate with each other. To do this, one method is to treat this mode sequence as arising from a Markov process with 27 states. Recall that the Markov property holds if the probability of future states depends only on the present state (i.e. independent of past states). One can then determine (from the time series) a transition matrix which represents the probability at each time step of going from one mode to another (see Figure 4.3). It is important to note that the transition probabilities are calculated as being constant over time, which is not the case as evidenced by Figure 4.1. These transition probabilities can therefore only be used qualitatively. In particular, one should not try to calculate the average consecutive time spent in a mode as it could be done for a Markov process with constant transitions. Figure 4.3 shows two distinct blocks: the `+**` block and the `-**` block. Only a few modes have a non-weak probability of transitioning from the `+**` to the `-**` and vice versa. As this is somewhat tedious to interpret in this form, the next paragraph along with Figure 4.4 attempt to summarize the essential features exhibited by Figures 4.1 and 4.3.

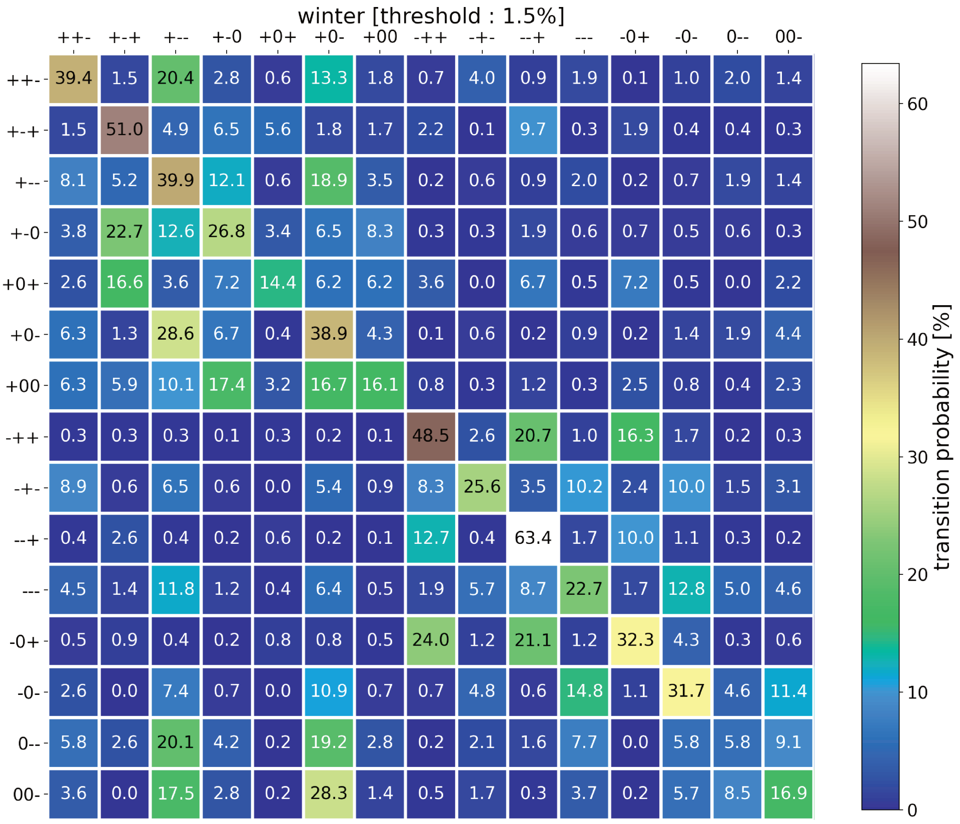

	++-	+-+	+--	+-0	+0+	+0-	+00	-++	-+-	--+	---	-0+	-0-	0--	00-
++-	39.4	1.5	20.4	2.8	0.6	13.3	1.8	0.7	4.0	0.9	1.9	0.1	1.0	2.0	1.4
+-+	1.5	51.0	4.9	6.5	5.6	1.8	1.7	2.2	0.1	9.7	0.3	1.9	0.4	0.4	0.3
+--	8.1	5.2	39.9	12.1	0.6	18.9	3.5	0.2	0.6	0.9	2.0	0.2	0.7	1.9	1.4
+-0	3.8	22.7	12.6	26.8	3.4	6.5	8.3	0.3	0.3	1.9	0.6	0.7	0.5	0.6	0.3
+0+	2.6	16.6	3.6	7.2	14.4	6.2	6.2	3.6	0.0	6.7	0.5	7.2	0.5	0.0	2.2
+0-	6.3	1.3	28.6	6.7	0.4	38.9	4.3	0.1	0.6	0.2	0.9	0.2	1.4	1.9	4.4
+00	6.3	5.9	10.1	17.4	3.2	16.7	16.1	0.8	0.3	1.2	0.3	2.5	0.8	0.4	2.3
-++	0.3	0.3	0.3	0.1	0.3	0.2	0.1	48.5	2.6	20.7	1.0	16.3	1.7	0.2	0.3
-+-	8.9	0.6	6.5	0.6	0.0	5.4	0.9	8.3	25.6	3.5	10.2	2.4	10.0	1.5	3.1
--+	0.4	2.6	0.4	0.2	0.6	0.2	0.1	12.7	0.4	63.4	1.7	10.0	1.1	0.3	0.2
---	4.5	1.4	11.8	1.2	0.4	6.4	0.5	1.9	5.7	8.7	22.7	1.7	12.8	5.0	4.6
-0+	0.5	0.9	0.4	0.2	0.8	0.8	0.5	24.0	1.2	21.1	1.2	32.3	4.3	0.3	0.6
-0-	2.6	0.0	7.4	0.7	0.0	10.9	0.7	0.7	4.8	0.6	14.8	1.1	31.7	4.6	11.4
0--	5.8	2.6	20.1	4.2	0.2	19.2	2.8	0.2	2.1	1.6	7.7	0.0	5.8	5.8	9.1
00-	3.6	0.0	17.5	2.8	0.2	28.3	1.4	0.5	1.7	0.3	3.7	0.2	5.7	8.5	16.9

Figure 4.3: Transition matrix of dominant wind modes (whose proportion over the period considered is at least 3 %) for winters from 2011 to 2018. The element (i, j) represent the averaged probability to transition from mode i to mode j at the next time-step (hour).

Summary: a typical diurnal cycle during wintertime can be determined based on local wind modes Except for particular large-scale forcing, from 8 pm to 8 am, the `+--` and `+0-` modes dominate. These two modes switch from one to the other and seem to be concomitant. This corresponds to down-valley winds, which may be intermittent or close to the detection threshold in the Grésivaudan valley. When the synoptic wind comes from the southwest, west or northwest, these modes can be forced into the `++-` mode. Around mid-day, the down-valley wind in the southern branch fades (`+-0`) and then reverses (`+-+`). It is quite possible that the southern branch of the Grenoble Y, due to its steeper slopes and the fact that it is less well defined, has a signature closer to that of a slope-wind than a valley-wind. This could explain why the wind direction reverses there before it does in the Voreppe and Grésivaudan valleys.

In the middle of the afternoon, around 3 pm, the `--+` and `-++` modes dominate. The valley wind is now also up-valley in the Voreppe valley. Surprisingly, the mode where the valley flow remains down-valley in the Grésivaudan (`--+`) dominates the mode corresponding to the up-valley winds (`-++`). This is not completely abnormal given that some valleys are known to have very different intensities of up- and down-valley winds. For instance the Kali Gandaki valley in Nepal exhibits up-valley winds that are stronger than down-valley winds (Egger et al., 2000, 2002). In addition, down-valley winds are often more intense than their counterparts when the valley opens onto a plain (Zardi and Whiteman, 2013), which is the case here. It is also possible that one mode is more likely than the other depending on the large-scale meteorological conditions. However, according to Figure 4.2, the synoptic wind direction does not seem to favour the development of one mode over the other. Finally, it is also possible that this is related to a topographical feature of the Grenoble Y, which would be very interesting to understand. To support

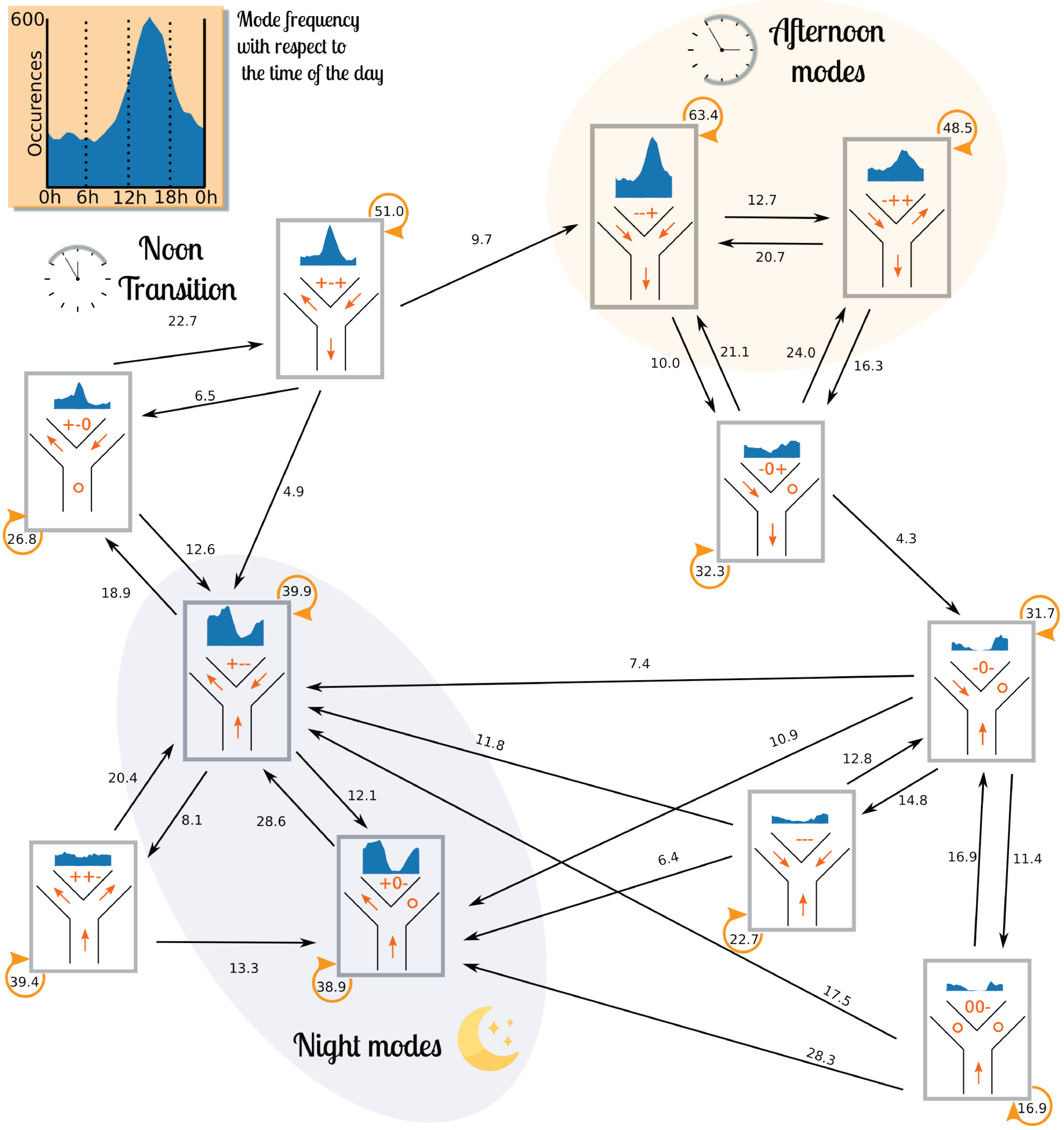

Figure 4.4: Schematic representation of the connections between the different wind circulation modes in the Grenoble valley. The numbers indicate the probability (averaged over the 24 hours) of transition from one hour to the next. A black arrow for a transition to another state, and an orange arrow when the state does not change. For the sake of clarity, not all states and transitions are shown, but only those that appear to be most important. In particular many transition states are left out. The PDF in blue represents the likelihood of a state given a certain time, as indicated on the gray sub-scheme at the top left. They correspond to the individual components of Figure 4.1.

this hypothesis, the `--+` mode is also largely dominant in summer and in the middle of the afternoon (see Figure A.7 shown in appendix).

The transition from day modes to night modes is not as well marked as its night to day counterpart. One option, although rather unlikely, is to pass through the `-0+` mode to join the `-0-`, `---` and `00-` modes. The remainder of the transitions reside in the 12 modes that do not meet the minimum representation threshold and can be assumed as essentially transient.

In summary, the main modes observed are intraday and mostly associated with a specific period of the day, indicating that they are essentially driven by thermal effects. By putting together their preferred transitions and their preferred periods of occurrence, it is possible to reconstruct a complete diurnal cycle (see Figure 4.4). This succession of local wind circulation patterns appears to be the general footprint of thermal effects in the Y-shape Grenoble valley during the winter period.

4.2 Similarities and differences between the episodes

The objective of this section is to determine whether the atmospheric circulation identified as representative of WAB episodes in the Grenoble Y in the previous section is reflected in the numerical simulations of the episodes considered. To do so, an inter-comparison of the atmospheric dynamics obtained for the four episodes selected is carried out. These episodes are first compared with respect to their dynamics at the very near surface in section 4.2.1. The vertical structure of the winds is considered in section 4.2.2 and of the temperature field is considered in section 4.2.3.

4.2.1 Near-surface flows

Since a strong impact of thermal effects is expected, the comparison is first carried out for nighttime (between 5pm and 8am, see Figure 4.5) and daytime (the rest of the day, see Figure 4.5) separately.

4.2.1.1 Night time

Figure 4.5 shows the simulated winds at 20 m AGL averaged over nighttime for the four episodes. These episodes share many characteristics, the most notable common feature being the systematic presence of a valley wind coming down the Grésivaudan valley and engulfing the Voreppe valley. This down-valley wind then forms a valley exit jet, enhanced by a topographic constriction, which is discussed in more detail in section 4.2.1.3. For the present configuration, another topographic element forces this jet to curl into the valley leading to Valence, thus forming a recirculation zone immediately downstream of the Voreppe valley.

For each episode, the Grésivaudan down-valley flow is accompanied by a gentle down-valley flow from the southern branch towards the Grenoble basin. As for the Romanche valley, it does not seem to be associated with a down-valley wind, at least at this altitude. This observation is not so surprising, as pointed out by another study of the Grenoble Y (Largeron, 2010). The Romanche valley is the steepest among the prevailing valleys in the system: it connects – within the innermost domain – the Bourg d'Oisans plateau (720 m ASL) to the Grenoble basin ($\approx$ 200 m ASL). (Largeron, 2010) showed that, at the core of a very marked anticyclonic inversion episode in 2006, the Romanche valley wind could be less cold than the Grenoble basin CAP and so detrain at its level of neutral

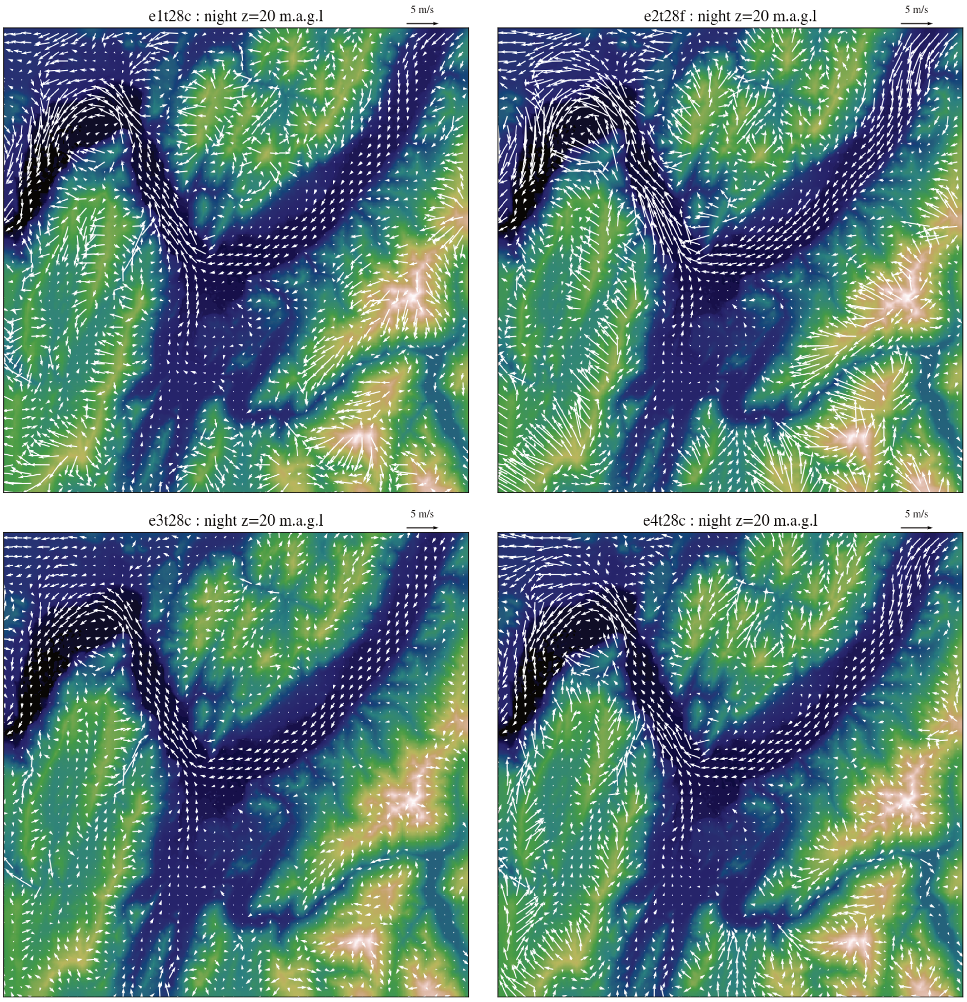

Figure 4.5: Wind vectors at 20 m AGL, averaged over nighttime, in the innermost domain for the 4 episodes considered.

buoyancy, about 800 m ASL. The relative contributions of the different valleys in terms of volume flow rates in the Grenoble basin are examined in further detail in section 4.2.1.4.

Within the massifs, the winds tend to blow down the slopes of the highest topographical features. However, it is difficult to observe an imprint of down-slope winds on the lower slopes of the mountain flanks (see for example the Belledonne flank). This is perhaps due to the fact that the vertical resolution is insufficient to capture properly the down-slope winds.

4.2.1.2 Day time

Figure 4.6 shows the simulated winds at 20 m AGL averaged over the daytime period for the four episodes. The most remarkable feature is that in each episode, one observes a down-valley wind in the Voreppe valley that persists on average during the day. This simulated feature is in agreement with the available observations shown in Figure 3.21. This indicates that, when a temperature inversion is present, the diurnal change of direction of the valley wind – generally observed over the winter (see Figure 4.4) – does not happen. This observation is also observed statistically from measurements available for winters from 2011 to 2018 in Figure 2.18.

A constant down-valley flow has already been observed elsewhere, for example in the Inn Valley in Austria (Emeis et al., 2007). It was accounted for by the presence of

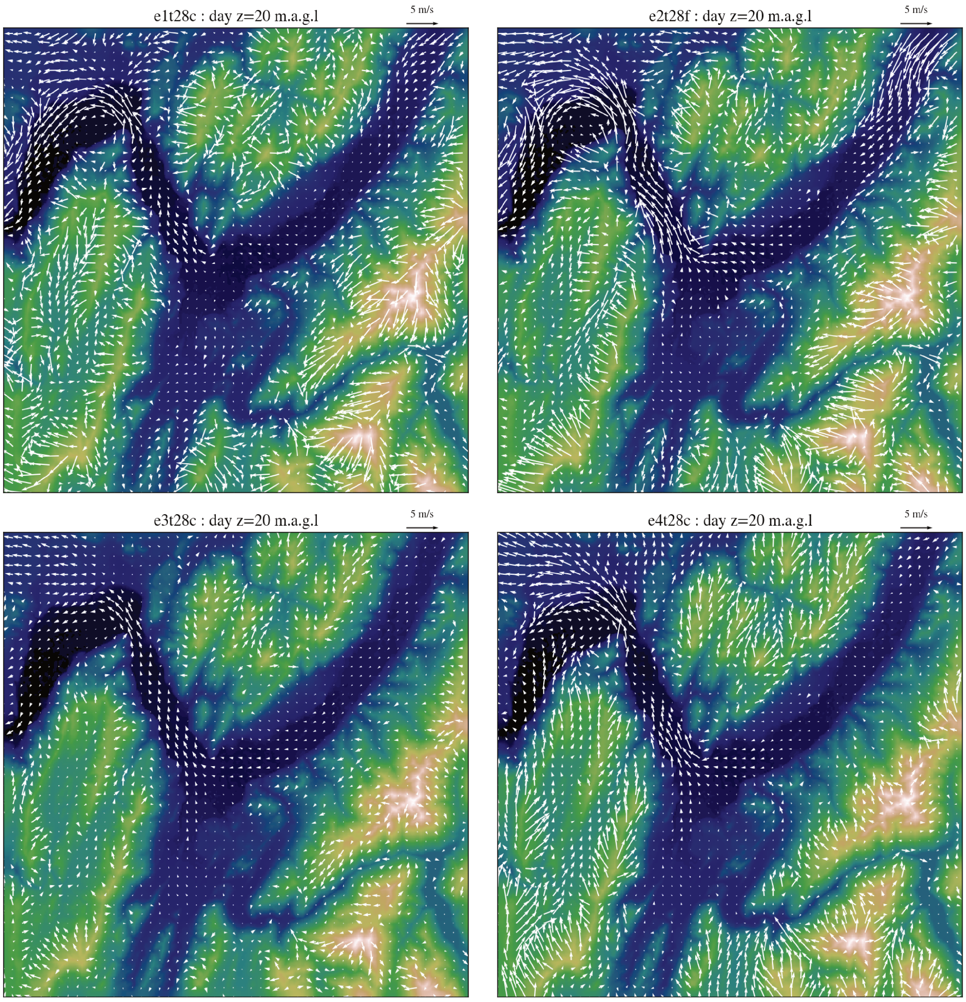

Figure 4.6: Wind vectors at 20 m AGL, averaged over daytime, in the innermost domain for the 4 episodes considered.

snow on the flanks of the valley, which, through a greater albedo, strongly decreases the radiative heating of the ground and thus the establishment of up-slope winds. In the case of Grenoble, this explanation does not seem to be sufficient. Indeed, the mountains are covered with snow for most of the winter and the up-valley winds in the afternoon are statistically present during the whole winter (see Figure 4.4) except when thermal inversions set up (see Figure 2.18). The persistence of the CAP very likely counteract the establishment of these up-valley winds by maintaining a higher pressure in the valley than in the adjacent plain.

In contrast to the Voreppe valley, the Grésivaudan down-valley flow fades away without being replaced by a prevailing well-defined atmospheric circulation. The episodes also share a valley exit jet at Voreppe's exit and an up-valley wind in the Romanche valley, where it opens onto the Bourg d'Oisans plateau.

4.2.1.3 Characterization of the valley exit jet

Valley exit jets are common features in complex terrain. For example it has been simulated by Zängl (2004) at the Inn's valley exit in Austria or observed in the Adige valley in Italy (Zardi et al., 2021). Figure 4.8 displays the average horizontal flow velocity over $\mathcal{E}_1$ for a vertical cross-section defined along the axis of the Voreppe valley (see `vrp_par`; Figure 4.7). The valley exit jet reaches a maximum intensity of about 5 m s^{-1} between 250 m ASL (near ground level) and 500 m ASL. It can also be seen that the valley exit jet detaches from the valley floor downstream of a local depression of the valley floor. This explains the slight decrease of the valley wind intensity at 20 m AGL observed for each episode in this part of the Voreppe valley (see Figures 4.5 and 4.6). Figure 4.8 shows a snapshot of the same vertical cross-section on 8 December 2013 at 10 pm. A very stably stratified layer can be observed downstream of the depression, which prevents any penetration of the valley wind in this area and forces the wind to detach. This valley exit jet is observed, with similar characteristics, in all the episodes considered. It should be noted, however, that it is weaker for $\mathcal{E}_3$, an episode for which the atmospheric circulation at the valley scale is less marked as discussed in section 4.2.2.

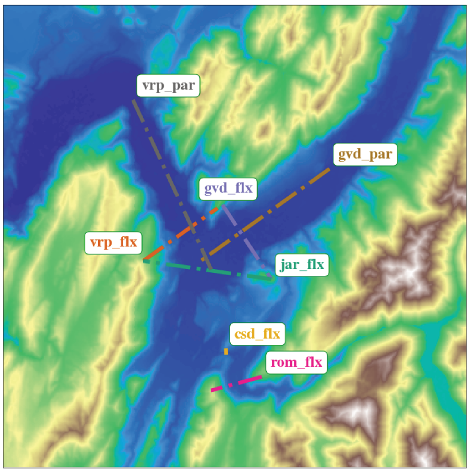

Figure 4.7: **(a)**

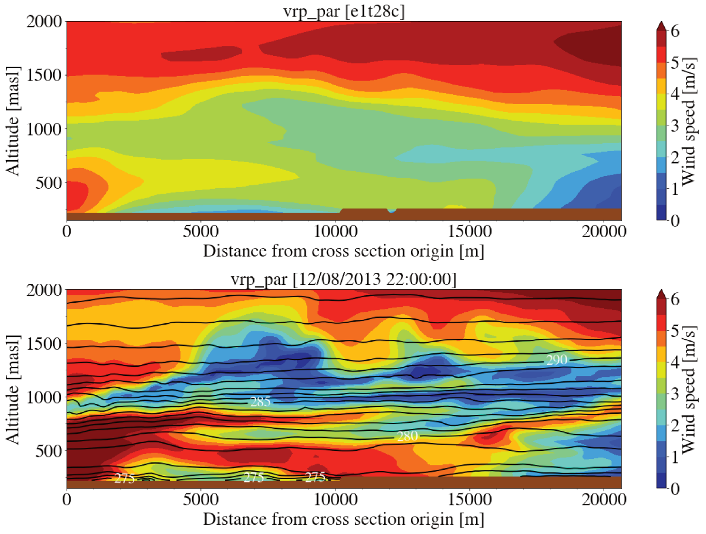

Figure 4.8: (**b**)

(a) Location of the vertical cross-sections used for the analysis of atmospheric dynamics. **(b)** Time-averaged wind speed over $\mathcal{E}_1$ (top figure) along with a snapshot at 10 pm on December 8, 2013 (bottom figure) for the Voreppe valley cross-section (`vrp_par`). The greater is the distance from the origin, the closer is the Grenoble basin. The snapshot also depicts iso-contours of potential temperarure with one level per K.

4.2.1.4 Near-ground interactions among the different valleys of the Grenoble Y

In the previous sections it has been shown that, close to the surface, a characteristic atmospheric circulation dominates both during the day and at night. This section aims at characterizing the interactions between the different branches of the valley system.

To do so, flows through different vertical cross-sections, all defined in Figure 4.7, are analyzed. Three of these cross-sections (`jar_flx`, `vrp_flx` and `gvd_flx`) form a control volume around the Grenoble basin and allow to perform a mass budget of the exchanges between the different branches of the Grenoble Y. Two additional vertical cross-sections are used to characterize the impact of the Romanche valley on the atmospheric circulation near the ground in the Grenoble basin. The first one, `rom_flx`, is located at the bottom of the Romanche valley, when it is at its widest and reaches an altitude close to that of the Grenoble basin. A second one, `csd_flx`, is located at the exit of a very narrow constriction, which separates the opening of the Romanche valley from the southern branch of the Grenoble Y. Figure 4.9 shows the temporal evolution of the volume flow rates associated with the Grenoble basin and Table 4.1 summarizes volume flow rates time-averaged over the different episodes. Note that, since the density of the air varies only little in the first 200 meters above the ground level, the volume flow rates are almost proportional to the mass flux.

	`e1t28c`	`e2t28f`	`e3t28c`	`e4t28c`
`vrp_flx`	1.49 (1.57)	2.0 (2.5)	0.71 (0.94)	1.25 (1.61)
`gvd_flx`	-0.62 (0.71)	-1.3 (1.55)	-0.27 (0.62)	-0.61 (0.98)
`jar_flx`	-0.59 (0.68)	-0.2 (0.61)	-0.34 (0.56)	-0.36 (0.5)
`rom_flx`	0.01 (0.02)	0.0 (0.03)	0.01 (0.02)	0.01 (0.02)
`csd_flx`	-0.02 (0.02)	-0.01 (0.02)	-0.01 (0.02)	-0.01 (0.02)

Table 4.1: Average (absolute) volume flow rate in $1 \times 10^2\,\mathrm{m^3\,s^{-1}}$ through the cross-sections defined in Figure 4.7 and computed up to 400 m ASL.

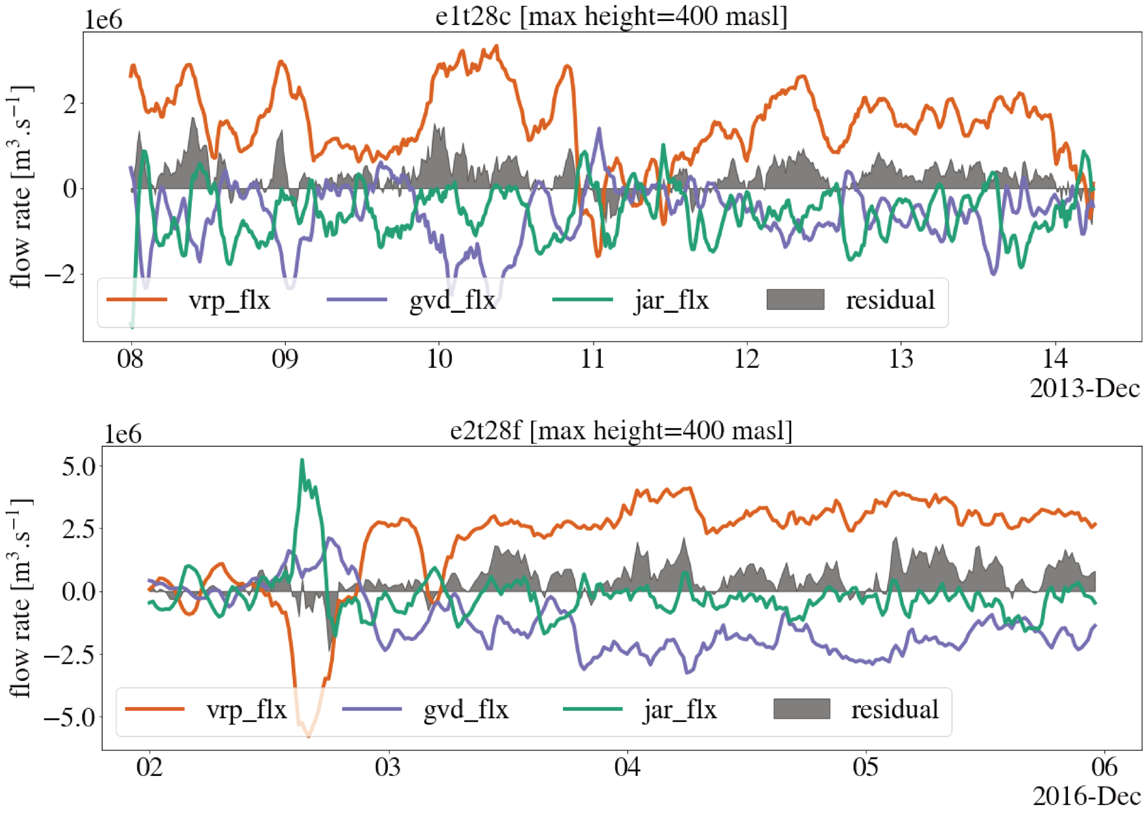

Figure 4.9: Volume flow rates through cross sections (whose locations are depicted in Figure 4.7) from the ground up to 400 m ASL for $\mathcal{E}_1$ (top) and $\mathcal{E}_2$ (bottom). A positive flow rate characterizes an outflow from the Grenoble basin. Residuals of the budget are colored in black.

Table 4.1 confirms that, up to 400 m AGL, the exchanges between the Grenoble Y and the Romanche valley are negligible. Indeed time-averaged volume flow-rates between the Romanche valley and the southern branch are one to two orders of magnitude smaller than the ones between the three branches of the Grenoble Y and the Grenoble basin. Figure 4.9 confirms that the Grésivaudan valley and the southern branch act as sources for the Grenoble basin (being associated with negative flow rates). The intensity of these sources is either comparable ($\mathcal{E}_1$, $\mathcal{E}_3$) or with a strong prevalence of the Grésivaudan valley ($\mathcal{E}_2$, $\mathcal{E}_4$). For most of the time the outflow is down the Voreppe valley and hence the flow rates associated with the Grésivaudan valley and the southern branch are opposite in phase.

4.2.2 Vertical structure of the winds

Figures 4.10 and 4.11 present vertical profiles of wind speed and direction averaged over the Voreppe and Grésivaudan valleys for the four episodes considered (see Figure 3.8 for the spatial extent used for averaging). The sheltering effect from the surrounding massifs is distinctly observed (e.g. Vosper and Brown, 2008). Indeed, there is a sharp transition in wind direction for all the episodes (except for $\mathcal{E}_3$ in the Grésivaudan) around 1000 m AGL, which corresponds to the average height of the Vercors and Chartreuse (1250 m ASL). In the case of a perfect decoupling of the dynamics in the valley from the large-scale conditions, a single pattern corresponding to thermal winds would dominate under 1000 m AGL irrespective of the winds aloft. One indeed observe a dominant pattern for the four episodes with an east-southeast wind (purple color in the figures) below 1000 m AGL for the Voreppe valley and a northeast (orange color in the figures) wind for the Grésivaudan valley. This dominant pattern corresponds to the down-valley wind continuously observed just above the ground in the previous section. In the Voreppe valley, a slight change in direction around 500 m AGL corresponds to a slightly different channeling of the wind in the higher section of the valley due to its gradual widening. Overall this down-valley wind does not appear to be sensitive the large-scale wind direction.

Seen from this perspective, there is a marked decoupling between the dynamics that are taking place within the valley and the large-scale wind. But the picture is not so simple. For example, on 11 December 2013 the synoptic wind strengthens. This forces the passage of an air mass from the plain towards the Grésivaudan valley through the Voreppe valley and Grenoble, which suppresses the down-valley wind despite a well-established thermal inversion. For 2 December 2016, the large-scale wind blows from the north as for 8 and 9 December 2013. However in this case the channeled large-scale wind eventually dominates the Voreppe valley wind over the entire height of the valley and is channeled through the lower layers of the Grésivaudan valley, despite the stable stratification in place.

Finally, $\mathcal{E}_3$ (7-11 December 2016) does not show such a well-defined vertical structure in terms of wind direction as the other episodes do. For the Voreppe valley the direction is still mostly that of the down-valley wind. However one can hardly speak of a prevailing down-valley wind in the Grésivaudan valley. This is because the winds are weak or even null within the Grenoble Y. Yet it is rather surprising that the down-valley flow fails to develop properly over the valley's height as the large-scale winds are weak and the stratification is strong and constant.

To sum up, even if a dynamical decoupling is observed between the valley flow and the flow above, this decoupling is far from complete. Depending on the direction and strength of the large-scale wind, the thermally driven atmospheric circulation in the valley may be impacted. The fact that Grenoble is located in the pre-Alps might play a role in the partial decoupling observed. Indeed, Grenoble is only separated from the Rhône plain by the Vercors or the Chartreuse. Moreover, the topography of the Voreppe valley is conducive to the channeling of winds blowing from south-west to north (which are among common large-scale wind direction) towards Grenoble. Hence, the shielding effect, crucial for decoupling, is probably weaker in Grenoble than what it would be in another valley located in the middle of a mountain range.

4.2.3 Atmospheric stability

The vertical structure of the atmospheric stability for the different episodes is compared in Figure 4.12. $\mathcal{E}_1$ until 13 December 2013 and $\mathcal{E}_3$ display inversion heights between 1000 and 1400 m ASL (800 and 1200 m AGL). These results are consistent with those from numerical simulations by Largeron (2010) for Grenoble during a WAB episode with a

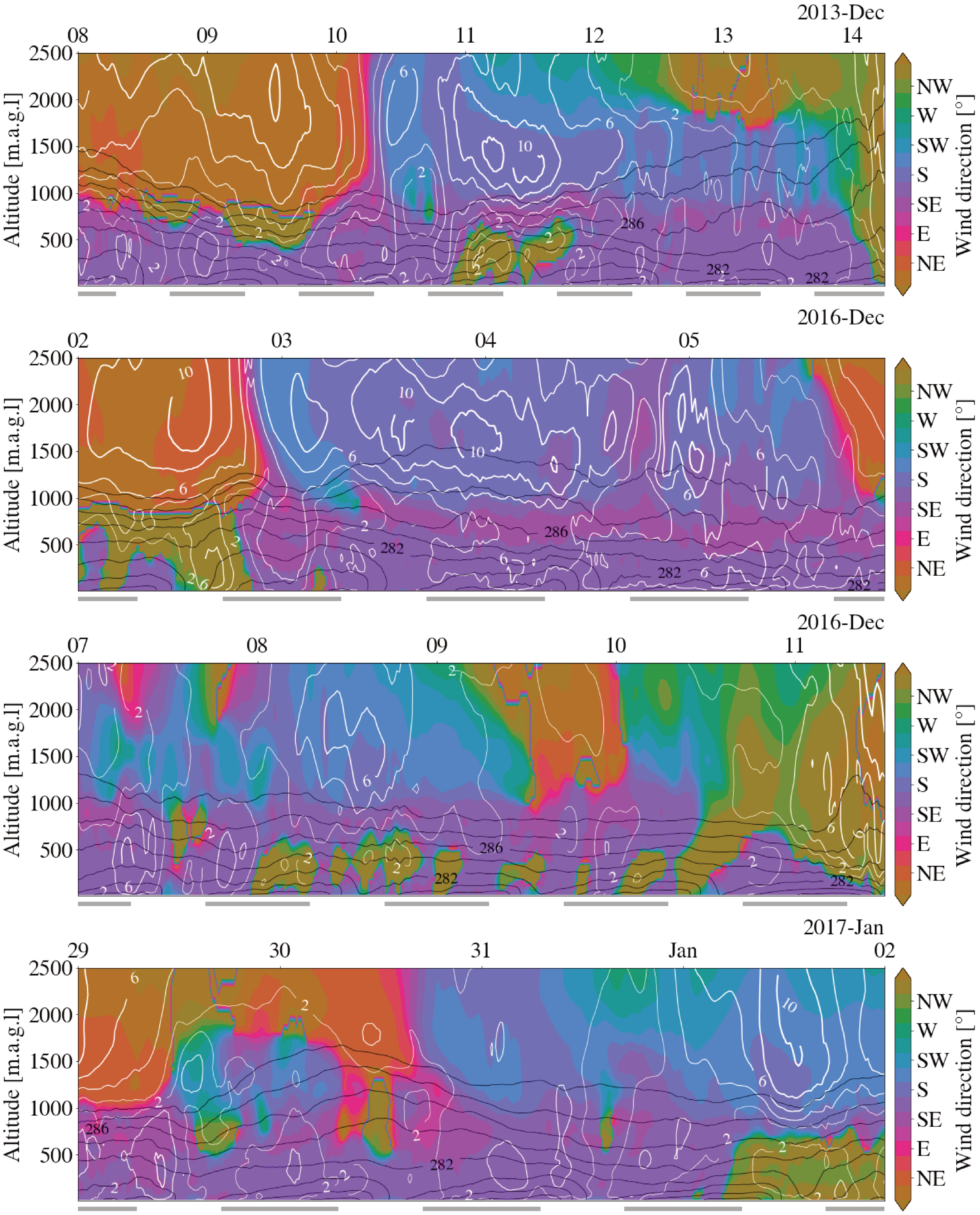

Figure 4.10: Vertical profiles averaged over the Voreppe valley (see Figure 3.8) for $\mathcal{E}_1$, $\mathcal{E}_2$, $\mathcal{E}_3$ and $\mathcal{E}_4$ from top to bottom respectively. Color shading represents wind direction. White contours show the horizontal wind speed, with one line every $2\,\mathrm{m\,s^{-1}}$ from $2\,\mathrm{m\,s^{-1}}$ to $14\,\mathrm{m\,s^{-1}}$. Black contours represent the potential temperature with intervals of $2\,\mathrm{K}$.

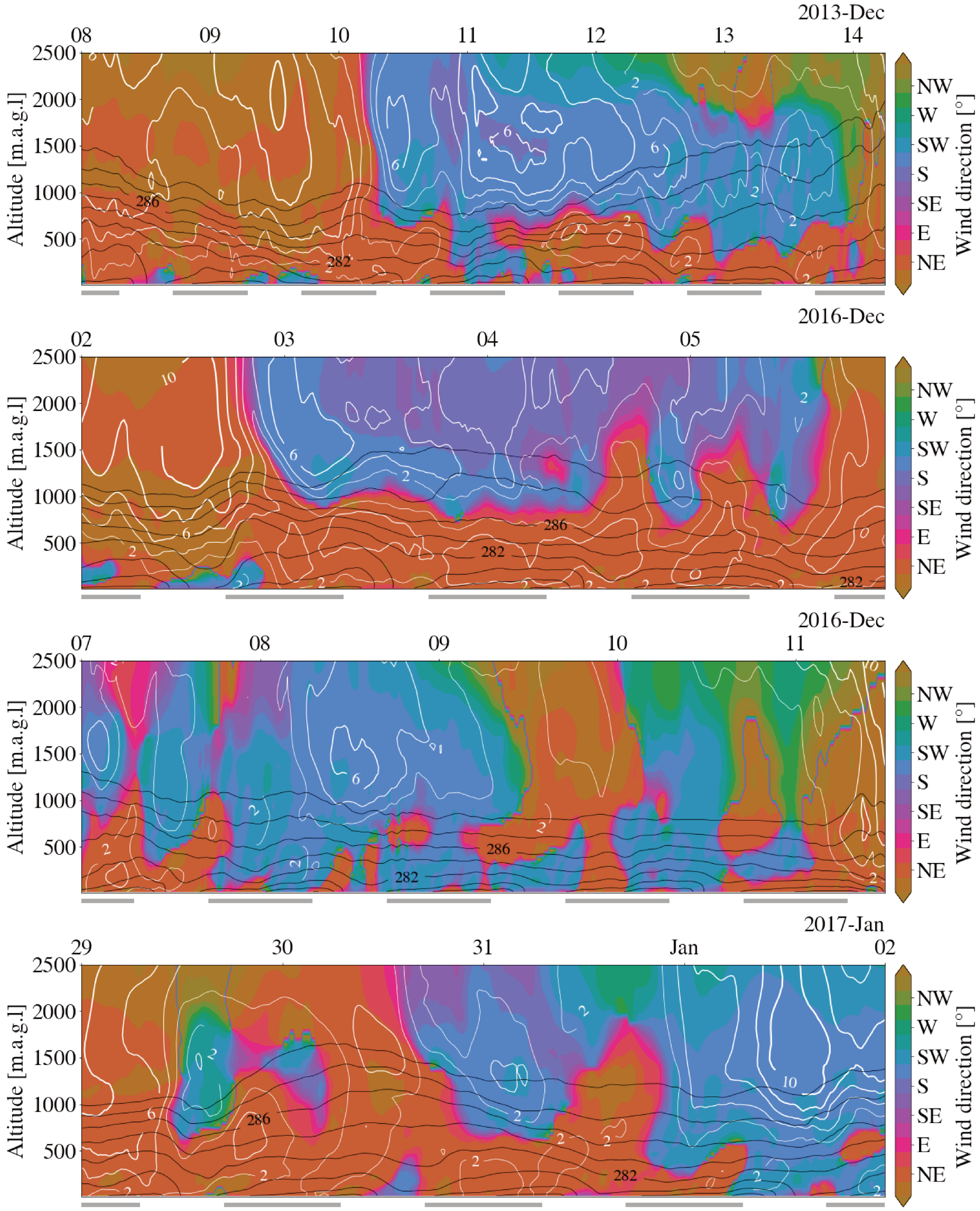

Figure 4.11: Vertical profiles averaged over the Grésivaudan valley (see Figure 3.8) for $\mathcal{E}_1$, $\mathcal{E}_2$, $\mathcal{E}_3$ and $\mathcal{E}_4$ from top to bottom respectively. Color shading represents wind direction. White contours show the horizontal wind speed, with one line every $2\,\mathrm{m\,s^{-1}}$ from $2\,\mathrm{m\,s^{-1}}$ to $14\,\mathrm{m\,s^{-1}}$. Black contours represent the potential temperature with intervals of $2\,\mathrm{K}$.

strong thermal inversion in 2006, when, an inversion height varying between 1200 and 1400 m ASL developed over a period of 48 hours. This is also consistent with Whiteman's conjecture associating the inversion height with the mean height of the surrounding relief, which is about 1250 m ASL for the Vercors and Chartreuse massifs.

In contrast $\mathcal{E}_2$, from the 3rd of December 2016, has a constant thermal inversion with a top at around 800 m ASL. This difference probably lies in the choice of this episode. Indeed, one notes that the inversion layer is almost completely eroded on December 3rd at noon, which corresponds to the minimum temperature difference observed between the upper and lower stations in the valley (see Figure 3.3).

The thermal structure for $\mathcal{E}_4$, for which the inversion strength is also moderate, is fragmented. A first inversion is eroded around 29 December 2016 and then warm air above subsides almost to the ground and inhibits midday convection on 31 December 2016. This allows an inversion to develop over the height of the valley the following night.

Figure 4.12 also shows the temporal evolution of the valley heat deficit H and the inversion height. The latter is computed as the highest height – up to 1500 m AGL, i.e. in the high range of observed inversion heights – with a vertical gradient of potential temperature greater than the dry adiabatic gradient ($\frac{\partial\theta}{\partial z} > 9.8\,\mathrm{K\,km^{-1}}$). The heat deficit is a metric first introduced by Whiteman et al. (1999). It is calculated from equation 4.1 where z and h_0 are the integration height and ground height, respectively. As for the inversion heights, the integration height z is chosen to be 1500 m AGL.

$$H(z) = c_p \int_{h_0}^{z} \rho(z')\,[\theta(z) - \theta(z')]\,dz' \tag{4.1}$$

Let us consider a column of air with a unit surface area, for which the vertical profile of potential temperature between the ground h_0 and a certain height z is known. The heat deficit is the amount of energy that would have to be injected into this air column to restore a dry adiabatic gradient over its entire height, namely to fully mix the air column. It is considered as a bulk measure of atmospheric stability and regularly used in CAP studies (Silcox et al., 2011; Chemel et al., 2016; Largeron and Staquet, 2016b). Interestingly such studies include, for example, strong correlations between heat deficit and PM concentrations. For example, Chemel et al. (2016) obtains an $r^2 \approx 0.7$ between daily PM_{10} concentrations and H in Passy (another French Alpine valley) for an observation period from 10 January to 28 February 2015.

According to Figure 4.12, high correlations ($0.68 < r < 0.95$) are obtained between the temporal variation of the inversion layer height and that of the heat deficit. Although the heat deficit is not explicitly calculated, Figure 3 of Lareau et al. (2013) – reproduced in this manuscript for simplicity in Figure A.8 – visually lead to similar conclusions.

To summarize, at the core of a marked thermal inversion episode, the inversion height is of the order of 1000 to 1400 m ASL. This height is consistent with i) the simulations carried out by Largeron for the winter of 2006-2007 in the Grenoble Y and ii) the Whiteman conjecture based on the average height of the surrounding massifs (1250 m ASL). However, the structure of the thermal inversion is sensitive to many factors such as the direction and speed of the large-scale wind. The large-scale wind can either erode the thermal inversion by mechanical shear at the inversion height or force the channeling of a wind into the valley (sometimes down to the ground) and disrupt the existing stratification. According to these simulations, the temperature inversion height is likely to be linked to the CAP intensity (through the heat deficit H) whilst being bounded by the mean height of the surrounding topography (following Whiteman's conjecture).

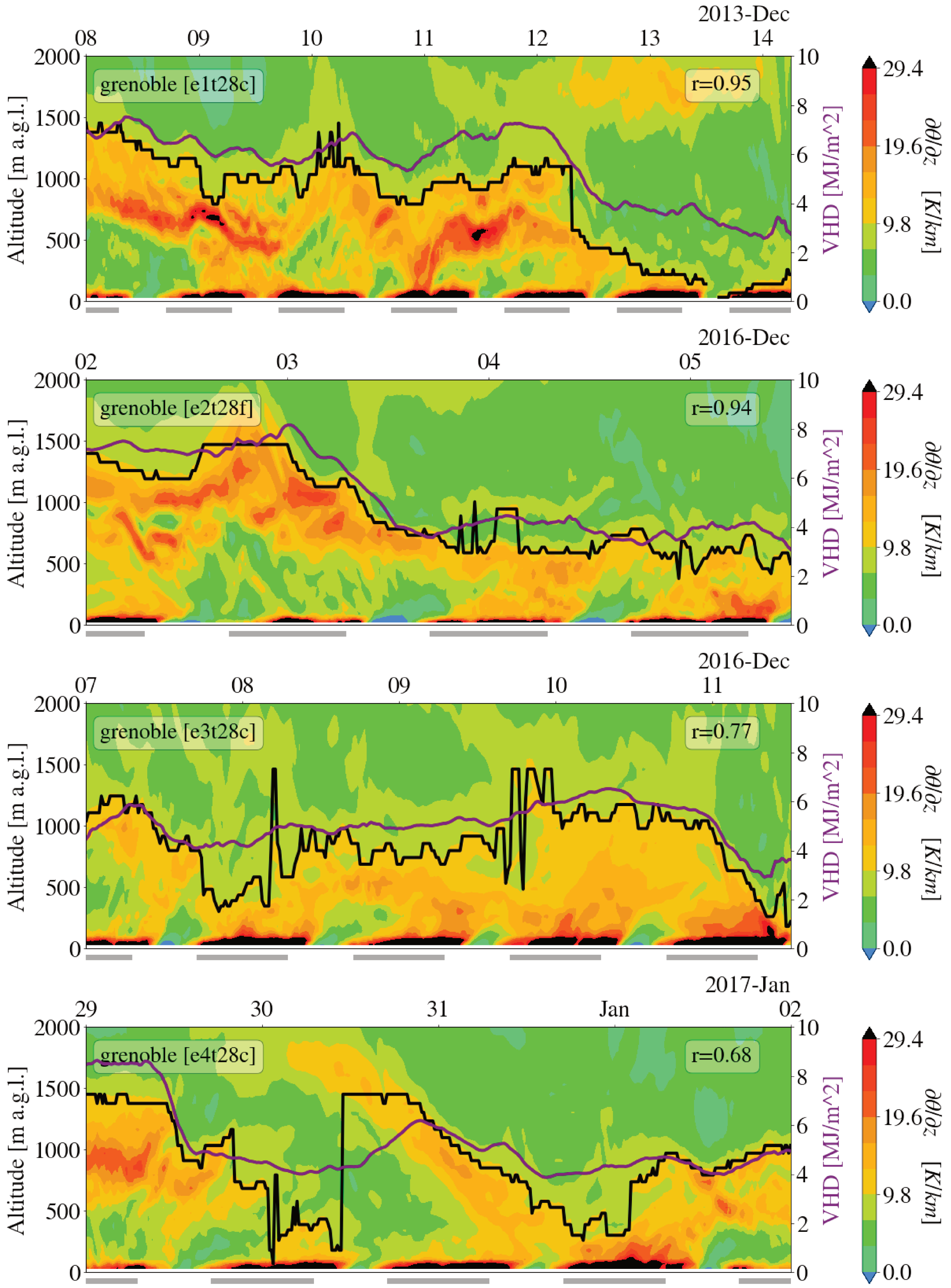

Figure 4.12: Vertical gradient of θ, averaged over Grenoble (see Figure 3.8), for episodes $\mathcal{E}_1$, $\mathcal{E}_2$, $\mathcal{E}_3$ and $\mathcal{E}_4$. The inversion height (solid black line) corresponds to the highest value in altitude from the ground up to 1500 m AGL where $\frac{\partial\theta}{\partial z} > 9.8\,\mathrm{K\,km^{-1}}$. The heat deficit H (purple dotted curve, on the right-hand side) is calculated for Grenoble from the ground up to 1500 m AGL. The coefficient r (reported on the top-right corner of each figure) correspond to the correlation between the inversion height and H.

4.3 About low level stratus formation

Most of the studies in the literature focus on CAP occurring under clear sky conditions. However, CAP can form under the presence of persistent fog or low-level stratus. Clouds impact the dynamics of the ABL, particularly through the diurnal cycle (Whiteman et al., 2001; Zhong et al., 2001). They drastically reduce the diurnal warming of the surface by reducing the amount of shortwave radiation that reaches it. Hence the presence of stratus can allow a CAP to persist over several days even in autumn or spring when the daytime shortwave radiation is strong enough to erode any inversions (Zhong et al., 2001). It also reduces the cooling of the surface through reflections of long-wave radiation at night.

According to Whiteman et al. (2001), based on observations in the Columbia Basin, the atmospheric stability profile is very different when clouds are present in the CAP. These authors observe a gradient close to the moist adiabatic gradient up to the cloud layer, which in turn is topped by a very strong temperature inversion. The near-surface atmosphere would therefore be much more stable in the absence of clouds. Holmes et al. (2015) compares two 5-day WABs episodes in Salt Lake City: one with and one without clouds. A much lower concentration of pollutants was found when clouds are present. This is consistent with Whiteman's observation, as a less stable atmosphere implies more mixing. The same finding was reported for the Yakima Valley (Washington State) by VanReken et al. (2017). Hence, the severity of pollution episodes seems to depend on the presence of stratus. These studies focused on the impact of clouds on the vertical mixing and on the concentration of pollution, not on the local dynamics. In particular, what atmospheric dynamics take place at ground level when thermal effects are inhibited? What happens to valley winds and slope winds?

$\mathcal{E}_4$, which begins with 3 days of thermal inversions under clear skies and continues with the formation of stratus over one day, offers such opportunity. Unfortunately, the stratus was not captured by the numerical simulation, probably due to an insufficient moisture level, as shown in Figure 4.13. One can observe a good correlation between simulation and measurements, mainly imposed by the diurnal cycle. It can also be seen that, for $\mathcal{E}_4$, there is an underestimation of the background level of humidity in the air. On 29 and 30 December 2016 it oscillates between 40 and 60 % in the simulations while the measurements are between 60 and 80 %. The increase in humidity observed during the night of the 31st is well captured by the simulation but as the background humidity level is much lower, it does not allow the air to be saturated. The discrepancies between measurements and simulations are smaller for $\mathcal{E}_3$ than for $\mathcal{E}_4$. However, both figures show the same: systematic underestimation of the humidity in the air, which is also found for $\mathcal{E}_1$ and $\mathcal{E}_2$.

The difficulty in recreating stratus in the simulations is not surprising as this difficulty is widely reported in the literature (Hughes et al., 2015; Zhong et al., 2001; Pu et al., 2016; Westerhuis et al., 2020). In particular, Pu et al. (2016), who also use the WRF model, report different behaviors for two stations. For one of the stations, the simulations produce fog and clouds in contrast to what is observed due to excessive moisture content in the air and an underestimation of the winds. Conversely, for the other station, the simulations fail to reproduce fog because the atmosphere is too dry and the temperatures are overestimated. In our case, the systematic underestimation of moisture could be the result of an incorrect initialization of the soil moisture.

It should be noted, however, that according to the measurements (see Figure 3.5), the temperature difference between PlC (≈ 1000 m ASL) and CHM (≈ 1700 m ASL) does not change drastically with the establishment of stratus. It is likely that if, as in Whiteman et al. (2001), an almost adiabatic profile was observed up to the stratus, a marked dif-

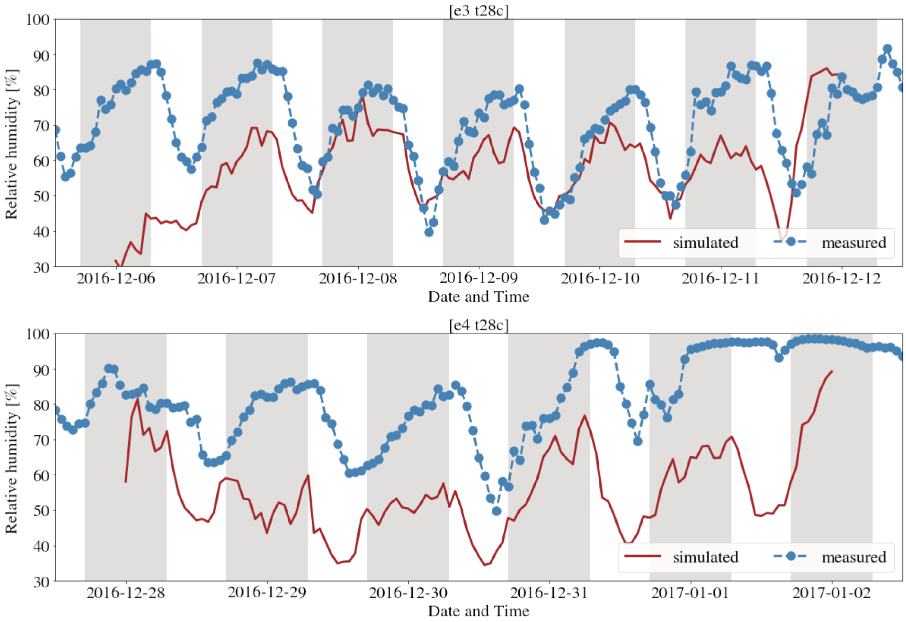

Figure 4.13: Comparisons of measured and simulated relative humidity at ILL for $\mathcal{E}_3$ (top) and $\mathcal{E}_4$ (bottom).

ference would have been observed. Similarly, the reduction of pollutants concentration is not drastic either. It would be therefore very interesting to see if the characteristics established in the studies mentioned above are reproduced in Grenoble. In order to do this, in addition to refining the initialization of humidity, the choice of an episode in which stratus are maintained over several days would be more appropriate for future studies.

4.4 Concluding remarks

- The wintertime near-surface atmospheric circulation observed in the Grenoble Y is analyzed using a classification based on the wind direction in each branch of the Grenoble Y. Each class corresponds to a local circulation mode which is driven by a large-scale forcing, thermal effects, or a combination of both (see Figure 4.1). The consecutive time spent in each circulation mode is mostly intraday (only 12 % of the modes last more than 6 hours). The sequence of the most probable local circulation modes according to the time of the day is typical of a mountain valley wind system (see Figure 4.4). The alternance between the down-valley winds at night and the up-valley winds during the day is particularly marked.

- The horizontal winds at 20 m AGL are compared over 4 episodes with different characteristics, both in terms of large-scale forcing and strength of thermal inversion. Both at night and during the day, the near-surface atmospheric circulations for the episodes share the same main features (see Figures 4.2.1.1 and 4.2.1.2). At nighttime, valley winds descend the Grésivaudan valley and the southern branch of the Grenoble Y to flow into the Voreppe valley. The volume flow rates contributions to the volume of air in the Grenoble basin of the southern branch and the Grésivaudan valley, within the first 200 m AGL, are either similar for $\mathcal{E}_1$ and $\mathcal{E}_3$ or largely dominated by the Grésivaudan valley for $\mathcal{E}_2$ and $\mathcal{E}_4$ (see Figure 4.9). The volume flow rate between the Romanche valley and the Grenoble basin is, again within the first 200 m AGL, negligible as it is one to two orders of magnitude smaller than the contributions from the southern branch and the Grésivaudan valley. A topographic constriction at the exit of the Voreppe valley generates a valley exit jet reaching about 5 m s^{-1} between the ground and 500 m ASL (see Figure 4.8). This valley exit jet then partially roll-up on itself due to a topographic forcing, thus creating a recirculation zone. At day time, for each of the simulated WAB episodes, there is no reversal of the valley wind direction in the Voreppe valley. However, this day-time reversal of the wind direction is a known phenomenon in valleys (see section 1.1.4.2) and is usually observed in winter in the Grenoble Y (see Figure 4.4). The presence of a persistent CAP probably allows the maintenance of the pressure gradient responsible for the nocturnal down-valley wind even during the daytime. Figure 2.18 statistically corroborates that the valley wind direction reversal in the Voreppe valley disappears when thermal inversions are present. Therefore, close to the ground, a common atmospheric circulation has been identified for the four episodes considered. This near-surface atmospheric circulation can be extrapolated as being representative for this weather type.

- The vertical structure of the winds has been compared for the 4 episodes considered (see section 4.2.2). Overall, as for Largeron and Staquet (2016a), a decoupling at ridge height appears between the atmospheric circulation in the valley and the large-scale winds. As a matter of fact, thermal winds can be established even when the channeling of the synoptic winds in the valley would result in an opposite wind direction. This decoupling is, however, far from being perfect. The fact that Grenoble is only separated from the Rhône plain by the Vercors and the Chartreuse may explain why the Grenoble basin benefits from a limited shielding effect. Moreover, the Voreppe valley (which separates the Vercors from the Chartreuse) is conducive to channeling of winds from south-west to north, which further reduces the shielding effect. Hence, large-scale winds stronger than 10 m s^{-1} or winds well oriented with respect to the Voreppe valley can disturb the thermal circulation in the Grenoble Y, sometimes even close to the valley floor. In conclusion, the variability of the atmospheric circulations observed over the entire basin height appears to be much greater than for the winds near the surface. A close inspection of the vertical structure of the winds in the valley allows to conclude that the height over which this characteristic atmospheric circulation for WAB episodes develops depends on the synoptic conditions. For the four simulated episodes, it is typically comprised between 500 and 1000 m AGL.

- At the core of a thermal inversion episode, the inversion height in the Grenoble valley is of the order of 1000 to 1400 m ASL. This height is consistent with i) previous simulations carried out on the Grenoble valley Largeron (2010) and ii) Whiteman's conjecture that this height is set by the average height of the surrounding massifs (1250 m ASL). The temperature inversion height appears to be linked to the CAP intensity (through the heat deficit H) whilst being bounded by the mean height of the surrounding topography (following Whiteman's conjecture). However, the structure of the thermal inversion is sensitive to many factors such as the direction and speed of the large-scale wind, as mentioned in Lareau et al. (2013).

- According to the literature, when a CAP is topped by a low-level stratus, the atmospheric structure changes in response to the disruption of radiative exchanges. In particular, atmospheric stability is drastically reduced up to the stratus, thereby reducing pollutant concentrations at ground level (Holmes et al., 2015; VanReken et al., 2017). To the best of the author's knowledge, the impact of a stratus within the CAP on the development of valley winds and slope winds has not been studied numerically. This is a point for future work as it seems likely that the presence of stratus disturbs the characteristic circulation pattern obtained for the WAB episodes (see Figure 4.6). This study could not be carried out in the present work because the stratus episode considered did not lead to cloud formation in the simulations. It seems that, as in Pu et al. (2016), the stratus was not reproduced due to a lack of moisture in the air, possibly due to a lack of soil moisture.

Chapter 5

Valley-scale dispersion during Winter Anticyclonic Blocking episodes

In Chapter 4, a characteristic atmospheric circulation close to the ground has been identified for the simulated WAB episodes. This circulation provides a reasonable picture of that of typical WAB episodes, as shown by a statistical analysis of measurements (see Figure 2.18). Hence, one may wonder whether this characteristic atmospheric circulation generates areas that are constantly polluted or for which the emitted pollution can hardly escape. Two major axes are explored to answer this question. The first axis is to identify areas of stagnation and ventilation based solely on atmospheric dynamics (see section 5.1). The second axis is to analyze directly the PM concentration fields obtained from the simulations (see section 5.3.1), which are evaluated against in-situ measurements in section 5.2. The simulated vertical PM concentration profiles resulting from vertical mixing are analyzed in section 5.3.2. Finally section 5.3.4 investigates whether the characteristic atmospheric dynamics lead to significant decoupling between locations of high emission and high pollution.

5.1 Identification of stagnation and ventilation zones

Mapping ventilation and stagnation zones in the valley is key to identifying regions where pollution accumulates and regions where emissions should be avoided. To study these aspects in the Grenoble valley, it is possible take advantage of a method derived by Allwine and Whiteman (1994), which allows to identify stagnation and ventilation zones. It will be introduced in the next section.

5.1.1 Definition of stagnation and ventilation zones

Allwine and Whiteman (1994) proposed a method to characterize whether an area was ventilated or not, based on time series of horizontal velocity components measured at single stations. Let τ be the time between two consecutive observations, over which velocity components are averaged. Let T be the length of the timeseries and N the number of samples. Let also u_i and v_i denote the i-th timestep of the timeseries of measurements of U and V, respectively. The following parameters are introduced (*and are schematically illustrated in Figure 5.1*):

- the windrun S is the total distance traveled by a particle that would be advected by the wind measured at the station : $S = \tau \sum_{i=0}^{N} \sqrt{u_i^2 + v_i^2}$

- the transport distance L corresponds to the effective distance that this advected fluid particle would have traveled from its starting point : $L = \sqrt{\left(\tau \sum_{i=0}^{N} u_i\right)^2 + \left(\tau \sum_{i=0}^{N} v_i\right)^2}$
- the recirculation index R is a measurement of L relative to S and characterizes the variability in the direction of advection. : $R = 1 - \frac{L}{S}$

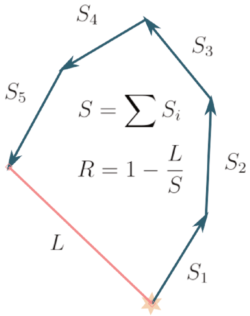

Figure 5.1: Illustration of the windrun S, the effective transport distance L and the recirculation index R as introduced in Allwine and Whiteman (1994) (from which this figure is fully inspired).

From these parameters Allwine and Whiteman (1994) identified the following typologies:

- S is small, irrespective of the value of R. The station observes winds that are not strong enough to effectively flush the particle away: it is in a **stagnation** zone. Let S_c be the threshold such that $S < S_c$ implies a stagnation zone (S).
- S is large in comparison to L. Then the theoretical particle travels a significant distance but ends close to its starting point: the station experiences **recirculation**. Let R_c be the threshold such that $R > R_c$ implies a recirculation.
- S and L are of the same order. It implies that the station observes winds with a constant direction: it is therefore well **ventilated**. Let S_{cv} and R_{cv} be the thresholds such that $R < R_{cv}$ and $S > S_{cv}$ imply a ventilation zone.

Following Largeron (2010), two categories are added so that each flow corresponds to one and only one category: critical stagnation where stagnation is also paired with recirculation; and weak ventilation which corresponds to intermediate situations. All these categories and their respective conditions are summarized in Table 5.1.

The concept of zone typology (stagnation, ventilation or recirculation) introduced by Allwine and Whiteman (1994) has been presented here qualitatively. To define them quantitatively, it is necessary to set certain parameters and threshold values (T,R_c,R_{cv},S_c and S_{cv}). This is discussed in the following section.

5.1.2 Definition of thresholds and statistical significance

The methodology in the original study by Allwine and Whiteman (1994) uses thresholds based on average R and S computed from raw hourly averaged measurements ($\tau = 1\,\mathrm{h}$). At Desert view in the Grand Canyon region, averaged daily windruns ($T = 24\,\mathrm{h}$) and recirculation index over the first 86 days of 1990 were respectively of 250 km and 0.18. Following these observations, the following set of parameters was retained at that site: $T = 24\,\mathrm{h}$, $S_c = 170\,\mathrm{km}$ ($\approx 2\,\mathrm{m\,s^{-1}}$), $S_{cv} = 250\,\mathrm{km}$ ($\approx 3\,\mathrm{m\,s^{-1}}$), $R_c = 0.4$ and $R_{cv} = 0.2$.

Flow classification	**Criteria**
Critical stagnation zone (critical stagnation zone (CS))	$R > R_c$ and $S < S_c$
Stagnation zone (S)	$S < S_c$
Recirculation zone (recirculation zone (R))	$R > R_c$
Ventilation zone (ventilation zone (V))	$S > S_{cv}$
Low ventilation zone (low ventilation zone (LV))	$S_c \leq S \leq S_{cv}$ and $R \leq R_c$ or $S \geq S_{cv}$ and $R_{cv} \leq R \leq R_c$

Table 5.1: Definition of criteria for the flow classification introduced by Largeron (2010) following the original work by Allwine and Whiteman (1994).

Note that windruns are extensive variables in the thermodynamical sense as they scale with T. For that reason they can be conveniently replaced by equivalent wind speeds, removing the time dependence.

Quimbayo-Duarte et al. (2021) used this method to analyze numerical simulations for the Passy valley, which is located near Grenoble. Based on the fact that their domain of interest is of the order of a few tens of kilometers wide, a shorter time window ($T = 6\,\mathrm{h}$) was chosen to keep the windruns interpretable at the valley scale. The rest of the parameters were determined by physical considerations. For instance, the choice of S_c corresponds to a speed that allows to flush the main valley in a single period of $T = 6\,\mathrm{h}$. The parameters were then set as follows: $T = 6\,\mathrm{h}$, $S_c = 20\,\mathrm{km}$ ($\approx 0.9\,\mathrm{m\,s^{-1}}$), $S_{cv} = 32\,\mathrm{km}$ ($\approx 1.5\,\mathrm{m\,s^{-1}}$), $R_c = 0.6$ and $R_{cv} = 0.2$.

The different flow types are discriminated based on thresholds that are fundamentally subjective. For example, to determine S_c, mean winds were used in Allwine and Whiteman (1994), but using median winds or 40th percentiles winds may have been equally justifiable. As a consequence, this method is best suited for relative comparisons between neighboring areas rather than to derive an absolute feature of the area. Following this reasoning, the approach taken here is to determine these thresholds and parameters based on different considerations.

The objective is to use this method to determine zones that i) are statistically significant and ii) allow to illustrate the impact of the local circulation patterns identified in the previous chapter on pollutants accumulation. By statistically significant it is meant that one tries to verify that the observed result is not the consequence of a sampling error (e.g. due to a non representative sample). To limit these errors it is necessary to have a large number of samples, which implies here using Ts shorter than in the other studies mentioned. In doing so, it allows to classify a point several times per day or night period. It was decided to initiate a calculation for each simulation output (every 15 min). For example, for the daytime period with $T = 4\,\mathrm{h}$, one compares the results obtained between 8 am and 12 am ($8 + T$), 8:15 am ($8 + \tau$) and 12:15 pm ($8 + \tau + T$), ... etc. The classification is considered statistically significant if the proportion of [CS, S, R] or [V, LV] exceeds a certain threshold. If so, the regime finally retained is the most frequent regime for the period considered. $T = 4\,\mathrm{h}$ was retained after verifying that the results did not change substantially for $T = 3\,\mathrm{h}$ or $T = 5\,\mathrm{h}$. For this range of Ts, equivalent wind speed thresholds for stagnation and ventilation of $0.8\,\mathrm{m\,s^{-1}}$ and $1.6\,\mathrm{m\,s^{-1}}$ respectively, are found to discriminate well neighboring zones. Recirculation indexes are kept identical to those used in Quimbayo-Duarte et al. (2021). To summarize, the following set of parameters has been used to determine the results presented below: $T = 4\,\mathrm{h}$, $S_c = 11.5\,\mathrm{km}$ ($\approx 0.8\,\mathrm{m\,s^{-1}}$), $S_{cv} = 23\,\mathrm{km}$ ($\approx 1.6\,\mathrm{m\,s^{-1}}$), $R_c = 0.6$ and $R_{cv} = 0.2$. The threshold for statistical representativeness is set to 60 %.

5.1.3 Discussion about the advection velocity

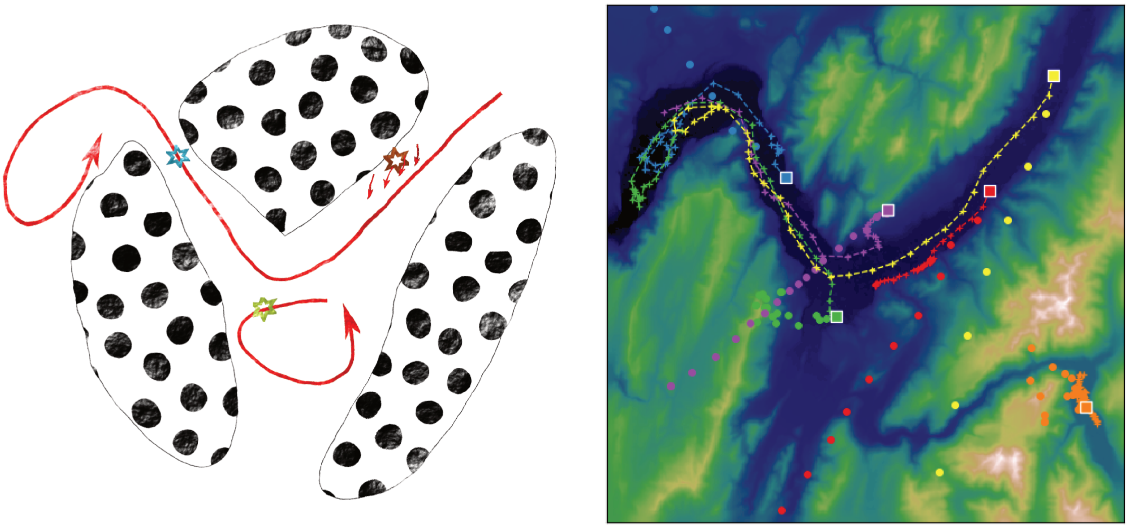

Figure 5.2: *Left:* Schematic illustration of possible situations that could be misleading using the single station advection method. Points of interest are marked with a star symbol and the flows depicted with red lines. *Right:* Comparison of two methods to determine the advection velocity: SSA (dots) and INA (dashed line). Particles are advected from midnight until 6 am for 7 December 2016 ($\mathcal{E}_3$). The initial position of the particles are indicated by the squares.

The original method characterizes an area from single point measurements. This imposes a technical limitation: the particle is necessary advected from the velocities measured at the station considered as the velocity field is unknown elsewhere. This formalism is applied here to simulation outputs, for which this constraint disappears as the velocity field can be interpolated irrespective of the new particle's position. Interpolation however constrains the particle to remain within the simulated domain.

Figure 5.2 illustrates schematically some situations, possibly present for the Grenoble Y, which could lead to very different results using one advection velocity determination method or another. For the sake of brevity, let Single Station Advection (SSA) refer to the method to determine advection velocities presented in Allwine and Whiteman (1994) and INterpolated Advection (INA) to that for which advection velocities are interpolated from simulation outputs. Consider for example a station sitting in a perfectly rotating fluid (yellow star in Figure 5.2). Using SSA one would observe a constant flow direction, and hence classify the station as ventilated when it is in fact in a recirculation zone. Similarly, a station sitting on a constant flow that immediately leads to a recirculated area (blue star) will also be classified as ventilated via SSA. In contrast, INA would have no problem capturing these recirculation zones. The opposite situation also exists. A point of interest on a very poorly ventilated area but leading to an area with constant wind (red star) could be wrongly interpreted as stagnant with SSA. Moreover, as shown on the right side of Figure 5.2, using INA allows to keep a physical interpretation of the windrun as they remain constrained by the topography (unlike SSA).

Figure 5.3 the results of the classification using INA and SSA for $\mathcal{E}_3$. It is possible to recognize some of the differences mentioned in Figure 5.2. For example, at night, the valley exit jet at Voreppe, which generates a recirculation (see Figure 4.5), is well captured

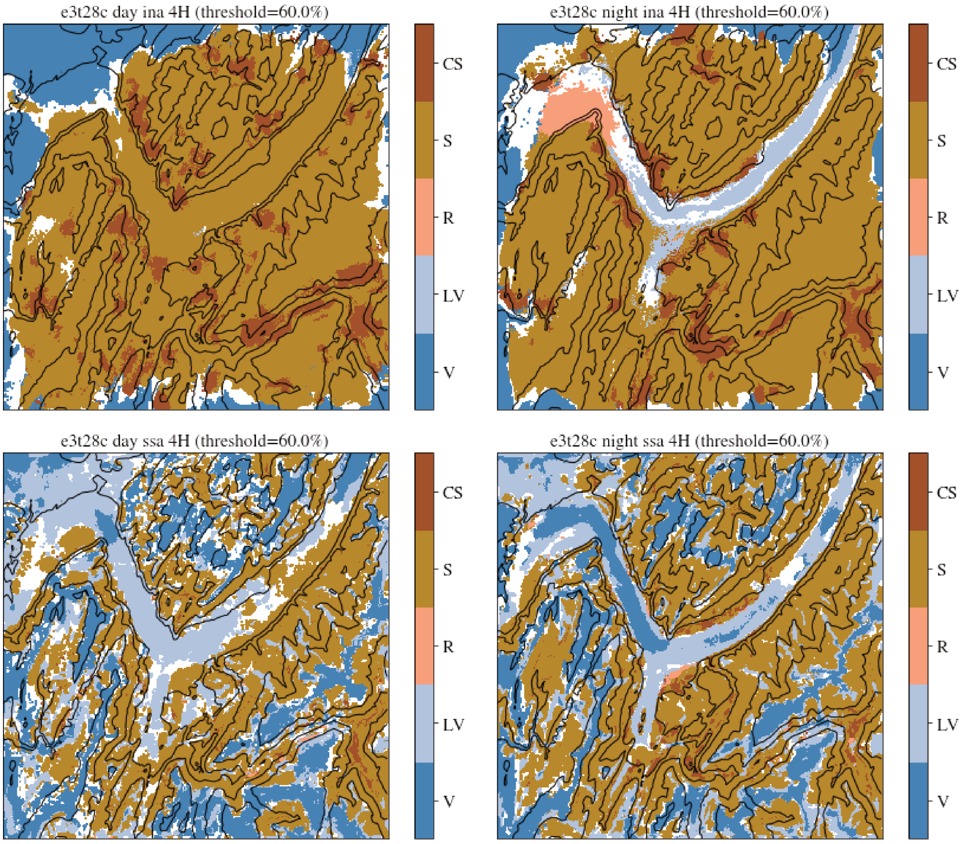

Figure 5.3: Comparison of stagnation and ventilation zones for $\mathcal{E}_3$ using INA (top) and SSA (bottom). Zones are presented for the daytime (left) and nighttime (right). Black contours represent the 300, 500, 1000 and 1500 isocontours of terrain height (m ASL). White areas are those that do not meet the minimum threshold of representativeness (see section 5.1.2).

by INA but not by SSA which sees it as a ventilation zone. In general, typologies seem more statistically significant with SSA than with INA. One possible explanation could be that at a single point the nearby topography constrains the observed flow more than the general circulation of the valley. On the other hand, as seen on the three massifs, the INA zones are more spatially homogeneous. This is intuitively understandable since the particles flow down the gradients of the topography and thus share the same typology as the valley floor underneath.

The SSA approach is still a very good proxy to characterize the flow type from single station measurements. However, in the case of simulation results, using the spatially-resolved velocity field provides more relevant information. This is why the results presented in the following are derived only from calculations where the advection velocity is interpolated from simulation outputs.

5.1.4 Application to the simulated winter anticyclonic blocking episodes

The purpose of this section is to determine if the flow classification is robust within an episode and from one episode to another. In order to take into account the thermal effects, the classification is performed for daytime and nighttime separately. Figure 5.4 shows the classifications obtained for each of the 4 episodes using the set of parameters discussed in section 5.1.2 and by determining advection velocities using interpolation (using the INA method; see section 5.1.3).

The proportion of grid cells that does not meet the 60% representativeness threshold is fairly low, ranging from 10 to 20 %. This implies that the zones identified are significant within an episode and for a given period of the day. Moreover, the non-assigned grid cells do not appear as noise but rather as contiguous zones at the border of statistically significant areas. They are therefore to be considered as transition zones between the ventilation class [V, LV] and the stagnation class [S, CS, R].

From a general point of view, the distribution of flow types for both daytime and nighttime are similar from one episode to another. At night the flow going from the Grésivaudan valley to the Voreppe valley, identified in Figure 4.5, induces a zone of persistent weak ventilation in these valleys. The same is true for the weaker flow from the southern branch towards the Grenoble basin. The Voreppe valley exit jet, constrained by the topography to wrap around itself, leads to significant recirculation zones. The spatial extent of these recirculation zones varies slightly depending on the episode.

On average, the down-valley wind weakens but is maintained over the daytime period in the Voreppe valley (see Figure 4.6). Hence the Voreppe valley remains systematically weakly ventilated, except for $\mathcal{E}_3$ when the thermal winds are generally weaker (see for example Figures 4.10 and 4.11). The recirculation zone at the exit of the Voreppe valley is replaced at daytime by LV or V zones due to the weakening of the valley exit jet. In particular, the V zones at the edge of the domain indicate that the particles are essentially ejected from the domain. For the Grésivaudan valley and the southern branch, the down-valley wind either weakens considerably or transitions to a very weak up-valley wind. This is why these two branches of the Grenoble Y alternate between a weak ventilation at night and a stagnation during the day.

Whether during the day or at night, massifs are identified as critical stagnation or stagnation areas. Similarly, the Romanche valley and the Bourg d'Oisans plain are systematically classified as stagnation zones. This is consistent with the fact that no dominant valley wind has been observed at ground level in this valley (see section 4.2.1). There is also a persistent critical stagnation zone at the exit of the Romanche valley generated by the constriction that separates this valley from the Grenoble Y (located at the vertical section `csd_flx` in Figure 4.7). Finally, the foothills of the Chartreuse in the Grésivaudan valley, located between 300 and 500 m ASL, are also characterized by stagnation despite their proximity to the Grésivaudan valley wind.

In this section, areas with strong and weak potential for air pollution have been identified solely based on the velocity field. However, the actual pollution levels result from a coupling between atmospheric dynamics and emissions. Therefore, the results of this section are to be put in perspective of those using passive scalar advection presented in section 5.3.

5.2 Evaluation of simulated pollution levels

5.2.1 Comparison to measured pollution levels

This section focuses on the comparison between measured and simulated PM_{10} concentrations. Let us start by briefly reviewing these two quantities that are being compared.

For the simulations, PM concentrations are derived from the advection and diffusion (see section 1.2.3) of a scalar field. The scalar field is initially zero and emissions act as a source (of scalar), which, given the vertical resolution used, are emitted only in the first grid cell above the ground. Simulated concentrations represent average concentrations in each cell. For example, for the first vertical level, the values obtained correspond to the

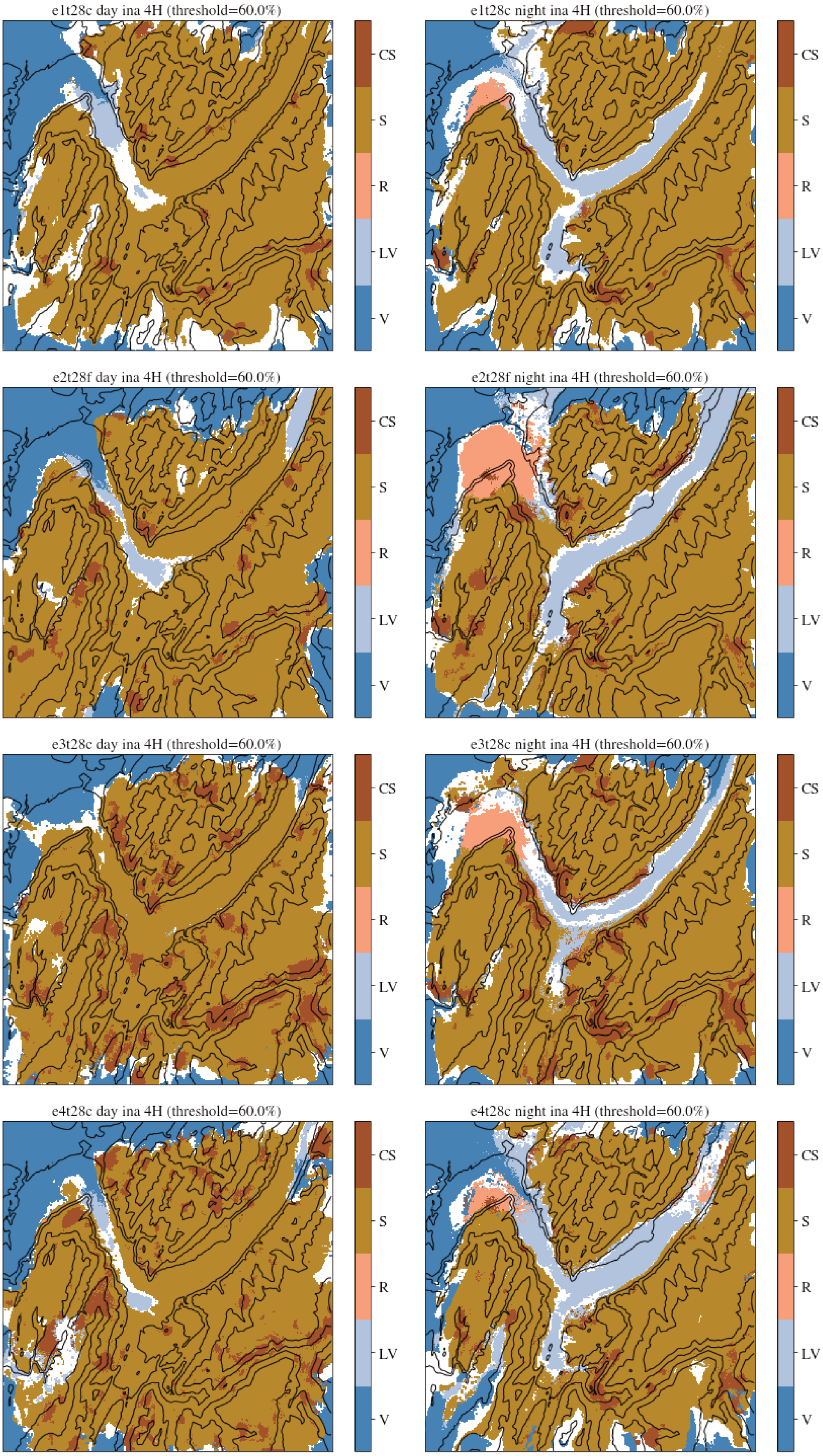
e1t28c day ina 4H (threshold=60.0%)

e1t28c night ina 4H (threshold=60.0%)

e2t28f day ina 4H (threshold=60.0%)

e2t28f night ina 4H (threshold=60.0%)

e3t28c day ina 4H (threshold=60.0%)

e3t28c night ina 4H (threshold=60.0%)

e4t28c day ina 4H (threshold=60.0%)

e4t28c night ina 4H (threshold=60.0%)

Figure 5.4: Inter-comparison of stagnation and ventilation zones for $\mathcal{E}_1$, $\mathcal{E}_2$, $\mathcal{E}_3$ and $\mathcal{E}_4$ from top to bottom, respectively. Zones are presented for the daytime (left) and nighttime (right). Black contours represent the 300, 500, 1000 and 1500 isocontours of terrain height (m ASL). White areas are those that do not meet the minimum threshold of representativeness (60 %; see section 5.1.2).

average concentration over a volume of approximately 111 × 111 × 26 cubic meters. It should also be noted that the advection is carried out from the values available for each grid cell. Thus, for the cells closest to the ground, horizontal and vertical advection are calculated from velocities calculated at about 15 and 30 m AGL, respectively.

The measurements are made a few meters above the ground and characterize a type of environment. A distinction is made between background stations (e.g. FRE located in a park), traffic stations (RSU next to the ring road), urban stations, etc... In the literature it is commonly stated that, in general, concentration of a chemical species in the air emitted continuously from a point source decreases inversely with downwind distance (Huang, 1979; Quimbayo-Duarte et al., 2019). It is therefore difficult to assess how representative a measurement is with respect to its surrounding volume, and hence how to relate measured concentrations to simulated concentrations. Such difficulties are discussed in Taylor et al. (2016).

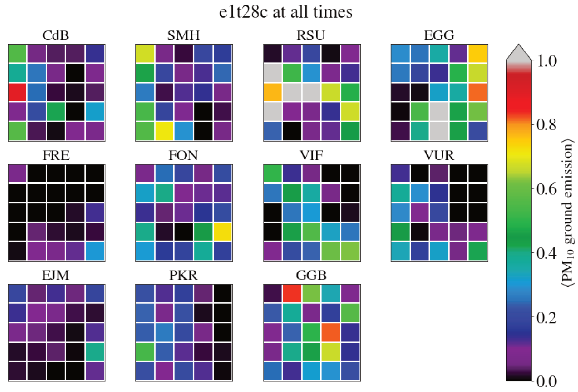

Figure 5.5: Average PM_{10} emissions used for $\mathcal{E}_3$ near measurement stations. *Colorbar units are not shown purposely.*

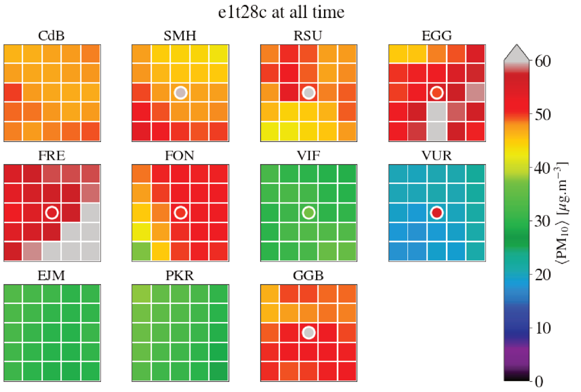

Figure 5.6: Average simulated PM_{10} concentration near measurement stations for $\mathcal{E}_1$. Colors in circle represent the average concentration measured at the station for the same period.

Figures 5.5 and 5.6 illustrates the previous point. Let us take the example of the RSU traffic station. It is located in the immediate vicinity of the Grenoble's ring road and is therefore subject to high PM concentrations. This is taken into account in the simulations through areas of very high emissions along these roads (see aerial photos in Figure A.1 and Figure 5.5). The cells corresponding to the ring road are indeed more polluted than their neighbors, but the relative differences are less pronounced for concentrations than for emissions. Indeed, concentrations can vary by 30 % ($20\,\mu g\,m^{-3}$) when emissions vary by an order of magnitude. In this sense, a "traffic cell" is not directly comparable to a "traffic station".

Differences in the spatial representativeness of the simulations and measurements may result in differences in the underlying physical phenomena. For example, horizontal wind components at mass point height (≈ 15 m AGL) are on average significantly stronger than a few meters above the ground. Moreover, the impact of buildings on the near-surface wind is crudely integrated in the model through the roughness length. Simulated concentrations are therefore expected to be more sensitive to advection than the measurements. Conversely, measurements are much more sensitive to the intensity of nearby emissions.

Figure 5.7 compares simulated and measured PM concentrations at FRE for episodes $\mathcal{E}_1$, $\mathcal{E}_3$ and $\mathcal{E}_4$. Although the average level seems to be captured, there is significantly more variability in the simulations than in the measurements. As expected from a background pollution monitoring station, the measurements show relatively small variations around

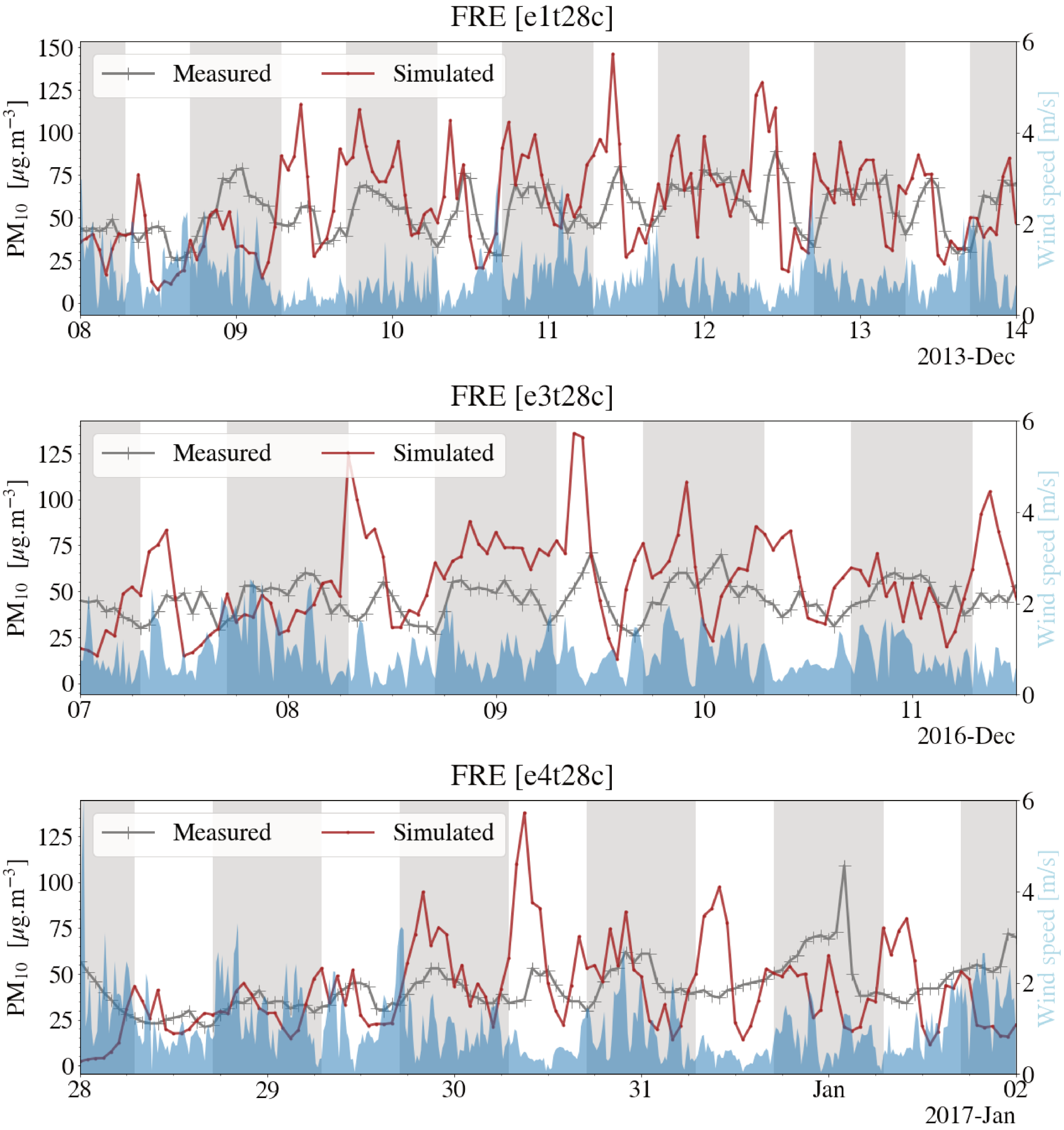

Figure 5.7: Comparisons of simulated (light brown) and measured (gray) PM_{10} concentrations at FRE for $\mathcal{E}_1$,$\mathcal{E}_3$ and $\mathcal{E}_4$. Horizontal wind speed simulated at FRE is also shown (blue shading; values to be read on the right y-axis).

a mean value as they are not directly exposed to emissions sources. Simulations show much more variability from one hour to the next. In particular, high concentration peaks appear in the simulations, especially in the morning. Note, however, that for $\mathcal{E}_1$, there is a better agreement between measured and simulated concentrations and that the two time series are reasonably correlated.

Even if the average levels seem to be correctly captured, it is difficult to qualify the agreement between measurement and simulation as good due to the very high pollution peaks. The possible origin of those peaks is the subject of the next section.

5.2.2 Possible reasons for the discrepancies

Simulated concentrations result from the effects of advection and diffusion on a source term provided by the emission inventory. Since the simulated winds are in relatively good agreement with the available measurements (see section 3.4.1), advection is probably not the main factor at the origin of the observed discrepancies. However, as mentioned previously, it is possible that advection plays a role in PM dispersion that is more important for the simulations than for the measurements. Indeed, winds at 15 m AGL are much less impacted by the surface than winds a few meters above the ground. Figure 5.8, which shows a sequence of instantaneous PM_{10} concentrations, supports this hypothesis. It can be seen that the spatial gradients of PM concentrations can be very large. In view of the temporal variability of the high and low concentration structures, it is not emissions directly but rather the transport of the pollutants that seems to generate these strong gradients. A slight movement of these air masses with very heterogeneous PM concentrations by advection can then generate a pollution peak at a specific location.

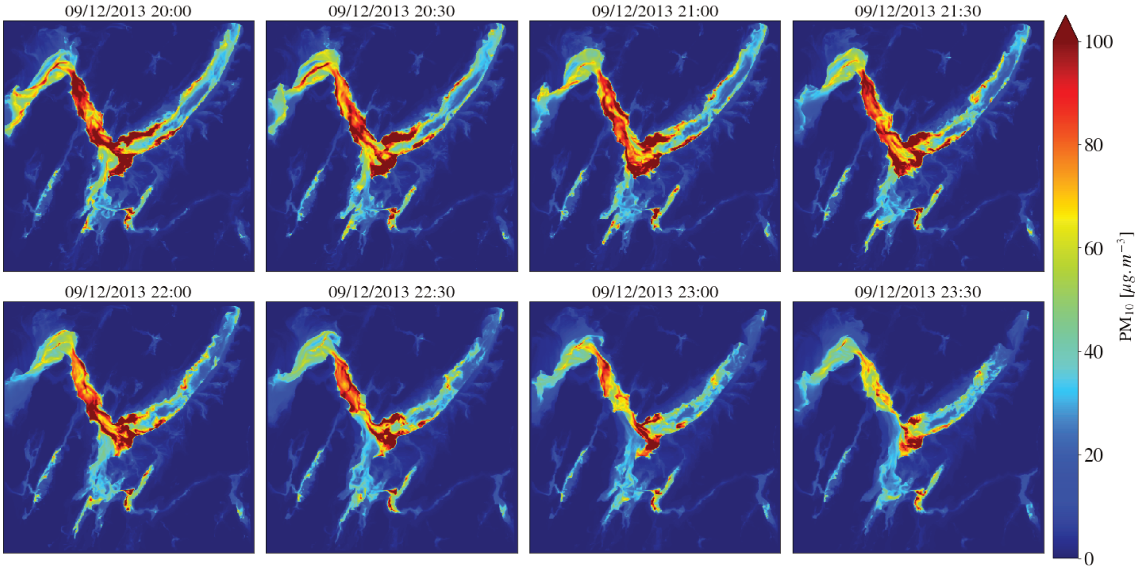

Figure 5.8: Instantaneous PM_{10} concentrations simulated on 9 December 2013.

As explained in section 3.2.4, anthropogenic emissions are dominated by domestic heating and road transport for the Grenoble Y. The typical emission profile at ground level therefore exhibits two peaks, one in the morning and one in the late afternoon/early evening. Emissions are very low at night and intermediate between the two peaks during daytime. The most intense pollution peaks are in the early morning, when emissions are at their highest and a strong surface temperature inversion has formed, thereby suppressing any vertical mixing. However, the evening emission peak, as intense as the morning peak, is not associated with concentration peaks. Moreover, concentration peaks, albeit less intense, occur at any time of the day or night. These differences do not appear to directly coincide with the emission deconvolution pattern. Hence the deconvolution of the emissions is probably not responsible for the peaks either. For this reason, the next section focuses on investigating the role of diffusion. Additional reasons for discrepancies between measured and simulated concentrations are discussed in 5.2.2.2.

5.2.2.1 Underestimation of subgrid scale eddy diffusivity

Pollutant transport in the atmosphere is impacted by all scales of motion. The large scales are mainly responsible for long range transport and the smaller scales act as a sort of diffusion (referred to as turbulent diffusion). By definition, any discretization does not allow to resolve the subgrid scale (SGS) motions (SGS turbulence), which must be parameterized. The model proposed by Deardorff (1980), used for the innermost domain, relies on the classical mixing-length model for SGS turbulent diffusivity for momentum K_m (Eq. 5.1).

$$\mathrm{K}_m = \mathrm{C}_k \times \sqrt{E_k} \times l_m \tag{5.1}$$

The Turbulent kinetic energy E_k is defined to be half the sum of the variances (square of standard deviations) of the turbulent velocity components (see Eq. 5.2) which are defined as the differences between the instantaneous and the average velocity $\tilde{u_i} = u_i - \bar{u_i}$.

$$E_k = 0.5 \times \left(\tilde{u}^2 + \tilde{v}^2 + \tilde{w}^2\right) \tag{5.2}$$

C_k is a dimensionless coefficient equal to 0.1. l_m is the mixing length which is formulated to be dependent on atmospheric stability:

$$l_m = \begin{cases} \Delta & \textbf{if } \text{unstable atmosphere } (\mathrm{N}^2 \leq 0) \\ \min\left[\Delta, 0.76\frac{\sqrt{E_k}}{\mathrm{N}}\right] & \textbf{if } \text{stable atmosphere } (\mathrm{N}^2 > 0) \end{cases} \tag{5.3}$$

where $\Delta = \sqrt[3]{\Delta x \Delta y \Delta z}$ is the effective grid spacing and N is the Brunt Vaisala frequency (defined in Eq. 1.1). Schumann (1991) interprets this reduced l_m as "the height to which a parcel of fluid of a given kinetic energy can rise until all the kinetic energy is converted into potential energy". The turbulent Prandtl number is parameterized using Eq. 5.4, from which the SGS turbulent diffusivity for heat (subgrid scale turbulent diffusion for heat (K_h)) can be inferred from Eq. 5.5.

$$Pr_t = 1/(1 + 2l_m/\Delta) = \frac{\mathrm{K}_m}{\mathrm{K}_h} \tag{5.4}$$

$$\mathrm{K}_h = \left(1 + 2\frac{l_m}{\Delta}\right)\mathrm{K}_m \tag{5.5}$$

A stably stratified atmosphere can be characterized by weak and highly anisotropic turbulence, low-level jets and gravity waves. These phenomena are not present in neutral or unstable conditions and complicate LES in the stably stratified case (Mahrt, 1998; Bou-Zeid et al., 2010). Using the Deardorff parametrization in a strongly stably stratified environment brings additional difficulties. Indeed, in such circumstances, E_k can only be generated if its production by shear overcomes its destruction by buoyancy effects (assuming that E_k is sufficiently small so that the dissipation is negligible). Hence, using Deardorff's model, E_k can only be generated if $Pr_t > R_i$ (Mauritsen, 2011) where R_i is defined by

$$R_i = \frac{\mathrm{N}^2}{\left(\frac{d\mathrm{U}}{dz}\right)^2 + \left(\frac{d\mathrm{V}}{dz}\right)^2} \tag{5.6}$$

In stably stratified conditions, the Richardson number is greater than 1. However, using Deardorff's model, $Pr_t \leq 1$ (see Eq. 5.4), which prevents any turbulence production in a stably stratified atmosphere. This is in contradiction with many observations and simulations. It is known, for example, that turbulence is generated in very strongly stratified atmospheres by intermittent wave breaking. Zhou and Chow (2014) showed that when using the Deardorff model they fail to reproduce shear instability waves, leading to erroneous laminar flows. Solutions exist to overcome this problem but are not yet implemented in WRF. For example, Zilitinkevich et al. (2013) proposes a modification of this turbulence closure scheme by adding an equation for the turbulent potential energy. This allows the Prandtl number to grow linearly (well above 1) with the Richardson number in the case of a highly stratified atmosphere, as observed in several numerical and experimental studies (results that are compiled in the aforementioned study).

The suppression of E_k for stably stratified atmospheres due to the use of the Deardorff model without correction is equivalent to setting the turbulent diffusion coefficients K_m and K_h to zero. As K_h is the turbulent diffusion coefficient used for scalars, its underestimation could partially account for the existence of spurious pollution peaks. For this reason, an empirical method based on observations is proposed to determine a more appropriate minimum threshold for K_h.

Empirical determination of a minimum $\mathbf{K}_h$ It has been observed in the simulations that the SGS diffusion coefficients are very weak (equal or very close to their minimal value set by a E_k seed: $\mathrm{K}_h \approx 5 \times 10^{-2}\,\mathrm{m}^2\,\mathrm{s}^{-1}$ and $\approx 1.1 \times 10^{-3}\,\mathrm{m}^2\,\mathrm{s}^{-1}$ for the horizontal and vertical diffusion, respectively) close the valley floor for all night periods.

The objective here is to determine empirically a minimum threshold for K_h that would be more consistent for the simulated domain when the conditions are stably stratified.

The approach is to use the theoretical framework of Deardorff's parametrization to estimate this value. K_m and K_h are calculated from E_k and N, which one must therefore be able to estimate.

Using the ILL data, recorded at most every 5 minutes, it is possible to estimate E_k using Eq. 5.9 assuming that E_k is predominantly the result of horizontal fluctuations. The fact that horizontal velocities largely dominate vertical velocities in a stably stratified atmosphere makes this hypothesis realistic.

$$\tilde{u}^2(t) = \left[u(t) - \bar{u}_{6\mathrm{H}}(t)\right]^2 \tag{5.7}$$

$$\tilde{v}^2(t) = \left[v(t) - \bar{v}_{6\mathrm{H}}(t)\right]^2 \tag{5.8}$$

$$E_k(t) = 0.5 \times \left(\tilde{u}^2(t) + \tilde{v}^2(t)\right) \tag{5.9}$$

The deviations are calculated with respect to rolling average over 6 hours. The motivations behind the choice of 6 hours are twofold: i) to average over a sufficiently large set so that it is not dominated by fluctuations and ii) not to average over too long a time at the risk of incorporating trend changes. Although this is arguable, one can consider that 6 hours appropriate to capture enough of the energetic eddies. One however must keep in mind that E_k obtained in this way is a full E_k while for the Deardorff model it is the subgrid scale component. In addition, the measurements allow the estimation of a pointwise E_k calculated from temporal variations, while the model estimates an instantaneous E_k in a volume.

The Brunt Vaisala frequency is estimated by:

$$\mathrm{N} \approx \sqrt{\frac{g}{\mathrm{T}_{2\mathrm{m}}} \frac{\Delta \mathrm{T}_{(60,2)}}{\Delta z}} \tag{5.10}$$

K_h is calculated from Eqs. 5.5 and 5.1. Figure 5.9 shows the comparison between K_h determined empirically and simulated for $\mathcal{E}_3$. First of all, it can be observed that there is a good agreement during daytime, though K_h is systematically underestimated by the simulation. This mismatch could result from the empiric estimation of the E_k. At night (when the atmosphere is stable), however, the model underestimates the turbulent diffusion by almost an order of magnitude.

As the idea is to implement a minimum threshold for K_h in stable condition, typical values of E_k and N in stable condition ($\mathrm{N}^2 > 0$) must be used. In this sense median values seems more appropriate than average values. To be consistent with the Deardorff model used in WRF, l_m is determined from Eq 5.3 in stable condition. Using this approach,

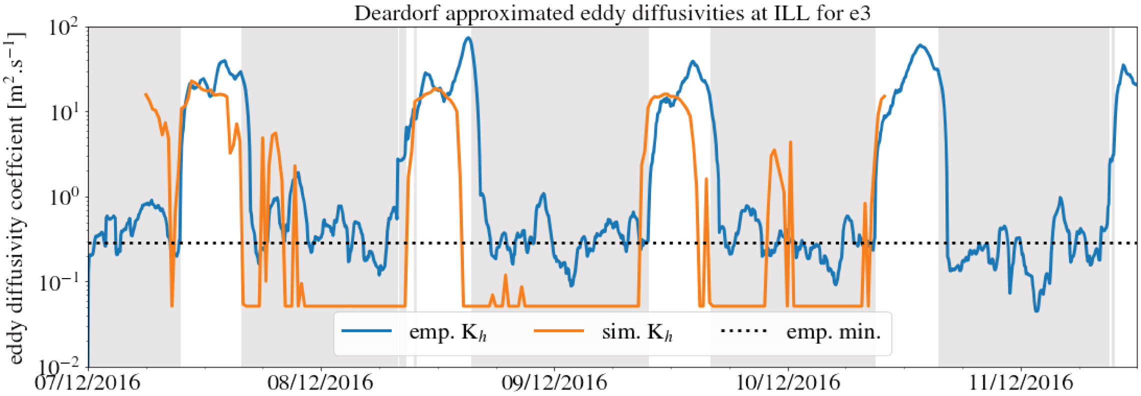

Figure 5.9: Timeseries of K_h computed empirically from the measurements at ILL (as described in this section; blue curve) and the corresponding simulated K_h for horizontal diffusion for $\mathcal{E}_3$ without correction (orange curve). The dotted black line represent the new empirical minimum K_h set in WRF for scalars, obtained using the median of empirical K_h when the atmosphere is stable ($N^2 > 0$; *indicated by a gray shading*).

one gets a minimum threshold for K_h of $0.285\,\mathrm{m}^2\,\mathrm{s}^{-1}$. Using rolling averages of 4 or 8 h instead of 6 h to determine E_k gives a minimum threshold of 0.255 and $0.302\,\mathrm{m}^2\,\mathrm{s}^{-1}$, respectively. Since this range of values is not very large, the minimum threshold for K_h is set to $0.285\,\mathrm{m}^2\,\mathrm{s}^{-1}$.

By applying the minimum threshold determined previously to the turbulent diffusion of scalars (taking the maximum of the orange and black line at each time in Figure 5.9), the agreement between the two time series is improved.

Impact on simulated pollutant concentration Since the dynamics seems relatively well captured, it was decided to use the empirical minimum threshold for turbulent diffusion only on the tracers (for both the horizontal and vertical diffusion), leaving the dynamics completely unchanged. This section focuses on analyzing the impact of this additional turbulent diffusion on the simulated PM_{10} concentrations. To do so, comparisons with measurements are first addressed before the impact of this correction on the spatial structure of the concentration field is considered.

Figures 5.10 and 5.11 show the comparison of measured and simulated concentrations with and without the increased minimum turbulent diffusion threshold at three stations (SMH, FRE and RSU) for $\mathcal{E}_3$ and $\mathcal{E}_4$. It can be seen that the very high concentration peaks observed in the original configuration are smoothed out by the increased minimal turbulent mixing, at all stations and for both $\mathcal{E}_3$ and $\mathcal{E}_4$. In this sense, the modification of the diffusion has fulfilled its purpose. As this modification has no impact on the dynamics, the two time series remain very strongly correlated. For example, smaller peaks remain noticeable when high pollution peaks are simulated in the original configuration. Indeed, the mechanisms causing these peaks – accumulation of pollutants in the morning under stable atmosphere and strong horizontal gradients linked to advection – are still present; only the addition of diffusion reduces their impact by smoothing the strong spatial gradients of concentration.

For $\mathcal{E}_3$, the modification of the minimum turbulent diffusion allows, in addition to smoothing the peaks, to have a good agreement between measurements and simulations. This is particularly remarkable for FRE. However, this picture is more contrasted when considering $\mathcal{E}_4$. At FRE, the modification allows to better capture the temporal evolution of the concentration, despite an underestimation that becomes more and more pronounced

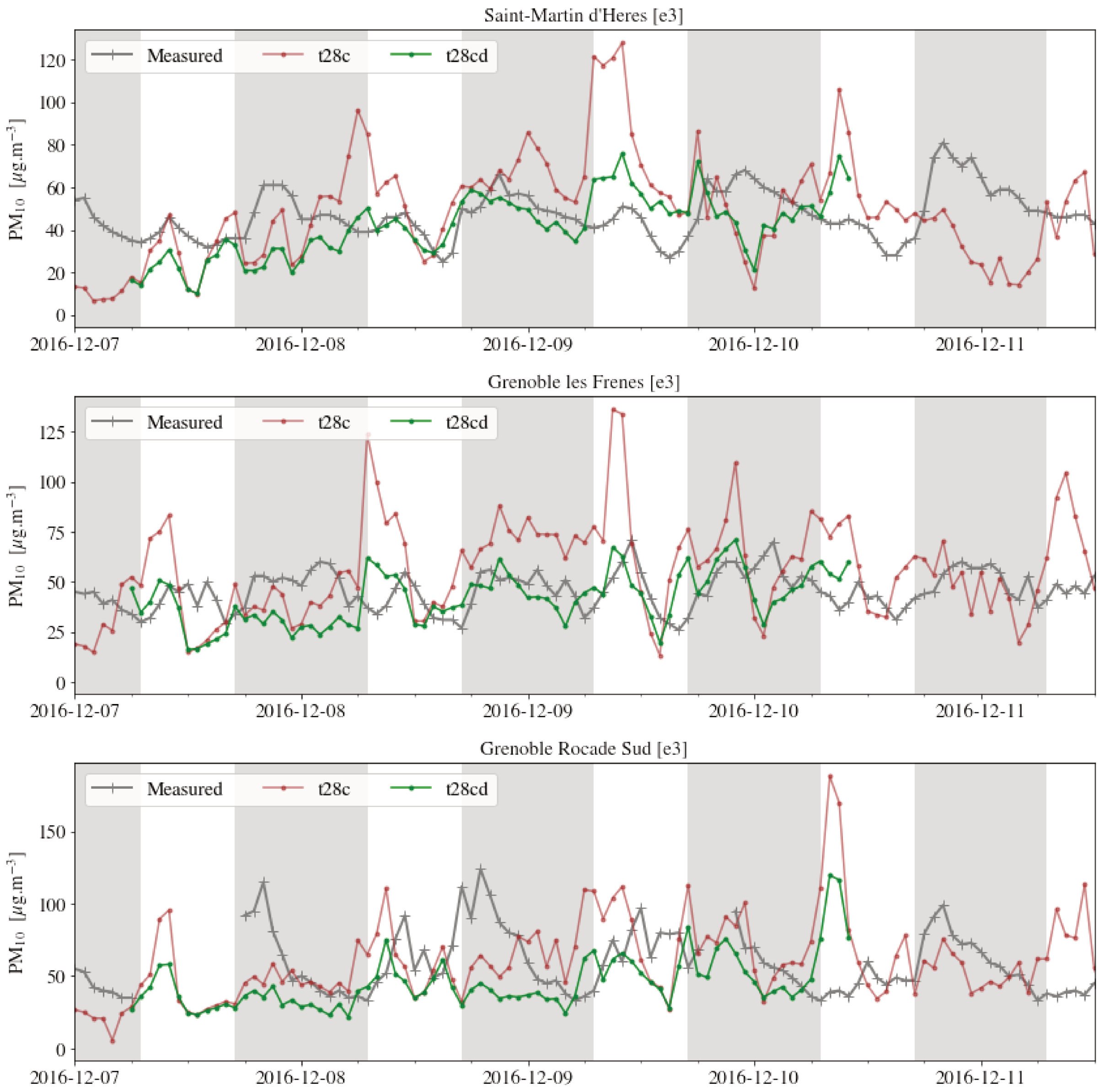

Figure 5.10: Comparisons of simulated and measured PM_{10} concentrations with (*t28cd*) and without (*t28c*) additional minimum turbulent diffusion for $\mathcal{E}_3$ at SMH, FRE and RSU, respectively from top to bottom.

with time. However at SMH and RSU the simulations significantly underestimate the time-averaged concentrations.

Figure 5.12 shows the average PM_{10} concentrations at 20 m AGL for $\mathcal{E}_4$, with and without additional minimum turbulent diffusion, and incorporates a comparison with the average measured concentrations at the stations. Without modification of the minimum turbulent diffusion threshold, the simulated concentrations are in fairly good agreement with the average levels observed at the stations. Indeed the colors in the center of the white circles (representing the measurements) are close to the color of their immediate environment. In contrast, the measured concentrations are clearly higher than those simulated when diffusion is enhanced, in agreement with Figure 5.11.

In light of the simulation results with an increased minimum turbulent diffusion threshold, it seems that diffusion now plays an excessive role, significantly reducing the simulated average concentrations. Minimum thresholds were increased from about $1.1 \times 10^{-3}\,\mathrm{m}^2\,\mathrm{s}^{-1}$ and $5 \times 10^{-2}\,\mathrm{m}^2\,\mathrm{s}^{-1}$ for the vertical and horizontal SGS eddy diffusivity coefficients, re-

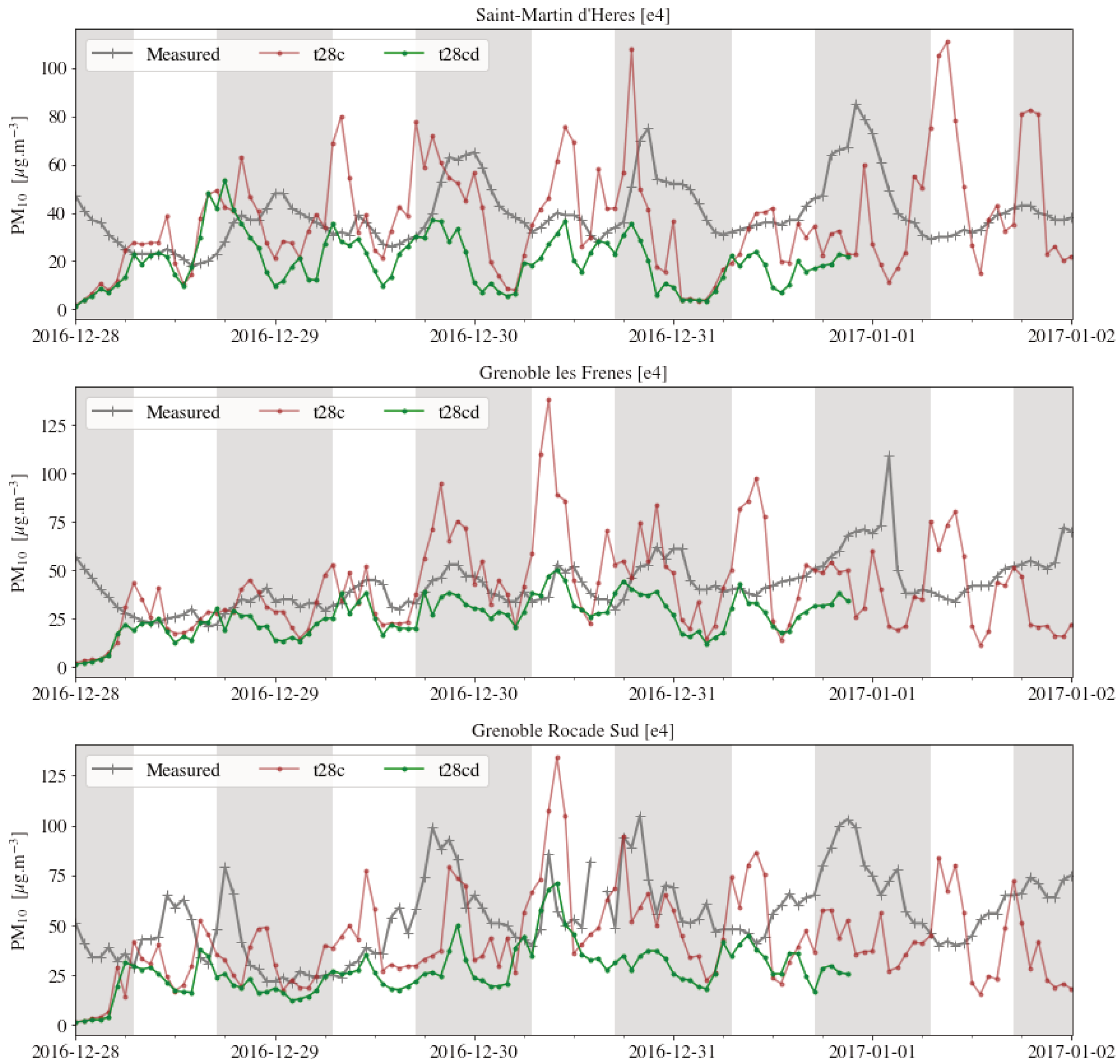

Figure 5.11: Comparisons of simulated and measured PM_{10} concentrations with and without additional minimum turbulent diffusion for $\mathcal{E}_4$ at SMH, FRE and RSU, respectively from top to bottom.

spectively, to $2.85 \times 10^{-1}\,\mathrm{m}^2\,\mathrm{s}^{-1}$ for $\mathcal{E}_3$. One can foresee several reasons as to why this enhanced turbulent diffusion has an excessive effect. Firstly, the modification introduced is extremely simple, replacing one minimal threshold by another. It is certain that this threshold would ideally not be constant in time, as shown in Figure 5.9. For example, a variation of a factor 10 is observed during the night of 9 December 2016. It is also certain that turbulent diffusion depends on space. Here, the minimum threshold is being determined at one specific location (ILL). It would have been very interesting to have at least one other station allowing the same calculation in order to evaluate the amplitude of the spatial variation. From a methodological point of view it has been decided to apply this threshold value to both horizontal and vertical turbulent diffusion. It may have been more relevant to apply it only to the horizontal because of the effects of the stratification in the vertical.

In sum, increasing the minimum turbulent diffusion coefficient threshold suppresses intense short-lasting pollution peaks (see Figures 5.10 and 5.11). However, this increase in diffusion also brings its own problems. The simulated concentration fields are then well

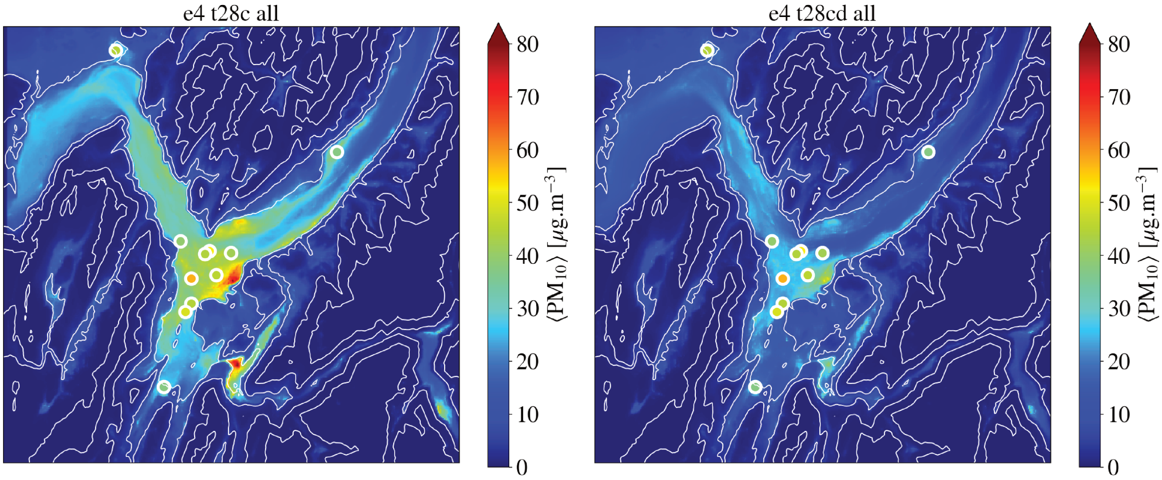

Figure 5.12: Comparisons of simulated PM_{10} concentrations without (left) and with (right) increased minimum turbulent diffusion threshold for $\mathcal{E}_4$. The white circles indicate the position of the measuring stations, and the colors the average concentration measured at this station (to be read on the same color scale as the concentration field).

below the average measured concentrations (see Figure 5.12). It was preferred to retain the simulations without the increased minimum turbulent diffusion coefficient threshold for the analyses presented in the rest of the chapter.

5.2.2.2 Further hypotheses on the origin of the discrepancies

Earlier in this section, the differences between measured and simulated PM concentrations have been justified by two main factors: i) the lack of turbulent diffusion and ii) the fact that the two quantities are not necessarily comparable as such. However, even if these two problems were to be solved, several sources of error would persist.

PM emissions, like all inputs in this model, are based on assumptions. The most uncertain assumption is probably that used to convert from annual emissions to hourly emissions. It was suggested by Chemel et al. (2016) that the temporal deconvolution profile used does not perfectly match that of an Alpine valley. Furthermore, emissions are not included beyond the boundaries of the innermost domain. This can be a problem when comparing with background pollution or when dealing with cases of long range transport of PM. The assumption of treating PM as passive scalars, hence neglecting their chemical reactions, is also a strong working hypothesis. The same could be said for ignoring deposition and re-suspension.

5.3 Spatial variations of simulated PM concentrations

5.3.1 Ground-level variations

This section focuses on air quality where it is most important as far as humans are concerned: in the immediate vicinity of the ground. Figure 5.13 shows the average pollution levels observed at 20 m AGL during daytime and nighttime for $\mathcal{E}_3$.

The spatial distribution of the average PM_{10} concentrations, both at night and during the day, is strongly influenced by the average winds identified in Figures 4.5 and 4.6. Indeed, at night, the down-valley winds are ubiquitous. This results in the transport of pollutants emitted in the Grésivaudan valley towards Voreppe via Grenoble. This

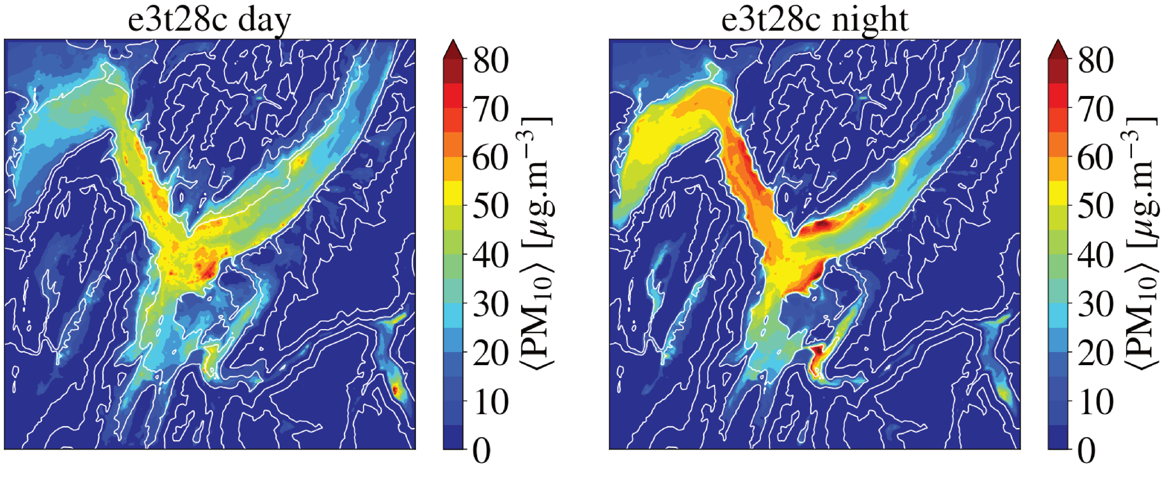

(a) day (b) night

Figure 5.13: Average PM_{10} levels simulated at 20 m AGL during daytime (a) and nighttime (b) for $\mathcal{E}_3$.

transport is highlighted by the inflow of relatively clean air from the Grésivaudan valley. A significant amount of pollutants is removed from the Grenoble Y through the Voreppe valley exit jet. The area downstream, which is less urbanized is therefore exposed to pollutants emitted in the Grenoble metropolis. For the daytime period, the atmospheric circulation in the Grenoble Y is weaker and the most polluted areas correspond to the areas of high PM emissions.

Although the patterns of PM concentrations are slightly different between day and night, it is the average concentrations to which people are exposed that generally matter in terms of adverse health consequences. Episodes are compared in terms of average PM concentration in Figure 5.14.

Several concentration hotspots appear, for example immediately upstream of the southern tip of the Chartreuse massif and at the foothills of the Belledonne massif, southeast of the Grenoble basin. The first one results from a recirculation/stagnation zone in this area. The second one sits at the bottom of the Grenoble basin but slightly away from the corridor of the down-valley wind flowing from either the Grésivaudan valley or the southern branch of the Grenoble Y. Vizille, located at the junction of the Romanche valley with the southern branch of the Grenoble Y, is also a PM concentration hotspot in all three simulations. This is likely the result of almost zero flow through the constriction between the Romanche valley and the Grenoble Y, as shown in Table 4.1.

The hotspots along the Chartreuse flank and at the entrance of the Romanche valley are detected as stagnation or critical stagnation zones (both during the night and day) in section 5.1. The south-east of the Grenoble basin is almost systematically in a stagnation zone during the daytime. For the nighttime, only the part in the immediate vicinity of the relief – where the highest concentrations are observed – is characterized as a stagnation or critical stagnation zone. Finally, one can also notice that the recirculation area at the exit of the Voreppe valley is not effectively highly polluted, probably because the local emissions are low.

Figure 5.15 shows the relative contribution of the main SNAPs to the time-averaged PM_{10} concentration observed for $\mathcal{E}_3$ (see Figure 5.14). In general, SNAP 2 – predominantly domestic heating and accounting for 66 % of the emissions in the domain – dominates with contributions ranging from 50 % in the Grenoble Y to more than 90 % in

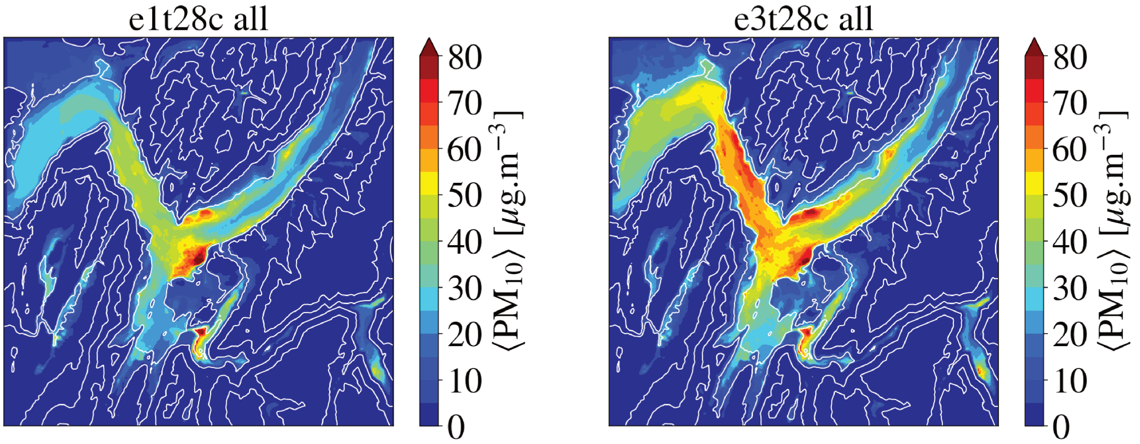

(a) $\mathcal{E}_1$ (b) $\mathcal{E}_3$

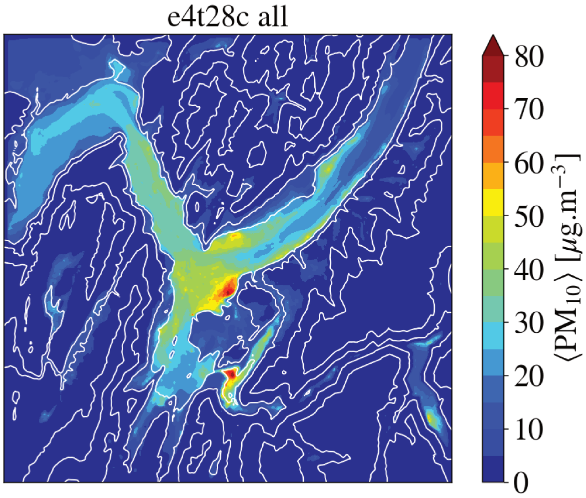

(c) $\mathcal{E}_4$

Figure 5.14: Average PM_{10} levels simulated on the first mass point for $\mathcal{E}_1$, $\mathcal{E}_3$ and $\mathcal{E}_4$.

the highlands. For the Grenoble Y, industry (SNAP 4) accounts for 5 to 10 % of PM_{10} concentrations and road transport for 20 to 50 % depending on the distance from the main roads. Agriculture has relatively little impact on the valley floor, with a maximum contribution of about 5 % in the upper part of the Grésivaudan valley.

5.3.2 Vertical profiles

Let us start with a brief overview of the literature on this topic. Focusing on gaseous pollutant dispersion over a plain, Elliott (1961) proposed that pollutant concentration as a function of the height above the emission location follows a vertical exponential decay of the form $a \times exp(b \times z^{\alpha})$ where a, b and α are coefficients to be determined from measurements. Using measurements collected between 1 and 10.5 m AGL, Elliott (1961) found that the value of α depends on atmospheric stability: $\alpha = 1.4$ provided the best fit for unstable atmospheric conditions while $\alpha = 1.5$ agreed better with measurements for stable atmospheric conditions. Relying on the Monin Obukhov Similarity Theory and assuming a stationary wind profile, Huang (1979) proposed an analytical solution to derive α in stable atmospheric conditions, yielding $\alpha = 1.17$. Zheng et al. (2021) showed that an exponential decay fit of the form $c + a \times exp(b \times z^1)$ gave a good agreement with

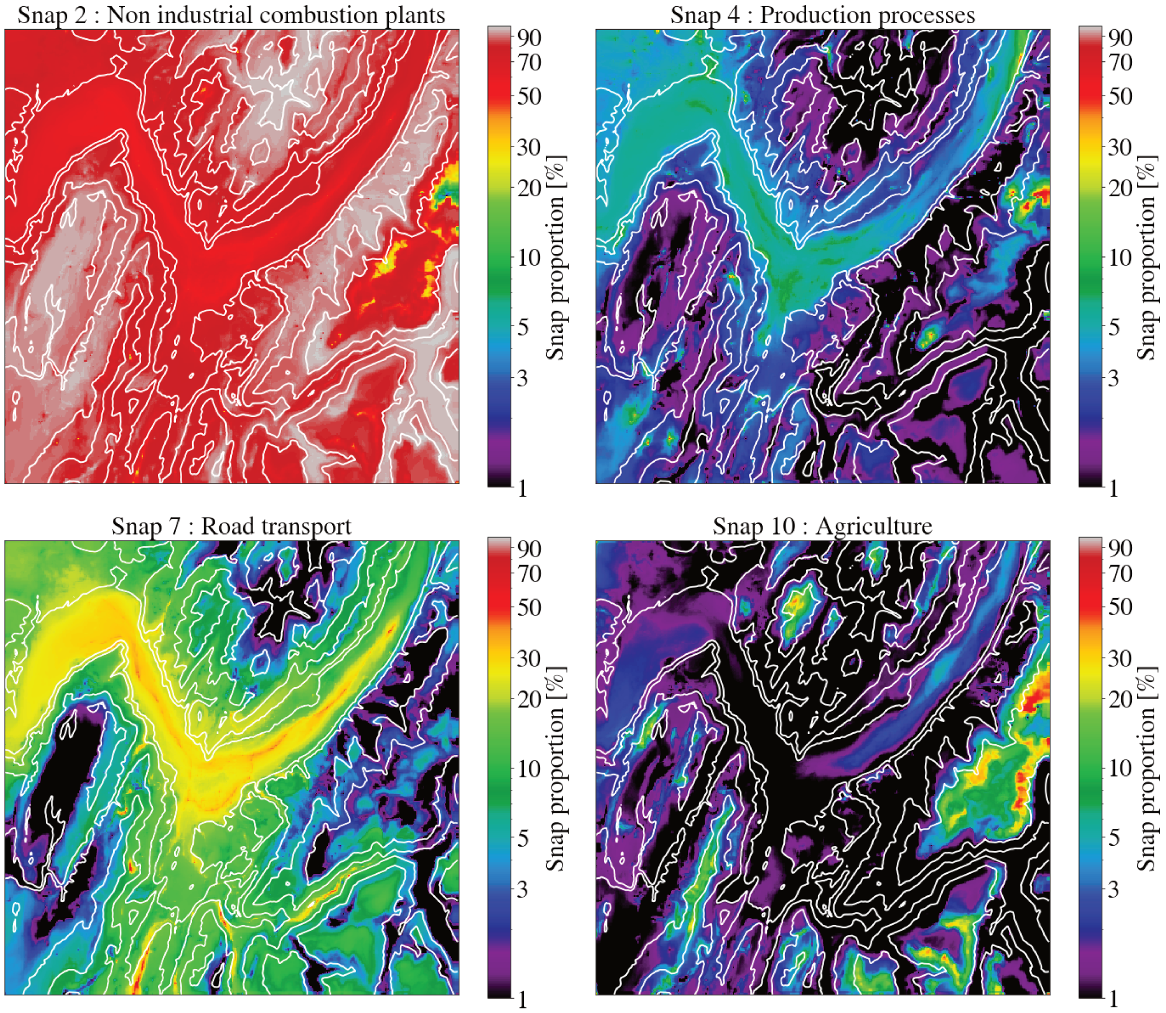

Figure 5.15: Contributions of the emission from the main SNAP sectors to the average PM_{10} concentration for $\mathcal{E}_3$.

measurements made between the ground and 50 m AGL for PM near a road in Shanghai (China).

Studies reporting on the vertical dispersion of PM showed that the finer are the particles, the less abrupt is the decrease of their concentration with altitude. For example Pateraki et al. (2019) found that PM_{10} concentrations were reduced by 18% between the ground floor and the 5th floor (19 meters) of a building in Athens while for $PM_{2.5}$ this reduction was only of 11%. Similarly, Zheng et al. (2021) observed a reduction of more than 20% 20 meters above the ground for PM_{10} while the reduction was of 8% for $PM_{2.5}$. In the same study, that trend extended for PM_1, PM_4 and PM_{15}. In the numerical simulations performed in the present work, the tracers have no mass and are not subject to gravity. This limitation must be taken into account when interpreting the results. In particular, simulations would have a tendency to overestimate PM concentrations at altitude (particularly for PM_{10}).

A recent study by Liu et al. (2021), compared simulated $PM_{2.5}$ vertical profiles from the WRF-Chem model (v3.9) with measurements made by drone for a severe haze pollution episode in Nanjing (China). Vertical profiles were reasonably well captured when daytime convection dominated. Conversely, at night, the ABL height is underestimated, leading to an overestimation of $PM_{2.5}$ concentration near the ground. It is interesting to note that this overestimation was significantly reduced by increasing the minimum turbulent diffusion threshold, as shown in the present work (see section 5.2.2.1). Unfortunately, Liu et al. (2021) did not model the decay rate of the $PM_{2.5}$ concentration with altitude.

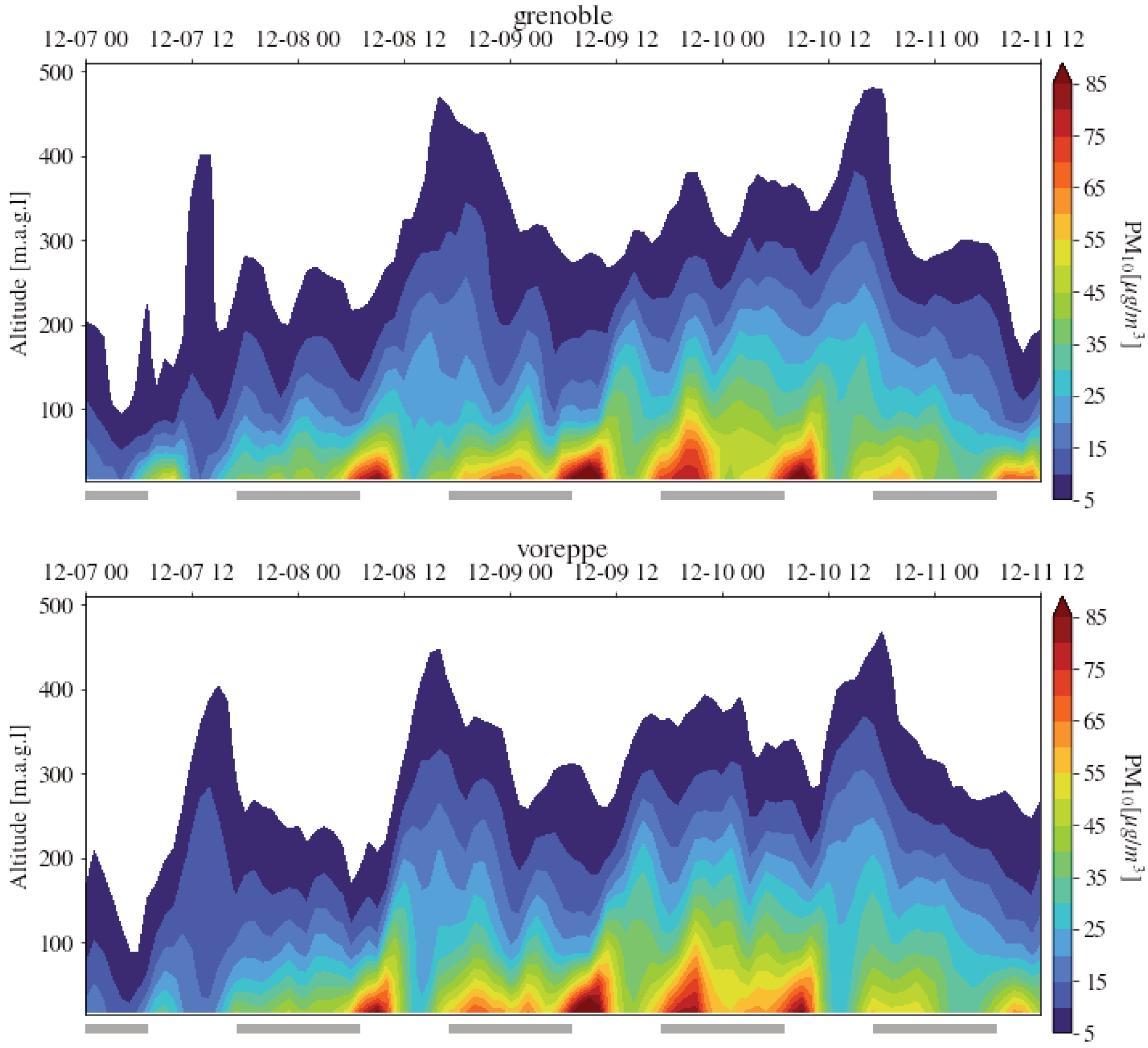

Figure 5.16: Vertical profile of PM_{10} concentration averaged over Grenoble and Voreppe (as a function of time) for $\mathcal{E}_3$. *Dashed grey lines at the bottom indicate night time periods.*

Figure 5.16 presents simulated vertical profiles of PM_{10} concentration, averaged over Grenoble and Voreppe (see Figure 3.8 for the spatial extent of the areas used for averaging), for $\mathcal{E}_3$. PM_{10} concentration decreases constantly with altitude and tend to zero at 300 to 400 m AGL. On average over the considered areas, one does not distinguish the presence of elevated pollution layers.

The impact of the diurnal cycle is clearly marked at both "locations". Around sunrise, a strong accumulation of pollution takes place near the surface as a result of the morning rush hour while the ground-based temperature inversion is still present. After a few hours, natural convection sets up over a column of about three hundred meters, thereby diluting the pollution (in the column). From sunset onwards, the air masses near the ground will become denser as the low level inversion forms again, resulting in an accumulation of PM_{10} near the ground.

Figure 5.17 shows the vertical profile of PM_{10} concentration – normalized by the concentration in the first grid cell – averaged over each of the episodes. Some profiles correspond to measurement stations, others to spatial averages. Each of the profiles is fitted by a function of the form proposed in Elliott (1961): $a \times exp(b \times z^{\alpha})$. If the three

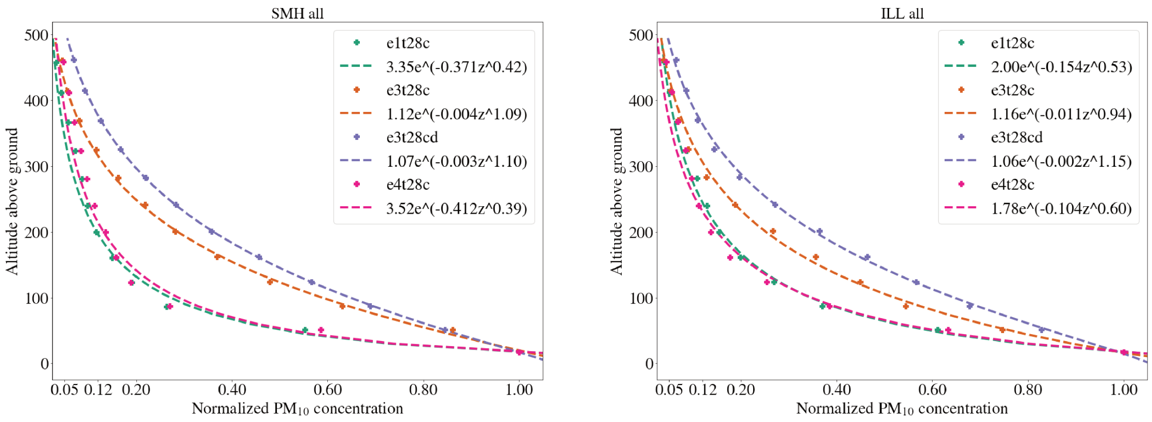

(a) SMH (b) RSU

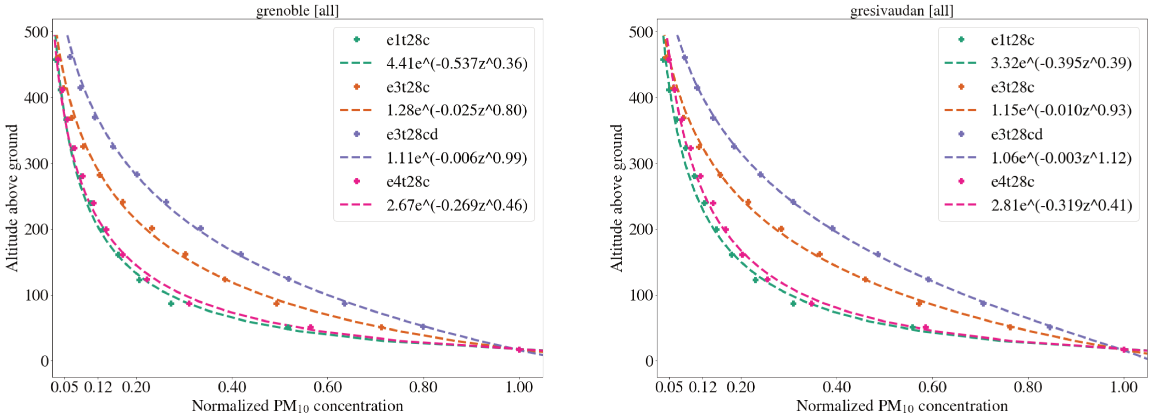

(c) Grenoble (d) Grésivaudan

Figure 5.17: Temporal average of normalized PM_{10} vertical profiles at individual stations (SMH and ILL; top figures) and over specific areas (Grenoble and Grésivaudan; bottom figures) for several configurations and episodes.

parameters of the function are determined for each "location" separately, the function fits the data remarkably. Note that α values are similar for a given episode irrespective of the "location" but they may differ significantly from one episode to another. α values are greater for $\mathcal{E}_3$ than for $\mathcal{E}_1$ and $\mathcal{E}_4$. The fact that the heat deficit below 500 m ASL is larger for $\mathcal{E}_3$ (1.38 MJ) than for $\mathcal{E}_1$ and $\mathcal{E}_4$ (1.10 and 1.03 MJ, respectively) corroborates that α depends of stratification.

5.3.3 Impact of slope winds

Several studies have shown that slope winds can be responsible for significant transport of pollutants. Wakimoto and MacElroy (1986), using a downward looking airborne lidar, identified air layers with high ozone concentrations several hundred meters above the ground in Los Angeles. These layers would result from the conjunction of natural convection and transport by up-slope winds during the day. This phenomenon was also reported by McKendry et al. (1997) in the Fraser Valley near Vancouver. More recently, other studies reported elevated pollution layers in the Alps. For example, Gohm et al. (2009) observed – using a lidar in the Inn valley – an elevated pollution layer that developed first along a sunny slope and then spread out across the valley (likely below the inversion height). In Sabatier et al. (2020), numerical simulations in the Arve valley showed a very similar picture.

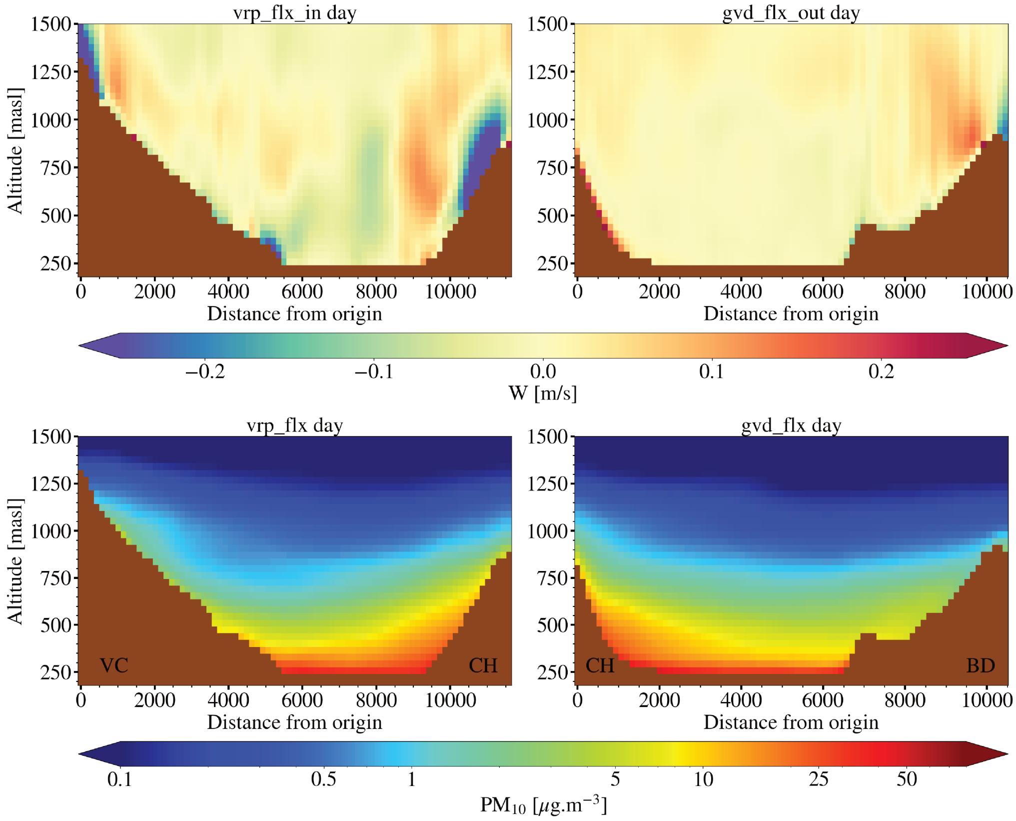

Figure 5.18: Averaged vertical wind speed and PM$_{10}$ concentration over day time for all episodes in cross-sections `vrp_flx` (Voreppe) and `gvd_flx` (Grésivaudan); see Figure 4.7). VC, CH and BD stands for the Vercors, Chartreuse and Belledonne massifs.

Figures 5.18 and 5.19 display vertical cross-sections of vertical wind velocities and PM$_{10}$ concentrations, respectively, averaged over the diurnal period and for a specific snapshot. For the Grésivaudan valley (`gvd_flx`), up-slope winds are observed to the west (Chartreuse flanks) and very weak down-slope winds to the east (Belledonne flanks). The isentropes, displayed for the snapshot, show that the air is slightly warmer along the western flank than at the same elevation but further away from the landforms. To the east, no clear departure from horizontal isentropes is observable. The diurnal course of the sun, which illuminates the western flank more than the eastern flank, can account for this difference. Such asymmetry in the slope winds development due to the valley orientation is documented in the literature (Bader and Whiteman, 1989; Gohm et al., 2006). On one side, enough energy is received through short-wave incoming radiation to reverse the nocturnal down-slope winds, while on the other side, it is barely enough to stop them. In the Voreppe valley cross-section (`vrp_flx`), up-slope winds are not directly observable in the temporally averaged signal but they are in the snapshot. On average, down-slope winds are indeed maintained during the day on the flanks of the Vercors, likely linked to the fact that down-valley winds are also maintained throughout the day. Up-slope winds are found on the flanks of the Chartreuse massif. The orientation and shape of the valley (at least in this cross-section) do not allow for the daytime reversal of the slope winds on average over the day, even on the most exposed side.

To sum-up, effective pollutant transport is observed mostly along the sunny slope of the Grésivaudan valley, although there is evidence of some more limited transport along the flank of the Chartreuse massif. This transport is also evidenced by Figure 5.15 through the presence of PM originating from road transport, that are almost exclusively emitted

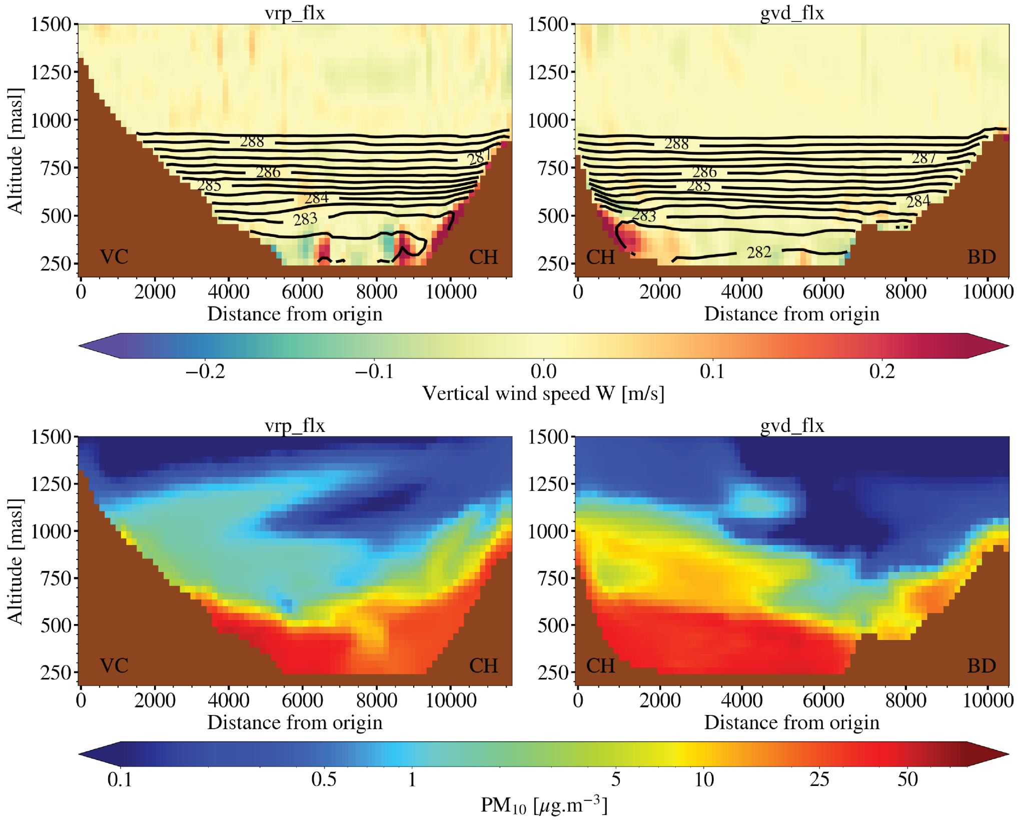

Figure 5.19: Same caption as in Figure 5.18, but for a snapshot on 10 December 2016 at 1:40 pm. The black contours on the top figure represent isentropes with 0.5 K intervals.

at the valley floor, on the flanks of the Chartreuse massif. But the net impact is small on average over the episodes considered. Note that no air quality station is present on the valley flanks, thus preventing a comparison with measurements there.

5.3.4 Interplay between atmospheric dynamics and emissions

Additional information on dynamical processes can be gained by investigating pollutant transport in less urbanized area. As a matter of fact, passive scalars can be used as a tool to examine integrated effects of atmospheric processes in the boundary layer (Sabatier et al., 2020; Zardi et al., 2021). This section focuses on understanding whether the atmospheric circulation present during WAB episodes leads to a partial "decorrelation" between emissions and simulated concentrations.

Figure 5.20 illustrates the relationship between PM emissions and simulated concentrations through a classification based on two thresholds: high or low emissions and high or low concentrations (more or less than 20 µg m^{-3}, respectively). It should be noted that the thresholds are set so as to highlight certain processes and does not correspond to regulatory thresholds. Most of the Grenoble Y corresponds to a polluted area, irrespective of local emissions. This is a direct consequence of the down-valley wind that dominates WAB episodes, transporting pollutants down the valley. On the other hand, up-valley winds have no clear footprint as there are no polluted areas with low emissions upstream of the first high emission areas in the Grésivaudan valley.

Assuming that slope winds have a significant impact on pollutant transport, they would transport polluted air from the more urbanized valley floor (high emission zone) to the necessarily less urbanized flanks (low emission zone). Low emission but high pollution zones (`Pe`) would then be observed along the sunniest flanks of the valleys – where most up-

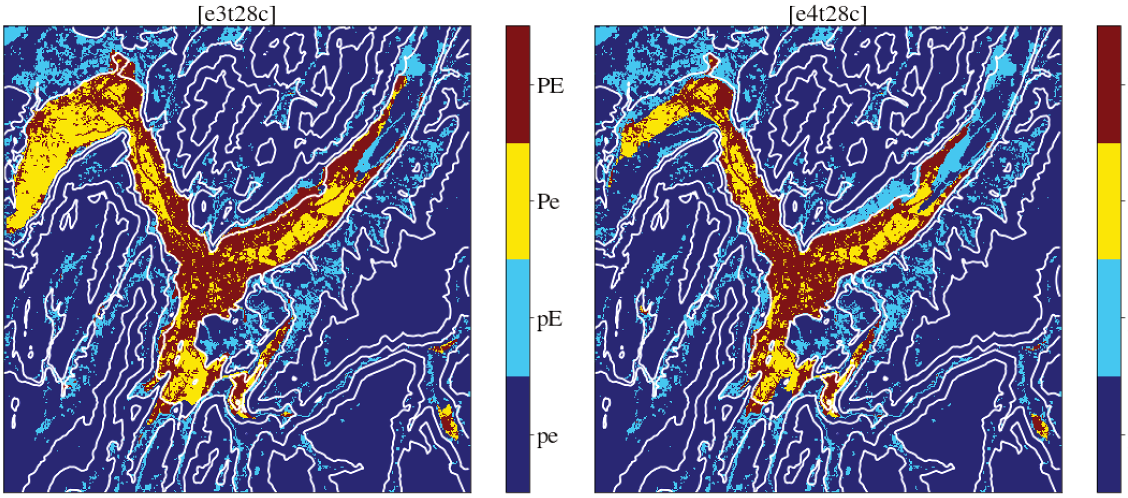

Figure 5.20: Classification of the innermost domain for $\mathcal{E}_3$ (left) and $\mathcal{E}_4$ (right) into i) low pollution low emissions (`pe`), ii) low pollution high emissions (`pE`), iii) high pollution low emissions (`Pe`), and iv) high pollution high emissions (`PE`) zones. The threshold between low and high pollution is set to $20\,\mu g\,m^{-3}$ while the threshold for emissions is not specified for confidentiality reasons.

slope winds are observed at daytime (see section 5.3.3) – such as the western flank of the Grésivaudan valley. However, `pE` areas are observed where the terrain allows residential areas and `pe` areas where it does not. This configuration is not observed in the Voreppe valley either. This further illustrates that up-slope winds, though they convey pollutants (see section 5.3.3), have no significant net impact (see Figure 5.20), likely due to the limited daylight hours allowing for up-slope winds to develop.

It is interesting to note that, except for Bourg d'Oisans, areas sitting above the valley floor of the Grenoble Y (about 500 m ASL and above) experience low pollution irrespective of local emissions and despite being classified as stagnation zones. For example, the Belledonne hillsides may be locally urbanized – thus with significant emissions – but not polluted (less than $20\,\mu g\,m^{-3}$). The prevailing winds are therefore weak enough to produce stagnation zones but strong enough to dilute pollutants in cleaner air masses. The only measurements available for medium altitude areas in the Grenoble Y come from a campaign conducted on the Vercors plateau by the local air quality agency [1]. The background concentration of PM_{10} at 1000 m ASL was measured for the whole year 2018. During this period, no day exceeded the $50\,\mu g\,m^{-3}$ threshold. Furthermore, the winter median concentration was $6\,\mu g\,m^{-3}$, indicating very low air pollution. During the only polluted episode in Lans in 2018, the concentrations observed were very close to those measured at the valley floor, in contrast to the rest of the year. It was therefore likely to be associated with a long-range transport phenomenon. Hence, the only source of measurement available corroborates simulations in the sense that the villages of medium altitude are little subjected to PM pollution. Additional measurements are necessary to confirm this finding, for example by instrumenting the flanks of the Grésivaudan valley.

---

[1] `https://www.atmo-auvergnerhonealpes.fr/sites/ra/files/atoms/files/fiche_synthetique_mesures_anuelles_lans_en_vercors.pdf`

5.4 Concluding remarks

- The method proposed by Allwine and Whiteman (1994) to identify stagnation and ventilation zones – based solely on the atmospheric dynamics – has been adapted to take advantage of spatially resolved simulations outputs. In particular, spatially-resolved near-surface winds are used to determine transport rather than the winds at the initial positions (see section 5.1.3). The zones identified are statistically significant within an episode and are consistent from one episode to another (see Figure 5.4). At night, prevailing down-valley flows are responsible for the development of a low ventilation zone in most of the Grenoble Y. At daytime, the Voreppe valley remains mostly slightly ventilated but the southern branch, the Grésivaudan valley and the city-center of Grenoble are classified as stagnation zones. This is consistent with Figure 4.6, which illustrates that down-valley flows fades in the Grésivaudan valley and the southern branch of the Grenoble Y but not in the Voreppe valley.

- The PM concentration field simulated in this study does not seem to be directly comparable with the measurements at the monitoring stations. This is evidenced in Figures 5.5 and 5.6 by the local homogeneity of the average simulated concentration field around measurement stations when emissions can vary substantially. The sizes of the grid cells used, both horizontally (111 m) and vertically (26 m), are most probably too large to capture the variability seen in the measurements. Specifically, it appears that advection is of greater importance in the simulations, as illustrated by Figure 5.8.

- The comparison of simulated and measured PM concentrations highlights intense concentration peaks that do not coincide with measurements. The possible underestimation of the turbulent diffusion was examined since the use of the Deardorff model in WRF can lead to the suppression of turbulence in a stably stratified atmosphere. Using a semi-empirical approach also based on Deardorff's model, a new minimum threshold for turbulent diffusion of tracers has been determined. Its implementation in the model successfully smoothed-out the spurious concentration peaks, confirming they may be a result of too little diffusion in the model. The increased minimum turbulent diffusion generally improves the results for the background pollution station FRE but tends to reduce the simulated concentrations too much.

- For this study, the most detailed (100 m of horizontal resolution) emission inventory for the region available at the time is used. Since atmospheric dynamics are correctly captured (see section 3.4), it is interesting to analyze qualitatively the PM dispersion results in terms of average concentration, even if the comparison of simulated concentration with measurements is not fully satisfactory. Average concentration levels are better captured in the simulations without increasing the minimum turbulent diffusion, and so result using the original WRF configuration have been used for this purpose.

- Time-average PM_{10} concentrations reveal significant and consistent spatial contrasts for all the episodes considered (see Figure 5.14). Within the urbanized valley floor of the Grenoble Y, the time-averaged concentrations can vary twofold from one neighborhood to the other. The simulated concentrations in the Grenoble Y are generated by industrial activities (5 to 10 %), road transport (20 to 50 % depending on the distance to the main roads) and domestic heating for the rest (50 to 70 %).

The pollution hotspots respond to atmospheric dynamics in the sense that they are located outside the preferred traffic corridor of the valley winds. The pollution hotspots (foothills of the Chartreuse massif, the entrance of the Romanche valley and the southeast of the Grenoble basin) are systematically classified as stagnation or critical stagnation zones (see Figure 5.4). In contrast, the recirculation zone at the exit of the Voreppe valley is not found to be highly polluted, probably due to low local emissions. This underlines the complementarity of both approaches, allowing to determine which areas are particularly at risk and which are actually highly polluted.

- During WAB episodes, pollutant transport is dominated by the down-valley wind (see Figure 5.20). Pollutant transport by up-slope winds is observed in the simulations during the day (see Figures 5.18 and 5.19) in agreement with observations (Gohm et al., 2009) and simulations (Sabatier et al., 2020) in other deep valleys. However, this transport has no net effect as it does not significantly modify the average pollution levels (see Figures 5.18 and 5.20). None of the mid-altitude villages, apart from Bourg d'Oisans, appear to be affected by poor air quality. Observation that is consistent with the only available monitoring station at medium altitude available, indicating very low PM concentrations near Lans on the Vercors plateau in 2018. Finally, no systematic presence of elevated pollution layer has been observed.

- The simulated PM concentrations decrease with altitude in excellent agreement with the model proposed by Huang (1979). However, the coefficients resulting from the fit do not perfectly match the ranges proposed by Elliott (1961) and Huang (1979).

Conclusions & Perspectives

General conclusion

The purpose of this research work is to identify a framework to assess spatial heterogeneity of airborne particulate matter (PM) over long time scales while having an accurate representation of the effects of atmospheric dynamics in a mountainous topography. Let us recall that the originality of this work lies in the coupling between high-resolution numerical simulations and Weather Type Decomposition (WTD). In particular, it addresses the question: is it possible to associate a characteristic atmospheric circulation to a WT on the basis of one or several simulations of episodes belonging to this WT ? This work considers the case of an urbanized Alpine valley, namely the Y-shape Grenoble valley system. The key conclusions in response to the objectives introduced in section 1.5 are summarized here.

> **I** *Can a limited number of WT characterize most of the atmospheric circulations observed within the Grenoble valley ?*

A WTD is essential to meeting the stated end goal. A review of the literature shows that there is no consensus on a single solution to achieve a WTD. Several approaches are possible and they all have their own advantages and disadvantages. In order to choose the most relevant approach, the expected characteristics of the WTD are explored. In particular, the WTD should be composed of few WTs that are i) temporally persistent ii) synoptically similar and iii) associated with a characteristic local atmospheric circulation.

In view of these expected characteristics, an approach based on a PCA+K-MEANS applied to Z_{500} anomalies (Michelangeli et al., 1995) is selected. At first (see section 2.4.2), this approach is tested without modifications in order to identify if it is suitable or, if not, what are the aspects of this approach that need improvements. The main shortcoming is that this WTD does not give any particular importance to Grenoble with respect to the rest of the domain. Thus, the WTs that are identified make sense at large-scale but not necessarily for Grenoble, which may lie at the interface between positive and negative anomalies in the centroids (c.f. Figure 2.2). In a second step (see section 2.4.3), this WTD is tuned for Grenoble. To do so, local meteorological data are introduced in the reduced dataset in order to allow the K-MEANS to favor the clustering of synoptic situations yielding similar atmospheric conditions in the Grenoble Y. A parametric study allows to identify the maximum weight that can be given to local data while preserving the centroids of the original method and the average duration of the episodes. Despite the introduction of local data, the weather conditions in the Grenoble Y are not sufficiently discriminating. To illustrate this, it is possible to encounter situations where Grenoble is located in a negative Z_{500} anomaly for the winter anticyclonic blocking (WAB) regime. The problem appears to be over-constrained (in the sense that desired characteristics are mutually exclusive), at least using this WTD approach. On the one hand, giving more importance to local data reduces the duration of episodes and the interpretability of WTs.

On the other hand, the variability of local weather conditions within a WT is too high to expect a characteristic atmospheric circulation in the Grenoble Y.

Another *a-priori* promising approach, based on recent developments in deep learning, is considered (see section 2.4.4). Using a deep neural network (ConvLSTM) allows to perform a non linear dimension reduction of the synoptic data taking also into account the temporal component using 4-day sequences (long short term memory part; LSTM) and spatial correlations (convolutional part). The clustering is then achieved using a hierarchical ascendant clustering (HAC) algorithm and without local data so as to evaluate the benefits of this new approach. Using the same number of clusters as for the PCA+K-MEANS classifications, the results are similar. The HAC allows to extend the analysis further and shows that a temporal evolution within a 4-day sequence centroid appears only for a higher number of clusters (see Figure 2.14). The potential for improvement allowed by the use of a more complex method such as ConvLSTM is thus masked by the drastic constraint on the number of WTs. Seen in this light, the centroids of the PCA+K-MEANS approach also take into account the temporal component. The intense and localized poles correspond to blocking while the diffuse and widespread poles reflect a certain synoptic circulation.

Besides, a simple classification of the winter data according to the temperature inversion intensity and atmospheric pressure allows to draw interesting conclusions (see section 2.4.5). First of all, it is possible to identify 4 regimes in terms of PM pollution in the Grenoble Y: a weakly polluted regime (weak temperature inversion, low atmospheric pressure), two moderately polluted regimes (strong temperature inversion and low atmospheric pressure or vice versa) and a strongly polluted regime (strong temperature inversion, high atmospheric pressure). These two simple meteorological parameters thus show the key role of atmospheric dynamics in determining air pollution episodes for the Grenoble Y. By combining this classification with patterns of the atmospheric circulation in the Grenoble Y, it is shown that the highly polluted regime is associated with a characteristic circulation (outflow from the Voreppe valley to the Rhone plain) for about 70 % of the time (see Figure 2.18).

In summary, the various approaches undertaken to produce a WTD that meet the requirements have not proved to be successful. Two major difficulties have stood in the way. The first one is intrinsic to the problem with the lack of internal structure in the synoptic data which forms a dense and continuous space (Philipp et al., 2016). Extracting a WTD is therefore difficult and often depends on the method and the data used (variables considered, domain extension, period, etc...). The other major difficulty is related to the objectives of this study, specifically to obtain a limited number of WTs. Due to the large diversity of synoptic conditions, it seems hardly feasible to accurately represent synoptic conditions from a few groups with a low internal variability. Moreover, the topography imposes a non-linearity between large-scale atmospheric circulations and their corresponding local responses. It follows that the large-scale intracluster variability must be very low so as to expect a characteristic local response within each WT, thereby imposing to consider a very large number of clusters. This point leads the author to conclude that the problem as initially stated was probably over-constrained. However, high pollution episodes (accounting for 30 % of winter PM air pollution) occur almost exclusively during the WAB regime. This regime corresponds to a synoptic blocking system – thus with reduced synoptic variability over the area of interest – and is often assumed to lead to an atmospheric circulation within valleys that decouples from synoptic conditions (Whiteman, 2000; Largeron and Staquet, 2016a). It is therefore possible to shift the objectives to the study of the WAB regime, which is the most important in terms of PM air pollution and for which one can reasonably expect few episodes to be representative of this regime.

II a) *How to capture the main atmospheric processes in the Grenoble Y in numerical simulations?*

The WRF model is a very versatile numerical code offering many parametrizations and options that must be chosen according to the characteristics of the meteorological events to be simulated. For this study, several elements have been carefully considered.

First of all, as the periods of interest are in winter, the initialization of the snowpack is performed from satellite observations (MODIS). This allows an improvement on an initialization with a horizontal resolution of 25 km (ERA5) down to 500 m, which is close to the resolution of the innermost domain. Regarding land cover the Corine Land Cover dataset with a horizontal resolution of 100 m is used. The PM emission inventory is also provided with a horizontal resolution of 100 m by the local air quality agency (and then passed to the WRF advection diffusion module).

Particular attention has been paid to the representation of the topography. Indeed, it is known that strong gradients in the topography can generate numerical instabilities, especially if a high vertical resolution is used (e.g. Mahrer, 1984; Connolly et al., 2021). The finer the vertical resolution, the more the model can capture the boundary layer dynamics which is an essential requirement for the stably-stratified situations considered here. Two configurations have been compared to determine the best compromise between vertical resolution and topographic fidelity. The first mass point heights are 13 and 17 m AGL for maximum slopes of 28 and 42°, respectively. The topographies are obtained from an optimal topography smoothing algorithm newly introduced in the course of this work (see 3.3). Note that these mass point heights correspond to the lowest values allowing for numerically stable results. Surprisingly, the different configurations produce very similar results in the Grenoble Y – over an episode in terms of mean wind, mean temperature and atmospheric stability – despite marked topographic differences (see section 3.3.3). Obviously, significant differences can be found where the topography is substantially affected. The author concludes that the large scales of topography are the main driver of atmospheric dynamics at the Grenoble Y scale.

II b) *Are the simulations representative of what has been observed in the selected episodes?*

For this study four persistent episodes, all belonging to the WAB regime, have been simulated (see section 3.1). These episodes have different atmospheric conditions in terms of temperature inversion strength, atmospheric pressure and cloud cover in order to reflect the internal variability of the WAB regime.

The simulated episodes are systematically compared with available measurements in the Grenoble valley, such as temperature, wind, humidity and atmospheric pressure (see section 3.4.1). In general, the simulations are in good agreement with the measurements. For example the diurnal cycle with a persistent down-valley wind, which is more pronounced at night than during the day, is well captured (see Figure 3.23). However, the simulations slightly but systematically underestimate the intensity of this valley wind, indicating that a physical process is poorly or partially captured (which may be a misrepresentation of the down-slope winds). Temperatures are also correctly reproduced, especially at the valley floor and at mid-valley height. For the last days of $\mathcal{E}_1$ and the last half-day of $\mathcal{E}_3$, the simulations show an atmospheric circulation in the Voreppe valley that is opposite of that measured. Several hypotheses are explored to try to understand the origin of this discrepancy in section 3.4.2.2. Among them, one can mention the fidelity of the topography; the large-scale flow; the sensitivity to the size and horizontal resolution of the domain and the sensitivity to the initialization date. None of these factors, at least in the ranges explored, can explain the origin of this erroneous wind channeling. The most likely hypothesis remains the underestimation of the valley wind which could shelter less the Grenoble Y from an external synoptic disruption.

Excluding from the analyses parts of the simulations for which the wind orientation in the Grenoble Y does not match the measurements, the simulations are considered to be in good enough agreement with the measurements to be meaningful. This conclusion is notably supported by the good representation of temperatures at least up to 1000 m ASL as well as the reproduction of the impact of the diurnal cycle on the valley wind system.

> **III** *Is it possible to identify an atmospheric circulation in the Grenoble Y that is representative for WAB episodes?*

Before WAB episodes are considered, the atmospheric circulation observed in general in winter over the period 2011-2017 is analyzed. This analysis is based on the classification of local atmospheric circulations observed in the Grenoble Y, introduced in section 2.4.2. These local circulation modes are essentially intraday (88 % of them last less than 6 hours). From their frequency of occurrence as a function of the day one can determine whether these modes are mainly generated by thermal effects, channeling of the synoptic flow or a combination of both processes. By analyzing how these modes interact, the general trend shows a thermally driven circulation with valley winds mainly flowing down at night and up during the day. A specificity of the Grenoble Y also appears: the Grésivaudan valley is regularly dominated by a down-valley wind during daytime. The day-night transition passes through a sequence of well identified modes, contrary to the night-day transition.

The simulated episodes are first compared in terms of their time-averaged winds near the surface during both day- and night-time. In both cases, the four episodes show very similar mean patterns (see Figures 4.5 and 4.6). The nighttime is dominated by down-valley winds in the three branches of the Grenoble Y. In the Voreppe valley, the down-valley wind detaches from the ground slightly after a topographic depression, reducing the average wind speed observed in the downstream section of the valley. A valley exit jet of the order of $5\,\mathrm{m\,s^{-1}}$ is generated between ground-level and 500 m ASL under the effect of a topographic constriction at the exit of the Voreppe valley (see Figure 4.8). This topographic constriction channels this valley exit jet to form a recirculation cell. During the day, the down-valley wind weakens or even disappears in the Grésivaudan valley and in the southern branch of the Grenoble Y. But the down-valley wind is systematically maintained in the Voreppe valley. This observation is in agreement with the measurements (see section 3.4.1.2) and the statistical analysis that extends this observation to 70 % of the WAB episodes (see Figure 2.18). Thus, in contrast to what happens during most of the winter (see Figure 4.4), the valley wind does not undergo a diurnal change of direction when a thermal inversion is present. It is likely that a persistent cold air pool (persistent cold air pool) maintains the pressure gradient between the valley and the plain by preserving their temperature differential also throughout the day. A study of the volumetric flow rates in the Grenoble basin allows to determine the contributions of each valley over the full diurnal cycle (see section 4.2.1.4). The net outflow in the Voreppe valley is compensated by a contribution from the Grésivaudan valley, which is either equal to ($\mathcal{E}_1$ and $\mathcal{E}_3$) or much greater than that of the southern branch ($\mathcal{E}_2$ and $\mathcal{E}_4$).

The vertical structure of the wind is also compared between the different episodes (see section 4.2.2). A decoupling between the atmospheric dynamics in the Grenoble Y and the flow above, as generally expected for a valley (Whiteman, 2000; Largeron and Staquet, 2016a), is observed for most of the episodes. Indeed, down-valley winds generally dominate, even when a synoptic wind channeling would impose a reverse wind direction. However, this decoupling is not perfect. Indeed, the dynamics that develop in the valley are definitely impacted by the synoptic conditions, as found in other valleys by Reeves and Stensrud (2009) and Lareau et al. (2013). For example, the height over which these valley winds develop varies between 500 and 1000 m AGL depending on the synoptic conditions. Sometimes, disturbances of large-scale flow disrupt the valley winds down to the ground (as for beginning of $\mathcal{E}_2$). The fact that Grenoble is located on the outer border of the Alpine arc may explain why the Grenoble Y benefits from a limited sheltering effect. Moreover, the orientation of the Voreppe valley – which leads directly to the Rhône plain – is conducive to channeling of the prevailing synoptic winds, further reducing the sheltering effect.

The episodes are also compared in terms of atmospheric stability, notably through the inversion height (maximum altitude for which the vertical gradient of potential temperature is higher than the dry adiabatic gradient). For $\mathcal{E}_1$ and $\mathcal{E}_3$ (episodes with the most pronounced thermal inversions) this inversion height oscillates about 1000 m AGL. This result is consistent with the findings of a previous study on the Grenoble Y (Largeron, 2010) and Whiteman's conjecture that the inversion develops up to the average height of the surrounding massifs. However, over the 4 episodes, the inversion height varies significantly, ranging from 500 to 1500 m AGL. This observation is consistent with the results of Lareau et al. (2013) indicating that PCAPs structures can be largely modified by large-scale advection or subsidence. Besides, it is shown in Figure 4.12 that a strong correlation ($0.68 < r < 0.95$) is obtained between the valley heat deficit and the inversion height for the episodes considered. This leads the author to think that the inversion height depends on the intensity of this thermal inversion, but is capped by the height of the surrounding massifs (Whiteman's conjecture). Figure 3 of Lareau et al. (2013) (reproduced in Figure A.8) illustrates a similar behavior in the Salt Lake Valley.

In summary, the simulated episodes exhibit a characteristic atmospheric circulation close to the surface for the Grenoble Y. This characteristic circulation is dominated by down-valley winds. Based on a statistical analysis of wind measurements in the Grenoble Y, this conclusion can reasonably be extended to WAB episodes in general. However, the height over which these valley winds develop as well as the atmospheric stability within the valleys are markedly affected by the synoptic condition.

IV a) *What are the stagnation and ventilation zones based on an analysis of the atmospheric dynamics?*

Allwine and Whiteman (1994) developed a typology to classify a measurement station and its surrounding area based on pointwise wind data as a stagnation zone, a ventilation zone or a recirculation zone. The present work uses a slightly modified version of this method (introduced in Largeron, 2010), which considers the addition of a low ventilation zone and a critical stagnation zone so that the typology covers all possible scenarios. It is also shown in the present work that it is relevant, if this method is applied to a simulation result, to use for the advection the spatially resolved velocity field rather than the velocity field at the "fictitious station" considered. Moreover, as several episodes are compared, a notion of statistical significance has also been introduced. The analyses are performed separately for day and night, to take into account the diurnal cycle in the atmospheric circulation. The results are very consistent for the episodes considered and statistically significant (see Figure 5.4). At night, most of the valley floor of the Grenoble Y is in a low ventilation zone due to the transport resulting from the down-valley winds. The valley rim on the flanks of the mountains – as well as the mountains in general – are in a stagnation or critical stagnation zone. The jet at the exit of the Voreppe valley generates a recirculation zone, of varying extent depending on its intensity. During the day, the Voreppe valley remains categorized overall as a low ventilation zone because of the continued existence of the down-valley wind. The southern branch of the Grenoble Y and the Grésivaudan valley switch to a stagnation zone as their valley-wind decrease in intensity. The Romanche valley, where the valley wind does not develop near the surface, remains stagnant during both day and night. From a dynamical point of view, the situation in the Grenoble Y is not the most critical, in the sense that, at night, a descending valley wind allows to partially evacuate the pollution towards the Rhône plain. However, the situation is not ideal in terms of air quality: the valley wind does not allow the Grenoble Y to be washed out (a "low" ventilation zone) and it weakens strongly during the day, when emissions are at their highest. This typology makes it possible to determine whether the atmospheric dynamics tend to accumulate or disperse the locally emitted pollutants. In order to evaluate the health impacts it is necessary to couple this analysis with the emissions.

> **IV b)** *Taking into account PM emissions, what can be inferred about heterogeneities of spatial distribution of PM concentration?*

The PM emission inventory with a horizontal resolution of 100 m allows, thanks to the WRF advection diffusion module, to simulate the concentration field observed during the episodes considered (neglecting chemistry and deposition). However, the comparison with measurements is not entirely satisfactory. Firstly, the temporal variability of the simulated concentrations is higher than that observed in the measurements. It is likely that advection plays a more important role at 13 m AGL (height at which the pollutants are advected in the simulations) than at a few meters above ground level (height at which the pollutants are measured) and partially explains this higher variability. In addition, very high concentration peaks are present in the simulations and absent from the measurements. They are attributed to an underestimation of the SGS turbulence by the Deardorff model in the ground-based inversion (under stably stratified conditions, see Mauritsen (2011)). A new minimum SGS turbulent diffusion threshold based on available measurements in the Grenoble Y is introduced. This modification allows to smooth the concentration peaks obtained in the simulations. However, with this modification, the concentrations are mostly underestimated compared to the observations. This may be due to the fact that the minimum SGS turbulent diffusion threshold has been applied on the horizontal and on the vertical while applying it only on the horizontal would have allowed for a better consideration of the stratification. The approach without modification of the SGS turbulence has been retained for the analysis of the concentration fields as the temporally averaged concentrations are closer to the measurements.

Near-surface PM_{10} concentrations, time-averaged over the episodes, are compared for the different episodes (see Figure 5.14). Strong spatial heterogeneities – responding to the valley wind footprint – are observed for each episode. Pollution hotspots are the same from one episode to the other and they are located in areas standing away from the prevailing valley wind corridors: on the foothills of Chartreuse in the Grésivaudan valley and in the south-east of the Grenoble basin. Another pollution hot spot is at the junction of the Grenoble Y with the Romanche valley, where pollutants are trapped by a topographic constriction. These hotspots correspond to stagnation zones identified solely through atmospheric dynamics.

In general, the simulated PM concentrations decrease exponentially with altitude, in agreement with a theoretical model proposed by Huang (1979). The upward flow along the slopes in the afternoon causes a vertical transport of pollutants but not to a sufficiently large extent to significantly impact the time-average concentrations. Similarly, elevated pollution layer footprints are not observed in the time-averaged concentrations, even though they do appear from time to time. Generally speaking, PM accumulates mainly at the valley floor. The air in the valley wind corridor, downwind of the first pollution areas, is polluted whether there are local PM emissions or not.

To summarize, the common atmospheric circulation observed during the simulated episodes is responsible for a heterogeneous distribution of PM in the Grenoble Y (which is consistent from one episode to another). As it has been shown that this circulation is in fact characteristic of WAB episodes in general – including most of the pollution events – the health impact on the inhabitants probably depends on where they live and work. This impact is supposed to be all the more important as they live close to the valley floor and outside the prevailing valley wind circulation corridor.

Perspectives

The author envisions several axes to pursue the current research work.

- **Atmospheric processes:** It would be beneficial to increase the resolution of the domain, especially the vertical resolution, in order to be able to correctly capture the down-slope winds. Of course, this is not an easy task and has proven to be one of the most challenging aspect of this research work. It would be important to consider the possible impact of low level stratus. A study was attempted but turned out to be unsuccessful. It would be necessary to choose an episode of stratus persisting over several days and to ensure that the moisture in the ground is sufficiently well initialized such that the stratus forms.

- **WTD:** During the course of this work, the topography has been perceived as a constraint, in particular because a slight change of synoptic wind direction can generate a complete inversion of the atmospheric circulation observed in the Grenoble Y. With hindsight, the author wonders if it would not be possible to see this constraint as an opportunity. Is it not possible to identify most of the possible local circulations in the Grenoble Y under the constraints of this topography? To do so, it would be interesting to carry out a semi-idealized simulation of the Grenoble Y and its surroundings (to which the Chambéry Y should be included) for different synoptic wind directions. This would perhaps allow to establish a typology of passive effects of the Grenoble topography on large-scale wind. It would enable to identify the stagnation and ventilation zones for each of these circulations.

- **Population exposure to PM:** It would be interesting to compare high resolution simulation results (e.g. the results at 111 m) with intermediate resolution results (e.g. 500 or 1000 m). This would allow to determine at which horizontal resolution the circulation in the Grenoble valley is sufficiently well captured to be used for the dispersion of pollutants. For example, this would also challenge the development of operational models: is the new horizontal resolution of the French operational model (1200 m) sufficient to correctly capture the synoptic wind channeling in the Grenoble valley (6 km at the widest)? Does it allow the reproduction of thermal winds? If not, what is the horizontal resolution needed to achieve this? Is it possible to simulate a complete winter with this resolution?

Key to the success of such future is access to more observations. In particular, it is imperative to obtain at least one vertical wind profile measurement (e.g. using a lidar) in the Grenoble basin or in the Voreppe and Grésivaudan valleys. This would allow to evaluate the simulations at altitudes higher than 100 m AGL so as to identify which characteristics of the wind field are or are not correctly reproduced. If the means allow it, it seems very promising to instrument simultaneously the Grenoble Y and the Chambéry Y so as to investigate their interactions in terms of atmospheric dynamics. Concerning PM, it would be interesting to measure vertical concentration profiles in the Grenoble basin (using tethered balloons, drones or lidars) and near the surface for different altitudes along the Belledonne flank. This would allow to evaluate the effective decay rate of PM with altitude and to verify that villages at medium altitudes are effectively not exposed to high PM concentrations. Finally, placing temporary monitoring stations in the hot spots of PM concentrations would allow to identify if specific public policies are to be undertaken in these areas.

Conclusions for the Mobil'Air comity

This work was funded by the interdisciplinary Mobil'Air program, which seeks to identify specific measures to limit Particulate Matter air pollution and associated health impacts in cities, using the Grenoble Metropolis as a reference. The objective of this work within the program was to improve the knowledge on the spatial distribution of pollutants at long time scales by focusing on better characterizing their transport, that is partially driven by the surrounding topography. The approach undertaken in this work to meet this objective, i.e. a weather type approach, has only proven successful for winter anticyclonic episodes. Consequently, the concentration fields produced do not allow for an analysis of the long-term impact of Particulate Matter on the population.

It should be stressed, however, that winter anticyclonic episodes are responsible for a significant proportion of the Particulate Matter air pollution episodes, thus accounting for 30 % of the winter pollution and 18 % of the annual pollution. The pollution hotspots identified are therefore relevant as the pollution levels associated with winter anticyclonic episodes are high enough to impact the annual average concentration level. Furthermore, the discrepancies observed between areas of high emissions and areas of high Particulate Matter concentration demonstrates the usefulness of a fine resolution of the pollutant transport at the valley scale.

It appears that these pollution hot spots are topographically driven and, at least for some of them, independent on the local atmospheric circulation mode in the valley, further reinforcing the interest of having identified these areas. A semi-idealized study of the Grenoble valley system or a wind tunnel experiment would allow to evaluate this hypothesis and to identify precisely the stagnation zones, whatever the atmospheric conditions.

Finally, a path of investigation initiated during this work showed that an intermediate horizontal resolution (of the order of a few hundred meters) allows for the identification of atmospheric dynamics similar to that obtained with a resolution of 111 m. Such resolutions may allow for direct simulation of a complete year, and thus allow an assessment of the impact of air pollution on an annual time scale.

Bibliography

Allwine, K. and Whiteman, C. (1994). Single-station integral measures of atmospheric stagnation, recirculation and ventilation. *Atmospheric Environment*, 28(4):713–721.

Alpine convention (2015). DEMOGRAPHIC CHANGES IN THE ALPS : Report on the state of the Alps. Technical report.

Anderson, J. O., Thundiyil, J. G., and Stolbach, A. (2012). Clearing the Air: A Review of the Effects of Particulate Matter Air Pollution on Human Health. *Journal of Medical Toxicology*, 8(2):166–175.

Arduini, G. (2017). *Wintertime Stable Boundary-Layer Processes in Alpine Valleys*. PhD thesis, Université de Grenoble Alpes, Grenoble.

Arduini, G., Chemel, C., and Staquet, C. (2020). Local and nonlocal controls on a persistent coldair pool in the Arve River Valley. *Quarterly Journal of the Royal Meteorological Society*, 146(731):2497–2521.

Bader, D. C. and Whiteman, C. D. (1989). Numerical Simulation of Cross-Valley Plume Dispersion during the Morning Transition Period. *Journal of Applied Meteorology and Climatology*, 28(7):652–664. Publisher: American Meteorological Society Section: Journal of Applied Meteorology and Climatology.

Balanzino, A., Ferrero, E., Pirovano, G., and Riva, G. M. (2012). Particulate matter pollution simulations in complex terrain. *International Journal of Environment and Pollution*, 48(1-4):8.

Bao, J., Chow, F. K., and Lundquist, K. A. (2018). Large-Eddy Simulation over Complex Terrain Using an Improved Immersed Boundary Method in the Weather Research and Forecasting Model. *Monthly Weather Review*, 146(9):2781–2797.

Beck, C., Weitnauer, C., and Jacobeit, J. (2014). Downscaling of monthly PM 10 indices at different sites in Bavaria (Germany) based on circulation type classifications. *Atmospheric Pollution Research*, 5(4):741–752.

Bohren, C. F. and Beschta, R. L. (1979). Snowpack albedo and snow density. *Cold Regions Science and Technology*, 1(1):47–50.

Bou-Zeid, E., Higgins, C., Huwald, H., Meneveau, C., and Parlange, M. B. (2010). Field study of the dynamics and modelling of subgrid-scale turbulence in a stable atmospheric surface layer over a glacier. *Journal of Fluid Mechanics*, 665:480–515.

Boé, J. and Terray, L. (2008). A Weather-Type Approach to Analyzing Winter Precipitation in France: Twentieth-Century Trends and the Role of Anthropogenic Forcing. *Journal of Climate*, 21(13):3118–3133.

Carrera, M. L., Gyakum, J. R., and Lin, C. A. (2009). Observational Study of Wind Channeling within the St. Lawrence River Valley. *Journal of Applied Meteorology and Climatology*, 48(11):2341–2361.

Cassou, C. (2004). loscillation nord-atlantique. *La Météorologie*, page 12.

Cassou, C. (2008). Intraseasonal interaction between the MaddenJulian Oscillation and the North Atlantic Oscillation. *Nature*, 455(7212):523–527.

Castelli, S. T., Belfiore, G., Anfossi, D., Elampe, E., and Clemente, M. (2011). Modelling the meteorology and traffic pollutant dispersion in highly complex terrain: the ALPNAP Alpine Space Project. *International Journal of Environment and Pollution*, 44(1/2/3/4):235.

Chemel, C., Arduini, G., Staquet, C., Largeron, Y., Legain, D., Tzanos, D., and Paci, A. (2016). Valley heat deficit as a bulk measure of wintertime particulate air pollution in the Arve River Valley. *Atmospheric Environment*, 128:208–215.

Chemel, C., Chaxel, E., and Couach, O. (2005). INFLUENCE OF THE INTERACTIONS OF LOCAL DYNAMICAL PROCESSES WITH LARGE-SCALE FLOW ON AIR QUALITY IN THE GRENOBLE AREA. page 4.

Chen, F. and Dudhia, J. (2001). Coupling an Advanced Land SurfaceHydrology Model with the Penn StateNCAR MM5 Modeling System. Part I: Model Implementation and Sensitivity. *Monthly Weather Review*, 129(4):569–585.

Chow, F. K., De Wekker, S. F., and Snyder, B. J., editors (2013). *Mountain Weather Research and Forecasting: Recent Progress and Current Challenges*. Springer Atmospheric Sciences. Springer Netherlands, Dordrecht.

Cohen, A. J., Brauer, M., Burnett, R., Anderson, H. R., Frostad, J., Estep, K., Balakrishnan, K., Brunekreef, B., Dandona, L., Dandona, R., Feigin, V., Freedman, G., Hubbell, B., Jobling, A., Kan, H., Knibbs, L., Liu, Y., Martin, R., Morawska, L., Pope, C. A., Shin, H., Straif, K., Shaddick, G., Thomas, M., van Dingenen, R., van Donkelaar, A., Vos, T., Murray, C. J. L., and Forouzanfar, M. H. (2017). Estimates and 25-year trends of the global burden of disease attributable to ambient air pollution: an analysis of data from the Global Burden of Diseases Study 2015. *The Lancet*, 389(10082):1907–1918.

Conangla, L., Cuxart, J., Jiménez, M. A., Martínez-Villagrasa, D., Miró, J. R., Tabarelli, D., and Zardi, D. (2018). Cold-air pool evolution in a wide Pyrenean valley. *International Journal of Climatology*, 38(6):2852–2865.

Connolly, A., Chow, F. K., and Hoch, S. W. (2021). Nested Large-Eddy Simulations of the Displacement of a Cold-Air Pool by Lee Vortices. *Boundary-Layer Meteorology*, 178(1):91–118.

Couach, O., Balin, I., Jimenez, R., Ristori, P., Perego, S., Kirchner, F., Simeonov, V., and Calpini, B. (2003). An investigation of ozone and planetary boundary layer dynamics over the complex topography of Grenoble combining measurements and modeling. *Atmos. Chem. Phys.*, page 14.

Couach, O., Kirchner, F., Jimenez, R., Balin, I., Perego, S., and van den Bergh, H. (2004). A development of ozone abatement strategies for the Grenoble area using modeling and indicators. *Atmospheric Environment*, 38(10):1425–1436.

Cuxart, J. (2015). When Can a High-Resolution Simulation Over Complex Terrain be Called LES? *Frontiers in Earth Science*, 3.

Daellenbach, K. R., Uzu, G., Jiang, J., Cassagnes, L.-E., Leni, Z., Vlachou, A., Stefenelli, G., Canonaco, F., Weber, S., Segers, A., Kuenen, J. J. P., Schaap, M., Favez, O., Albinet, A., Aksoyoglu, S., Dommen, J., Baltensperger, U., Geiser, M., El Haddad, I., Jaffrezo, J.-L., and Prévôt, A. S. H. (2020). Sources of particulate-matter air pollution and its oxidative potential in Europe. *Nature*, 587(7834):414–419.

de Foy, B., Zavala, M., Bei, N., and Molina, L. T. (2009). Evaluation of WRF mesoscale simulations and particle trajectory analysis for the MILAGRO eld campaign. *Atmos. Chem. Phys.*, page 20.

de Franceschi, M., Zardi, D., Tagliazucca, M., and Tampieri, F. (2009). Analysis of second-order moments in surface layer turbulence in an Alpine valley: ANALYSIS OF SECOND-ORDER MOMENTS. *Quarterly Journal of the Royal Meteorological Society*, 135(644):1750–1765.

Deardorff, J. W. (1980). Stratocumulus-capped mixed layers derived from a three-dimensional model. *Boundary-Layer Meteorology*, 18(4):495–527.

Defant, F. (1949). Zur Theorie der Hangwinde, nebst Bemerkungen zur Theorie der Berg- und Talwinde. *Archiv für Meteorologie, Geophysik und Bioklimatologie Serie A*, 1(3-4):421–450.

Demuzere, M., Trigo, R. M., Vila-Guerau de Arellano, J., and van Lipzig, N. P. M. (2009). The impact of weather and atmospheric circulation on O_3 and PM_{10} levels at a rural mid-latitude site. *Atmospheric Chemistry and Physics*, 9(8):2695–2714.

Demuzere, M. and van Lipzig, N. P. (2010). A new method to estimate air-quality levels using a synoptic-regression approach. Part I: Present-day O3 and PM10 analysis. *Atmospheric Environment*, 44(10):1341–1355.

Deppe, A. J., Gallus, W. A., and Takle, E. S. (2013). A WRF Ensemble for Improved Wind Speed Forecasts at Turbine Height. *Weather and Forecasting*, 28(1):212–228.

Diémoz, H., Barnaba, F., Magri, T., Pession, G., Dionisi, D., Pittavino, S., Tombolato, I. K. F., Campanelli, M., Della Ceca, L. S., Hervo, M., Di Liberto, L., Ferrero, L., and Gobbi, G. P. (2019). Transport of Po Valley aerosol pollution to the northwestern Alps Part 1: Phenomenology. *Atmospheric Chemistry and Physics*, 19(5):3065–3095.

Drobinski, P., Bastin, S., Dusek, J., Zängl, G., and Flamant, P. H. (2006). Flow splitting at the bifurcation between two valleys: idealized simulations in comparison with Mesoscale Alpine Programme observations. *Meteorology and Atmospheric Physics*, 92(3-4):285–306.

Durand, Y., Laternser, M., Giraud, G., Etchevers, P., Lesaffre, B., and Mérindol, L. (2009). Reanalysis of 44 Yr of Climate in the French Alps (19582002): Methodology, Model Validation, Climatology, and Trends for Air Temperature and Precipitation. *Journal of Applied Meteorology and Climatology*, 48(3):429–449.

Eckman, R. M. (1998). Observations and Numerical Simulations of Winds within a Broad Forested Valley. *JOURNAL OF APPLIED METEOROLOGY*, 37:14.

Egger, J., Bajrachaya, S., Egger, U., Heinrich, R., Reuder, J., Shayka, P., Wendt, H., and Wirth, V. (2000). Diurnal Winds in the Himalayan Kali Gandaki Valley. Part I: Observations. *MONTHLY WEATHER REVIEW*, 128:17.

Egger, J., Bajrachaya, S., Heinrich, R., Kolb, P., Mmlein, S. L., Mech, M., Reuder, J., Per, W. S., Shakya, P., Schween, J., and Wendt, H. (2002). Diurnal Winds in the Himalayan Kali Gandaki Valley. Part III: Remotely Piloted Aircraft Soundings. *MONTHLY WEATHER REVIEW*, 130:17.

Ekhart, E. (1948). De la structure thermique de latmosphere dans la montagne [On the thermal structure of the mountain atmosphere]. *La météorologie*, 4(9):3–26.

Elliott, W. (1961). The vertical diffusion of gas from a continuous source. *International journal of air and water pollution*, 4:33–46.

Emeis, S., Jahn, C., Münkel, C., Münsterer, C., and Schäfer, K. (2007). Multiple atmospheric layering and mixing-layer height in the Inn valley observed by remote sensing. *Meteorologische Zeitschrift*, 16(4):415–424.

Esposito, E. and Abramson, S. F. (2021). The European coal curse. *Journal of Economic Growth*, 26(1):77–112.

European Environment Agency (2020). *Air quality in Europe: 2020 report.* Publications Office, LU.

Fern, S., Mart, A. L., Garc, E., Merino, S., Lorenzana, S., and Rodrigo, J. S. (2018). Sensitivity Analysis of the WRF Model: Wind-Resource Assessment for Complex Terrain. *JOURNAL OF APPLIED METEOROLOGY AND CLIMATOLOGY*, 57:21.

Ferrero, E., Alessandrini, S., Anderson, B., Tomasi, E., Jimenez, P., and Meech, S. (2019). Lagrangian simulation of smoke plume from fire and validation using ground-based lidar and aircraft measurements. *Atmospheric Environment*, 213:659–674.

Fowler, D., Pilegaard, K., Sutton, M., Ambus, P., Raivonen, M., Duyzer, J., Simpson, D., Fagerli, H., Fuzzi, S., Schjoerring, J., Granier, C., Neftel, A., Isaksen, I., Laj, P., Maione, M., Monks, P., Burkhardt, J., Daemmgen, U., Neirynck, J., Personne, E., Wichink-Kruit, R., Butterbach-Bahl, K., Flechard, C., Tuovinen, J., Coyle, M., Gerosa, G., Loubet, B., Altimir, N., Gruenhage, L., Ammann, C., Cieslik, S., Paoletti, E., Mikkelsen, T., Ro-Poulsen, H., Cellier, P., Cape, J., Horváth, L., Loreto, F., Niinemets, ., Palmer, P., Rinne, J., Misztal, P., Nemitz, E., Nilsson, D., Pryor, S., Gallagher, M., Vesala, T., Skiba, U., Brüggemann, N., Zechmeister-Boltenstern, S., Williams, J., O'Dowd, C., Facchini, M., de Leeuw, G., Flossman, A., Chaumerliac, N., and Erisman, J. (2009). Atmospheric composition change: EcosystemsAtmosphere interactions. *Atmospheric Environment*, 43(33):5193–5267.

Fuzzi, S., Baltensperger, U., Carslaw, K., Decesari, S., Denier van der Gon, H., Facchini, M. C., Fowler, D., Koren, I., Langford, B., Lohmann, U., Nemitz, E., Pandis, S., Riipinen, I., Rudich, Y., Schaap, M., Slowik, J. G., Spracklen, D. V., Vignati, E., Wild, M., Williams, M., and Gilardoni, S. (2015). Particulate matter, air quality and climate: lessons learned and future needs. *Atmospheric Chemistry and Physics*, 15(14):8217–8299.

Garavaglia, F., Gailhard, J., Paquet, E., Lang, M., Garcon, R., and Bernardara, P. (2010). Introducing a rainfall compound distribution model based on weather patterns subsampling. *Hydrol. Earth Syst. Sci.*, page 15.

Geiger, R., Aron, R. H., and Todhunter, P. (1995). *The Climate Near the Ground*. Vieweg+Teubner Verlag, Wiesbaden.

Giovannini, L., Ferrero, E., Karl, T., Rotach, M. W., Staquet, C., Trini Castelli, S., and Zardi, D. (2020). Atmospheric Pollutant Dispersion over Complex Terrain: Challenges and Needs for Improving Air Quality Measurements and Modeling. *Atmosphere*, 11(6):646.

Gohm, A., Harnisch, F., and Fix, A. (2006). BOUNDARY LAYER STRUCTURE IN THE INN VALLEY DURING HIGH AIR POLLUTION (INNAP). page 5.

Gohm, A., Harnisch, F., Vergeiner, J., Obleitner, F., Schnitzhofer, R., Hansel, A., Fix, A., Neininger, B., Emeis, S., and Schäfer, K. (2009). Air Pollution Transport in an Alpine Valley: Results From Airborne and Ground-Based Observations. *Boundary-Layer Meteorology*, 131(3):441–463.

Golzio, A., Ferrarese, S., Cassardo, C., Diolaiuti, G. A., and Pelfini, M. (2021). Land-Use Improvements in the Weather Research and Forecasting Model over Complex Mountainous Terrain and Comparison of Different Grid Sizes. *Boundary-Layer Meteorology*, 180(2):319–351.

Grell, G. A., Emeis, S., Stockwell, W. R., Schoenemeyer, T., Forkel, R., Michalakes, J., Knoche, R., and Seidl, W. (2000). Application of a multiscale, coupled MM5/chemistry model to the complex terrain of the VOTALP valley campaign. *Atmospheric Environment*, 34(9):1435–1453.

Hartigan, J. A. and Wong, M. A. (1979). Algorithm AS 136: A K-Means Clustering Algorithm. *Applied Statistics*, 28(1):100.

He, K., Zhang, X., Ren, S., and Sun, J. (2015). Deep Residual Learning for Image Recognition. *arXiv:1512.03385 [cs]*. arXiv: 1512.03385.

Held, I. M. (2002). Northern Winter Stationary Waves: Theory and Modeling. *JOURNAL OF CLIMATE*, 15:20.

Hewitson, B. and Crane, R. (2002). Self-organizing maps: applications to synoptic climatology. *Climate Research*, 22:13–26.

Hinneburg, A. and Keim, D. A. (1999). Optimal Grid-Clustering : Towards Breaking the Curse of Dimensionality in High-Dimensional Clustering. page 11.

Hoffmann, P. and Schlünzen, K. H. (2013). Weather Pattern Classification to Represent the Urban Heat Island in Present and Future Climate. *Journal of Applied Meteorology and Climatology*, 52(12):2699–2714.

Holmes, H. A., Sriramasamudram, J. K., Pardyjak, E. R., and Whiteman, C. D. (2015). Turbulent Fluxes and Pollutant Mixing during Wintertime Air Pollution Episodes in Complex Terrain. *Environmental Science & Technology*, 49(22):13206–13214.

Hong, S.-Y., Noh, Y., and Dudhia, J. (2006). A New Vertical Diffusion Package with an Explicit Treatment of Entrainment Processes. *Monthly Weather Review*, 134(9):2318–2341.

Hoskins, B. J. and Karoly, D. J. (1981). The Steady Linear Response of a Spherical Atmosphere to Thermal and Orographic Forcing. *Journal of the Atmospheric Sciences*, 38(6):1179–1196. Publisher: American Meteorological Society Section: Journal of the Atmospheric Sciences.

Hsu, C.-H. and Cheng, F.-Y. (2019). Synoptic Weather Patterns and Associated Air Pollution in Taiwan. *Aerosol and Air Quality Research*, 19(5):1139–1151.

Huang, C. (1979). A theory of dispersion in turbulent shear flow. *Atmospheric Environment (1967)*, 13(4):453–463.

Hughes, J. K., Ross, A. N., Vosper, S. B., Lock, A. P., and Jemmett-Smith, B. C. (2015). Assessment of valley cold pools and clouds in a very high-resolution numerical weather prediction model. *Geoscientific Model Development*, 8(10):3105–3117.

Hurrell, J. W., Kushnir, Y., Ottersen, G., and Visbeck, M. (2003). An overview of the North Atlantic Oscillation. In Hurrell, J. W., Kushnir, Y., Ottersen, G., and Visbeck, M., editors, *Geophysical Monograph Series*, volume 134, pages 1–35. American Geophysical Union, Washington, D. C.

Iacono, M. J., Delamere, J. S., Mlawer, E. J., Shephard, M. W., Clough, S. A., and Collins, W. D. (2008). Radiative forcing by long-lived greenhouse gases: Calculations with the AER radiative transfer models. *Journal of Geophysical Research*, 113(D13).

Jaffrezo, J.-L., Aymoz, G., Delaval, C., and Cozic, J. (2005). Seasonal variations of the water soluble organic carbon mass fraction of aerosol in two valleys of the French Alps. *Atmospheric Chemistry and Physics*, 5(10):2809–2821.

Jenkinson, A. F. and Collinson, F. P. (1977). An initial climatology of gales over the North Sea. *Synoptic climatology branch memorandum*, 62:18.

Jimenez, P. A. and Dudhia, J. (2013). On the Ability of the WRF Model to Reproduce the Surface Wind Direction over Complex Terrain. *JOURNAL OF APPLIED METEOROLOGY AND CLIMATOLOGY*, 52:8.

Jiménez, P. A., González-Rouco, J. F., Montávez, J. P., García-Bustamante, E., and Navarro, J. (2009). Climatology of wind patterns in the northeast of the Iberian Peninsula. *International Journal of Climatology*, 29(4):501–525.

Jones, P. D., Hulme, M., and Briffa, K. R. (1993). A comparison of Lamb circulation types with an objective classification scheme. *International Journal of Climatology*, 13(6):655–663.

Klemp, J. B., Skamarock, W. C., and Fuhrer, O. (2003). Numerical Consistency of Metric Terms in Terrain-Following Coordinates. *MONTHLY WEATHER REVIEW*, 131:11.

Kossmann, M. and Sturman, A. P. (2003). Pressure-Driven Channeling Effects in Bent Valleys. *JOURNAL OF APPLIED METEOROLOGY*, 42:8.

Krinitskiy, M., Verezemskaya, P., Grashchenkov, K., Tilinina, N., Gulev, S., and Lazzara, M. (2018). Deep Convolutional Neural Networks Capabilities for Binary Classification of Polar Mesocyclones in Satellite Mosaics. *Atmosphere*, 9(11):426.

Lamb, H. (1972). British isles weather types and a register of the daily sequence of circulation patterns 1861-1971. *METEOROL. OFF., GEOPHYS. MEM.; G.B.*, (116):1–85.

Lareau, N. P., Crosman, E., Whiteman, C. D., Horel, J. D., Hoch, S. W., Brown, W. O. J., and Horst, T. W. (2013). The Persistent Cold-Air Pool Study. *Bulletin of the American Meteorological Society*, 94(1):51–63.

Lareau, N. P. and Horel, J. D. (2015). Dynamically Induced Displacements of a Persistent Cold-Air Pool. *Boundary-Layer Meteorology*, 154(2):291–316.

Largeron, Y. (2010). *Dynamique de la Couche Limite Atmosphérique stable en relief complexe. Application aux épisodes de pollution particulaire des vallées alpines.* PhD thesis.

Largeron, Y. and Staquet, C. (2016a). The Atmospheric Boundary Layer during Wintertime Persistent Inversions in the Grenoble Valleys. *Frontiers in Earth Science*, 4.

Largeron, Y. and Staquet, C. (2016b). Persistent inversion dynamics and wintertime PM10 air pollution in Alpine valleys. *Atmospheric Environment*, 135:92–108.

Liu, C., Huang, J., Hu, X.-M., Hu, C., Wang, Y., Fang, X., Luo, L., Xiao, H.-W., and Xiao, H.-Y. (2021). Evaluation of WRF-Chem simulations on vertical profiles of PM2.5 with UAV observations during a haze pollution event. *Atmospheric Environment*, 252:118332.

Livneh, B., Xia, Y., Mitchell, K. E., Ek, M. B., and Lettenmaier, D. P. (2010). Noah LSM Snow Model Diagnostics and Enhancements. *Journal of Hydrometeorology*, 11(3):721–738.

Lutgens, F. K., Tarbuck, E. J., Herman, R., and Tasa, D. G. (2018). *The Atmosphere: An Introduction to Meteorology.* Pearson edition.

Mahrer, Y. (1984). An Improved Numerical Approximation of the Horizontal Gradients in a Terrain-Following Coordinate System. *Monthly Weather Review*, 112(5):918–922.

Mahrt, L. (1998). Stratified Atmospheric Boundary Layers and Breakdown of Models. *Theoretical and Computational Fluid Dynamics*, 11(3-4):263–279.

Marjanovic, N., Wharton, S., and Chow, F. K. (2014). Investigation of model parameters for high-resolution wind energy forecasting: Case studies over simple and complex terrain. *Journal of Wind Engineering and Industrial Aerodynamics*, 134:10–24.

Matthias, V., Bewersdorff, I., Aulinger, A., and Quante, M. (2010). The contribution of ship emissions to air pollution in the North Sea regions. *Environmental Pollution*, 158(6):2241–2250.

Mauritsen, T. (2011). Advancing closures for stably stratied turbulence in global atmospheric models. page 12.

McKee, T. B. and O'Neal, R. D. (1989). The Role of Valley Geometry and Energy Budget in the Formation of Nocturnal Valley Winds. *Journal of Applied Meteorology and Climatology*, 28:445–456.

McKendry, I., Steyn, D., Lundgren, J., Hoff, R., Strapp, W., Anlauf, K., Froude, F., Martin, J., Banta, R., and Olivier, L. (1997). Elevated ozone layers and vertical down-mixing over the Lower Fraser Valley, BC. *Atmospheric Environment*, 31(14):2135–2146.

Meløysund, V., Leira, B., Høiseth, K. V., and Lisø, K. R. (2007). Predicting snow density using meteorological data. *Meteorological Applications*, 14(4):413–423.

Michelangeli, P.-A., Vautard, R., and Legras, B. (1995). Weather Regimes: Recurrence and Quasi Stationarity. *Journal of the Atmospheric Sciences*, 52(8):1237–1256.

Morrison, H., Thompson, G., and Tatarskii, V. (2009). Impact of Cloud Microphysics on the Development of Trailing Stratiform Precipitation in a Simulated Squall Line: Comparison of One- and Two-Moment Schemes. *Monthly Weather Review*, 137(3):991–1007.

Neemann, E. M., Crosman, E. T., Horel, J. D., and Avey, L. (2015). Simulations of a cold-air pool associated with elevated wintertime ozone in the Uintah Basin, Utah. *Atmospheric Chemistry and Physics*, 15(1):135–151.

Novack, L., Shenkar, Y., Shtein, A., Kloog, I., Sarov, B., and Novack, V. (2020). Anthropogenic or non-anthropogenic particulate matter: Which one is more dangerous and how to differentiate between the effects? *Chemosphere*, 240:124954.

Pant, P. and Harrison, R. M. (2013). Estimation of the contribution of road traffic emissions to particulate matter concentrations from field measurements: A review. *Atmospheric Environment*, 77:78–97.

Pateraki, S., Manousakas, M., Bairachtari, K., Kantarelou, V., Eleftheriadis, K., Vasilakos, C., Assimakopoulos, V., and Maggos, T. (2019). The traffic signature on the vertical PM profile: Environmental and health risks within an urban roadside environment. *Science of The Total Environment*, 646:448–459.

Pelly, J. L. and Hoskins, B. J. (2003). A New Perspective on Blocking. *JOURNAL OF THE ATMOSPHERIC SCIENCES*, 60:13.

Philipp, A., Beck, C., Huth, R., and Jacobeit, J. (2016). Development and comparison of circulation type classifications using the COST 733 dataset and software. *International Journal of Climatology*, 36(7):2673–2691.

Pineda, N., Jorba, O., Jorge, J., and Baldasano, J. M. (2004). Using NOAA AVHRR and SPOT VGT data to estimate surface parameters: application to a mesoscale meteorological model. *International Journal of Remote Sensing*, 25(1):129–143.

Plaut, G. and Simonnet, E. (2001). Large-scale circulation classification, weather regimes, and local climate over France, the Alps and Western Europe. *Climate Research*, 17:303–324.

Pu, Z., Chachere, C. N., Hoch, S. W., Pardyjak, E., and Gultepe, I. (2016). Numerical Prediction of Cold Season Fog Events over Complex Terrain: the Performance of the WRF Model During MATERHORN-Fog and Early Evaluation. *Pure and Applied Geophysics*, 173(9):3165–3186.

Quimbayo-Duarte, J. (2019). *Numerical modelling of the wintertime boundary layer over complex terrain and application to air-quality.* PhD thesis, Université Grenoble Alpes, Grenoble.

Quimbayo-Duarte, J., Chemel, C., Staquet, C., Troude, F., and Arduini, G. (2021). Drivers of severe air pollution events in a deep valley during wintertime: A case study from the Arve river valley, France. *Atmospheric Environment*, 247:118030.

Quimbayo-Duarte, J., Staquet, C., Chemel, C., and Arduini, G. (2019). Dispersion of Tracers in the Stable Atmosphere of a Valley Opening onto a Plain. *Boundary-Layer Meteorology*, 172(2):291–315.

Ramos, A. M., Cortesi, N., and Trigo, R. M. (2014). Circulation weather types and spatial variability of daily precipitation in the Iberian Peninsula. *Frontiers in Earth Science*, 2.

Rampanelli, G., Zardi, D., and Rotunno, R. (2004). Mechanisms of Up-Valley Winds. *Journal of the Atmospheric Sciences*, 61(24):3097–3111.

Reeves, H. D. and Stensrud, D. J. (2009). Synoptic-Scale Flow and Valley Cold Pool Evolution in the Western United States. *Weather and Forecasting*, 24(6):1625–1643.

Rex, D. F. (1950). Blocking Action in the Middle Troposphere and its Effect upon Regional Climate. *Tellus*, 2(4):275–301.

Ritter, M., Müller, M. D., Tsai, M.-Y., and Parlow, E. (2013). Air pollution modeling over very complex terrain: An evaluation of WRF-Chem over Switzerland for two 1-year periods. *Atmospheric Research*, 132-133:209–222.

Russo, A., Gouveia, C., Levy, I., Dayan, U., Jerez, S., Mendes, M., and Trigo, R. (2016). Coastal recirculation potential affecting air pollutants in Portugal: The role of circulation weather types. *Atmospheric Environment*, 135:9–19.

Sabatier, T., Largeron, Y., Paci, A., Lac, C., Rodier, Q., Canut, G., and Masson, V. (2020). Semiidealized simulations of wintertime flows and pollutant transport in an Alpine valley. Part II: Passive tracer tracking. *Quarterly Journal of the Royal Meteorological Society*, 146(727):827–845.

Saide, P. E., Carmichael, G. R., Spak, S. N., Gallardo, L., Osses, A. E., Mena-Carrasco, M. A., and Pagowski, M. (2011). Forecasting urban PM10 and PM2.5 pollution episodes in very stable nocturnal conditions and complex terrain using WRFChem CO tracer model. *Atmospheric Environment*, 45(16):2769–2780.

Santos, J. A., Belo-Pereira, M., Fraga, H., and Pinto, J. G. (2016). Understanding climate change projections for precipitation over western Europe with a weather typing approach: Precipitation Projections for Europe. *Journal of Geophysical Research: Atmospheres*, 121(3):1170–1189.

Santos-Alamillos, F., Pozo-Vázquez, D., Ruiz-Arias, J., and Tovar-Pescador, J. (2015). Influence of land-use misrepresentation on the accuracy of WRF wind estimates: Evaluation of GLCC and CORINE land-use maps in southern Spain. *Atmospheric Research*, 157:17–28.

Schaap, M., Roemer, M., Sauter, F., Boersen, G., Timmermans, R., and Builtjes, P. (2005). LOTOS-EUROS Documentation. Technical Report 2005/297.

Schmidli, J., Böing, S., and Fuhrer, O. (2018). Accuracy of Simulated Diurnal Valley Winds in the Swiss Alps: Influence of Grid Resolution, Topography Filtering, and Land Surface Datasets. *Atmosphere*, 9(5):196.

Schumann, U. (1991). Subgrid length-scales for large-eddy simulation of stratified turbulence. *Theoret. Comput. Fluid Dynamics*, 2:279–290.

Serafin, S., Adler, B., Cuxart, J., De Wekker, S., Gohm, A., Grisogono, B., Kalthoff, N., Kirshbaum, D., Rotach, M., Schmidli, J., Stiperski, I., Veenaj, ., and Zardi, D. (2018). Exchange Processes in the Atmospheric Boundary Layer Over Mountainous Terrain. *Atmosphere*, 9(3):102.

Silcox, G. D., Kelly, K. E., Crosman, E. T., Whiteman, C. D., and Allen, B. L. (2011). Wintertime PM2.5 concentrations during persistent, multi-day cold-air pools in a mountain valley. *Atmospheric Environment*, page S1352231011011204.

Simonyan, K. and Zisserman, A. (2014). Very Deep Convolutional Networks for Large-Scale Image Recognition. *arXiv:1409.1556 [cs]*. arXiv: 1409.1556.

Skamarock, W. C. (2004). Evaluating Mesoscale NWP Models Using Kinetic Energy Spectra. *Monthly Weather Review*, 132(12):3019–3032.

Stull, R. B. (2003). *An introduction to boundary layer meteorology*. Number 13 in Atmospheric sciences library. Kluwer, Dordrecht, reprint edition.

Suárez-Molina, D. (2021). Sensitivity analysis of the WRF model_ Assessment of performance in high resolution simulations in complex terrain in the Canary Islands. *Atmospheric Research*, page 18.

Szintai, B., Kaufmann, P., and Rotach, M. W. (2010). Simulation of Pollutant Transport in Complex Terrain with a Numerical Weather PredictionParticle Dispersion Model Combination. *Boundary-Layer Meteorology*, 137(3):373–396.

Taylor, D. M., Chow, F. K., Delkash, M., and Imhoff, P. T. (2016). Numerical simulations to assess the tracer dilution method for measurement of landfill methane emissions. *Waste Management*, 56:298–309.

Tomasi, E., Giovannini, L., Falocchi, M., Antonacci, G., Jiménez, P. A., Kosovic, B., Alessandrini, S., Zardi, D., Delle Monache, L., and Ferrero, E. (2019). Turbulence parameterizations for dispersion in sub-kilometer horizontally non-homogeneous flows. *Atmospheric Research*, 228:122–136.

Tomasi, E., Giovannini, L., Zardi, D., and de Franceschi, M. (2017). Optimization of Noah and Noah_mp WRF Land Surface Schemes in Snow-Melting Conditions over Complex Terrain. *Monthly Weather Review*, 145(12):4727–4745.

Tong, H., Walton, A., Sang, J., and Chan, J. C. (2005). Numerical simulation of the urban boundary layer over the complex terrain of Hong Kong. *Atmospheric Environment*, 39(19):3549–3563.

Toro A, R., Kvaki, M., Klai, Z. B., Korain, D., Morales S, R. G., and Leiva G, M. A. (2019). Exploring atmospheric stagnation during a severe particulate matter air pollution episode over complex terrain in Santiago, Chile. *Environmental Pollution*, 244:705–714.

Trigo, R. M. and DaCamara, C. C. (2000). Circulation weather types and their influence on the precipitation regime in Portugal. *International Journal of Climatology*, 20(13):1559–1581.

Umek, L., Gohm, A., Haid, M., Ward, H. C., and Rotach, M. W. (2021). Largeeddy simulation of foehncold pool interactions in the Inn Valley during PIANO IOP 2. *Quarterly Journal of the Royal Meteorological Society*, 147(735):944–982.

VanReken, T. M., Dhammapala, R. S., Jobson, B. T., Bottenus, C. L., VanderSchelden, G. S., Kaspari, S. D., Gao, Z., Zhu, Q., Lamb, B. K., Liu, H., and Johnston, J. (2017). Role of persistent low-level clouds in mitigating air quality impacts of wintertime cold pool conditions. *Atmospheric Environment*, 154:236–246.

Vautard, R., Bessagnet, B., Chin, M., and Menut, L. (2005). On the contribution of natural Aeolian sources to particulate matter concentrations in Europe: Testing hypotheses with a modelling approach. *Atmospheric Environment*, 39(18):3291–3303.

Vlachas, P. R., Byeon, W., Wan, Z. Y., Sapsis, T. P., and Koumoutsakos, P. (2018). Data-driven forecasting of high-dimensional chaotic systems with long short-term memory networks. *Proceedings of the Royal Society A: Mathematical, Physical and Engineering Sciences*, 474(2213):20170844.

Vogel, B., Gro, G., and Wippermann, F. (1986). MESOKLIP (first special observation period): Observations and numerical simulation A comparison. *Boundary-Layer Meteorology*, 35(1-2):83–102.

Vosper, S. B. and Brown, A. R. (2008). Numerical Simulations of Sheltering in Valleys: The Formation of Nighttime Cold-Air Pools. *Boundary-Layer Meteorology*, 127(3):429–448.

Vosper, S. B., Hughes, J. K., Lock, A. P., Sheridan, P. F., Ross, A. N., Jemmett-Smith, B., and Brown, A. R. (2014). Cold-pool formation in a narrow valley: Cold-pool Formation in a Narrow Valley. *Quarterly Journal of the Royal Meteorological Society*, 140(679):699–714.

Vrac, M., Stein, M., and Hayhoe, K. (2007). Statistical downscaling of precipitation through nonhomogeneous stochastic weather typing. *Climate Research*, 34:169–184.

Vrhovec, T. (1991). A cold air lake formation in a basin ? a simulation with a mesoscale numerical model. *Meteorology and Atmospheric Physics*, 46(1-2):91–99.

Wagner, A. (1938). Theorie und Beobachtung der periodischen Gebirgswinde (Theory and observation of periodic mountain winds). *Gerlands Beitr. Geophys*, 52:408–449.

Wagner, J., Gerz, T., Wildmann, N., and Gramitzky, K. (2019). Long-term simulation of the boundary layer flow over the double-ridge site during the Perdigão 2017 field campaign. *Atmospheric Chemistry and Physics*, 19(2):1129–1146.

Wakimoto, R. M. and MacElroy, J. L. (1986). Lidar Observation of Elevated Pollution Layers over Los Angeles. *Journal of Applied Meteorology and Climatology*, pages 1583–1599.

Weber, R. O. and Kaufmann, P. (1998). Relationship of Synoptic Winds and Complex Terrain Flows during the MISTRAL Field Experiment. *JOURNAL OF APPLIED METEOROLOGY*, 37:11.

Weber, S., Uzu, G., Calas, A., Chevrier, F., Besombes, J.-L., Charron, A., Salameh, D., Jeek, I., Monik, G., and Jaffrezo, J.-L. (2018). An apportionment method for the oxidative potential of atmospheric particulate matter sources: application to a one-year study in Chamonix, France. *Atmospheric Chemistry and Physics*, 18(13):9617–9629.

Weijers, E. P., Schaap, M., Nguyen, L., Matthijsen, J., Denier van der Gon, H. A. C., ten Brink, H. M., and Hoogerbrugge, R. (2011). Anthropogenic and natural constituents in particulate matter in the Netherlands. *Atmospheric Chemistry and Physics*, 11(5):2281–2294.

Westerhuis, S., Fuhrer, O., Cermak, J., and Eugster, W. (2020). Identifying the key challenges for fog and low stratus forecasting in complex terrain. *Quarterly Journal of the Royal Meteorological Society*, 146(732):3347–3367.

Weyn, J. A., Durran, D. R., and Caruana, R. (2019). Can Machines Learn to Predict Weather? Using Deep Learning to Predict Gridded 500hPa Geopotential Height From Historical Weather Data. *Journal of Advances in Modeling Earth Systems*.

Whiteman, C. and Dreiseitl, E. (1984). Alpine meteorology: translations of classic contributions by A. Wagner, E. Ekhart, and F. Defant. Technical Report PNL-5141, ASCOT-84-3, 6665518.

Whiteman, C. D. (1982). Breakup of Temperature Inversions in Deep Mountain Valleys Part I. Observations.pdf. *Journal of Applied Meteorology and Climatology*, 21(3):270–289.

Whiteman, C. D. (2000). *Mountain meteorology: fundamentals and applications*. Oxford University Press, New York.

Whiteman, C. D., Bian, X., and Zhong, S. (1999). Wintertime Evolution of the Temperature Inversion in the Colorado Plateau Basin. *Journal of Applied Meteorology*, 38(8):1103–1117.

Whiteman, C. D. and Doran, J. C. (1993). The Relationship between Overlying Synoptic-Scale Flows and Winds within a Valley. *Journal of Applied Meteorology*, 32(11):1669–1682. Publisher: American Meteorological Society.

Whiteman, C. D., Hoch, S. W., Horel, J. D., and Charland, A. (2014). Relationship between particulate air pollution and meteorological variables in Utah's Salt Lake Valley. *Atmospheric Environment*, 94:742–753.

Whiteman, C. D., Zhong, S., Shaw, W. J., Hubbe, J. M., Bian, X., and Mittelstadt, J. (2001). Cold Pools in the Columbia Basin. *Weather and Forecasting*, 16(4):432–447.

Woollings, T., Franzke, C., Hodson, D. L. R., Dong, B., Barnes, E. A., Raible, C. C., and Pinto, J. G. (2015). Contrasting interannual and multidecadal NAO variability. *Climate Dynamics*, 45(1-2):539–556.

Xie, B., Fung, J. C. H., Chan, A., and Lau, A. (2012). Evaluation of nonlocal and local planetary boundary layer schemes in the WRF model: EVALUATION OF PBL SCHEMES IN WRF. *Journal of Geophysical Research: Atmospheres*, 117(D12):n/a–n/a.

Zardi, D., Falocchi, M., Giovannini, L., Tirler, W., Tomasi, E., Antonacci, G., Ferrero, E., Alessandrini, S., Jimenez, P. A., Kosovic, B., and Delle Monache, L. (2021). The Bolzano Tracer Experiment (BTEX). *Bulletin of the American Meteorological Society*, 102(5):E966–E989.

Zardi, D. and Whiteman, C. D. (2013). Diurnal Mountain Wind Systems. In Chow, F. K., De Wekker, S. F., and Snyder, B. J., editors, *Mountain Weather Research and Forecasting: Recent Progress and Current Challenges*, Springer Atmospheric Sciences, pages 35–119. Springer Netherlands, Dordrecht.

Zheng, T., Li, B., Li, X.-B., Wang, Z., Li, S.-Y., and Peng, Z.-R. (2021). Vertical and horizontal distributions of traffic-related pollutants beside an urban arterial road based on unmanned aerial vehicle observations. *Building and Environment*, 187:107401.

Zhong, S., Whiteman, C. D., Bian, X., Shaw, W. J., and Hubbe, J. M. (2001). Meteorological Processes Affecting the Evolution of a Wintertime Cold Air Pool in the Columbia Basin. *Monthly Weather Review*, 129(10):2600–2613.

Zhou, B. and Chow, F. K. (2014). Nested Large-Eddy Simulations of the Intermittently Turbulent Stable Atmospheric Boundary Layer over Real Terrain. *Journal of the Atmospheric Sciences*, 71(3):1021–1039.

Zilitinkevich, S. S., Elperin, T., Kleeorin, N., Rogachevskii, I., and Esau, I. (2013). A Hierarchy of Energy- and Flux-Budget (EFB) Turbulence Closure Models for Stably-Stratified Geophysical Flows. *Boundary-Layer Meteorology*, 146(3):341–373.

Zängl, G. (2004). A reexamination of the valley wind system in the Alpine Inn Valley with numerical simulations. *Meteorology and Atmospheric Physics*, 87(4):241–256.

Zängl, G., Gantner, L., Hartjenstein, G., and Noppel, H. (2004). Numerical errors above steep topography: A model intercomparison. *Meteorologische Zeitschrift*, 13(2):69–76.

Abbreviations

$\mathcal{E}_1$ episode from 7th December 2013 to 18th December 2013

$\mathcal{E}_2$ episode from 1st December 2016 to 5th December 2016

$\mathcal{E}_3$ episode from 6th December 2016 to 11th December 2016

$\mathcal{E}_4$ episode from 28th December 2016 to 2nd January 2017 1st

$\mathcal{W}_1$ weather type decomposition from section 2.4.2

$\mathcal{W}_2$ weather type decomposition from section 2.4.3

$\mathcal{W}_3$ weather type decomposition from section 2.4.4

$\mathcal{W}_4$ classification from section 2.4.5

PM$_{10}$ particulate matter with diameter of less than 10 µm

PM$_{2.5}$ particulate matter with diameter of less than 2.5 µm

ABL atmospheric boundary layer

CAP cold air pool

CLC Corine Land Cover

ERA5 reanalysis data from the European Centre for Medium-Range Weather Forecasts

INA interpolated advection

K-means K-Means algorithm (Hartigan and Wong (1979))

PCAP persistent cold air pool

PDF probability density function

PM particulate matter

SGS subgrid scale

SLP sea-level pressure

SNAP Selected Nomenclature for Air Pollution

SSA single station advection

WAB winter anticyclonic blocking

WPS WRF Pre-processing System

WRF Weather and Research Forecasting

WTD Weather Type Decomposition

WT weather type

ANN artificial neural network

AR atlantic ridge (WT name)

CNN convolutional neural network

Conv convolutional

ConvLSTM convolutional long short term memory

CS critical stagnation zone

DALY disability adjusted life years

ECMWF European Centre for Medium-Range Weather Forecasts

EEA European Environment Agency

HAC hierarchical ascendant clustering

LES large eddy simulation

LSTM long short term memory

LV low ventilation zone

MAE mean absolute error

NAO north atlantic oscillation

NWP numerical weather prediction

PBL planetary boundary layer

PCA principal component analysis

R recirculation zone

RMSE root mean squared error

S stagnation zone

TAF topographic amplification factor

V ventilation zone

Nomenclature

δt_s sound timestep

δt integration timestep

Δx horizontal resolution in x direction

Δy horizontal resolution in y direction

Δz vertical resolution

$\mathbf{T_{2m}}$ 2-meter air temperature

$\mathbf{T}$ temperature

θ potential temperarure

E_k turbulent kinetic energy

g acceleration due to gravity on Earth

Pr Prandtl number

r Pearson correlation coefficient

ϕ_m maximum slope angle in the topography

ρ air density

$\mathbf{K}_h$ subgrid scale turbulent diffusion for heat

$\mathbf{K}_m$ subgrid scale turbulent diffusion for momentum

c_p specific heat capacity of air at a constant pressure

H heat deficit (Whiteman et al. (1999))

l_m subgrid scale mixing length

n_x number of points in the x direction

n_y number of points in the y direction

$\mathbf{N}$ Brunt Vaisala frequency

$\mathbf{U}$ horizontal west -> east wind component

$\mathbf{V}$ horizontal south -> north wind component

$\mathbf{R}_i$ Richardson number

$\mathbf{Z}_{500}$ geopotential at 500 hPa

Appendix A

Supplementary figures

Figure A.1: 0.5m resolution aerial view of each available measurement station. Each square spans over 250 meters in each cardinal direction from the station. North points toward the top of each plot. Corresponding land-use in the model are presented in 3.10. *Data source :* `https://geoservices.ign.fr/documentation/diffusion/telechargement-donnees-libres.html`

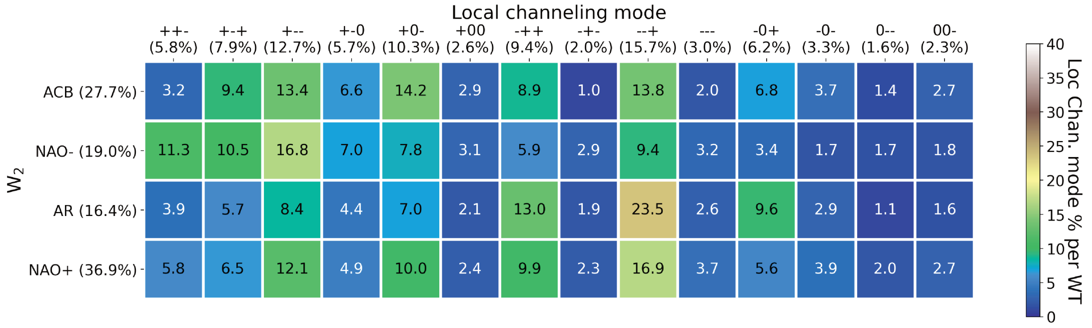

W_2	++- (5.8%)	+-+ (7.9%)	+-- (12.7%)	+-0 (5.7%)	+0- (10.3%)	+00 (2.6%)	-++ (9.4%)	-+- (2.0%)	--+ (15.7%)	--- (3.0%)	-0+ (6.2%)	-0- (3.3%)	0-- (1.6%)	00- (2.3%)
ACB (27.7%)	3.2	9.4	13.4	6.6	14.2	2.9	8.9	1.0	13.8	2.0	6.8	3.7	1.4	2.7
NAO- (19.0%)	11.3	10.5	16.8	7.0	7.8	3.1	5.9	2.9	9.4	3.2	3.4	1.7	1.7	1.8
AR (16.4%)	3.9	5.7	8.4	4.4	7.0	2.1	13.0	1.9	23.5	2.6	9.6	2.9	1.1	1.6
NAO+ (36.9%)	5.8	6.5	12.1	4.9	10.0	2.4	9.9	2.3	16.9	3.7	5.6	3.9	2.0	2.7

Figure A.2: Distribution for winters from 2011 to 2017 of local atmospheric circulation modes according to each of the $\mathcal{W}_2$ regimes.

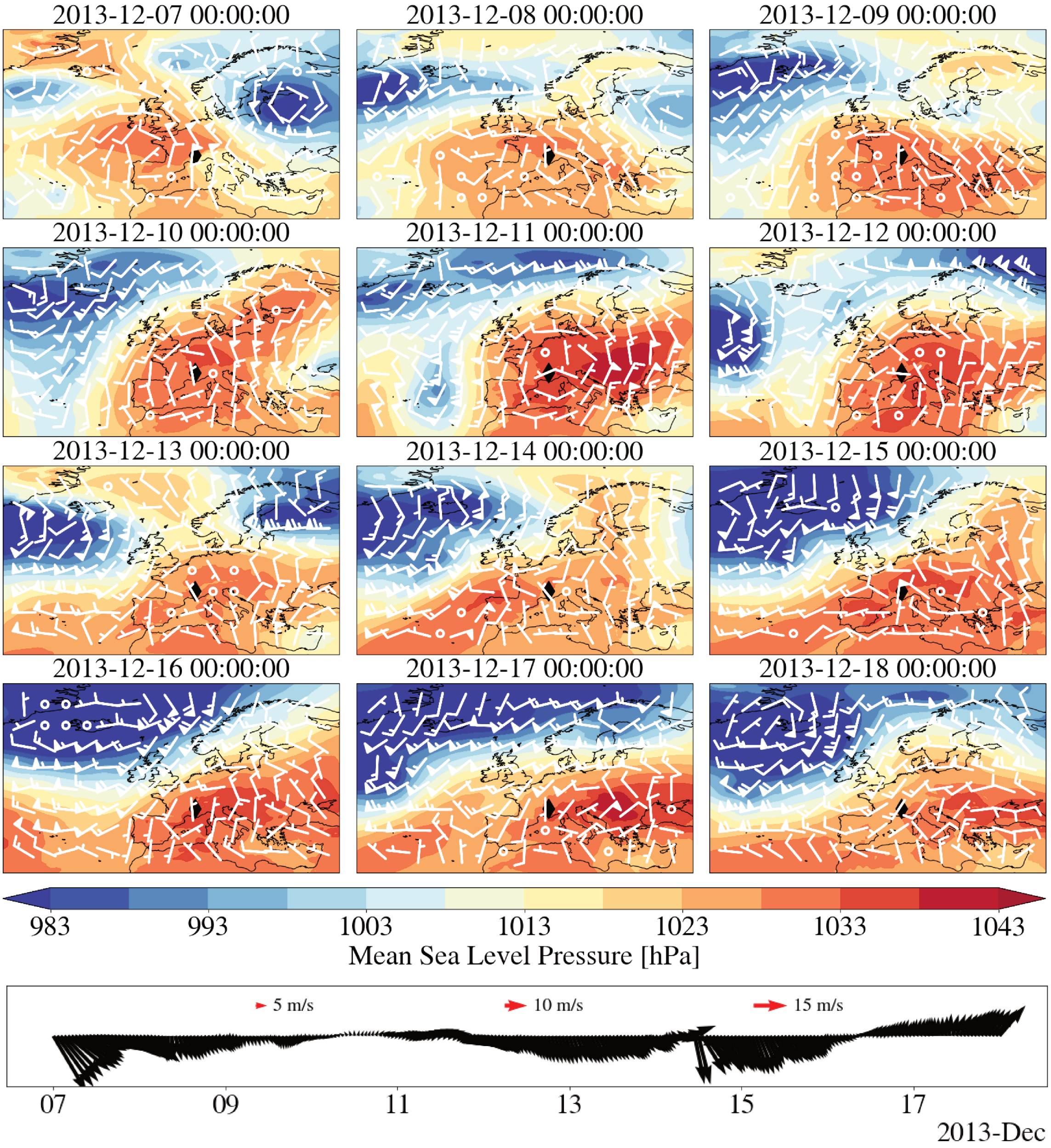

Figure A.3: SLP and 700 hPa winds from ERA5 for $\mathcal{E}_1$. *The black diamond locates Grenoble. For the wind speeds, half bar, full bar and flag represent respectively 5,10 and 20 meters per second.* The figure below shows the wind speed and direction at 700 hPa from ERA5 near Grenoble (45.25, 5.75). *This figure is associated with the description of* $\mathcal{E}_1$ *in section 3.1.2.1.*

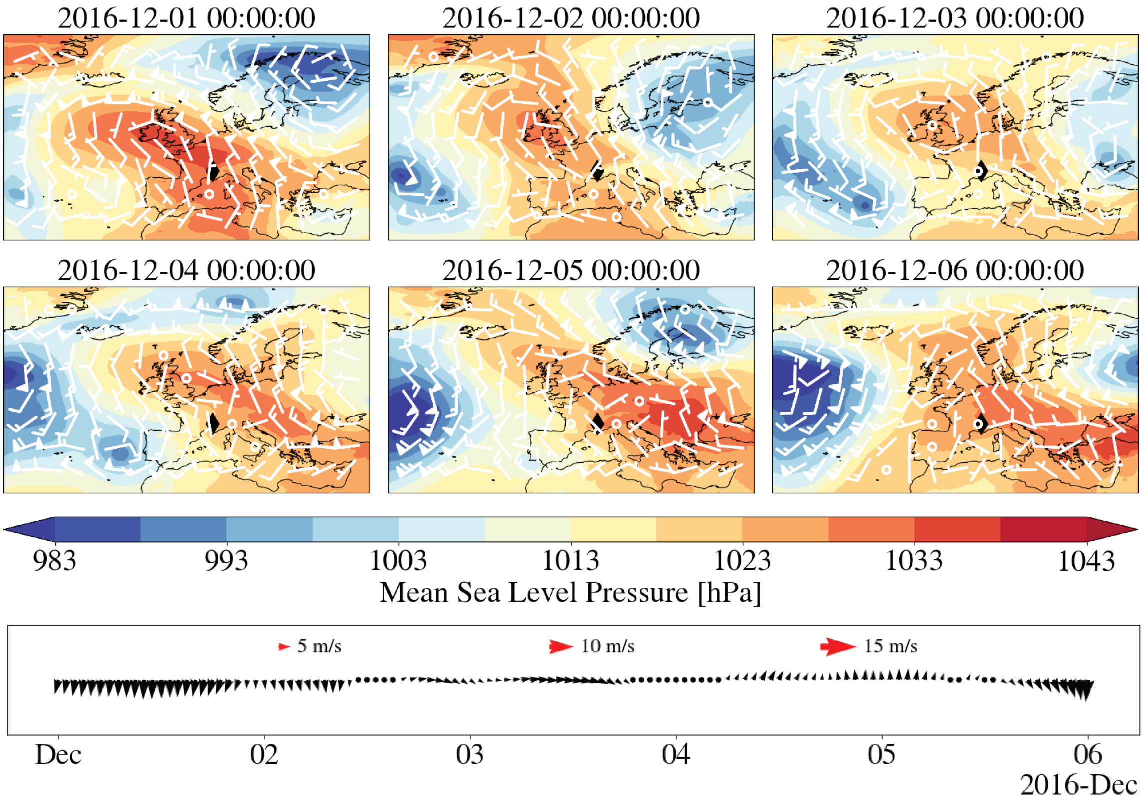

Figure A.4: SLP and 700 hPa winds from ERA5 for $\mathcal{E}_2$. *The black diamond locates Grenoble. For the wind speeds, half bar, full bar and flag represent respectively 5,10 and 20 meters per second.* The figure below shows the wind speed and direction at 700 hPa from ERA5 near Grenoble (45.25, 5.75). *This figure is associated with the description of* $\mathcal{E}_2$ *in section 3.1.2.2.*

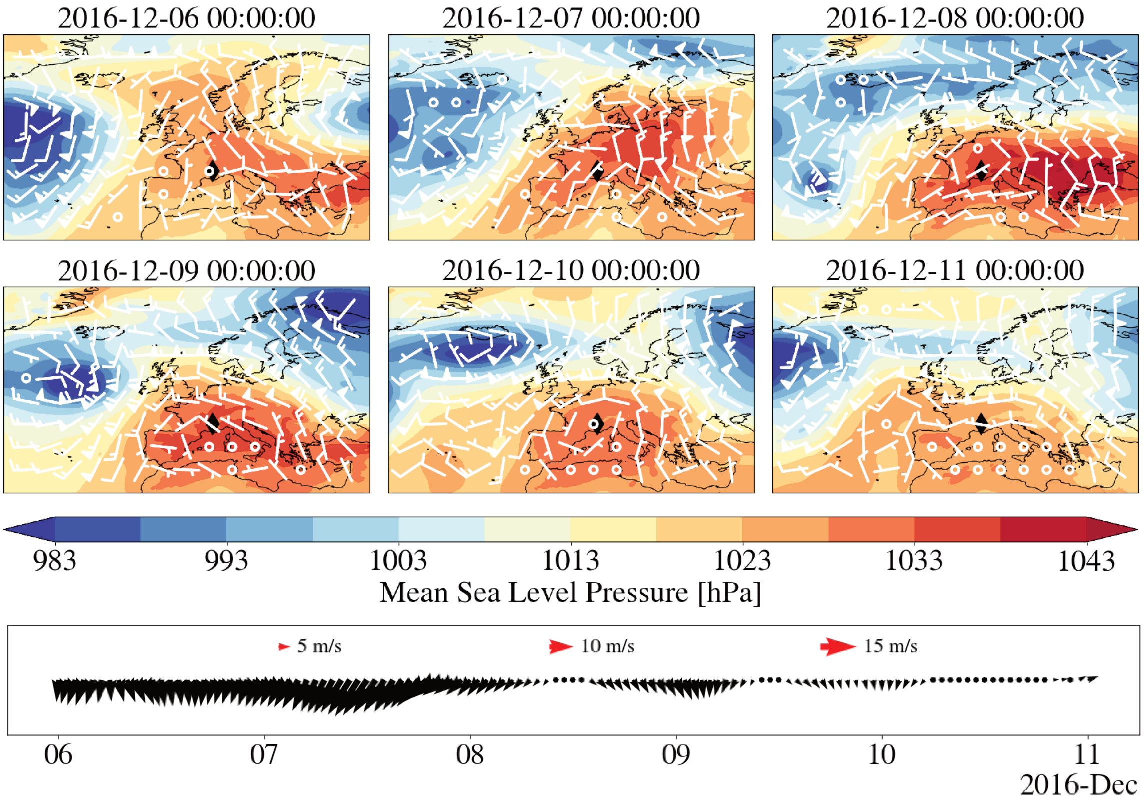

Figure A.5: SLP and 700 hPa winds from ERA5 for $\mathcal{E}_3$. *The black diamond locates Grenoble. For the wind speeds, half bar, full bar and flag represent respectively 5,10 and 20 meters per second.* The figure below shows the wind speed and direction at 700 hPa from ERA5 near Grenoble (45.25, 5.75). *This figure is associated with the description of* $\mathcal{E}_3$ *in section 3.1.2.3.*

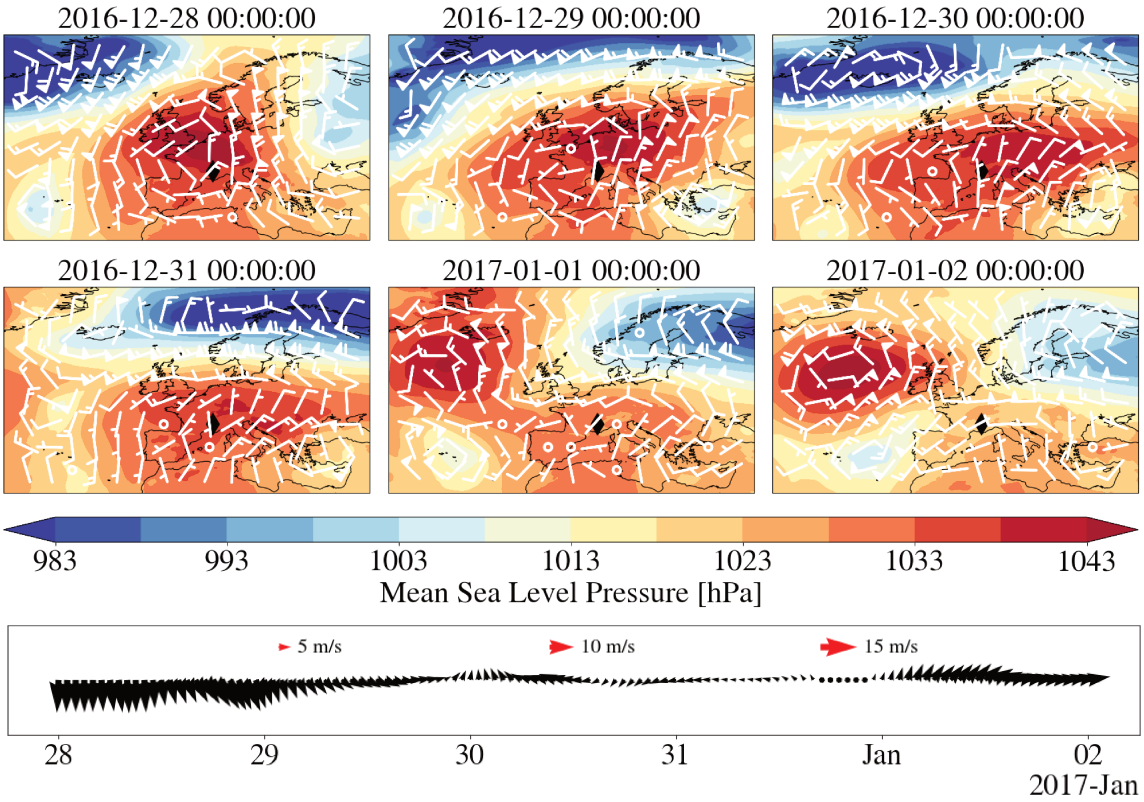

Figure A.6: SLP and 700 hPa winds from ERA5 for $\mathcal{E}_1$. *The black diamond locates Grenoble. For the wind speeds, half bar, full bar and flag represent respectively 5,10 and 20 meters per second.* The figure below shows the wind speed and direction at 700 hPa from ERA5 near Grenoble (45.25, 5.75). *This figure is associated with the description of $\mathcal{E}_4$ in section 3.1.2.4.*

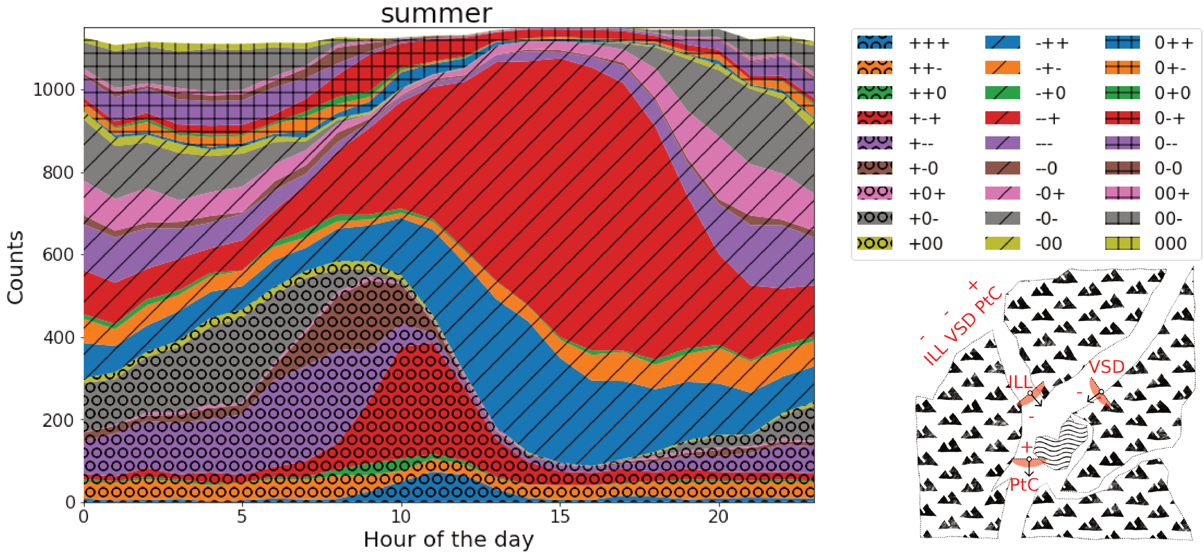

Figure A.7: Frequency of occurrence of each of the 27 local circulation modes as a function of the hour of day for summers from 2011 to 2018. The bottom right figure recalls the naming conventions for local inner-valley atmospheric circulation modes introduced in 2.4.2.

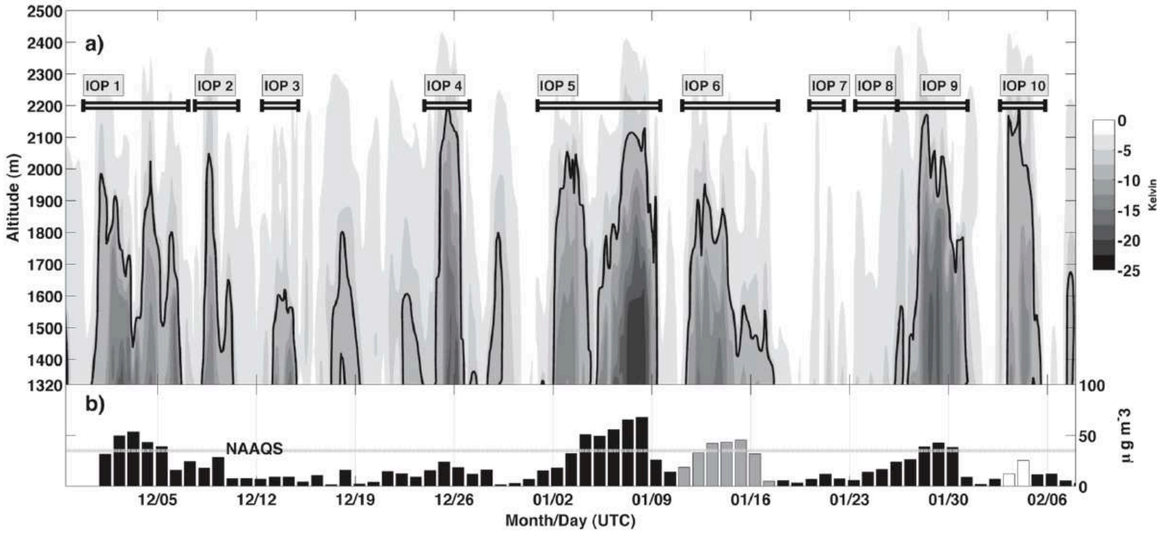

FIG. 3. Potential temperature deficit (K) during the PCAPS period 1 Dec 2010–7 Feb 2011. The deficit is taken relative to the potential temperature at 2,500 m MSL. Darker colors within the solid black line denote a potential temperature deficit greater than 8 K (i.e., a strong CAP). The span of each IOP is indicated by the labeled horizontal lines. The details of each IOP are included in Table 1. (b) The 0000–0000 MST (0700–0700 UTC) daily average $PM_{2.5}$ concentration measured at the Hawthorne Elementary (dark bars), Rose Park (gray bars), and Cottonwood (white bars) DAQ monitoring locations within the SLV. Data from Rose Park and Cottonwood are used when Hawthorne Elementary data are unavailable. The NAAQS of 35 μg m^{-3} is indicated by the gray horizontal line.

Figure A.8: Reproduction of Figure 3 from Lareau et al. (2013)

Circulation atmosphérique hivernale dans le bassin Grenoblois : caractérisation et impact sur la qualité de l'air

Wintertime characteristic atmospheric circulation in the Grenoble basin and impact on air pollution

Résumé

Ce travail de thèse porte sur le transport et la distribution spatiale de polluants de type particules fines dans la vallée alpine de Grenoble en hiver. Il est motivé par l'impact sanitaire de l'exposition à la pollution dans la vallée, qui se fait sur un temps long.

Temps long et échelles spatiales de la vallée ne pouvant être pris en compte simultanément dans le cadre d'une étude détaillée du transport de polluants, la première partie du travail de thèse concerne la recherche de types de temps à l'échelle synoptique qui puissent être chacun associés à une dynamique caractéristique dans la vallée de Grenoble. Pour obtenir cette décomposition en type de temps, des méthodes classiques (ACP+Kmeans) et moins classiques (réseau de neurones LSTM convolutifs) sont comparées. L'introduction de la composante temporelle ainsi que des contraintes reliant les échelles synoptiques et locales sont aussi étudiées. Il en résulte que, si un nombre restreint de type de temps est recherché, seul celui correspondant au blocage anticyclonique hivernal semble produire une réponse locale caractéristique.

Dans la seconde partie du travail de thèse, l'impact de la variabilité au sein du type de temps blocage anticyclonique hivernal sur cette réponse locale est étudié, via la simulation de quatre épisodes présentant des caractéristiques différentes. Des Simulations des Grandes échelles à haute résolution (jusqu'à 100 mètres environ de résolution horizontale) sont menées pour cela, qui permettent de capturer la dynamique atmosphérique en terrain complexe. Le cadastre d'émission implémenté dans le modèle numérique permet, en combinaison avec la dynamique, d'avoir une représentation spatiale fine de la pollution atmosphérique.

D'un point de vue dynamique, il ressort que la circulation atmosphérique en fond de vallée est très homogène d'un épisode sur l'autre et pilotée par les effets thermiques. A l'inverse, la hauteur de l'inversion thermique et la structure verticale des vents de vallées dépendent des conditions synoptiques. Concernant la pollution atmosphérique, la dynamique dominante en fond de vallée conduit à de fortes hétérogénéités spatiales dont la localisation ne dépend pas de l'épisode considéré.

Mots-clés : Pollution atmosphérique ; Circulation atmosphérique ; Terrain complexe ; Simulations numériques

Abstract

This PhD work investigates the transport and spatial distribution of particulate matter in the alpine valley of Grenoble during wintertime. It is motivated by the adverse health effects that impact the inhabitants of the valley as a result of long term exposition to pollutants.

Since detailed numerical modeling of the dispersion of pollutants at fine spatial scales is unpractical over long time scales, the first part of this PhD work attempts to identify large-scale weather types that can be associated with a characteristic atmospheric dynamics in the Grenoble valley. To obtain this weather type decomposition, classical (PCA+Kmeans) and less classical (convolutional LSTM neural network) methods are compared. The introduction of the temporal component as well as constraints linking synoptic and local scales are also studied. The result is that, for a limited number of weather types, only the one corresponding to the winter anticyclonic blocking seems to produce a characteristic local response.

In the second part of the thesis, the impact of the variability within the winter anticyclonic blocking weather type on this local response is studied, via the simulation of four episodes with different characteristics. To this end, High Resolution Mesoscale Simulations (down to about 100 meters horizontal resolution) are used to accurately capture the dynamics in complex terrain. The emission inventory implemented in the numerical model allows, in combination with the dynamics, to obtain an accurate spatial representation of the air pollution.

From a dynamical point of view, it appears that the atmospheric circulation at the valley bottom is very homogeneous from one episode to the next and driven by thermal effects. Conversely, the height of the thermal inversion and the vertical structure of the valley winds depend on the synoptic conditions. Concerning atmospheric pollution, the main result is that the concentration fields at the valley bottom are similar from one episode to the other because the winds flowing along the valley floor are similar. This concentration field contains the same hot spots of pollution whatever the episode, implying that the population living there might be exposed to poor air quality during anticyclonic winter episodes.

Keywords : Air pollution ; Atmospheric dynamics ; Complex Terrain ; Numerical simulations